

# JOURNAL OF TELECOMMUNICATIONS AND INFORMATION TECHNOLOGY

1/2022

## Enhancing Moon Crescent Visibility Using Contrast-Limited Adaptive Histogram Equalization and Bilateral Filtering Techniques

*W. N. J. H. W. Yussof et al.*

*Paper*

3

## Novel Feature Extraction for Pineapple Ripeness Classification

*H. H. Wang and S. Y. Chai*

*Paper*

14

## A Comparative Study of Various Edge Detection Techniques for Underwater Images

*E. A. Awalludin et al.*

*Paper*

23

## Detection of Monocrystalline Silicon Wafer Defects Using Deep Transfer Learning

*A. Ganum et al.*

*Paper*

34

## Preliminary Evaluation of Convolutional Neural Network Acoustic Model for Iban Language Using NVIDIA NeMo

*S. O. Michael, S. S. Juan, and E. Mit*

*Paper*

43

## How to Model an Engaging Online Quiz? The Emotion Modeling Approach

*S. F. binti Zulkifli et al.*

*Paper*

54

## Implementation of a Malicious Traffic Filter Using Snort and Wireshark as a Proof of Concept to Enhance Mobile Network Security

*R. Afzal and R. K. Murugesan*

*Paper*

64

## A DFT-based Low Complexity LMMSE Channel Estimation Technique for OFDM Systems

*J. P. Patra, B. B. Pradhan, and P. Singh*

*Paper*

72

(Contents Continued on Back Cover)

## ***Editor-in-Chief***

**Adrian Kliks**, *Poznan University of Technology, Poland*

## ***Steering Editor***

**Pawel Pławiak**, *National Institute of Telecommunications, Poland*

## ***Editorial Advisory Board***

**Hovik Baghdasaryan**, *National Polytechnic University of Armenia, Armenia*

**Naveen Chilamkurti**, *LaTrobe University, Australia*

**Luis M. Correia**, *Instituto Superior Técnico, Universidade de Lisboa, Portugal*

**Luca De Nardis**, *DIET Department, University of Rome La Sapienza, Italy*

**Nikolaos Dimitriou**, *NCSR "Demokritos", Greece*

**Ciprian Dobre**, *Politechnic University of Bucharest, Romania*

**Filip Idzikowski**, *Poznan University of Technology, Poland*

**Andrzej Jajszczyk**, *AGH University of Science and Technology, Poland*

**Albert Levi**, *Sabancı University, Turkey*

**Marian Marciniak**, *National Institute of Telecommunications, Poland*

**George Mastorakis**, *Technological Educational Institute of Crete, Greece*

**Constantinos Mavromoustakis**, *University of Nicosia, Cyprus*

**Klaus Mößner**, *Technische Universität Chemnitz, Germany*

**Imran Muhammad**, *King Saud University, Saudi Arabia*

**Mjumo Mzyece**, *University of the Witwatersrand, South Africa*

**Daniel Negru**, *University of Bordeaux, France*

**Ewa Orłowska**, *National Institute of Telecommunications, Poland*

**Jordi Perez-Romero**, *UPC, Spain*

**Michał Pióro**, *Warsaw University of Technology, Poland*

**Konstantinos Psannis**, *University of Macedonia, Greece*

**Salvatore Signorello**, *University of Lisboa, Portugal*

**Adam Wolisz**, *Technische Universität Berlin, Germany*

**Tadeusz A. Wysocki**, *University of Nebraska, USA*

## ***Publications Staff***

Content Editor: **Robert Magdziak**

Managing Editor: **Ewa Kapuściarek**

Technical Editor: **Grażyna Woźnica**

on-line: ISSN 1899-8852

© Copyright by National Institute of Telecommunications, Warsaw 2022

# JOURNAL OF TELECOMMUNICATIONS AND INFORMATION TECHNOLOGY

## *Inspiring Technologies for Digital Inclusivity*

Today digitalization becomes more and more important. Many countries have already channeled their effort to embrace digital inclusion as their main national agenda. However, there are still many challenges when harnessing digital technologies. One of the challenges is digital inclusivity. *Inspiring Technologies for Digital Inclusivity* has been chosen as the theme of the *12th International Conference on IT in Asia (CITA'21)*, which is perfectly align with the challenge.

CITA'21 is a regular series of biennial conferences organized since 1999 by the Faculty of Computer Science and Information Technology, Universiti Malaysia Sarawak, Malaysia. High quality articles have been selected from the papers submitted to the conference. There were overall 31 submissions. The papers were double-blind reviewed by at least two international experts in the field. Reviewers were selected by the *Special Issue Editor*. Final acceptance decisions were released by the *Editor-in-Chief after the recommendation from the reviewers and Special Issue Editor*. A total of seven articles were accepted (acceptance rate: 22%) for publication in the *Journal of Telecommunications and Information Technology*.

It is our highest privilege to collaborate with the *JTIT* editorial team and publish the selected articles in the special issue. It is noteworthy to mention that the *JTIT* only accepts high quality articles and practices a stringent yet effective process. Furthermore, the editorial team has been very responsive and efficient which made the collaboration not only very successful but also gratifying.

This special issue contains seven articles that include the area of image processing, artificial intelligence and mobile security. These articles are well suited for the selected theme and they are pertinent to the aims and scope of the *JTIT*.

Image processing is one of the important areas in computer vision and its advancement has contributed a lot in real-life applications. The article entitled *Enhancing Moon Crescent Visibility using Contrast-Limited Adaptive Histogram Equalization and Bilateral Filtering Techniques* has automated the determination of the religious festivals date based on the analysis of digital images. The article *Novel Feature Extraction for Pineapple Ripeness*

*Classification* investigates identification methods of ripeness level of pineapples. The authors have proposed a method that consists of six stages. Its core component is based on the analysis of color elements in the digital images. *A Comparative Study of Various Edge Detection Techniques for Underwater Images* is another article that contributes to the image processing area. The authors have used underwater images that contain coral reef images as their case study. Since underwater images are usually suffering from distortion and light attenuation, an efficient edge detection technique is very important. From the comparative study conducted, Canny edge detection technique has shown superior performance compared to other techniques for the underwater images.

The second research area covered in the special issue is artificial intelligence. The first two articles study deep learning and the third one examines agent-oriented modeling. The paper entitled *Detection of Monocrystalline Silicon Wafer Defects using Deep Transfer Learning* uses deep learning technique to detect defects in monocrystalline silicon wafer for industrial production. The proposed technique is able to detect and classify defected samples into six types, namely crack, double contrast, hole, microcrack, saw-mark and stain. The next article that uses deep learning is *Preliminary Evaluation of Convolutional Neural Network Acoustic Model for Iban Language Using NVIDIA NeMo*. The main objective of this article is to investigate and evaluate the utilization of convolutional neural networks for an under-resourced language in performing the automatic speech recognition task. Due to COVID-19 pandemic, education has encountered a major shift. Learning technology like Massive Open Online Courses is introduced to prepare a more engaging and interesting learning environment for students. The article, *How to Model an Engaging Online Quiz? The Emotion Modeling Approach* contributes to this shift by proposing a systematic method that is based on the agent-oriented approach. The main component is to model an engaging application through emotion modeling.

Advancement of digital technologies has led to the emergence of security concerns. They are appropriate and justified as digitalization processes involve a large volume of data communications and transactions. Needless to say, that data and information involved face increased risks and security threats. The article *Implementation of a Malicious Traffic Filter Using Snort and Wireshark as a Proof of Concept to Enhance Mobile Network Security* investigates mobile network security and proposes an anomalies detection mechanism. It works by identifying malformed parameters and intra-layer parameter discrepancies of SS7 network protocol layers.

Overall, the articles published in this special issue further emphasize the importance of information and communication technologies, especially for the digital inclusivity. The contributions of the articles have moved us a small step in the right direction, which in time may add up to a giant leap forward.

Kang Leng Chiew

 <https://orcid.org/0000-0002-0007-2608>

Faculty of Computer Science and Information Technology  
Universiti Malaysia Sarawak, Kota Samarahan, Malaysia

Josef Pieprzyk

 <https://orcid.org/0000-0002-1917-6466>

Institute of Computer Science  
Polish Academy of Sciences, Warsaw, Poland  
Data61, CSIRO, Sydney, Australia

Guest Editors

# Enhancing Moon Crescent Visibility Using Contrast-Limited Adaptive Histogram Equalization and Bilateral Filtering Techniques

Wan Nural Jawahir Hj Wan Yussof<sup>1</sup>, Mustafa Man<sup>1</sup>, Roslan Umar<sup>2</sup>, Ahmad Najmuddin Zulkeflee<sup>2</sup>, Ezmahamrul Afreen Awalludin<sup>1</sup>, and Nazhatulshima Ahmad<sup>3</sup>

<sup>1</sup> Universiti Malaysia Terengganu, Malaysia, <sup>2</sup> Universiti Sultan Zainal Abidin, Malaysia, <sup>3</sup> University of Malaya, Malaysia

<https://doi.org/10.26636/jtit.2022.155721>

**Abstract**—Image enhancement is becoming increasingly important with the advancement of space exploration techniques and the technological development of more durable and scientifically sound observatories equipped with more powerful telescopes. The enhancement of images helps astronomers analyze the results and act toward determining the dates of religious festivals. This work describes a technique known as contrast-limited adaptive histogram equalization (CLAHE) with grayscale contrast enhancement and bilateral filtering. We apply CLAHE on the L component of the CIE-Lab color space to adjust lightness contrast. Subsequently, grayscale contrast enhancement is performed to increase the visibility of the moon crescent. Noise caused by grayscale contrast enhancement is reduced using bilateral filtering. Two quantitative measures are selected (PSNR and MSE) to show the visual improvement achieved by the proposed algorithm.

**Keywords**— *bilateral filtering, CIE-Lab, CLAHE, image enhancement, moon crescent.*

## 1. Introduction

Image enhancement is an essential step in image processing. It improves an image's quality and visual appearance, so that the output is best suited for a specific goal [1]. Image enhancement techniques are used in different applications, such as face [2] and fingerprint recognition [3], watermarking [4], medical image processing [5]–[9] and many others [10], [11]. The aim is to achieve the finest image quality possible, since it influences the accuracy of information retrieval and interpretation process. Because each situation may necessitate a different approach, we should choose an enhancement technique based on the problems at hand and the properties of the image. Therefore, numerous enhancement methods have been proposed.

Medical imaging principles, for example, differ from general imaging principles. According to [8], many factors, such as the system used, random noise, sensor sensitivity,

analogue-to-digital conversion and so on, may impact the quality of medical imaging. Blurred edges and low contrast are experienced frequently, necessitating the need to enhance and highlight the image's detailed features in order to diagnose the disease. Some of the medical image enhancement methods have been proposed in recent years by [5]–[8]. Paper [5] proposed a generalized training approach that integrates previous anatomical information into CNNs via a new end-to-end regularization model. The new framework encourages models to adopt the underlying anatomy, referred to as image priors, through learnt nonlinear representations of the shape. Article [6] used an adaptive threshold and an improved fuzzy set based on the nonsubsampling contourlet transform (NSCT). The authors divided the original image into the NSCT domain using a low-frequency sub-band and multiple high-frequency sub-bands before applying a linear transformation to the coefficients of the low frequency component. They utilized an adaptive threshold technique to remove high-frequency image noise, and increased the global contrast level and enhanced image details by using an improved fuzzy set and the Laplace operator.

Enhancement techniques for satellite images are a promising trend, and there are several possibilities for improving the visual quality of remotely sensed images. Paper [12] reviewed several hyperspectral image enhancement methods and categorized them as non-fusion-based and fusion-based. Non-fusion-based enhancement methods concentrate on the spatial resolution of hyperspectral imaging systems. Meanwhile, their fusion-based counterparts combine a low spatial resolution hyperspectral image with auxiliary information to generate a high spatial resolution scene. Examples of non-fusion-based methods include the one proposed by [13]. Its authors trained BPNN relying on the learning-based technique and using low-resolution images and down-sampled versions. Then, they performed a super-resolution by taking into account the spatial correlation of various materials in hyperspectral images. These hyperspec-

tral images were used as training data for enhancing the coherence of the improved and original hyperspectral images. Satellite images are also prone to suffer from uneven illumination. To solve this problem, paper [14] proposed a spatially-adaptive gamma correction (SAGC) method that used relative total variation (RTV). With this method, its authors obtained two types of images with strong and weak structures. The one with strong structures is the base image, and the other one with weak structures, is the detailed image. They used an adaptive gamma correction method to enhance the base image, while an enhancement factor was relied upon to correct the detailed image. Subsequently, by combining these two images, they produced a high-contrast optical remote sensing image. The authors of [15] developed an enhancement method to identify both spatial and spectral response operators using multispectral and hyperspectral fusion models. This method yielded colors and brightness that were more akin to a low-resolution hyperspectral image.

In [16], the authors conducted an in-depth review of more than 120 underwater image enhancement and restoration studies. Remarkable progress that took place in underwater image visual quality in recent years was observed. The authors grouped the underwater enhancement methods into filtering-based methods, color correction-based methods, image fusion-based methods and deep learning-based methods. Article [17] proposed utilizing a turbid image to produce a color-corrected image and a contrast-enhanced image using the fusion technique. These two images were combined using four weight maps: Laplacian contrast, local contrast, saliency, and exposedness. The authors of [18] used a convolutional neural network-based image enhancement model to train a synthetic underwater image database. Their model relied on an automated end-to-end and data-driven training process to reconstruct a clear latent underwater image.

To the best of our knowledge, there is currently a lack of studies on enhancing telescopic images over medical, remote sensing, or underwater images. However, the importance of the analysis of telescope-obtained images is the same as for other types of images. In this paper, we start by analyzing the importance of studying the visibility of the moon crescent in astronomy. There are many methods for determining when the holy months of Ramadan (fasting), Syawal (Hari Raya), and Zulhijjah (pilgrimage) begin. Several countries, such as Malaysia, Brunei, Indonesia, and Singapore, use the Imkanurrukyah (Rukyah and Hisab) technique. The crescent is defined as the moon crescent after the *ijtimak* that first appears or is visible after sunset. Physically, the current phase of the moon is small in size and is close to the position of the setting sun. In addition, the appearance of the crescent is influenced by several other factors, such as the position of the crescent, sunlight refraction, sky brightness and the rate of atmospheric extinction. Therefore, it is quite difficult to notice it. The appearance of the moon crescent is discussed, from a scientific point of view, in physical terms. Physical knowledge is used to per-

form calculations on the movement of the moon, the earth and the sun and to ensure that the following Imkanurrukyah criteria have been met [19]:

- the moon's altitude at sunset must be at least 2 degrees, and the elongation between the moon and the sun must be at least 3 degrees, or
- the moon's age after conjunction is at least 8 hours when the moon sets.

However, MABIMS agreed to use new criteria: moon's altitude at sunset must be at least 3 degrees and the elongation between the moon and the sun must be at least 6.4 degrees [20].

Various methods have been developed to determine the visibility limit of the youngest moon crescent that can be seen and observed in essence [21]. In the Rukyah method, new tools are used, such as a large telescope attached to a digital camera, for imaging the new moon crescent [22]. The use of large telescopes ensures a high degree of magnification and enhances the ability to identify the moon crescent. But the high amplification rate results also in high noise levels [23]. Moreover, no significant differences exist between the crescent and its background, making it indistinguishable [24]. Therefore, this paper aims at increasing visibility of the moon crescent through a method that is not new, but still relevant, namely by relying on CLAHE and bilateral filtering. We organize the remainder of the paper as follows. Section 2 presents some related works using CLAHE. Section 3 contains a description of the proposed work. The results are discussed in Section 4. Finally, Section 5 concludes the paper.

## 2. Related Works

Histogram equalization (HE) is a relatively simple image processing method used for adjusting contrast based on the image's histogram. In article [25], a comprehensive study of HE-based contrast enhancement methods was conducted. HE typically improves the global contrast of images with poor lighting. It re-maps the image's grayscale, so that the distribution of the resulting histogram is as close as possible to being uniform. With this adjustment, the intensities on the histogram can be dispersed more evenly. It improves contrast in areas with low local contrast. Although this approach is very straightforward to apply as it is less computationally demanding, it has the disadvantage of increasing the contrast of background noise while diminishing the usable sign. The adaptive histogram equalization (AHE) technique, as opposed to the standard approach, is capable of providing significantly better results in this situation.

AHE, which was independently developed by [26]–[28], differs from conventional HE. The adaptive method computes a histogram for each distinct section of the image. These histograms are used to redistribute the image's lightness values. Consequently, AHE is suitable for enhancing

edge definitions and improving local contrast in each region of the image. AHE has the disadvantage of being computationally slow. In addition, it tends to overamplify noise in the homogenous regions of the image. Consequently, paper [29] proposed a variation of AHE called contrast limited adaptive histogram equalization (CLAHE) in order to increase its speed and improve the enhanced image. Paper [29] showed the great success of their CLAHE algorithm applied to a computer tomography (CT) image of the chest, surface coil MRI of the spine and an X-ray angiogram. CLAHE has been widely applied to improve image contrast in various computer vision and pattern recognition applications [30]–[33].

With the current global pandemic, COVID-19 detection is a crucial challenge for medical practitioners. Medical practitioners have utilized a variety of tools and strategies to detect and prevent COVID-19 transmission. Paper [34] introduced the COVIDLite technique in which the white balance method is followed by CLAHE. Then, an analysis is performed by a depth-wise separable convolutional neural network in order to help radiologists detect COVID-19 patients based on CXR images. The authors of [35] used CLAHE to detect COVID-19 infections using CT lung scans. Additionally, they classified the images using a convolutional neural network (CNN). In [36], a pretty similar approach as that adopted by [35] is used to classify a total of 100 X-Ray chest images of COVID-19 patients as well as 100 X-Ray chest images of healthy individuals. Paper [37] improved the sensitivity of chest X-rays utilizing the pipeline for advanced contrast enhancement (PACE) method. This non-linear post-processing approach combines adequately fast and adaptive bidimensional empirical mode decomposition (FABEMD) and CLAHE. Based on this highlight, CLAHE is still being adopted and is increasingly important in improving image quality.

### 3. Proposed Work

To solve the issues discussed in Section 1, we adopt the CLAHE method to increase the visibility of the moon crescent in an image. Our enhancement approach consists of several steps. CLAHE is applied to the L component of the Lab color space to adjust the lightness contrast in the first step. After that, we convert the transformed image back to an RGB image. Then, we perform contrast enhancement

on a selected component of the transformed RGB image. Finally, we utilize the image denoising step, using bilateral filtering, to reduce noise caused by the contrast enhancement process. Figure 1 illustrates the proposed enhancement approach for improving the visibility of the moon crescent.

#### 3.1. CLAHE on Lab Image

Paper [29] proposed CLAHE to overcome contrast over-amplification introduced by AHE. CLAHE clips the histogram using a contrast factor, called a clip limit, that prevents over-saturation of the image, especially in homogeneous areas. A variation of the contrast-limited technique, called adaptive histogram clip (AHC), can also be used to moderate the over-enhancement of background regions of images. It works by adjusting the clipping level. The Rayleigh distribution is one of the AHC that normally used, producing a bell-shaped histogram. The function is defined as follows:

$$Rayleigh_g = g_{min} + \left[ 2(\alpha^2) \ln \left( \frac{1}{1 - P_f} \right) \right]^{0.5} \quad (1)$$

In this function,  $g_{min}$  denotes a minimum pixel value. Cumulative probability distribution is written as  $P(f)$ , and  $\alpha$  is a positive real scalar specifying the distribution parameter. The clip limit in this study is set to equal 0.005 and  $\alpha$  value in the Rayleigh distribution function is set to 0.04.

The Lab color space mathematically defines all perceptible colors in three dimensions: L for lightness, a and b for the four color components of human visions: red, green, blue and yellow. The name “lab” comes from the Hunter 1948 color space.  $L^*$ ,  $a^*$ , and  $b^*$  values are typically absolute and have a predetermined range.  $L^* = 0$  yields the darkest black, and  $L^* = 100$  indicates the brightest white. In contrast to the RGB and CMYK color models, Lab color is intended to simulate human perception. It strives for perceptual consistency, and its L component closely corresponds to the human experience of lightness. Therefore, we modify the lightness contrast using the L component, as illustrated in Fig. 2.

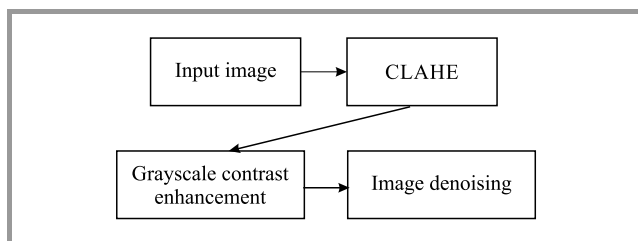


Fig. 1. The approach proposed to enhance the visibility of the moon crescent.

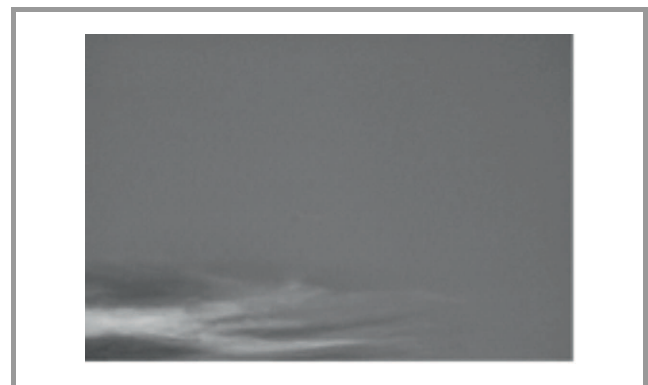
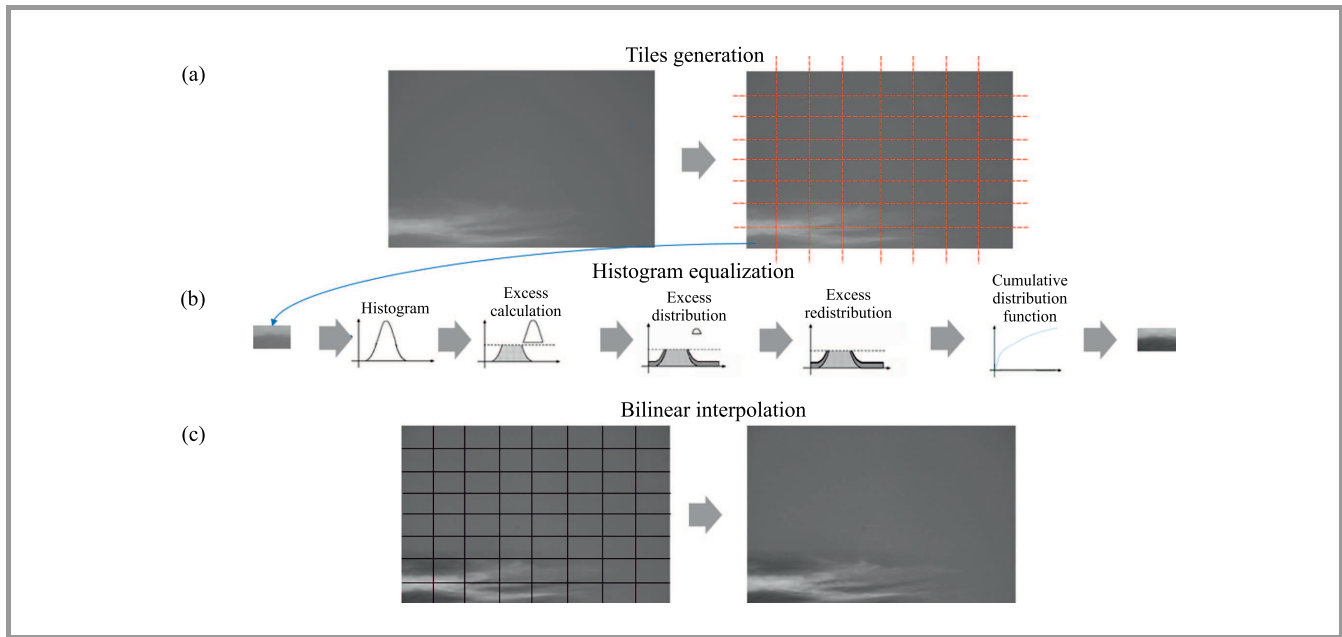


Fig. 2. L component of Lab image.



**Fig. 3.** CLAHE applied on L component of Lab color space.

The CLAHE algorithm, as presented in Fig. 3, is composed of three major parts:

1. Tile generation. The input image L is scaled into a range of [0–1] by dividing the L component by 100. As shown in Fig. 3a, it is first divided into  $8 \times 8$  sections called tiles.
2. Histogram equalization. This part consists of five steps:
  - Histogram computation. On each tile, calculate the histogram as a set of bins.
  - Excess calculation. Accumulate the histogram bin values that exceed the clip limit.
  - Excess distribution. Then, distribute them into other bins.
  - Excess redistribution. The redistribution will push specific bins back over the clip limit, allowing for an efficient clip limit that is more considerable than the specified limit, with its exact value depending on the image. If this is undesirable, recursively perform the redistribution procedure until the excess is negligible.
  - Scaling and mapping. Calculate the cumulative distribution function (CDF) for the histogram values. Then, scale and map the CDF values of each tile using the input image pixel values.
3. Bilinear interpolation. The resulting tiles are stitched using bilinear interpolation to improve the image contrast.

To convert again into RGB, we rescale the L component in the range of [0–100] by multiplying it by 100. In short,



**Fig. 4.** Result of CLAHE on Lab color space.

given an input image, a desired output image generated from CLAHE on Lab image is shown in Fig. 4. As per Fig. 4b, the image after CLAHE contains more detailed information, especially around the reddish-orange color part of the cloud.

To show that CLAHE is better than its counterpart in enhancing image quality, Fig. 5 presents images and their

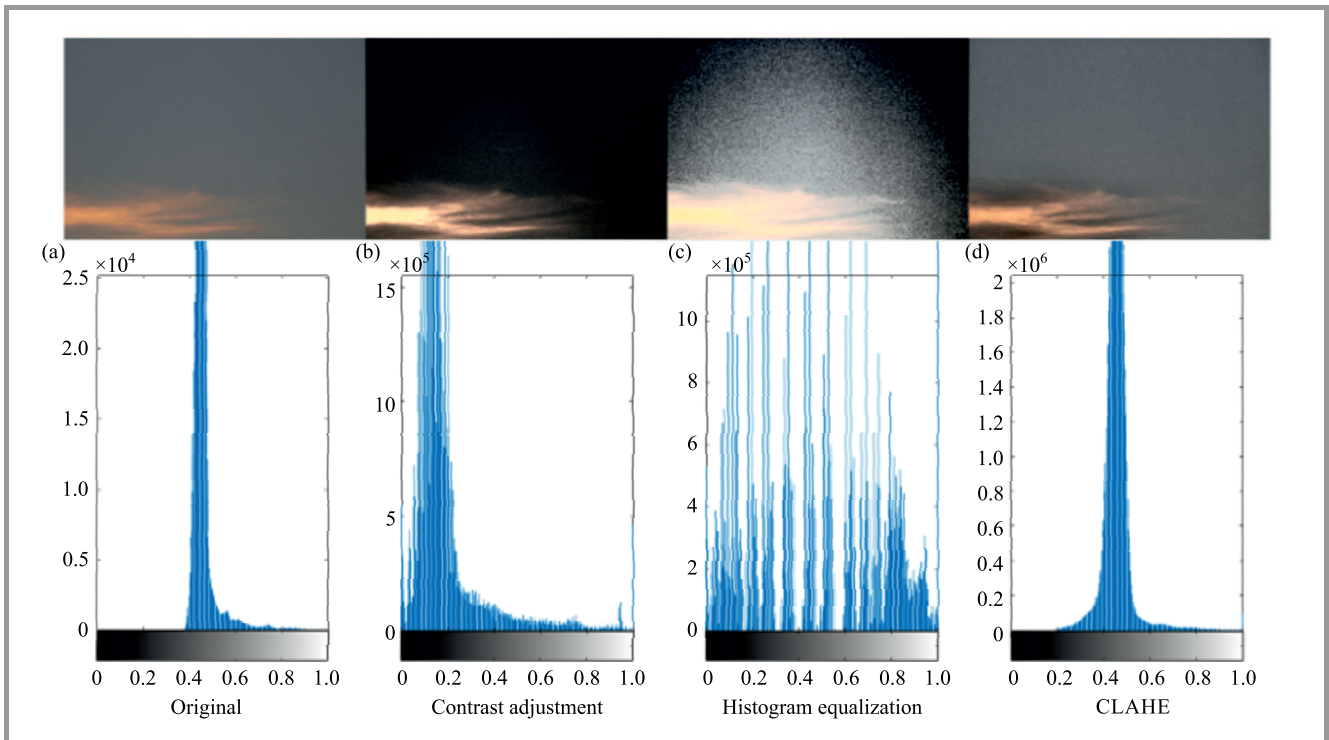


**Fig. 5.** Comparison between CLAHE and other enhancement techniques.

histogram distributions obtained with the use of three different methods. The left-most image is the original image. The second image is obtained by contrast adjustment (CA), while the third and the last images are obtained by using histogram equalization (HE) and CLAHE, respectively. It may be noticed in Fig. 5 that the original image consists primarily of grey color and a little bit of reddish-orange color, meaning that the middle bins show higher frequencies than the left and the right bins. When the CA process is applied, it saturates the bottom 1% and the top 1% of all pixel values, making the grey colors look darker and the reddish-orange color looks brighter than the original. HE distributes pixels equally at all levels, producing a uniform distribution of grey levels for the resulting image, but eventually, much noise is produced with this technique. Meanwhile, the result of CLAHE shows that it is clearly superior in preserving details and enhances the quality of the image significantly.

### 3.2. Grayscale Contrast Enhancement

The resulting image obtained from the previous process is used to select a component that is characterized by good moon crescent visibility. To do this, we calculate image histograms for the separated components. For each component, the histograms are distributed into three bins: 0, 0.5 and 1. The selection of components is based on the highest number of the middle bin (0.5 value), as compared to the left (0 value) and right (1 value) bins. This component is considered to be our grayscale image and is denoted by  $G(x,y)$ .

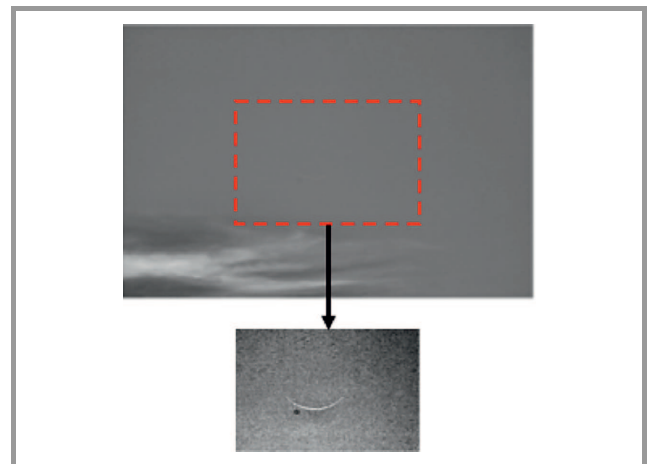


**Fig. 6.** Example of a result obtained with the grayscale contrast enhancement technique (bottom image). The upper CLAHE image is cropped to create the image at the bottom.

Next, we perform an auto-cropping process on the image to select the region of interest,  $I(x,y)$ . Based on the available data we know, that the moon is normally located in the center of the image. Therefore, the cropping process is performed by estimating the moon area from the center of the image with 40% of the original size (see Fig. 6). Using this cropped image, we further perform grayscale contrast enhancement by adjusting the image histogram based on the image's standard deviation. It is simply estimated using the following familiar expressions for mean,  $m$  and standard deviation,  $\sigma$ :

$$m = \frac{1}{MN} \sum_{x=0}^{M-1} \sum_{y=0}^{N-1} I(x,y) \quad (2)$$

and

$$\sigma = \sqrt{\frac{1}{MN} \sum_{x=0}^{M-1} \sum_{y=0}^{N-1} [I(x,y) - m]^2} . \quad (3)$$

For  $x = 0, 1, 2, \dots, M - 1$  and  $y = 0, 1, 2, \dots, N - 1$ . The histogram is stretched in the range between  $[m - 2\sigma, m + 2\sigma]$ .

### 3.3. Bilateral Filtering

The backgrounds of images with high magnification rates are characterized by high noise levels, similar to the well-known salt and pepper noise. We perform a bilateral filtering process to denoise and smooth the region's boundaries, since it is both an edge-preserving and noise reduction non-linear smoothing filter. The name of the bilateral filtering procedure was assigned by [38]. It replaces each pixel's intensity with a weighted average of intensity values from the neighboring pixels. The algorithm starts with an inspection of a patch from the sky portion of the image. Then, we compute the variance of the patch to approximate noise variance.

$$\sigma_p^2 = \frac{1}{ST} \sum_{x=0}^{S-1} \sum_{y=0}^{T-1} [P(x,y) - m]^2 , \quad (4)$$

with  $m$  being calculated using Eq. (2). The bilateral filter,  $BF$  is formulated as follows:

$$BF[I]_p = \frac{1}{W_p} \sum_{q \in s} G_{\sigma_s}(p - q) G_{\sigma_r}(I_p - I_q) I_q , \quad (5)$$

where  $W_p$  is a normalization factor:

$$W_p = \sum_{q \in s} G_{\sigma_s}(p - q) G_{\sigma_r}(I_p - I_q) \quad (6)$$

and  $G_{\sigma}(x)$  denotes the two-dimensional Gaussian kernel:

$$G_{\sigma}(x) = \frac{1}{2\pi\sigma^2} e^{-\frac{x^2}{2\sigma^2}} . \quad (7)$$

Parameters  $\sigma_s$  and  $\sigma_r$  in Eq. (5) will be used to calculate the amount of filtering applied to image  $I$ . Equation (6) is a normalized weighted average in which  $G_{\sigma_s}$  is a spatial Gaussian that reduces the effect of distant pixels and  $G_{\sigma_r}$  is a range Gaussian that reduces the influence of pixels  $q$  with an intensity value different from  $I_p$ . It is worth noting that the term "range" refers to amounts relative to pixel values, as opposed to space, which refers to pixel location. Figure 7 depicts an example of the output of the bilateral filter.

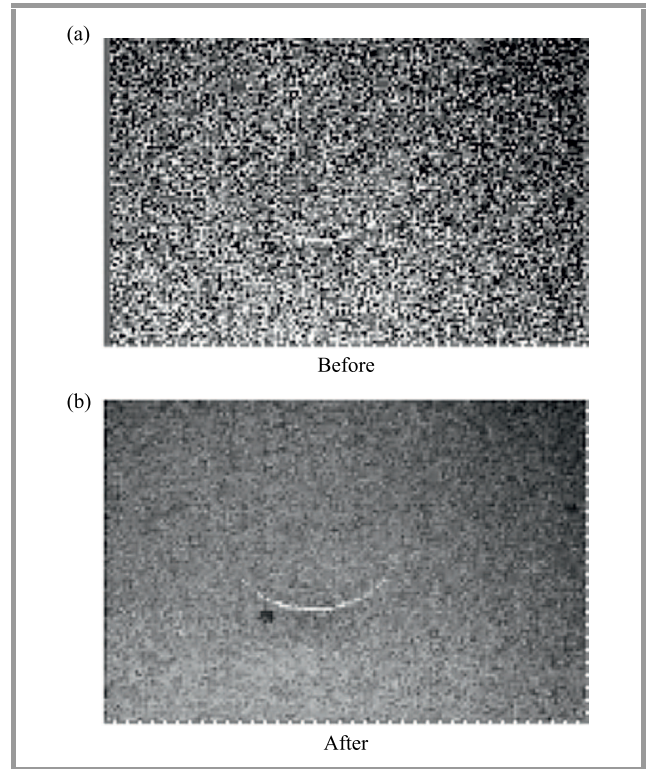


**Fig. 7.** Result before and after bilateral filtering of the cropped image.

## 4. Results and Discussion

The enhancement algorithm seeks to increase image quality by generating a processed image that is superior to the original image, for further processing. Such an improvement might be evaluated subjectively through a visual assessment of the image, or objectively through statistical measurements. In this paper, fifteen images are tested and analyzed with the proposed method. The images were obtained from Jabatan Kemajuan Islam Malaysia (JAKIM), Teluk Kemang Observatory and Pejabat Mufti Negeri Terengganu. All images were captured at different times using different types of equipment and were saved in jpeg and png formats. In Fig. 8, we present four examples of telescope-obtained images used in this study. As shown in Fig. 8c and Fig. 8d, the moon is invisible to the naked eye. Noise is present in Fig. 8a and Fig. 8b, hindering further processing.

The results obtained from the experiment are presented in Fig. 9. As demonstrated in the figure, the proposed method performed successfully for all images, proving its usefulness. The combination of CLAHE and grayscale contrast enhancement successfully increases the visibility of the moon crescent, even when it is invisible to the naked eye. Bilateral filtering (BF) was performed by smoothing the region concerned. The results were obtained with the bilateral filter using the same variance,  $\sigma_r$  of the range Gaussian kernel, which is set to double the variance of noise,  $\sigma_p^2$  obtained from Eq. (3). However, we set  $\sigma_s$  to different values. The leftmost images are the results of CLAHE

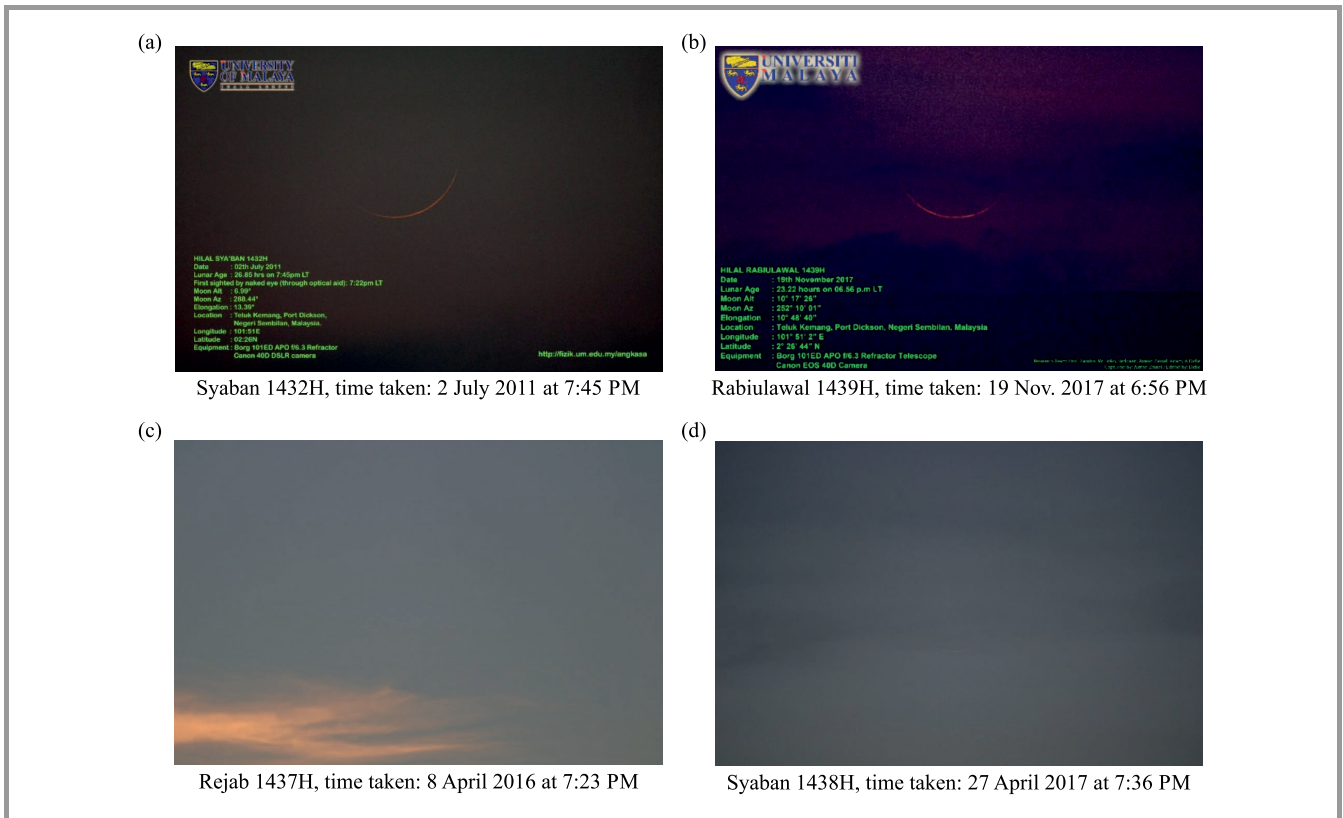


Fig. 8. Telescope-obtained images.

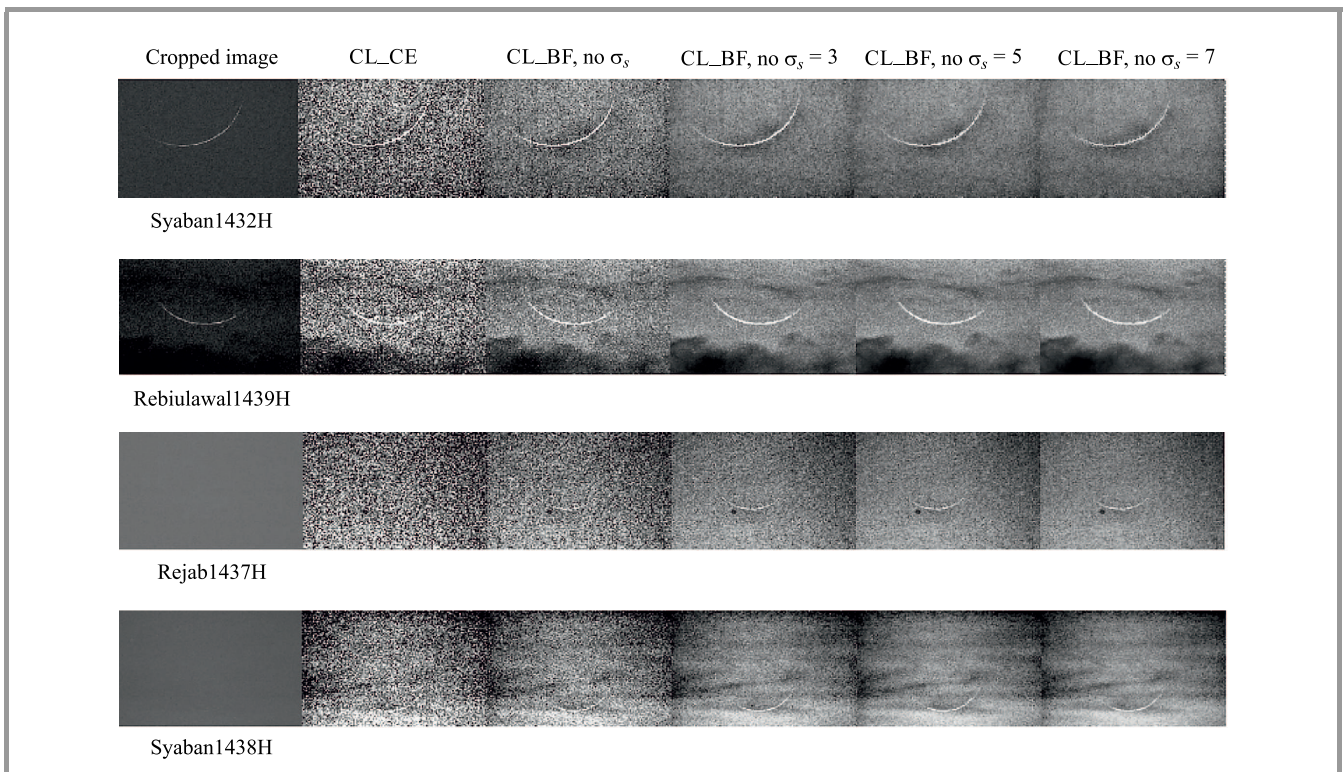


Fig. 9. Results obtained with the contrast enhancement and bilateral filtering methods, using different  $\sigma_s$  on the cropped CLAHE images.

Table 1

Comparison of PSNR and MSE values between contrast enhancement and bilateral filtering (BF) of different  $\sigma_s$ 

Image	CL_CE	CL_BF				CL_CE	CL_BF			
		–	3	5	7		–	3	5	7
1	58.12	59.66	60.21	60.28	60.31	0.05	0.03	0.02	0.01	0.01
2	57.17	58.23	58.45	58.47	58.47	0.12	0.10	0.09	0.09	0.09
3	60.70	63.51	66.27	67.00	67.28	0.05	0.03	0.02	0.01	0.01
4	60.07	61.42	62.30	62.45	62.50	0.06	0.05	0.04	0.04	0.04
5	61.78	64.67	65.83	66.24	66.56	0.04	0.02	0.02	0.02	0.01
6	59.27	59.40	59.44	59.45	59.46	0.08	0.07	0.07	0.07	0.07
7	64.57	69.43	70.44	70.49	70.51	0.02	0.01	0.01	0.01	0.01
8	59.61	59.71	59.79	59.83	59.86	0.10	0.07	0.06	0.06	0.06
9	60.39	61.65	62.01	62.08	62.13	0.06	0.04	0.04	0.04	0.04
10	63.51	63.76	63.96	64.14	64.30	0.03	0.03	0.03	0.03	0.02
11	59.73	61.30	61.93	62.00	62.03	0.07	0.05	0.04	0.04	0.04
12	63.45	63.98	64.10	64.13	64.14	0.03	0.03	0.03	0.03	0.03
13	60.43	62.69	64.67	65.11	65.28	0.06	0.04	0.02	0.02	0.02
14	60.42	60.80	61.05	61.09	61.10	0.06	0.06	0.05	0.05	0.05
15	63.41	66.26	66.48	66.43	66.43	0.03	0.02	0.01	0.01	0.01

grayscale contrast enhancement (CL\_CE). Images presented in column two are the results of CLAHE bilateral filtering (CL\_BF) without  $\sigma_s$ , while those in columns three to five are the results of CLAHE bilateral filtering with  $\sigma_s = 3$ ,  $\sigma_s = 5$ , and  $\sigma_s = 7$ , respectively. As can be observed from the figure, as  $\sigma_s$  increases, the images become smoother. However, the moon crescent becomes a little bit blurry. This can be seen based on the example of images zoomed around the moon crescent of bilateral filter with  $\sigma_s = 3$  and  $\sigma_s = 7$ , as presented in Fig. 9.

Based on Table 1, CL\_BF shows better PSNR values than CL\_CE for all images. With CL\_BF, increasing the  $\sigma_s$  improve the quality of enhanced image where PSNR for all images with  $\sigma_s = 7$  is higher than the PSNR with the lower setting. However, for all enhanced images, the difference of CL\_BF between  $\sigma_s = 7$  and  $\sigma_s = 3$  is less than 1.0 except for image 3. Similar to the MSE, for all enhanced images, changing the size of  $\sigma_s$  do not show much difference. Note that increasing the  $\sigma_s$  is actually increase the neighborhood size, which increases the filter execution time. So, using a small size of  $\sigma_s$  is enough in this case.

## 5. Conclusion

This paper described how to improve moon crescent images with the use of CLAHE, grayscale contrast enhancement, and bilateral filtering methods. We began by converting an RGB image into CIELab color space. CLAHE was applied to the L component of the image in order to improve visibility, before converting it back to an RGB image. The gray image was then chosen based on the R, G, or B component with the highest gray bin value (bin value = 0.5). After

that, we cropped the image to focus on the moon crescent, before enhancing the contrast of the grayscale image. This process was performed by adjusting the image's histogram based on the standard deviation of the image. In the last step, the bilateral filtering process was performed to remove noise resulting from grayscale contrast enhancement. The experiment conducted on fifteen moon crescent images demonstrates that our method has acceptable practical results. The moon crescent that is invisible in the original images may be seen after enhancing them with the use of the proposed method.

## Acknowledgements

We acknowledge the KUSZA Observatory, Universiti Sultan Zainal Abidin, Pejabat Mufti Negeri Terengganu, Jabatan Kemajuan Islam Malaysia (JAKIM) and the Teluk Kemang Observatory for providing moon crescent images required for this study. We are grateful to the Centre of Research and Innovation Management, Universiti Malaysia Terengganu for supporting us in our work.

## References

- [1] J. R. Tang and N. A. M. Isa, "Bi-histogram equalization using modified histogram bins", *Applied Soft Comput.*, vol. 55, 2017, pp. 31–43 (DOI: 10.1016/j.asoc.2017.01.053).
- [2] M. O. Oloyede, G. P. Hancke, and H. C. Myburgh, "Improving face recognition systems using a new image enhancement technique, hybrid features and the convolutional neural network", 2018, *IEEE Access*, vol. 6, pp. 75181–75191 (DOI: 10.1109/ACCESS.2018.2883748).

- [3] R. Gupta, M. Khari, D. Gupta, and R. G. Crespo, "Fingerprint image enhancement and reconstruction using the orientation and phase reconstruction", *Information Sci.*, 2020, vol. 530, pp. 201–218 (DOI: 10.1016/j.ins.2020.01.031).
- [4] O. Juarez-Sandoval *et al.*, "Improved unseen-visible watermarking for copyright protection of digital image", in *Proc. IEEE 5th Int. Workshop on Biometrics and Forensics (IWBF)*, Coventry, UK, 2017, pp. 1–5 (DOI: 10.1109/IWBF.2017.7935084).
- [5] O. Oktay *et al.*, "Anatomically constrained neural networks (AC-NNs): application to cardiac image enhancement and segmentation", *IEEE Trans. on Medical Imaging*, 2018, vol. 37, no. 2, pp. 384–395 (DOI: 10.1109/TMI.2017.2743464).
- [6] F. Zhou, Z. Jia, J. Yang, and N. Kasabov, "Method of improved fuzzy contrast combined adaptive threshold in NSCT for medical image enhancement", *BioMed Res. Int.*, vol. 2017, 10 pages, 2017 (DOI: 10.1155/2017/3969152).
- [7] J. Li, X. Zeng, and J. Su, "Medical image enhancement algorithm based on biorthogonal wavelet", *Acta Microscopica*, vol. 28, no. 1, 2019, pp. 100–107.
- [8] T. Qiu *et al.*, "Efficient medical image enhancement based on CNN-FBB model", *IET Image Processing*, vol. 13, no. 10, pp. 1736–1744, 2019 (DOI: 10.1049/iet-ipt.2018.6380).
- [9] K. J. Xia, J. Q. Wang, and J. Cai, "A novel medical image enhancement algorithm based on improvement correction strategy in wavelet transform domain" *Cluster Comput.*, vol. 22, no. 5, pp. 10969–10977, 2019 (DOI: 10.1007/s10586-017-1264-y).
- [10] J. S. Chiang *et al.*, "Adaptive image enhancement method for document", in *Proc. IEEE Int. Symp. on Intelligent Signal Process. and Commun. Systems (ISPACS)*, Xiamen, China, 2017, pp. 417–420 (DOI: 10.1109/ISPACS.2017.8266515).
- [11] M. Gharbi, J. Chen, J. T. Barron, S. W. Hasinoff, and F. Durand, "Deep bilateral learning for real-time image enhancement", *ACM Trans. on Graphics (TOG)*, vol. 36, no. 4, pp. 1–12 (DOI: 10.1145/3072959.3073592).
- [12] R. Ablin, C. H. Sulochana, and G. Prabin, "An investigation in satellite images based on image enhancement techniques", *European J. of Remote Sens.*, vol. 53, no. Sup. 2, pp. 86–94 (DOI: 10.1080/22797254.2019.1673216).
- [13] X. Han, J. Yu, J. Luo, and W. Sun, "Hyperspectral and multispectral image fusion using cluster-based multi-branch BP neural networks", *Remote Sens.*, vol. 11, no. 10, 2019 (DOI: 10.3390/rs11101173).
- [14] Z. Huang *et al.*, "Optical remote sensing image enhancement with weak structure preservation via spatially adaptive gamma correction", *Infrared Physics & Technol.*, vol. 94, pp. 38–47, 2018 (DOI: 10.1016/j.infrared.2018.08.019).
- [15] Q. Xie *et al.*, "Multispectral and hyperspectral image fusion by MS/HS fusion net", in *Proc. of the IEEE Conf. on Computer Vision and Pattern Recognition*, Long Beach, CA, USA, 2019, pp. 1585–1594 (DOI: 10.1109/CVPR.2019.00168).
- [16] M. Yang, J. Hu, C. Li, G. Rohde, Y. Du, and K. Hu, "An in-depth survey of underwater image enhancement and restoration", *IEEE Access*, vol. 7, pp. 123638–123657, 2019 (DOI: 10.1109/ACCESS.2019.2932611).
- [17] C. O. Ancuti, C. Ancuti, C. De Vleeschouwer, and P. Bekaert, "Color balance and fusion for underwater image enhancement", *IEEE Trans. on Image Process.*, vol. 27, no. 1, pp. 379–393, 2018 (DOI: 10.1109/TIP.2017.2759252).
- [18] S. Anwar, C. Li, and F. Porikli, "Deep underwater image enhancement", *ArXiv*, 2018 [Online]. Available: <https://arxiv.org/pdf/1807.03528.pdf>
- [19] M. Azhari, "Penetapan Awal bulan Hijriah: Ramadan, Syawal dan Zulhijjah 1433 H/ 2012 M", *NRE Executive Discourse*, pp. 1–22, 2012 (in Malaysian).
- [20] T. Djamaluddin, "Menuju Kriteria Baru MABIMS Berbasis Astronomi", 2016 [Online]. Available: <https://tdjmaluddin.wordpress.com/2016/10/05/menuju-kriteria-baru-mabims-berbasis-astronomi/> (in Indonesian)
- [21] K. Wahid, M. S. A. M. Nawawi, S. Man, and N. Ahmad, "Teknik Cerapan Anak Bulan: Satu Penelitian Literatur (Observation Techniques of Crescent: A Literature Review)", *UMRAN-Int. J. of Islamic and Civilizational Studies*, vol. 6, no. 3, pp. 47–55, 2019 (DOI: 10.11113/umran2019.6n3.349). (in Malaysian)
- [22] A. Joko Satria, C. W. Loon, and N. Ahmad, "Pensabitan Hilal Menerusi Teknik Pengimejan. Dalam Dimensi Penyelidikan Astronomi Islam", Saadan Man *et al.* Eds., Kuala Lumpur: Jabatan Fiqh dan Usul, Akademi Pengajian Islam, Universiti Malaya, 2013, vol. 95 (in Malaysian).
- [23] M. Fakhar, P. Moalem, and M. A. Badri, "Lunar crescent detection based on image processing algorithms", *Earth, Moon, and Planets*, vol. 114, no. 1, pp. 17–34, 2014 (DOI: 10.1007/s11038-014-9449-3).
- [24] M. N. M. Yatim, A. Haron, and A. Mohamed, "New Moon Observation Online Records", *2nd Int. Conf. on Islamic App. in Computer Sci. and Technol. (IMAN2014)*, Amman, Jordan, Paper ID: 72, 2014.
- [25] M. Kaur, J. Kaur, and J. Kaur, "Survey of contrast enhancement techniques based on histogram equalization", *Int. J. of Adv. Computer Sci. and App.*, vol. 2, no. 7, 2011 (DOI: 10.14569/IJACSA.2011.020721).
- [26] D. J. Ketcham, "Real-time image enhancement techniques", in *Image Processing*, vol. 74, pp. 120–125, 1976 (DOI: 10.1117/12.954708).
- [27] R. Hummel, "Image enhancement by histogram transformation", *Computer Graphics Image Process.*, vol. 6, no. 2, pp. 184–195, 1977 (DOI: 10.1016/S0146-664X(77)80011-7).
- [28] S. M. Pizer, "Intensity mappings for the display of medical images", *Functional Mapping of Organ Systems and Other Computer Topics*, Society of Nuclear Medicine, pp. 205–217, 1981.
- [29] S. M. Pizer *et al.*, "Adaptive histogram equalization and its variations", *Computer Vision, Graphics, and Image Process.*, vol. 39, no. 3, pp. 355–368, 1987 (DOI: 10.1016/S0734-189X(87)80186-X).
- [30] T. Ayyavoo and J. J. Suseela, "Illumination pre-processing method for face recognition using 2D DWT and CLAHE", *IET Biometrics*, vol. 7, no. 4, pp. 380–390, 2017 (DOI: 10.1049/iet-bmt.2016.0092).
- [31] L. Li, Y. Si, and Z. Jia, "Medical image enhancement based on CLAHE and unsharp masking in NSCT domain", *J. of Medical Imaging and Health Informatics*, vol. 8, no. 3, pp. 431–438, 2018 (DOI: 10.1166/jmhi.2018.2328).
- [32] J. Ma, X. Fan, S. X. Yang, X. Zhang, and X. Zhu, "Contrast limited adaptive histogram equalization-based fusion in YIQ and HSI colour spaces for underwater image enhancement", *Int. J. of Pattern Recognition and Artificial Intell.*, vol. 32, no. 7, 2018 (DOI: 10.20944/preprints201703.0086.v1).
- [33] S. Sahu, A. K. Singh, S. P. Ghreya, and M. Elhoseny, "An approach for de-noising and contrast enhancement of retinal fundus image using CLAHE", *Optics & Laser Technol.*, vol. 110, pp. 87–98, 2019 (DOI: 10.1016/j.optlastec.2018.06.061).
- [34] M. Siddhartha and A. Santra, "COVIDLite: A depth-wise separable deep neural network with white balance and CLAHE for detection of COVID-19", *ArXiv*, 2020 [Online]. Available: <https://arxiv.org/pdf/2006.13873.pdf>
- [35] R. M. James and A. Sunyoto, "Detection Of CT-Scan Lungs COVID-19 Image Using Convolutional Neural Network And CLAHE", in *Proc. IEEE 3rd Int. Conf. on Informat. and Commun. Technol. (ICOIACT)*, Yogyakarta, Indonesia, 2020, pp. 302–307 (DOI: 10.1109/ICOIACT50329.2020.9332069).
- [36] B. K. Umri, M. W. Akhyari, and K. Kusriani, "Detection of Covid-19 in Chest X-ray Image using CLAHE and Convolutional Neural Network", in *2nd IEEE Int. Conf. on Cybernet. and Intelligent System (ICORIS)*, Manado, Indonesia, 2020, pp. 1–5 (DOI: 10.1109/ICORIS50180.2020.9320806).
- [37] G. Siracusano *et al.*, "Pipeline for Advanced Contrast Enhancement (PACE) of Chest X-ray in Evaluating COVID-19 Patients by Combining Bidimensional Empirical Mode Decomposition and Contrast Limited Adaptive Histogram Equalization (CLAHE)", *Sustainability*, vol. 12, no. 20, 2020 (DOI: 10.3390/su12208573).
- [38] C. Tomasi and R. Manduchi, "Bilateral filtering for gray and color images", in *Sixth Int. Conf. on Computer Vision (IEEE Cat. No. 98CH36271)*, Bombay, India, 1998, pp. 839–846 (DOI: 10.1109/ICCV.1998.710815).



**Wan Nural Jawahir Hj Wan Yussof** is a Senior Lecturer at the Faculty of Ocean Engineering Technology and Informatics at the Universiti Malaysia Terengganu where she has been a faculty member since 2006 as a tutor. Wan Nural Jawahir completed her Ph.D. in 2014. Her research interests lie in the area of computer vision, ranging from theory to design and implementation.

 <https://orcid.org/0000-0002-3618-1638>

E-mail: wannurwy@umt.edu.my

Intelligent Informatics

Faculty of Ocean Engineering Technology and Informatics

Universiti Malaysia Terengganu

21030 Kuala Nerus

Terengganu, Malaysia



**Mustafa Man** is an Associate Professor at the Faculty of Ocean Engineering Technology and Informatics and also a Deputy Director at the Centre of Research and Innovation Management (CRIM), UMT. He started his Ph.D. in July 2009 and finished his studies in Computer Science at UTM in 2012. He received a Computer

Science Diploma, a Computer Science Degree and a Master's Degree from UPM. His research focuses on the development of models for integration of multiple database types, as well as on augmented reality, Android based, and IT related into across domain platform.

 <https://orcid.org/0000-0003-4071-721X>

E-mail: mus@umt.edu.my

Intelligent Informatics

Faculty of Ocean Engineering Technology and Informatics

Universiti Malaysia Terengganu

21030 Kuala Nerus

Terengganu, Malaysia



**Roslan Umar** pursues his Ph.D. degree from Universiti Malaya (UM), Malaysia in the field of Radio Astronomy. His interest in exploring the universe began during his bachelor degree internship program, when he was assigned to work at the Malaysia National Planetarium. After he finished his M.Sc., Roslan began his academic

career at Universiti Sultan Zainal Abidin (UNISZA) and was appointed the Head of Astronomy Unit at UNISZA Observatory. He is currently works as a Senior Lecturer and a research fellow at East Coast Environmental Research Institute (ESERI), UNISZA. Dr. Roslan's research interests are in the field of electromagnetic waves, radio frequency interference, radio astronomy and environmental studies.

 <https://orcid.org/0000-0002-8413-385X>

E-mail: roslan@unisza.edu.my

East Coast Environmental Research Institute (ESERI)

Universiti Sultan Zainal Abidin

21300 Kuala Terengganu

Terengganu, Malaysia



**Ahmad Najmuddin Zulkeflee** is a Master program student at the East Coast Environmental Research Institute (ESERI), Universiti Sultan Zainal Abidin (UniSZA), where he studies under the supervision of Dr. Roslan Umar. His academic career began by obtaining a Bachelor's degree from Shariah (Islamic) Astronomy Department,

Academy of Islamic Studies, University of Malaya (UM).

E-mail: muddinjr97@yahoo.com

East Coast Environmental Research Institute (ESERI)

Universiti Sultan Zainal Abidin

21300 Kuala Terengganu

Terengganu, Malaysia



**Ezmahamrul Afreen Awaludin** is currently a Senior Lecturer at the Faculty of Fisheries and Food Science, Universiti Malaysia Terengganu. He received his Ph.D. in Computer Science from Universiti Malaysia Terengganu in 2016. His research interests focus on computer vision, image processing and artificial intelligence.

He cooperates closely with researchers from a number of different fields, including marine sciences, fisheries and aquaculture, focusing on challenges related to image processing and image-based analysis.

 <https://orcid.org/0000-0003-4470-0052>

E-mail: e.afreen@umt.edu.my

Faculty of Fisheries and Food Science

Universiti Malaysia Terengganu

21030 Kuala Nerus

Terengganu, Malaysia



**Nazhatulshima Ahmad** has been a senior lecturer at the Department of Physics, Faculty of Science, University of Malaya, since 2013. She has been working at the University since 1999, as a tutor in the Physics Department. She obtained her B.Sc. in Physics from University of Malaya in 1998, M.Sc. (Astronomy) in 2003 and Ph.D. from

the same university in 2013. Her main research interests are in emission line stars, such as Be stars, and in binary star systems. She is currently conducting a research project on digital imaging and image processing techniques used for early detection of the young crescent moon.

 <https://orcid.org/0000-0002-0464-1652>

E-mail: [n\\_ahmad@um.edu.my](mailto:n_ahmad@um.edu.my)

Department of Physics, Faculty of Science

University of Malaya

50603 Kuala Lumpur

Federal Territory, Malaysia

# Novel Feature Extraction for Pineapple Ripeness Classification

Hui Hui Wang and Sze Ye Chai

*Universiti Malaysia Sarawak, Kota Samarahan, Sarawak, Malaysia*

<https://doi.org/10.26636/jtit.2022.156021>

**Abstract**—A novel feature extraction method has been proposed to improve the accuracy of the pineapple ripeness classification process. The methodology consists of six stages, namely: image acquisition, image pre-processing, color extraction, feature selection, classification and evaluation of results. The red element in the RGB model is selected as the threshold value parameter. The ripeness of pineapples is determined based on the percentage share of yellowish scales visible in images presenting the front and the back side of the fruit. The prototype system is capable of classifying pineapples into three main groups: unripe, ripe, and fully ripe. The accuracy of 86.05% has been achieved during experiments.

**Keywords**—*image processing technique, pineapple, ripeness grading.*

## 1. Introduction

With the area of 1,805 hectares, Sarawak is Malaysia's second largest pineapple plantation [1]. The pineapple industry is one of those agricultural sectors that are characterized by high productivity rates and expenditure levels. This means that it is highly recommended for them to implement advanced technologies in their production processes, for example to replace manual processes involving workers with innovative technical solutions. Sarawak still has room for improvement in terms of the technology used in the pineapple industry.

Fruit quality checks are important in the pineapple industry due to great demand levels and highly competitive markets [2]. A traditional method of identifying and grading the ripeness of a pineapple relies on a visual inspection during which the skin color is assessed. Visual inspections are usually conducted by well-trained workers. Such human inspections are inconsistent and subjective [3]. As production volumes grow, the number of cases in which visual inspections are performed inaccurately may increase as well. A human grader may also be inconsistent in terms of the quality of their work, as human eyes may get tired when large quantities of fruit need to be processed.

Therefore, computer-based technologies, such as image processing techniques, are very much needed and should be applied for the purpose of classifying pineapple ripeness levels.

## 2. Related Work

Several types of color-based models and techniques are used for identification and classification purposes in the agricultural industry. In this paper, the existing techniques that have been relied upon to identify and classify the ripeness of pineapples are discussed and reviewed. These techniques include neural network classification based on color image features, linear classification based on color image features and fuzzy logic classification based on color image features.

Paper [4] proposed a neural network classification based on color image features for classifying pineapple ripeness. Image acquisition in a controlled environment is crucial for the collection of data, because such an environment ensures that any noise compromising image quality may be eliminated and that the image captured is clear and suitable for processing in the subsequent stages of the process. A controlled environment is deemed to consist of a high-definition camera positioned at a fixed distance of 1.5 meters away from the fruit, at an angle of 90° relative to the ground, and with a constant exposure to light throughout the entire process.

During the pre-processing phase, the images are subjected to filtering in order to remove redundant information, such as noise. The background of each image is cropped and resized into a standard resolution to ensure all images may pass through the system. RGB extraction is performed to extract the green color from the RGB channel. It is then converted into grayscale to show the intensity of the image's green component.

During the feature extraction phase, the number of green and red pixels is extracted from a selected region of the image. Next, during the feature selection phase, the range of both yellow and green colors are populated to allow respective counters to count the number of red and green color pixels when a certain pixel lies within the range.

An artificial neural network (ANN) is used during the classification phase. According to [4], ANN is a set of interconnected nodes positioned between the input and the output for a system. In other words, the manner in which ANN is programmed to differentiate between ripe and unripe pineapples mimics the human brain. The ANN-derived result is then processed and is assigned with one of 4 in-

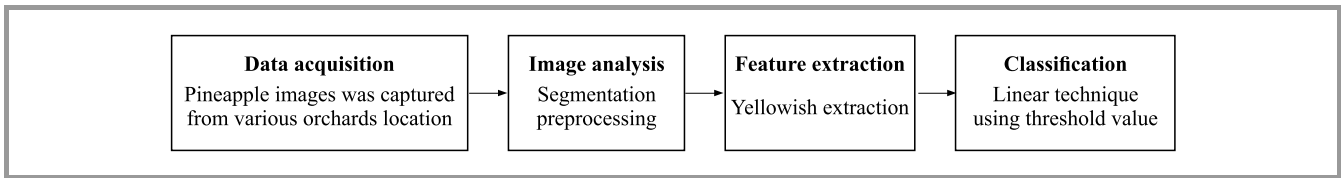


Fig. 1. Pineapple classification methodology using the image processing technique.

dexes. This system differentiates 4 index maturities only instead of 7 indexes requires under the Federal Agricultural Marketing Authority’s (FAMA) standard. This is because the fruit start to ripen when their index equals between 4 and 7, while those with the index of 1 to 3 remain greenish, which makes it hard to compare the change of the color of their skin.

This system has successfully classified the ripeness of pineapples using the neural network classification method based on color image features and has reached the accuracy rate of 75%.

[5] has implemented linear classification based on color image features to classify the ripeness index. Figure 1 shows the flow chart of used methodology of classification.

The data was collected from one of the pineapple orchards in Johor and Pahang, Malaysia. The images of N36 pineapples are taken at different angles and then stored in the database for future development of the system. Next, the segmentation pre-processing phase occurred (Fig. 2) [5]. The background of the image was removed because it comprises unwanted data, such as noise, which will affect the color analysis process. Segmentation is necessary because it is used to determine the objects of interest and their boundaries in the image.

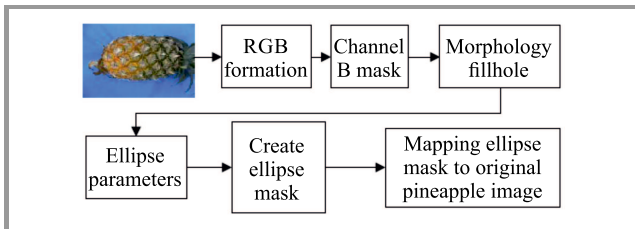


Fig. 2. Pineapple image segmentation process.

The B channel mask is used rather than R and G channel masks to delineate the area of the pineapple because it does not exist in the formation of the pineapple’s pixel value which then naturally eliminates the blue background image as shown in Fig. 3d. The image is then converted into a binary image for its later processing with the use of the morphology fillhole method. The purpose of implementing the morphology fillhole method during the segmentation process is to capture the outline of the fruit. The method fails, however, to produce a smooth rounded object after filling the image with white pixels. In other words, the stump and crown are still included in the image after filling it with white pixels. Therefore, a binary ellipse mask is used to

overcome this issue and to produce a smooth rounded object, as shown in Fig. 3g. The mask is then mapped onto the original image to obtain the region of interest (ROI), as shown in Fig. 3h.

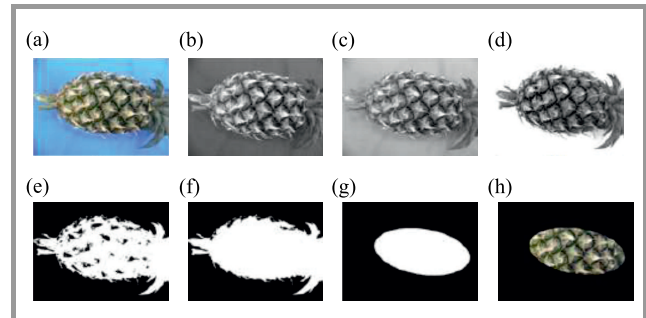


Fig. 3. Segmentation of the pineapple image: (a) original image, (b) red channel, (c) green channel, (d) blue channel, (e) binary image of the blue channel, (f) morphology fillhole, (g) binary ellipse mask, (h) segmented pineapple body using (g) as a mask (see the digital version for color images).

The efficiency of the classification result depends on the feature extracted from the processing stage. The percentage of yellowish scale pixels is the main factor relied upon to measure the maturity index of the pineapple by determining the ratio of all pixel values of ROI. The following formula was used to calculate the percentage of yellowish scale pixels:

$$Py = \frac{py}{pv + pg + py} \times 100\% , \tag{1}$$

where  $py$  is the number of yellowish scale pixels,  $pv$  is the number of dark violet scale pixels and  $pg$  is the number of green scale pixels.

The result obtained from Eq. (1) is used to determine the threshold level for classification process. 210 pineapple images were as a training set and the percentage of yellowish scale pixels for each image in each index was calculated and identified. Based on the result of linear classification, the threshold level of yellowish scale pixels is identified and categorized into 7 indexes in line with the FAMA standard. The efficiency of ripeness classification may be measured by using 700 images of pineapples considered to be a testing set. This system has achieved an overall accuracy and efficiency of 94.29%.

Paper [6] presented a fuzzy logic classification of ripeness based on color image features.

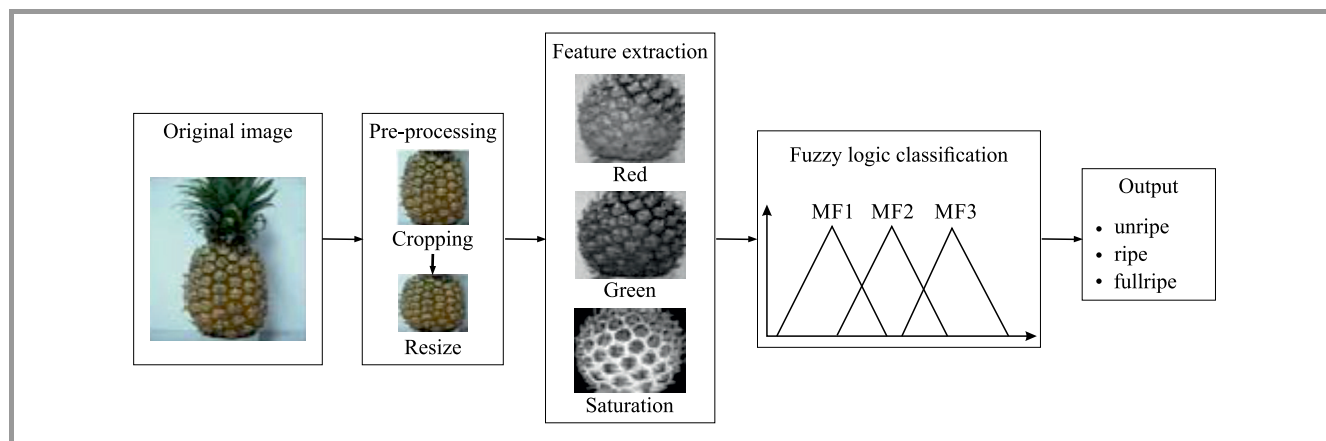


Fig. 4. System flow chart.

Based on Fig. 4, the three main parts of the system include the following: pre-processing, feature extraction, and classification. The procedure starts with data collection, whereby images of Josapine pineapples are obtained in a controlled environment, i.e. with the use of a high-definition camera positioned at a fixed distance from the fruit. Notice that no constant lighting conditions are ensured throughout the process. Therefore, HSI color maps are implemented, because HSI is capable of processing the image even when the lighting conditions are not constant.

Next, each image is filtered to remove redundant information, such as noise, and the unwanted background is cropped because it does not provide any useful information for the classification stage. The size of all images is standardized in  $600 \times 600$  pixels to ensure good accuracy of the classification process.

During the feature extraction stage, RGB and HSI spectrums are used to extract the necessary information from the image. The entire image is processed with the use of both spectrums. It is converted into the red and green channel in the RGB spectrum, while the HSI spectrum converts the image into the saturation channel.

Before proceeding to the classification stage, feature selection is step that needs to be performed – the data needs to be analyzed in order to meet the specific needs of the project. Data extracted during feature extraction stage is filtered and analyzed within a specific range of red, green and saturation channels. Other channels, such as blue, hue and intensity channel, are not taken in consideration because they do not provide any information needed. When a certain pixel lies within the range, the counters will count the number of pixels within the respective channels.

In the classification stage, fuzzy logic is used as a tool to map the input into a pattern and to match the data accordingly, based on a specific parameter setup, to generate an output. This project uses Matlab software to apply the fuzzy logic features to accept three values from red, green and saturation channels and to generate one output using a Mamdani-style system. Classification is performed based on ripeness and maturity levels.

This method has achieved average accuracy of 85% for ripe and unripe fruit and 100% accuracy for fully ripe fruit.

### 2.1. Analysis of Review

The superior features of three different types of color models and ripeness classification techniques reviewed above will be taken into consideration for the purpose of the project. Images taken in a controlled environment are required in order to obtain more accurate and consistent ripeness classification results. The background should be removed to ensure that the results the fruit classification procedure are accurate. After reviewing the techniques introduced in the previous section, all their superior features, such as color models, strengths and weaknesses are compared with each other. Each technique is summarized in Table 1.

By using the neural network classification method, the fruit may be categorized into four different types of ripeness, namely unripe, early ripe, ripe and overripe. The linear classification method is capable of assigning pineapples to up to seven categories, while the fuzzy logic classification method assigns the fruit into three major groups, i.e. unripe, ripe and fully ripe. Hence, in this project, pineapples will be graded and categorized into three major groups, namely unripe, ripe and fully ripe.

Furthermore, the RGB color model will be used in this project. This is because it serves as a good point of departure and is also well-known for most image applications used nowadays. Moreover, the RGB color model is capable of calculating the percentage of yellowish pixels through the red channel, based on an appropriate threshold value, and the ripeness of pineapple is usually determined by humans based on their yellowish skin color. Hence, the RGB model is the most suitable color model for the project in question.

Instead of using a single vertical line as proposed in [4], multiple diagonal lines will be produced and applied in the prototype as an indicator for grading the degree of ripeness. A training data set will be used to obtain the per-

Table 1  
Comparative analysis of the techniques reviewed

Technique	Neural network classification	Linear classification	Fuzzy logic classification
Dataset	Not stated	700	40
Training set	Not stated	210	20
Grades supported	Unripe, early ripe, ripe, overripe	7 levels: immature, early mature, mature, under ripe, early ripe, ripe, overripe	7 levels but categorizes into three major group: unripe, ripe, fully ripe
Color model	RGB	RGB	RGB and HIS
Accuracy of classification	75%	94.29%	85% for unripe and ripe, 100% for overripe
Strengths	Makes the process of data extraction more accurate and easier. Features from two regions of interest are extracted to obtain more accurate classification results.	Able to grade pineapples very accurately. Threshold value is identified to classify the maturity of pineapples.	HSI is able to process the image even when lighting conditions are not constant.
Weaknesses	Works on one type of pineapple (Josapine). Able to assign pineapples into four categories only.	Works on one type of pineapple (N36 only).	Lighting conditions may affect the accuracy of classification.

centage ranges of yellowish pixels for each index. Threshold values will be identified and used for classification of ripeness.

### 3. Proposed Solution

This section discusses the algorithms proposed for the automated pineapple ripeness grading system and presents the individual stages of the image processing technique, in-

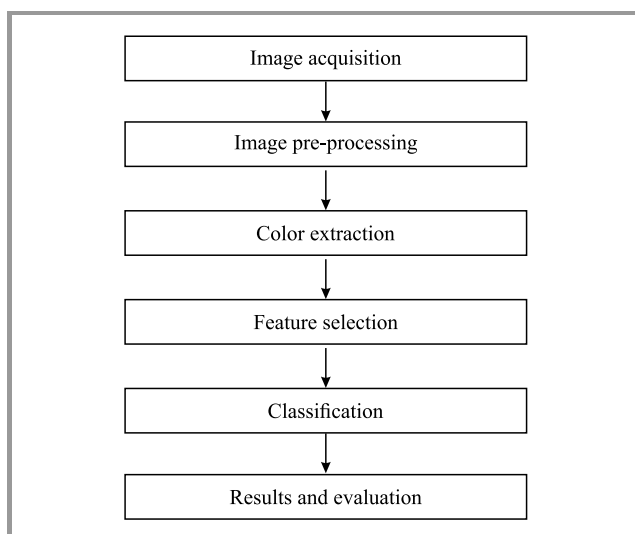


Fig. 5. Process flow of proposed technique.

cluding image acquisition, image pre-processing, color extraction, feature selection, classification of results and their evaluation (Fig. 5).

#### 3.1. Image Acquisition

Image acquisition is the first step of the image processing technique during which the pineapple image is collected. The sample is captured in a controlled environment, against a background that highly contrasts the fruit, at a constant distance from fruit, at an angle of 90° relative to the ground or parallel to the camera.

Such a setup helps reduce the amount of unwanted information, for example, in the form of noise, and ensures that the sample images are clear and suitable for processing during the subsequent stages. If the formats of sample images are different, they will be converted to JPEG for standardization purposes. This particular format is characterized by a small file size, meaning that the processing time is shorter and that efficiency is improved.

Sample images with fruit at different ripeness stages (from unripe to fully ripe) are captured, as shown in Fig. 6. For each category, 2 sample images (front and back side of the pineapple) are taken simultaneously to ensure more accurate classification. It is better to grade both sides of the fruit, as it may not ripe uniformly 86 sample images of 43 pineapples were taken in total and were used for the prototype system in this project.

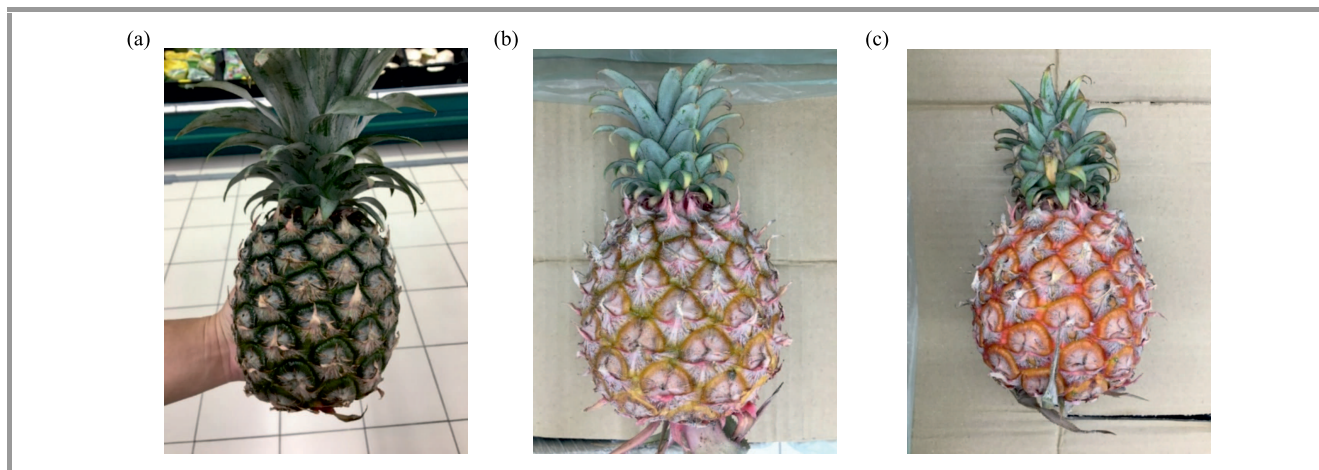


Fig. 6. Pineapple images captured in a controlled environment: (a) unripe, (b) ripe, and (c) fully ripe.

### 3.2. Image Pre-processing

At this stage, sample images are converted and formatted into an acceptable form in order to be processed during the subsequent stages. For example, they are cropped to remove redundant backgrounds and the crown of the pineapple, thus rendering more accurate results. They are then resized into the format of  $600 \times 600$  pixels, as shown in Fig. 7, to enhance further processing.



Fig. 7. Redundant background and crown are removed.

### 3.3. Color Extraction

Here, color extraction will be performed to extract the necessary information from the sample image. The RGB model is applied in this project to extract information required, as it is basic color model most commonly used in image-related applications.

The red elements are extracted from the sample image because they are the main component allowing to classify the pixels of a digital image into two categories, namely

yellow and green, based on an appropriate threshold value. Color extraction eliminates background and shortens processing time. Therefore, the red element from the RGB palette is chosen, as its extraction allows to determine the degree of ripeness. In the RGB spectrum, the image will be converted into the red channel to obtain pixel values that are similar to a grayscale image (within the range of 0 to 255) to show the intensity of the color component of the image.

### 3.4. Feature Selection

The red element of the sample image that was extracted in the previous step will be analyzed to meet the requirements of the project. Before analyzing the red element, six diagonal lines are created, as shown in Fig. 8. Only the pixels that lie along these lines will be analyzed and will be divided into two different categories, namely yellow pixels and green pixels, based on the applicable value of the red element.



Fig. 8. Six diagonal lines drawn across the sample image.

The reason of creating diagonal lines across the sample image, instead of using a single vertical line, is that a pineapple does not have a uniformly yellowish skin color, as shown in Figs. 9 and 10.



**Fig. 9.** A pineapple with uneven yellowish skin color – more yellowish color on the left.



**Fig. 10.** A pineapple with uneven yellowish skin color – more yellowish color on the right.

Uneven distribution of yellow on the skin may be a factor that affects the number of yellowish pixels identified if a vertical line is used in the prototype solution. It may be noticed in the examples shown above that the pineapples (depicted in Figs. 9 and 10) are more yellow on the left and on the right, respectively. If a single vertical line was applied in the prototype solution and used on both sample images, as shown in Fig. 11, misclassification could be occurred, as the vertical line does allow the yellowish pixels present on the sides to be taken into consideration. Furthermore, a vertical line used to analyze the red elements present along that line may produce less ideal results than those achieved based on six diagonal lines. This

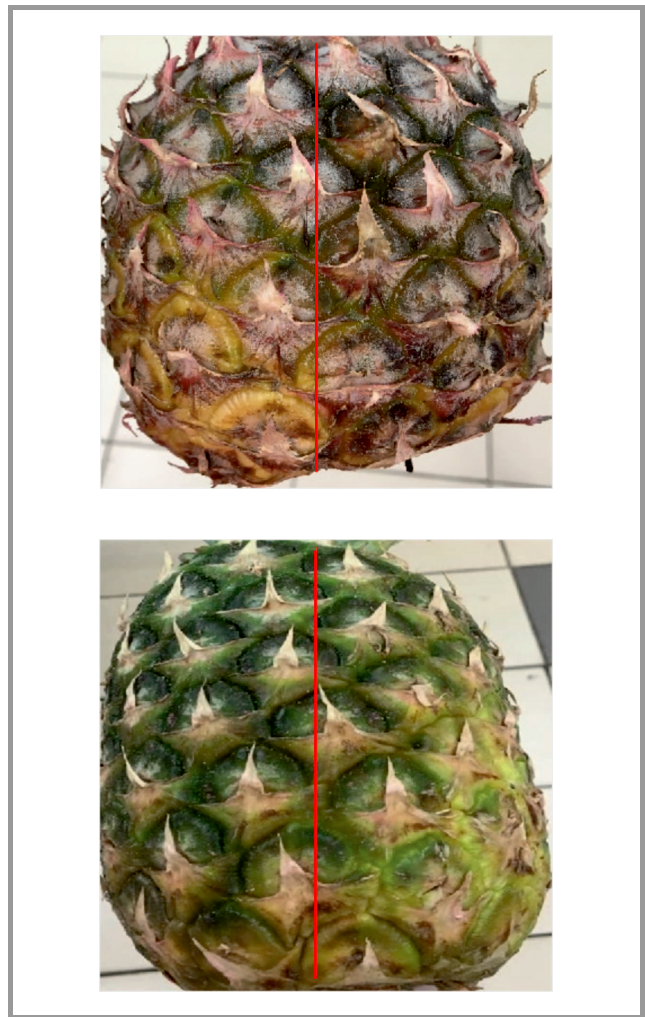


**Fig. 11.** A vertical line applies on an uneven fruit.

is because a longer section of the vertical line (compared to a diagonal line) runs over the eye of the pineapple, as shown in Fig. 12, and the eye of the fruit does not provide

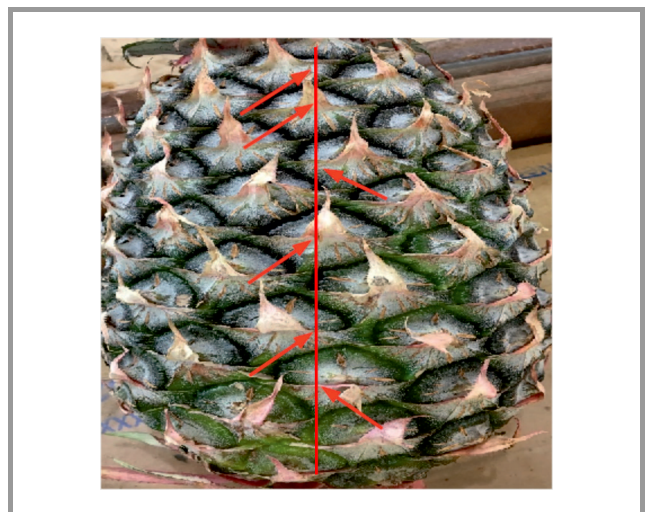


**Fig. 12.** Eye of the pineapple covered by the vertical line.

any important information for grading its ripeness. Hence, six diagonal lines are created and applied in the prototype solution to avoid the eye of the pineapple and to reduce the probability of misclassification errors as well as to increase the accuracy of the percentage of yellowish of fruit.

Once the six diagonal lines have been created and imposed on the sample image, the pixels that lie along those lines will be analyzed. Each pixel will contain information of the RGB color space, and each component color has the value between 1 and 255. However, only the red element is extracted and analyzed, because the red element from red channel of the RGB color model is capable of assigning the selected pixel into two different categories, namely yellow pixel and green pixel, based on an appropriate threshold value. These two colors can be considered of interest for our purposes.

The threshold value for the red element is set at 160, determined during preliminary tests. Thus, when the value of specific pixel is lower than that of the threshold, green color counters will be incremented. Otherwise, yellow color counters will be incremented. The flowchart presented in Fig. 13 shows the process of counting the number of green and yellow pixels based on threshold value.

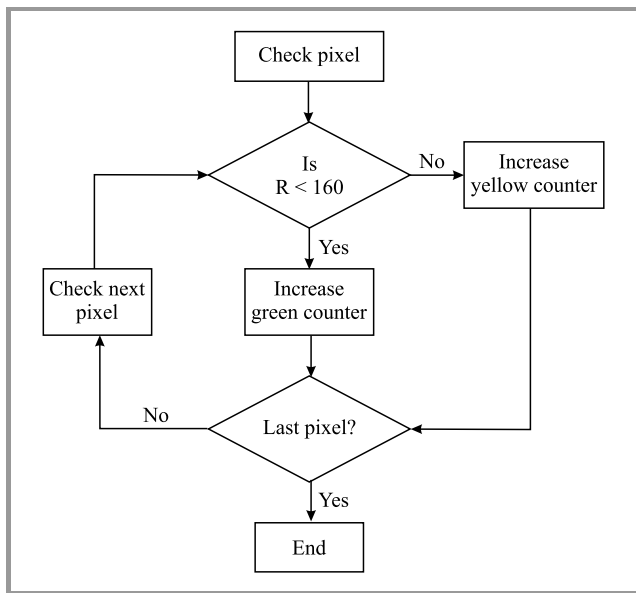


Fig. 13. Flow chart describing the process of counting green and yellow pixels.

This threshold value allows the respective registers to count the number of green and yellow pixels and these values will be used to calculate the percentage share of yellowish scales. Then percentage share will be used during the classification phase to determine ripeness and maturity categories. Six percentage ranges for each diagonal line need to be calculated using the following formula:

$$Y = \frac{N_y}{N_y + N_g} \times 100\% , \quad (2)$$

where  $N_y$  is the number of yellow pixels and  $N_g$  is the number of green pixels.

Once the six percentage ranges have been obtained for the six diagonal lines, the average value may be calculated for each side of the fruit:

$$Y = \frac{Y_1 + Y_2 + Y_3 + Y_4 + Y_5 + Y_6}{6} , \quad (3)$$

where  $Y_1, Y_2, Y_3, Y_4, Y_5, Y_6$  represent the six percentage shares of yellowish scales along the diagonal lines.

Nevertheless, the final percentage share of yellowish scales is calculated by taking the average from both sides of the fruit and it can be calculated in the following manner:

$$Y = \frac{Y_{sf} + Y_{sb}}{2} , \quad (4)$$

where  $Y_{sf}$  represents the percentage share of yellowish scales in the sample image showing the front side of the fruit and  $Y_{sb}$  represents the percentage share of yellowish pixels in the sample image showing the back side of the fruit.

### 3.5. Classification

36 sample images have been taken to determine 7 indexes corresponding to the percentage share yellowish scales in a given pineapple. Among 36 sample images, experts had determined that 5 sample images are used for index 1 to index 6 while 6 sample images are used for index 7 to obtain the percentage of yellowish scales.

During the preliminary test, values ranging from 130 to 200 (at intervals of 10, e.g. 130, 140, 150, ..., 200) were verified. After detailed observations, the value of 160 was selected as most suitable for the needs of the prototype system and was assumed to be the threshold value for determining whether the green or the yellow pixel counter should be incremented. The indexes of 1–7 were defined by experts from the Sarawak Land Consolidation & Rehabilitation Authority (SALCRA). 36 sample images were sent to experts in order to be assigned to the specific ripeness indexes.

Table 2  
Percentage shares of yellowish scales

Index	FAMA	Specified range
1	0%	0% < yellowish ≤ 9.57%
2	A little bit	9.57% < yellowish ≤ 19.86%
3	1–2 scales	19.86% < yellowish ≤ 24.70%
4	About 25%	24.70% < yellowish ≤ 39.40%
5	About 50%	39.40% < yellowish ≤ 58.00%
6	More than 75%	58.00% < yellowish ≤ 71.66%
7	100%	71.66% < yellowish ≤ 100%

The percentage shares of yellowish scales for each index are presented in Table 2. These 7 indexes of ripeness are grouped into three classes, namely unripe, ripe and fully ripe, based on the score of yellowish percentage and the ripeness level according to index maturity in Table 3.

Table 3  
Ripeness level according to the maturity index [1]

Ripeness	Index of maturity
Unripe	index 1, index 2
Ripe	index 3, index 4, index 5
Fully ripe	index 6, index 7

### 4. Results and Evaluation

An experiment was carried out to improve the accuracy of ripeness classification procedures. 86 sample images of 43 pineapples, including those used in Subsection 3.5, were sent to the SALCRA in order to be graded manually by local experts. Based on the manual grading process, 12 of the samples were classified as unripe, 12 as ripe and 19 as fully ripe. The expert grader’s assessment was then compared with the data obtained with the use of the prototype system (Table 4).

It turned out that six pineapple samples had been misclassified. All samples classified manually as fully ripe were misclassified as ripe when using the prototype system. One of the reasons is that some samples have large pineapple eyes, meaning that the diagonal lines took those areas into consideration as well. Also, some pineapple samples are characterized by huge differences in the percentage share of yellowish scale between front and back sides of the fruit (Fig. 14). On top of that, classification inaccuracy may also be caused by poor light conditions prevailing when taking sample images.

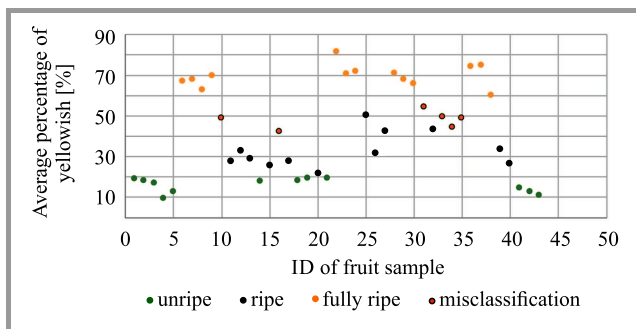


Fig. 14. Results achieved with the use of the proposed solution.

The accuracy of fruit ripeness classification can be calculated as:

$$\text{Classification accuracy} = \frac{\text{Number of correct classifications}}{\text{Number of experiments involving fruit samples}} \cdot (5)$$

The results show that the accuracy rate achieved by the prototype system while classifying an grading pineapples equals 86.05%.

Table 4  
Results achieved by the prototype system and manual grading

Sample number	Percentage of yellowish (front image) [%]	Percentage of yellowish samples (back image) [%]	Average percentage of yellowish samples (whole fruit) [%]	Ripeness category (manual grading)	Ripeness category (automated grading – prototype system)
1	17.74	20.31	19.02	U	OK
2	17.99	18.01	18.00	U	OK
3	23.78	9.57	16.68	U	OK
4	9.79	8.46	9.13	U	OK
5	9.92	15.15	12.49	U	OK
6	71.72	62.60	67.16	FR	OK
7	72.94	62.90	67.92	FR	OK
8	59.12	66.65	62.89	FR	OK
9	62.73	76.05	69.39	FR	OK
10	47.51	49.96	48.73	FR	M
11	25.93	29.08	27.51	R	OK
12	40.15	24.71	32.43	R	OK
13	31.67	25.30	28.49	R	OK
14	15.22	19.86	17.54	U	OK
15	27.43	23.17	25.30	R	OK
16	43.48	41.00	42.24	FR	M
17	31.60	23.15	27.37	R	OK
18	18.38	18.00	18.19	U	OK
19	17.58	21.51	19.55	U	OK
20	23.18	20.19	21.68	R	OK
21	23.68	14.78	19.23	U	OK
22	82.39	80.59	81.49	FR	OK
23	72.54	67.90	70.22	FR	OK
24	66.73	77.04	71.88	FR	OK
25	54.90	45.70	50.30	R	OK
26	33.88	28.90	31.39	R	OK
27	36.19	48.28	42.24	R	OK
28	69.38	72.18	70.78	FR	OK
29	63.28	72.79	68.04	FR	OK
30	62.44	68.86	65.65	FR	OK
31	55.42	53.10	54.26	FR	M
32	39.52	46.40	42.96	R	OK
33	41.43	57.39	49.41	FR	M
34	55.03	33.94	44.49	FR	M
35	47.43	50.65	49.04	FR	M
36	72.83	75.95	74.39	FR	OK
37	71.66	77.24	74.45	FR	OK
38	61.76	58.01	59.89	FR	OK
39	29.37	37.27	33.32	R	OK
40	27.46	24.99	26.23	R	OK
41	14.54	14.51	14.52	U	OK
42	16.79	8.81	12.80	U	OK
43	14.04	7.61	10.82	U	OK

FR – fully ripe, U – unripe, R – ripe, M – misclassified

## 5. Conclusions

In this paper, the proposed algorithms are used to classify the ripeness and to improve the accuracy of the process of grading pineapples. The system's algorithms are capable of classifying pineapple samples into three main groups, namely unripe, ripe and fully ripe. The overall accuracy rate achieved equaled 86.05%.

One of the limitations is that the system relies on two sample images for each classification procedure, showing the front and the back of the fruit. Thus, a specimen with uneven distribution of yellowish scales around its body may be improperly classified based on the average percentage share of yellowish scales.

In addition, the image of the sample must be captured in a controlled environment. Images taken in differing circumstances affect the end result as well. The positions of six diagonal lines are currently fixed, meaning they may intersect with the eye of the pineapple. The prototype system is also operating offline.

Future work will consist in capturing more pineapples in the same sample and in adding images of a larger number of sides of the fruit (the current prototype system is limited to two sides per sample) in order to achieve higher efficiency and accuracy of the classification process. Furthermore, the system may be improved to estimate the weight and the species of pineapples based on their size and shape.

Many improvements are still needed in order to enhance the operation of the system prior to its real-life application. The prototype system may only be operated under certain controlled conditions. All of its limitations must be addressed in the course of the work to be performed in the future.

## Acknowledgements

The project was funded under a research grant obtained from UNIMAS.

## References

- [1] C. Edward, "Uggah: Sarawak aims to be top producer of pineapples" [Online]. Available: <http://www.theborneopost.com/2016/08/09/uggah-sarawak-aims-to-be-top-producer-of-pineapples/>
- [2] J. Sung, J. H. Suh, A. H. Chambers, J. Crane, and Y. Wang, "Relationship between sensory attributes and chemical composition of different mango cultivars", *J. of Agricultural and Food Chemistry*, vol. 67, no. 18, pp. 5177–5188, 2019.
- [3] M. Mohd Ali, N. Hashim, S. Abd Aziz, and O. Lasekan, "An overview of non-destructive approaches for quality determination in pineapples", *J. of Agricultural and Food Engineer.*, vol. 1, pp. 1–7, 2020 (DOI: 10.37865/jafe.2020.0011).

- [4] J. I. Asnor, S. Rosnah, Z. W. H. Wan, and H. A. B. Badrul, "Pineapple maturity recognition using RGB extraction", *Int. J. of Electrical, Computer, Energetic, Electronic and Commun. Engineer.*, vol. 7, no. 6, pp. 597–600, 2013 (DOI: 10.5281/zenodo.1077855).
- [5] S. Mohammad, K. H. Ghazali, N. Che Zan, S. S. Mohd Radzi, and R. Abdul Karim, "Classification of fresh N36 pineapple crop using image processing technique", *Advanced Materials Res.*, vol. 418–420, pp. 1739–1743, 2011 (DOI: 10.4028/www.scientific.net/amr.418-420.1739).
- [6] J. I. Asnor, S. Rosnah, Z. W. H. Wan, and H. A. B. Badrul, "Ripeness level classification for pineapple using RGB and HSI colour maps", *J. of Theoretical and Applied Informat. Technol.*, vol. 57, no. 3, pp. 587–593, 2013 [Online]. Available: <http://www.jatit.org/volumes/Vol57No3/33Vol57No3.pdf>



**Hui Hui Wang** is currently a Senior Lecturer at the Faculty of Computer Science and Information Technology, Universiti Malaysia Sarawak (UNIMAS). She received her Ph.D. in Computer Science from Universiti Teknologi Malaysia (UTM). Her main research interests are in image retrieval, computer vision and pattern recognition.

 <https://orcid.org/0000-0002-5511-1993>

E-mail: [hhwang@unimas.my](mailto:hhwang@unimas.my)  
Universiti Malaysia Sarawak  
94300 Kota Samarahan  
Sarawak, Malaysia



**Sze Ye Chai** is currently an Application Consultant at an information technology company of NCS Pte Ltd that is based in Singapore. She received her degree in Computer Science from Universiti Malaysia Sarawak (UNIMAS).

 <https://orcid.org/0000-0002-4921-470X>

E-mail: [aliciachai\\_93@hotmail.com](mailto:aliciachai_93@hotmail.com)  
Universiti Malaysia Sarawak  
94300 Kota Samarahan  
Sarawak, Malaysia

# A Comparative Study of Various Edge Detection Techniques for Underwater Images

Ezmahamrul Afreen Awalludin<sup>1</sup>, Tengku Noorfarahana T. Arsad<sup>1</sup>,  
Wan Nural Jawahir Hj Wan Yussof<sup>2</sup>, Zainudin Bachok<sup>3</sup>, and Muhammad Suzuri Hitam<sup>2</sup>

<sup>1</sup> Faculty of Fisheries and Food Science, Universiti Malaysia Terengganu, Malaysia

<sup>2</sup> Intelligent Informatics, Faculty of Ocean Engineering Technology and Informatics, Universiti Malaysia Terengganu, Malaysia

<sup>3</sup> Institute of Oceanography and Environment, University Malaysia Terengganu, Malaysia

<https://doi.org/10.26636/jtit.2022.155921>

**Abstract**—Nowadays, underwater image identification is a challenging task for many researchers focusing on various applications, such as tracking fish species, monitoring coral reef species, and counting marine species. Because underwater images frequently suffer from distortion and light attenuation, pre-processing steps are required in order to enhance their quality. In this paper, we used multiple edge detection techniques to determine the edges of the underwater images. The pictures were pre-processed with the use of specific techniques, such as enhancement processing, Wiener filtering, median filtering and thresholding. Coral reef pictures were used as a dataset of underwater images to test the efficiency of each edge detection method used in the experiment. All coral reef image datasets were captured using an underwater GoPro camera. The performance of each edge detection technique was evaluated using mean square error (MSE) and peak signal to noise ratio (PSNR). The lowest MSE value and the highest PSNR value represent the best quality of underwater images. The results of the experiment showed that the Canny edge detection technique outperformed other approaches used in the course of the project.

**Keywords**—edge detection, mean square error, median filtering, peak signal to noise, wiener filtering.

## 1. Introduction

Exploration of the underwater environment with the use of video and images is a challenging and fascinating procedure due to several problems, including noise, limited visibility, light scattering, attenuation concerns, non-uniform lighting, and other factors affecting the seawater environment [1], [2]. Artificial light sources also cause image blur, haziness, and are a source of a bluish or greenish hue in underwater images, leading to high absorption, scattering, color distortion, and noise [3]. As a result of this scenario, researchers will find it difficult to perform more extensive research harnessing computer technology, particularly while classifying, recognizing and segmenting coral reef components and numerous fish species. It is vital to

understand the underwater ecology to manage and monitor marine resources effectively. Therefore, image analysis techniques based on computer vision and image processing technologies have been established to monitor marine resources properly. However, no quantitative or qualitative assessment of all underwater marine resources has been conducted, according to [4].

With these constraints in mind, the edge detection process is used as the first computation approach aiming to reduce noise in underwater images, while preserving the important edges. It is commonly used in low-level image processing to retain the best possible edges for higher-level processing [5], [6]. On the other hand, noise content and the density of edges in the image all influence how well edge detection works. Apart from image enhancement, edge detection is extensively applied in pattern recognition and classification techniques [8], [9]. Advanced research concerned with underwater image analysis also used edge detection techniques, for instance in recognizing underwater sonar images [10]. Edge detection techniques also have also been used in conjunction with autonomous underwater vehicles (AUVs) [11] and acoustic devices [12].

The remainder of this paper is organized in the following manner. Several related works on underwater image and edge detection techniques are discussed in Section 2. The technique's principles and hypotheses related to multiple edge detection algorithms, data acquisition, experimental design, and image quality measurement based on mean square error (MSE) and peak signal noise ratio (PSNR) are discussed in Section 3. The analysis of the experimental results using coral reef image datasets are presented in Section 4. Section 5 concludes the discussion.

## 2. Related Works

Most underwater images are texture images that contain both living and non-living objects. For segmenting and

detecting objects in underwater images, many researchers have carried out several different studies. We review some of the studies that are similar to the proposed work.

Acoustic underwater images are challenging to edge-identify. Article [12] improved underwater acoustic images by applying edge detecting algorithms. The authors employed Wiener filtering to reduce speckle noise while maintaining high-frequency components. Meanwhile, the median filter was used to remove small objects from the image. Overall performance was assessed by obtaining a local minimum and maximum from morphological operations. The resulting edge maps tracing objects in underwater acoustic images were compared with Canny and Sobel edge detection algorithms. The results outperformed conventional methods but were still contaminated by noise. Paper [13] suggested an edge identification method based on fractional order differentiation for underwater images. A texture improvement filter based on the Grünwald Letnikov (G-L) fractional differential operator was devised and explored. Diverse underwater images were selected to analyze both conventional and fractional differential operators, respectively. The findings were also compared with the Riemann-Liouville fractional differential operator technique (R-L). The recommended strategy outperformed both traditional and R-L-based methods in recognizing the edges of low-contrast underwater images, offering a high level of accuracy, excellent brightness and more information.

Almost all segmentation approaches aim to classify images. However, images can be misclassified into various clusters, leading to overlapping pixels being identified over the actual edges. Article [15] used Canny edge detection for segmentation to manage challenging underwater images and to expose essential information without distortion. The paper showed that Canny improves the signal-to-noise ratio, reduces analytical error rate, and ensures high efficiency, good localization, and precise response while dealing with underwater images.

Paper [11] used edge detection methods and the Lab color model to improve underwater image quality. The authors performed edge detection after color correction and contrast enhancement. Due to light illumination, water velocity, and suspended particles, they preferred to use color detection due to the poor results obtained from direct edge recognition performed on underwater images. Although their approach was efficient at detecting the shapes of objects, some noise remained. They hoped to improve current edge detection results by applying deep networks for automated operations.

According to [16], underwater environmental research still has a great deal of unrealized potential. They discussed numerous alternative image quality enhancement techniques in their review paper, including a deep learning approach, color restoration, color evaluation metrics, and image processing approaches. Meanwhile, article [17] suggested segmenting selected underwater objects in the images using Canny edge detection and the active contour model. Furthermore, [4] used contrast limited adaptive histogram

equalization (CLAHE) in conjunction with an adaptive histogram and a Haar wavelet to reduce noise in underwater images while maintaining their edges. PSNR, contrast to noise ratio (CNR), image enhancement metric (IEM), and absolute mean brightness error (AMBE) are all used to quantify edge detection efficiency.

### 3. Methodology

Detecting edges is a crucial task in digital image processing and is required to increase confidence levels related to image segmentation, pattern recognition and detection of objects. This study uses various edge detection techniques, such as Sobel, Prewitt, Roberts, LoG and Canny. Figure 1 presents a flowchart of the comparative study of various edge detections techniques for underwater images. First, we intentionally corrupted such images with Gaussian noise, as well as salt and pepper noise (SPN). In the next

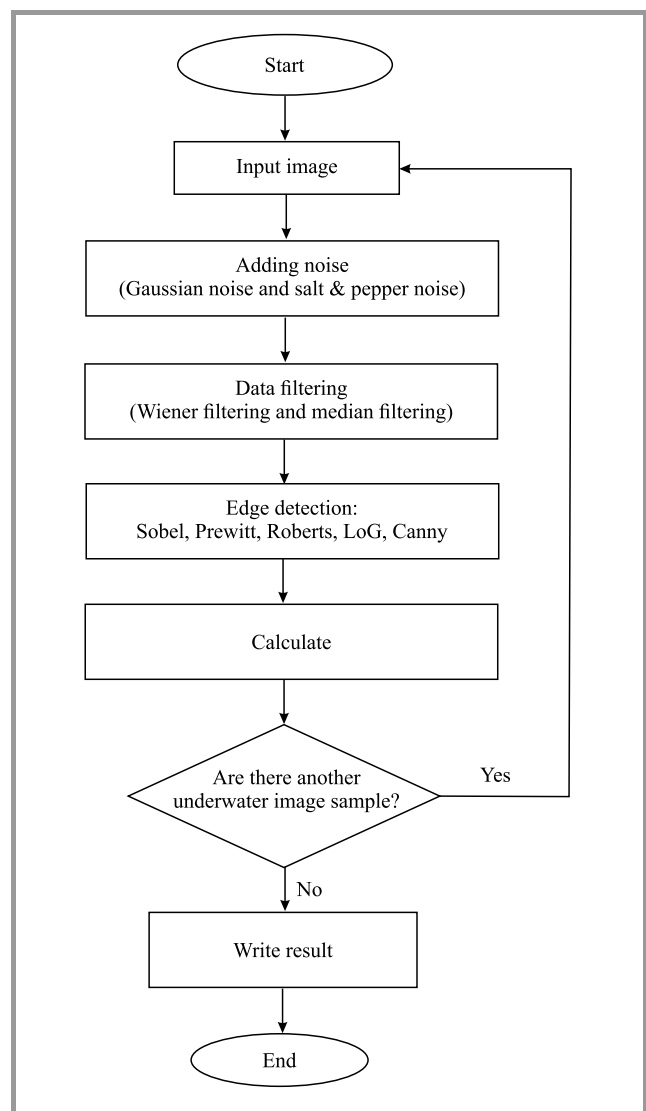


**Fig. 1.** Flowchart presenting a comparative study of edge detection techniques for underwater images.

step, Wiener filtering and median filtering were applied to effectively remove noise disorder from images. Then, all edge detection techniques mentioned above are used as a pre-processing stage in the study. The best edge detection result is determined based on successfully preserving true edges and minimizing noise from the image. We use MSE and PSNR to evaluate edge detection algorithms for quantitative measurement.

**3.1. Data Acquisition**

The study used Acropora branching images that served as an underwater image sample dataset. The data was collected from three different sample sites in the Redang islands, such as Pulau Lima, Pulau Kerengga and Pasir Panjang. Our group worked with the Institute of Oceanography and Environment (INOS) at Universiti Malaysia Terengganu to collect the data. Line intercept transect (LIT) video images were obtained with the use of a high-quality underwater video camera. 100 m transect lines were built at each dive site using measuring tape positioned at the depth of 3 m and 10 m. A diver towed the transect line to record videos and images of the coral reef. The Acropora branching images were set to measure 300 × 300 pixels, as shown in Fig. 2b.

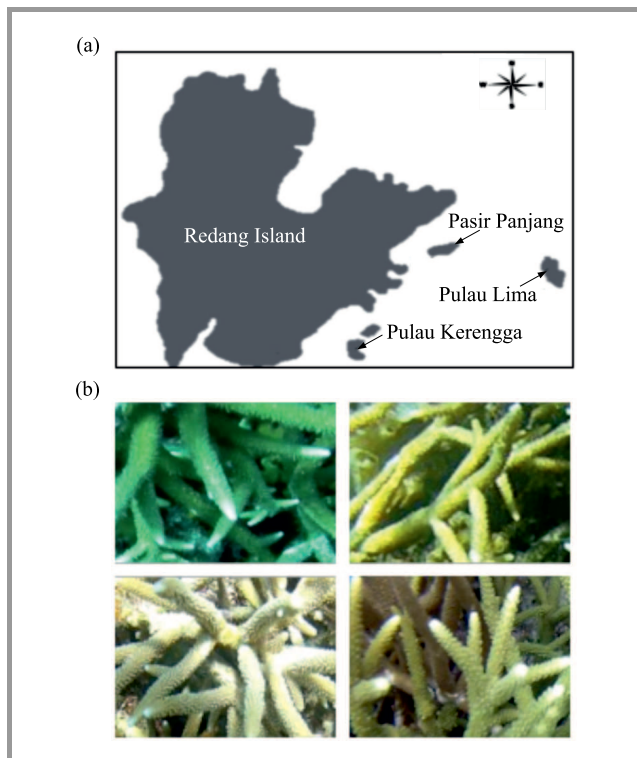


**Fig. 2.** (a) Data collection at Redang islands, (b) Acropora branching images.

**3.2. Theoretical Edge Detection Techniques**

Edge detection is an excellent way to discover crucial edges in an image while reducing noise. Edge detection using

first and second-order derivatives has been widely used for image enhancement [18], [19]. First-order derivative operators are more prone to noise and spurious edges. First-order derivative operators include Sobel, Prewitt, Roberts, and Canny. Second-order derivative operators are more efficient but still sensitive to noise [20], [21]. Two examples of second-order derivative edge detection techniques the include difference of Gaussian (DoG) and the Laplacian of Gaussian (LoG) (e.g. the Marr-Hildreth meth).

**Table 1**  
Kernel mask of each edge detection techniques

Technique	Kernel mask $G_x$	Kernel mask $G_y$
Sobel	$G_x = \begin{bmatrix} -1 & 0 & +1 \\ -2 & 0 & +2 \\ -1 & 0 & +1 \end{bmatrix}$	$G_y = \begin{bmatrix} -1 & 0 & +1 \\ -2 & 0 & +2 \\ -1 & 0 & +1 \end{bmatrix}$
Prewitt	$G_x = \begin{bmatrix} -1 & 0 & +1 \\ -1 & 0 & +1 \\ -1 & 0 & +1 \end{bmatrix}$	$G_y = \begin{bmatrix} -1 & -1 & +1 \\ 0 & 0 & 0 \\ +1 & +1 & +1 \end{bmatrix}$
Roberts	$G_x = \begin{bmatrix} +1 & 0 \\ 0 & -1 \end{bmatrix}$	$G_y = \begin{bmatrix} 0 & +1 \\ -1 & 0 \end{bmatrix}$
LoG	$G_x = \begin{bmatrix} 0 & -1 & 0 \\ -1 & 4 & -1 \\ 0 & -1 & 0 \end{bmatrix}$	$G_y = \begin{bmatrix} -1 & -1 & -1 \\ -1 & 8 & -1 \\ -1 & -1 & -1 \end{bmatrix}$
Canny	$G_x = \begin{bmatrix} -1 & 0 & +1 \\ -2 & 0 & +2 \\ -1 & 0 & +1 \end{bmatrix}$	$G_y = \begin{bmatrix} -1 & 0 & +1 \\ -2 & 0 & +2 \\ -1 & 0 & +1 \end{bmatrix}$

**Table 2**  
Formula for gradient magnitude and orientation angle

Gradient magnitude $ G $	Orientation angle $\theta$
$ G  = \sqrt{G_x^2 + G_y^2}$	$\theta = \arctan \frac{G_y}{G_x}$

As shown in Table 1, different kernel masks are used in different edge detection techniques. The aspects of the input image that affect the kernel mask operator include brightness and lighting [22], [23]. Typically, two mask kernels respond to vertical and horizontal edges. These were created by mixing two convolution mask kernels. Edge orientation was computed using magnitude gradient data. Table 2 shows the gradient’s magnitude and angle direction. These methods work best when edges are well retained. Image localization is sound and minimal noise disturbance is experienced.

The  $x$ - and  $y$ -gradients are generated using a set of  $3 \times 3$  kernel masks based on each edge detection, as shown in Table 1. The gradient magnitude is computed by adding  $G_x$  and  $G_y$ . Table 2 explains how to use the Pythagoras' law to calculate gradient magnitude. We can also determine the orientation angle of the edge location  $(x, y)$  with the gradient magnitude.

The Canny operator is a well-known technique for recognizing edges since it removes image noise. It uses a multi-stage method to find absolute edge boundaries affected by noise and position selection, and it only responds to single edges. The Gaussian kernel is used to smooth out image noise and can be described as:

$$G_\sigma = \frac{1}{\sqrt{2\sigma^2}} e^{-\frac{x^2+y^2}{2\sigma^2}}, \quad (1)$$

where standard deviation is used to calculate the distance between Gaussian distributions. The gradient magnitude and orientation are computed using the equations from Table 2. Non-maximum suppression is also used to thin out the edges while eliminating pixels that are not part of the edge. Meanwhile, non-maximum suppression pixels can be measured using:

$$g_T(x, y) = \begin{cases} g(x, y), & \text{if } g(x, y) \geq T \\ 0, & \text{otherwise} \end{cases}. \quad (2)$$

Non-maxima pixels are suppressed by comparing them with two neighbors in the gradient's direction. If nothing changes, set the number to 1. When the density gradient value approaches a higher threshold, double thresholding considers the pixels as edges. Pixels are eliminated as edges if the gradient strength is less than a threshold. A pixel is only taken into account if it is adjacent to another pixel above the upper threshold.

The Laplacian operator is a second-order derivative edge detector commonly used in signal processing. A second-order derivative edge detection approach produces a lot of noise in the output image, necessitating a smoothing procedure. A Gaussian filter is applied to the image before applying the LoG operator. The Gaussian filter formula is:

$$G_\sigma = \frac{1}{\sqrt{2\pi\sigma^2}} e^{-\frac{x^2+y^2}{2\sigma^2}}, \quad (3)$$

and the Laplacian operator is computed as:

$$\nabla^2 g = \frac{(\partial^2 f)}{(\partial^2 x)} + \frac{(\partial^2 f)}{(\partial^2 y)}, \quad (4)$$

$$\nabla^2 g(x, y) = \frac{1}{\sigma^2} \left[ \frac{x^2+y^2}{\sigma^2} - 2 \right] e^{-\frac{(x^2+y^2)}{2\sigma^2}}. \quad (5)$$

The image gradient output is marked by the symbol  $\nabla^2 g$ , and the Laplacian edge operator is denoted by the sign  $g(x, y)$ . It is responsible for determining the location of

the pixel intensity in the image. The LoG is a convolution mask that may be calculated using the Eqs. (4) and (5). In this case, the gradient output value of LoG is  $g(x, y)$ . Meanwhile, the  $x$  and  $y$  axes reflect the horizontal and vertical direction values of the input image, respectively. The sign  $\sigma$  denotes the standard deviation value that is utilized in the Gaussian distribution.

### 3.3. Wiener and Median Filtering

The median filter is a simple and effective non-linear filter. It is used to reduce the difference in intensity between two pixels. The median is calculated by ascending all pixel values and then replacing the calculated pixel with the middle pixel value. The median filter can be calculated as:

$$I'(u, v) \leftarrow \text{median} \{I(u+i, v+j) \mid (i, j) \in w\}. \quad (6)$$

The  $w$  sign signifies a user-defined neighborhood inside the image centered on  $(u, v)$ . Meanwhile,  $i$  and  $j$  represent the coordinates of the image's pixel values.

On the other hand, the Wiener filter reduces the amount of noise that has distorted a signal. The goal of the Wiener filter is to minimize the mean square error as much as possible. It is a useful technique for reducing image noise and blurring. As part of image processing, it considers both the degradation mechanism and noise. The formula given below can be used to calculate the Wiener filter:

$$\nabla^2 g(x, y) = \frac{H^*(u, v)}{|H(u, v)|^2 P_s(u, v) + P_n(u, v)}. \quad (7)$$

$H(u, v)$  shows the degradation conjugate complex form.  $P_s(u, v)$  represents the signal power spectrum density, which is the most crucial thing when it comes to noise. Meanwhile,  $P_n(u, v)$  indicates the power spectral distribution density of the original image. Finally,  $H(u, v)$  denotes the degradation function.

### 3.4. Quantitative Measurement

MSE and PSNR are numerical measures used to evaluate edge detection efficiency. An underwater image of the best quality has the lowest mean square error and the highest peak signal to noise ratio. We measured the parameters below to compare the original and filtered images. The MSE computes the change in square error between the encoded and original images. It is the most crucial factor to consider when evaluating a predictor or estimator. Instead of an absolute difference, the loss between two separate edge detectors is calculated using a squared difference in a random variable. MSE is expressed as follows:

$$MSE = \frac{1}{mn} \sum_m \sum_n (x_{mn} - y_{mn})^2, \quad (8)$$

where:  $m$  – number of rows in cover image,  $n$  – number of columns in cover image,  $x_{mn}$  – pixel value from original image,  $y_{mn}$  – pixel value from filtered image.

The  $x$  symbol represents the original image, whereas the  $y$  symbol represents the filtered version of the same image. The images have a resolution of  $m \times n$  pixels in resolution, representing the number of rows and columns, respectively. PSNR is the ratio between the maximum possible power of a signal and the power of corrupting noise [14]. It determines how well an image is reconstructed. PSNR can be calculated as:

$$PSNR(x,y) = \frac{10\log_{10}[\max(\max(x), \max(y))]^2}{|x - y|^2} . \quad (9)$$

### 3.5. Sensitivity Measurement

In this section, sensitivity estimation distribution is used to evaluate the performance of each edge detection algorithm. The fraction of edges that are correctly categorized as edges is addressed in the study as sensitivity. The sensitivity curve has the form of a series of distinct threshold values ranging from 0 to 0.5. The formula for calculating the quantitative value of sensitivity is:

$$Sensitivity = \frac{TP}{TP + FN} . \quad (10)$$

Table 3  
Sensitivity variable definition

	Edges present	Edges absent
Edges detected	True positive (TP)	False positive (FP)
Edges not detected	False negative (FN)	True negative (TN)

## 4. Experimental Results

The experiments were all conducted using Matlab. All edge detection techniques were evaluated using Wiener and median filters. The effects of both filters were compared using Gaussian and SPN. The best edge detection algorithms have the lowest MSE and the highest PSNR values.

### 4.1. Experiment 1

The effects of processing Acropora branching images by applying the Wiener filter with additional Gaussian noise are shown in Fig. 3. The effects of processing Acropora branching images by applying the Wiener filter with additional Gaussian noise are shown in Fig. 3, these edge detection techniques generally suffer from information loss due to Gaussian noise sensitivity. While the LoG algorithm is able to categorize edges, it fails to obtain ideal edges and struggles to reduce Gaussian noise in the image. The Canny edge detection technique surpasses all other edge detection algorithms because it incorporates Gaussian filtering. The

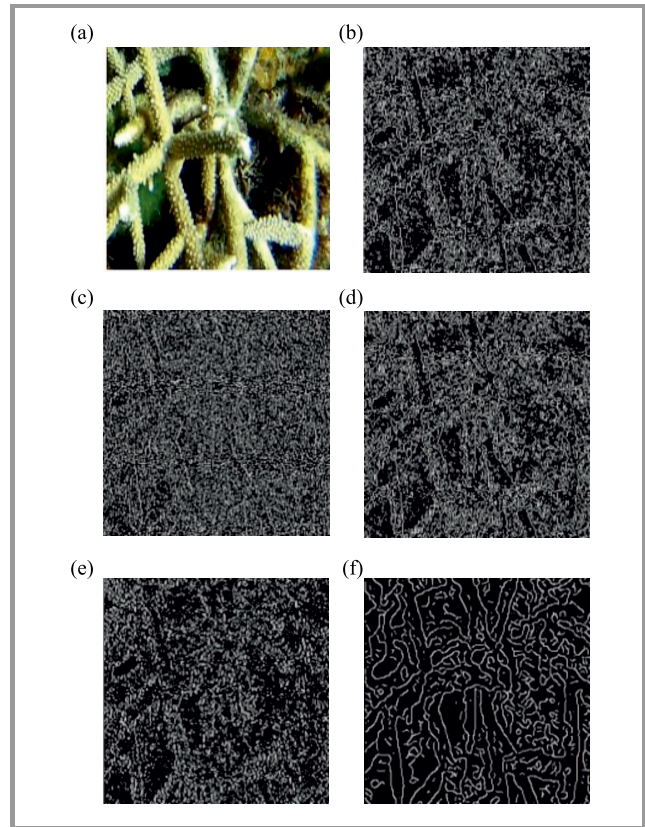


Fig. 3. (a) original image, (b) Prewitt, (c) Roberts, (d) Sobel, (e) LoG, and (f) Canny edge detectors.

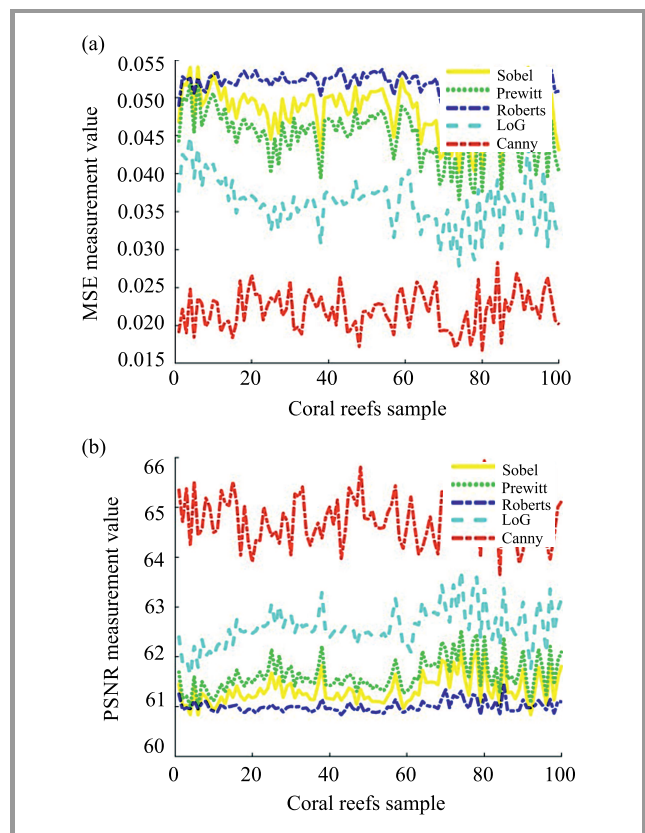


Fig. 4. (a) MSE and (b) PSNR analysis of various edge detection algorithms with Wiener filtering by adding Gaussian noise.

technique is capable of reducing the Gaussian noise while maintaining good edge orientation.

In terms of quantitative measurements, the Canny algorithm outperforms Sobel, Prewitt, Roberts, and LoG algorithms when using 100 sample images. The Canny algorithm achieves the lowest MSE values and the highest PSNR values, ensuring good quality while minimizing noise. This shows that the Canny algorithm could eliminate Gaussian noise. The results are presented in Fig. 4. Meanwhile, Table 4 shows the average MSE and PSNR values measured.

Table 4

Average MSE and PSNR values for experiment 1

	Sobel	Prewitt	Roberts	LoG	Canny
MSE	0.051	0.048	0.058	0.081	0.022
PSNR	61.144	61.386	60.527	59.092	64.768

**4.2. Experiment 2**

Figure 5 shows the results achieved with the use of all edge detection techniques by deploying Wiener filtering and adding SPN to the image. From the experimental results, one can observe that Prewitt, Sobel, Roberts and LoG algorithms cannot preserve Acropora coral reef branching edges and are not capable of suppressing unwanted noise

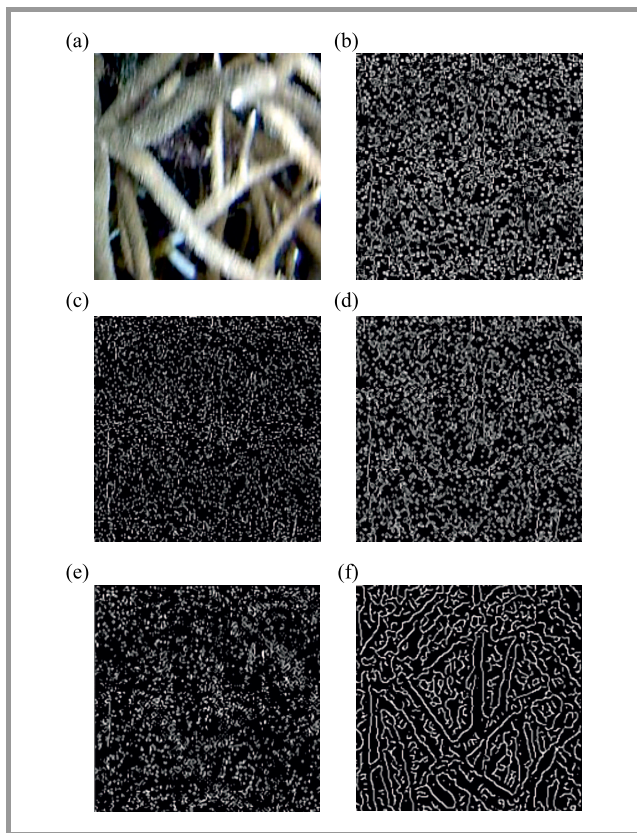


Fig. 5. (a) original image, (b) Prewitt, (c) Roberts, (d) Sobel, (e) LoG, and (f) Canny edge detectors.

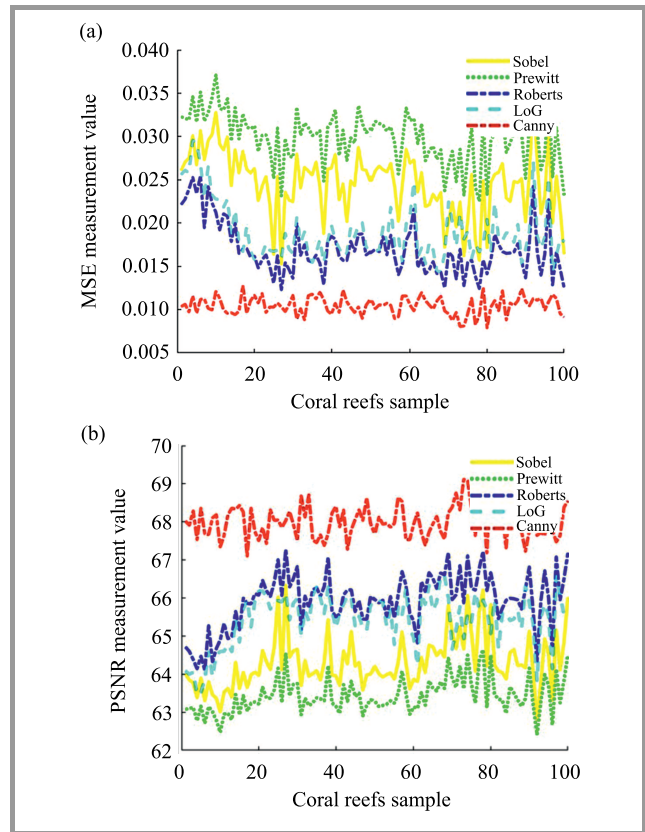


Fig. 6. (a) MSE and (b) PSNR analysis of various edge detection algorithms with Wiener filtering by adding SPN.

properly. In addition, high MSE and low PSNR values produced by these techniques are significant as well – see Fig. 4. Meanwhile, the Canny algorithm outperforms all other edge detection techniques in this scenario, with the lowest MSE and the highest PSNR. However, some edges are not sufficiently simplified by Canny edge detection techniques. This problem occurs when the two filters interact. The first of them was the Wiener filter used to reduce the noise from underwater images. The other was the Gaussian filter to affect the pixel edges by removing noise with information. Table 5 shows the average MSE and PSNR values for 100 Acropora branching images.

Table 5

Average MSE and PSNR values for experiment 2

	Sobel	Prewitt	Roberts	LoG	Canny
MSE	0.025	0.03	0.017	0.019	0.010
PSNR	64.312	63.428	65.925	65.446	67.999

**4.3. Experiment 3**

Figure 7 shows the effects of using median filtering and Gaussian noise. Similar results are obtained as in the previous experiment, with LoG, Roberts, Sobel, and Prewitt techniques failing to decrease Gaussian noise consider-

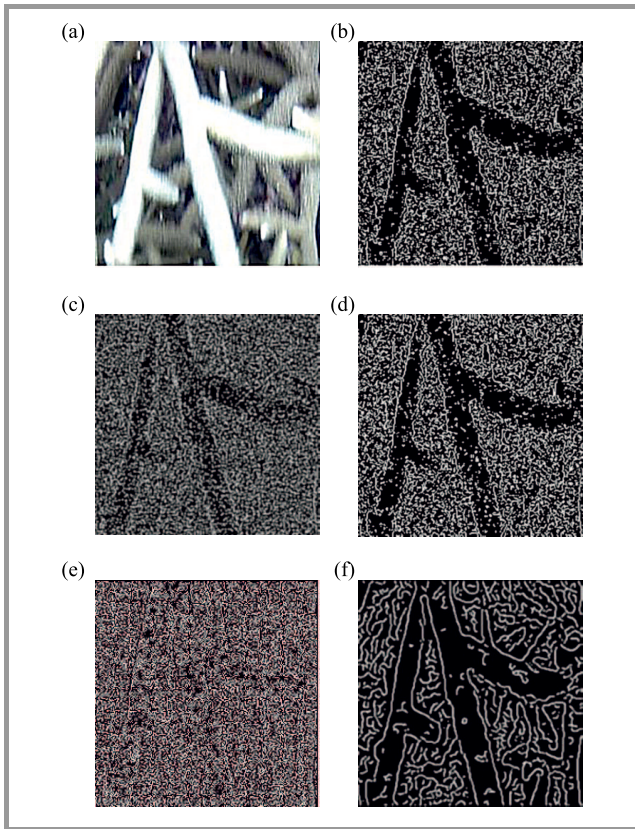


Fig. 7. (a) original image, (b) Prewitt, (c) Roberts, (d) Sobel, (e) LoG, and (f) Canny edge detectors.

ably. When applied to Gaussian noise images, these techniques tend to distort edges and cannot remove Gaussian noise. When applied to Gaussian noise images, these techniques tend to distort edges and cannot remove Gaussian noise. The Canny algorithm offered better image quality than the LoG, Roberts, Sobel, and Prewitt techniques during the experiment. However, some edges are missing when using the Canny approach.

The LoG, Roberts, Sobel, and Prewitt algorithms produce the worst image quality, as illustrated in Fig. 8. Again, the Canny edge detection algorithm produces the best edge detection result for the second part of the experiment, with the lowest MSE and the highest PSNR. Table 6 below shows the average MSE and PSNR values for 100 coral reef Acropora branching images.

Table 6  
Average MSE and PSNR values for experiment 3

	Sobel	Prewitt	Roberts	LoG	Canny
MSE	0.050	0.048	0.017	0.058	0.022
PSNR	61.144	61.386	60.526	59.092	64.767

#### 4.4. Experiment 4

The Acropora branching image effects are shown in Fig. 9 using median filtering with SPN. As a result, the Canny

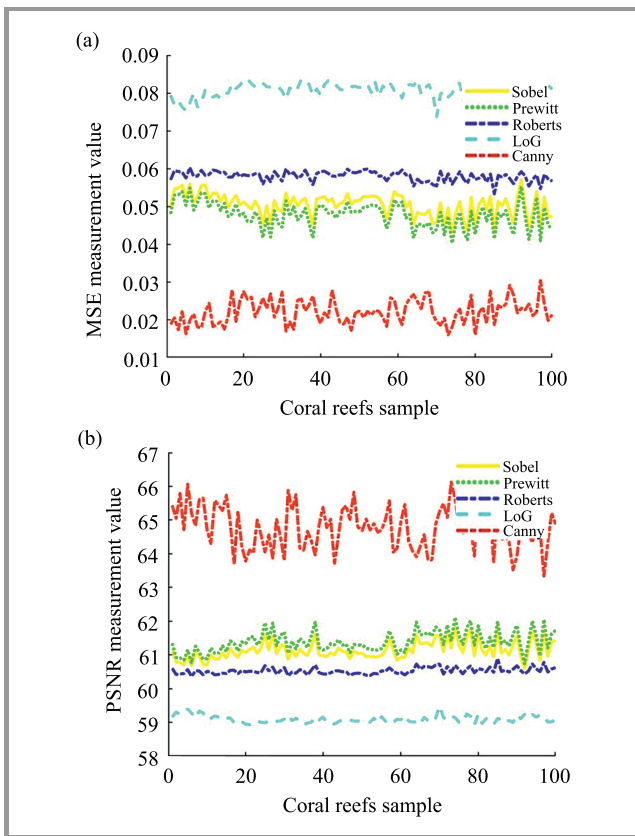


Fig. 8. (a) MSE and (b) PSNR analysis of various edge detection algorithms with median filtering by adding Gaussian noise.

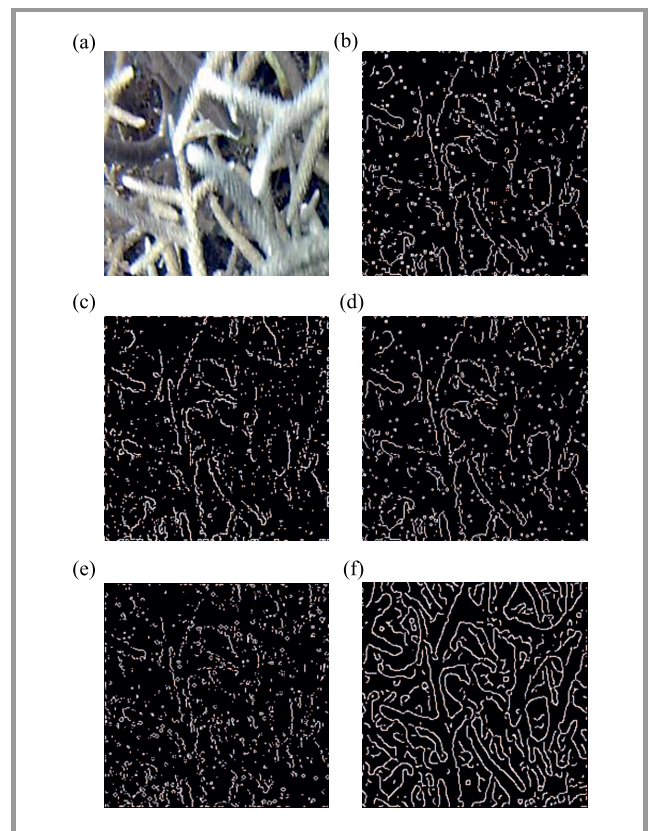
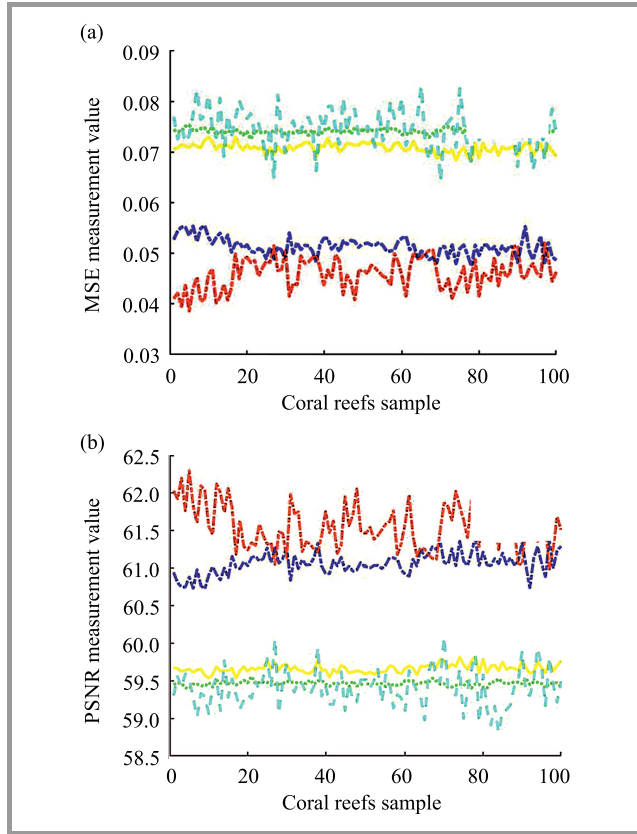


Fig. 9. (a) original image, (b) Prewitt, (c) Roberts, (d) Sobel, (e) LoG, and (f) Canny edge detectors.

approach outperforms conventional edge detection techniques when it comes to maintaining critical edges while decreasing noise. Quantitative measurements reveal that the LoG, Prewitt, Sobel and Roberts algorithms provided the lowest image quality due to the highest MSE and lowest PSNR values, respectively. However, the Canny approach offers better results based on the quantitative measurement analysis, which achieving the lowest MSE (Fig. 10a) and the highest PSNR (Fig. 10b) values (Table 7).



**Fig. 10.** (a) MSE and (b) PSNR analysis of various edge detection algorithms with median filtering by adding salt and pepper noise.

Table 7

Average MSE and PSNR value for experiment 4

	Sobel	Prewitt	Roberts	LoG	Canny
MSE	0.071	0.074	0.051	0.075	0.046
PSNR	59.664	59.464	61.065	59.493	61.551

#### 4.5. Sensitivity Results

Sensitivity is increased by varying the threshold value, as illustrated in Fig. 12. Table 8 summarizes the results of all detectors with various threshold values. Meanwhile, Fig. 11 presents the graph of the sensitivity of different edge detectors. As a consequence of the average, it was

determined that the Canny operator was the most susceptible to all other operators. Sensitivity of the Canny edge detection approach offers the average success rate of approximately 85%.

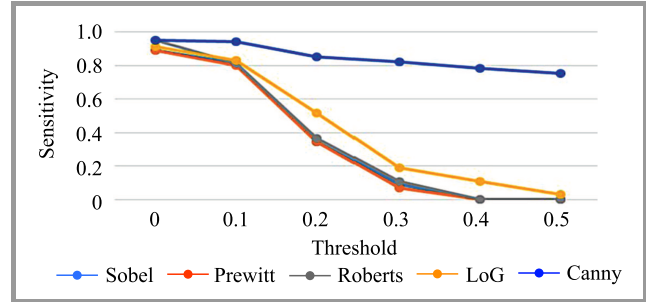


**Fig. 11.** Sensitivity of different edge detectors.

Table 8

Results concerning sensitivity of specific edge detectors

Threshold	Sobel	Prewitt	Roberts	LoG	Canny
0.00	0.891	0.891	0.950	0.911	0.950
0.10	0.812	0.802	0.812	0.832	0.941
0.20	0.347	0.347	0.366	0.515	0.852
0.30	0.089	0.069	0.109	0.188	0.822
0.40	0.000	0.000	0.000	0.109	0.782
0.50	0.000	0.000	0.000	0.030	0.752
Average	0.356	0.351	0.373	0.431	0.850

## 5. Conclusion

Prewitt, Sobel, Roberts, and LoG techniques suffer from some difficulties when extracting noise from underwater images compared with the well-known Canny edge detection algorithm. While the latter is better at eliminating most noise, it is not capable of easily distinguishing certain important edges. The effectiveness of each edge detection method was compared using Wiener and median filtering. Wiener filtering did not improve the images significantly. The Wiener filter is suitable just when it comes to removing noise, but not when it comes to maintaining edges in underwater images. Meanwhile, by incorporating median filtering into the edge detection algorithms, Gaussian as well as salt and pepper noise can be removed with the edges still being effectively preserved in the images.

## 6. Acknowledgements

The authors wish to thank the Ministry of Higher Education (MOHE) for supporting the project with funding from the Fundamental Research Grant Scheme (FRGS) FRGS/1/2018/ICT02/UMT/03/1 (vote no. 59544).

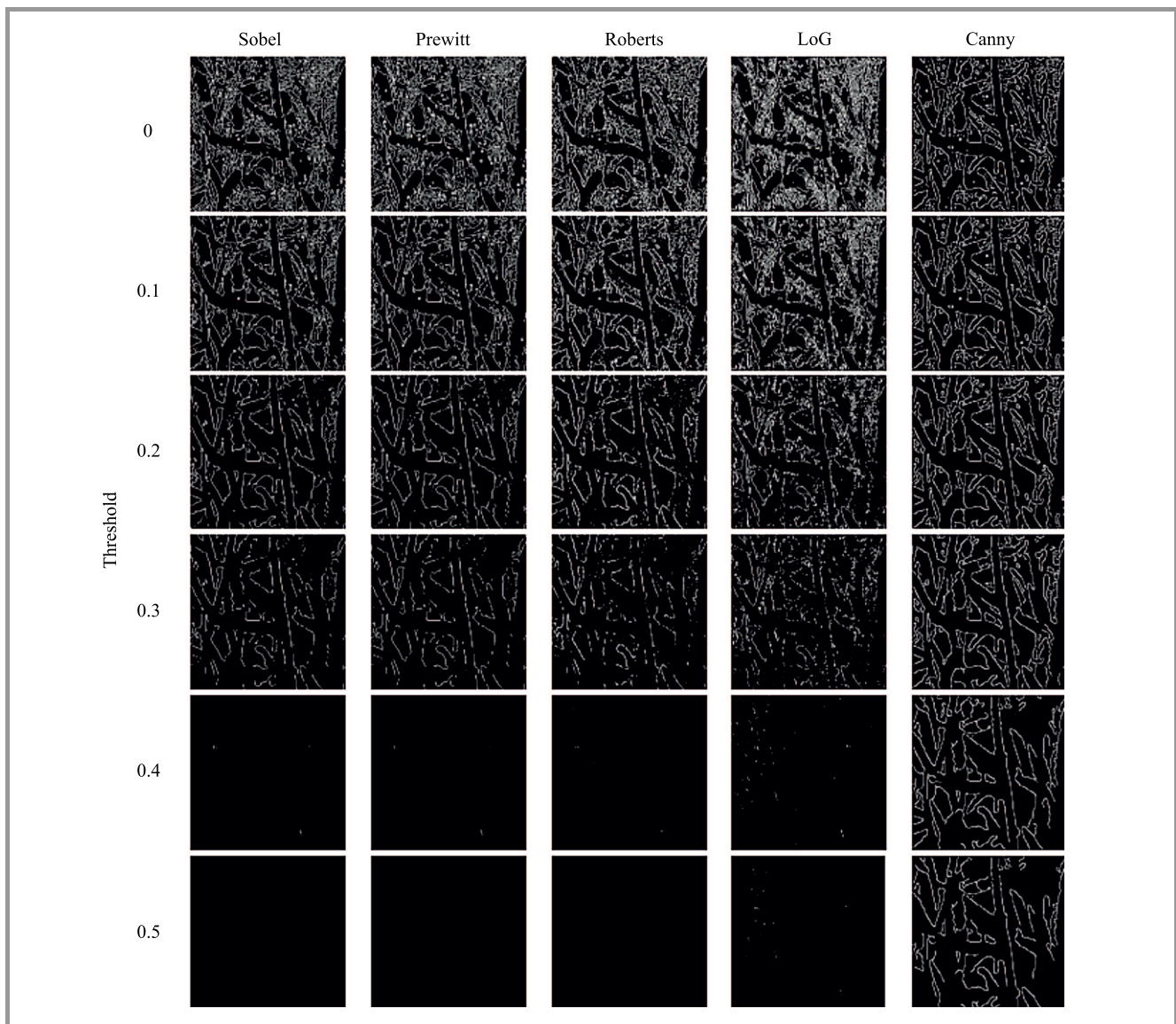


Fig. 12. The sensitivity results of images are affected by different threshold values.

## References

- [1] M. Fatan, M. Daliri, and A. Shahri, "Underwater cable detection in the images using edge classification based on texture information", *Measurement*, vol. 91, pp. 309–317, 2017 (DOI: 10.1016/j.measurement.2016.05.030).
- [2] A. Saini and M. Biswas, "Object detection in underwater image by detecting edges using adaptive thresholding", in *Proc. of 3rd Int. Conf. on Trends in Electron. and Informat. ICOEI 2019*, Tirunelveli, India, 2019, pp. 628–632 (DOI: 10.1109/ICOEI.2019.8862794).
- [3] P. Princess, S. Silas, and E. B. Rajasingh, "Performance analysis of edge detection algorithms for object detection in accident images", in *Proc. of Global Conf. for Advan. in Technol. GCAT 2019*, Bangalore, India, 2019 (DOI: 10.1109/GCAT47503.2019.8978438).
- [4] K. Srividhya and M. Ramya, "Performance analysis of pre-processing filters for underwater images", in *Proc. of Int. Conf. on Robot., Autom., Contr. and Embed. Syst. RACE 2015*, Chennai, India, 2015 (DOI: 10.1109/RACE.2015.7097234).
- [5] M. A. Malborg, L. L. Lacatan, R. M. Dellosa, Y. D. Austria, and C. F. Cunanan, "Edge detection comparison of hybrid feature extraction for combustible fire segmentation: A Canny vs Sobel performance analysis", in *Proc. of 11th IEEE Contr. and Syst. Graduate Res. Colloq. ICSGRC 2020*, Shah Alam, Malaysia, pp. 318–322 (DOI: 10.1109/ICSGRC49013.2020.9232632).
- [6] R. Ramnarayan, N. Saklani, and V. Verma, "A review on edge detection technique canny edge detection", *Int. J. of Comp. Appl.*, vol. 178, pp. 28–30, 2019 (DOI: 10.5120/ijca2019918828).
- [7] R. Song, Z. Zhang, and H. Liu, "Edge connection based Canny edge detection algorithm", *Pattern Recog. and Image Anal.*, vol. 27, pp. 740–747, 2017 (DOI: 10.1134/S1054661817040162).
- [8] C. Jeong, H. Yang, and K. Moon, "A novel approach for detecting the horizon using a convolutional neural network and multi-scale edge detection", *Multidimens. Syst. and Sig. Proc.*, vol. 30, pp. 1187–1204, 2019 (DOI: 10.1007/s11045-018-0602-4).
- [9] Y. Zhang, X. Han, H. Zhang, and L. Zhao, "Edge detection algorithm of image fusion based on improved Sobel operator", in *Proc. of IEEE 3rd Inform. Technol. and Mechatron. Engin. Conf. ITOEC 2017*, Chongqing, China, 2017, pp. 457–461 (DOI: 10.1109/ITOEC.2017.8122336).

[10] Y. Tian, L. Lan, and L. Sun, "A review of sonar image segmentation for underwater small targets", in *Proc. of the 2020 Int. Conf. on Pattern Recogn. and Intell. Sys., Athens, Greece, 2020* (DOI: 10.1145/3415048.3416098).

[11] M. Sudhakara and M. Meena, "An edge detection mechanism using L\*A\*B color-based contrast enhancement for underwater images", *Indonesian J. of Elec. Engin. and Com. Sci.*, vol. 18, pp. 41–48, 2020 (DOI: 10.11591/ijeecs.v18.i1).

[12] R. Priyadharsini, T. Sharmila, and V. Rajendran, "An efficient edge detection technique using filtering and morphological operations for underwater acoustic images", in *Proc. of the 2nd Int. Conf. on Inform. and Commun. Technol. for Competit. Strat.*, Udaipur, India, 2016 (DOI: 10.1145/2905055.2905168).

[13] A. Bist and S. Sondhi, "Fractional order differentiator based filter for edge detection of low contrast underwater images", *Int. J. of Electron., Elec. and Computat. Syst.*, vol. 6, no. 7, pp. 376–383, 2017.

[14] H. A. Elsennary, M. E. Hussien, and A. E. Ali, "Edge detection of an image based on extended difference of Gaussian", *Amer. J. of Comp. Sci. and Technol.*, vol. 2, no. 3, pp. 35–47, 2019 (DOI: 10.11648/j.ajst.20190203.1).

[15] S. Raj, C. Jose, and M. Supriya, "Hardware realization of Canny edge detection algorithm for underwater image segmentation using field programmable gate arrays", *J. of Engin. Sci. and Technol.*, vol. 12, no. 9, pp. 2536–2550, 2017 [Online]. Available: [http://jstec.taylors.edu.my/Vol%2012%20Issue%202017%20September%202017/12\\_9\\_19.pdf](http://jstec.taylors.edu.my/Vol%2012%20Issue%202017%20September%202017/12_9_19.pdf)

[16] M. Han, Z. Lyu, T. Qiu, and M. Xu, "A review on intelligence dehazing and color restoration for underwater images", *IEEE Trans. on Syst., Man, and Cybernet.: Syst.*, vol. 50, no. 5, pp. 1820–1832, 2020 (DOI: 10.1109/TSMC.2017.2788902).

[17] T. Liu, L. Wan, and X. Liang, "An image segmentation method of underwater targets based on active contour model", *Appl. Mechan. and Mate.*, vol. 511–512, pp. 457–461, 2014 (DOI: 10.4028/www.scientific.net/AMM.511-512.457).

[18] M. Gandhi, J. Kamdar, and M. Shah, "Preprocessing of non-symmetrical images for edge detection", *Augmented Human Research*, vol. 5, Article no. 10, pp. 1–10, 2020 (DOI: 10.1007/s41133-019-0030-5).

[19] A. Baareh, A. Al-Jarrah, A. M. Smadi, and G. Shakah, "Performance evaluation of edge detection using Sobel, Homogeneity and Prewitt algorithms", *J. of Softw. Engin. and Appl.*, vol. 11, pp. 537–551, 2018 (DOI: 10.4236/jsea.2018.1111032).

[20] B. Dhruv, N. Mittal, and M. Modi, "Comparative analysis of edge detection techniques for medical images of different body parts", in *Data Science and Analytics, 4th International Conference on Recent Developments in Science, Engineering and Technology, REDSET 2017, Gurgaon, India, October 13–14, 2017, Revised Selected Papers*, B. Panda, S. Sharma, and N. Roy, Eds. *Communications in Computer and Information Science*, vol. 799, pp. 164–176. Springer, 2018 (DOI: 10.1007/978-981-10-8527-7\_15).

[21] P. Ganesan and G. Sajiv, "A comprehensive study of edge detection for image processing applications", in *Proc. Int. Conf. on Innovat. in Inform., Embedded and Commun. Syst. ICIECS 2017*, Coimbatore, India, 2017 (DOI: 10.1109/ICIECS.2017.8275968).

[22] R. Li, D. Han, J. Dezert, and Y. Yang, "A novel edge detector for color images based on MCDM with evidential reasoning", in *Proc. 20th Int. Conf. on Inform. Fusion Fusion 2017*, Xi'an, China, 2017 (DOI: 10.23919/ICIF.2017.8009727).

[23] F. Bachofer, G. Quänähervä, T. Zwiener, M. Maerker, and V. Hochschild, "Comparative analysis of edge detection techniques for SAR images", *Eur. J. of Remote Sens.*, vol. 49, pp. 205–224, 2016 (DOI: 10.5721/EuJRS20164912).



**Ezmahamrul Afreen Awalludin** is currently a Senior Lecturer at the Faculty of Fisheries and Food Science, Universiti Malaysia Terengganu. He received his Ph.D. in Computer Science from Universiti Malaysia Terengganu in 2016. His research interests focus primarily on computer vision, image processing and artificial

intelligence.

 <https://orcid.org/0000-0003-4470-0052>

E-mail: e.afreen@umt.edu.my

Faculty of Fisheries and Food Science

Universiti Malaysia Terengganu

21030 Kuala Nerus

Terengganu, Malaysia



**Tengku Noorfarahana T. Arsad** is a master student at the Faculty of Fisheries and Food Science at Universiti Malaysia Terengganu. She completed her bachelor's degree in Fisheries Sciences from Universiti Malaysia Terengganu. She is currently studying the relationship between coral reef components and fish detection

from underwater video feeds, using image processing.

E-mail: p3827@pps.umt.edu.my

Faculty of Fisheries and Food Science

Universiti Malaysia Terengganu

21030 Kuala Nerus

Terengganu, Malaysia



**Wan Nural Jawahir Hj Wan Yussof** is a Senior Lecturer at the Faculty of Ocean Engineering Technology and Informatics at the Universiti Malaysia Terengganu, which she has been a faculty member since 2006, working there as a tutor. Wan Nural Jawahir completed her Ph.D. in 2014. Her research interests lie in the area of computer vision and span all aspects, from theory to design to implementation.

computer vision and span all aspects, from theory to design to implementation.

 <https://orcid.org/0000-0002-3618-1638>

E-mail: wannurwy@umt.edu.my

Faculty of Ocean Engineering Technology and Informatics

Universiti Malaysia Terengganu

21030 Kuala Nerus

Terengganu, Malaysia



**Zainudin Bachok** is currently a Professor at the Institute of Oceanography and Environment, Universiti Malaysia Terengganu. He received his Ph.D. in Marine and Environmental Science from University of the Ryukyus, Okinawa, Japan. His research interests focus on marine ecology and, more recently, on coral reef community structures in the South China Sea.

 <https://orcid.org/0000-0002-3221-3540>  
E-mail: zainudinb@umt.edu.my  
Institute of Oceanography and Environment  
Universiti Malaysia Terengganu  
21030 Kuala Nerus  
Terengganu, Malaysia



**Muhammad Suzuri Hitam** is currently a Professor at the Faculty of Ocean Engineering Technology and Informatics at the Universiti Malaysia Terengganu. His research interests cover include image processing, content based image retrieval and pattern recognition.

 <https://orcid.org/0000-0002-0545-4437>  
E-mail: suzuri@umt.edu.my  
Faculty of Ocean Engineering Technology and Informatics  
Universiti Malaysia Terengganu  
21030 Kuala Nerus  
Terengganu, Malaysia

# Detection of Monocrystalline Silicon Wafer Defects Using Deep Transfer Learning

Adriana Ganum<sup>1</sup>, D. N. F. Awang Iskandar<sup>2</sup>, Lim Phei Chin<sup>2</sup>, and Ahmad Hadinata Fauzi<sup>2</sup>

<sup>1</sup>LONGi (Kch) Sdn Bhd, Kuching, Sarawak, Malaysia

<sup>2</sup>Universiti Malaysia Sarawak (UNIMAS), Kota Samarahan, Sarawak, Malaysia

<https://doi.org/10.26636/jtit.2022.156321>

**Abstract**—Defect detection is an important step in industrial production of monocrystalline silicon. Through the study of deep learning, this work proposes a framework for classifying monocrystalline silicon wafer defects using deep transfer learning (DTL). An existing pre-trained deep learning model was used as the starting point for building a new model. We studied the use of DTL and the potential adaptation of MobileNetV2 that was pre-trained using ImageNet for extracting monocrystalline silicon wafer defect features. This has led to speeding up the training process and to improving performance of the DTL-MobileNetV2 model in detecting and classifying six types of monocrystalline silicon wafer defects (crack, double contrast, hole, microcrack, saw-mark and stain). The process of training the DTL-MobileNetV2 model was optimized by relying on the dense block layer and global average pooling (GAP) method which had accelerated the convergence rate and improved generalization of the classification network. The monocrystalline silicon wafer defect classification technique relying on the DTL-MobileNetV2 model achieved the accuracy rate of 98.99% when evaluated against the testing set. This shows that DTL is an effective way of detecting different types of defects in monocrystalline silicon wafers, thus being suitable for minimizing misclassification and maximizing the overall production capacities.

**Keywords**—automated optical inspection, machine learning, neural network, wafer imperfection identification.

## 1. Introduction

Detecting silicon wafer defects is one of the challenges faced by silicon wafer manufacturers. Currently, silicon wafer inspections are performed manually by relying on visual inspection (VI) or using an automated optical inspection (AOI) process. VI involves an analysis of the products on the production line. Inspectors must visually identify any defects on the wafer surface, either using their naked eyes or under a microscope, before the finished goods are transferred for packing. Manual inspections involve a contact-based verification of the wafer surface. It is characterized by a low degree of automation and high

labor intensity, as the elements need to be handled by humans. Such an approach is labor intensive, inefficient and means that the process of detecting defects is inaccurate. It may also lead to the application of various standards due to objective human judgments, thus failing to meet the strict requirements of modern industry. On top of that, early detection of defects is important, as production may be halted to address the root cause of the defect, and manufacturers may mitigate their potential economic losses (time and cost) incurred in connection with withdrawing defective wafers from circulation.

Monocrystalline silicon is commonly used for photovoltaic (PV) devices. To produce a high-quality solar panel, silicon wafers must be clean and free from any impurities. However, various types of defects may occur, such as scratches, chips and cracks. Other visual defects may also be present on the surface of solar cells due to uncontrollable factors encountered during the production phase. Many types of silicon wafer defects exist that may be detected on the wafer surface. For the purpose of our study, we obtained digital images of monocrystalline silicon wafer defects from LONGi's production facility based in Kuching, Sarawak, Malaysia.

AOI is a key technique used in manufacturing to ensure the quality of printed circuit boards assemblies (PCBA) used in electronics. By detecting incorrect, missing, and incorrectly placed component, it is a swift and accurate inspection tool ensuring that the PCBs leaving the production line are defect-free. As such, the technology is capable of replacing human inspectors, as it is faster with offers higher accuracy rates.

The AOI-based silicon wafer defect recognition process is divided into three phases, i.e. image processing, pattern recognition and classification. Image processing is used to enhance the images and extract specific, useful features. Pattern recognition, meanwhile uses statistical information or machine learning techniques to classify the features into distinct categories based on their shape, color and texture. Lastly, the classification stage allows to assign the silicon wafer defect patterns recognized to specific types. AOI is

Table 1  
The comparison between manual visual inspection (VI) and automated optical inspection (AOI)

Factor	VI	AOI
Cost	High labor cost	AOI replaces visual inspection staff, thus reducing headcount and resulting in lower labor cost
Efficiency	The average time, more than 5 minutes need to be spent on inspecting 3,000 wafer elements, and the defects cannot be identified accurately	AOI may test the same amount in 10 seconds, and each machine is capable of handling 1.5 production lines
Stability	Humans suffer from fatigue and emotions, meaning that they may work while being focused for approximately 3 hours	AOI uses visual simulations, offering extremely high stability, and is capable of maintaining the same standard operating continuously over periods of time that exceed 24 hours

capable of efficiently handling the detection of particular defects. However, it continues to suffer from some misclassification issues due to the fact that the visual appearance of silicon wafer defects may be similar. Table 1 is based on LONGI's production line experience and presents a comparison between manual visual inspection and AOI, in terms of cost, efficiency, and stability [1].

Since deep learning (DL) requires a lot of data, transfer learning is the best way to address the DL requirement. DTL is an approach adopting the model parameters learned from a well-known deep learning architecture that has proven to be effective in learning new data on ImageNet. In this paper, we present our findings on transfer learning between an ImageNet dataset and the wafer defect dataset, using the MobileNetV2 model to classify six defect types shown in Fig. 1.

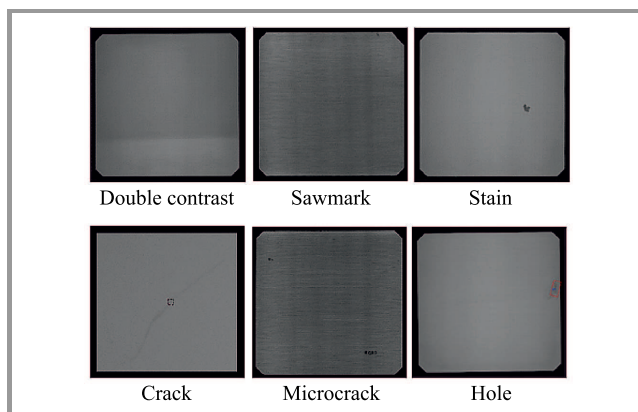


Fig. 1. Sample images of monocrystalline silicon defect types (see the digital version for color images).

The double contrast defect may occur in two situations: it may be caused by an abnormal stoppage of the line and resumption of its work with different a quality level of the wire and a different process recipe. It may also be caused by slicing the wire due to a sudden change caused by an abnormal stoppage resulting from previous cuts. Saw-marks, also known as sawlines, are caused by an abnormal stoppage occurring during slicing, and by resuming with a wire of different quality or with a different process recipe. This

phenomenon is restricted to a specific area only, but double contrast and saw-marks may occur together in one cut. Microcracks are caused by the general handling during the singulation process (wafer-dicing saw process to cut or separate each row and column of the wafer). Stain defects are caused by dirty wafers or reduced efficiency of the cleaning machine. Cracks are caused by knocking from singulation side or full breakage from microcrack. A hole defect is a bubble formed during the silicon pulling process.

The motivation behind this study was to address the current shortcomings of the AOI visual inspection method used to identify the aforementioned defects. We adopted the deep transfer learning (DTL) approach by using the MobileNetV2 architecture [2], [3] to detect and classify silicon wafer defects. Supervised learning was used, as we were using labeled data. This approach is simpler and more accurate compared to unsupervised learning. This paper expands the current knowledge on wafer classification, relying on a DLT approach that differs from that relied upon by Mat Jizat *et al.* [4] for six types of monocrystalline silicon wafer defects. The methodology was developed based on our objective to classify monocrystalline silicon wafer defects into six different categories following a single AOI pass performed during the quality control process on the production line. The monocrystalline silicon wafer defects were re-run through the AOI to check for false reject. Healthy silicon wafers are not covered by the scope of this study, as they are not identified in the course of the AOI inspection.

The rest of the paper is outlined as follows. The related work is discussed in Section 2. Section 3 describes, in detail, the DTL approach, network architecture, and the process of building the model. Experimental results are analyzed in Section 4. Section 5 contains the conclusion and presents the future work to be performed.

## 2. Related Work

Deep learning is a branch of the machine learning domain in which DL algorithms are less dependent on human intervention to learn a hierarchy of features from input data [5].

DL has been widely used for image classification [6]. The essence of DL is to learn relevant features by building learning models with multiple hidden layers. In order to enhance the accuracy of classification, vast amounts of training data are required in such an approach.

Deep transfer learning (DTL) is an adaptation of the transfer learning approach, where the knowledge from existing DL models is stored and transferred to another model to solve a different, but related problem. DTL is gaining popularity as the amount of time required to develop the model and collect the data is reduced drastically. Hence, less effort is needed for updating DTL models, as once it has been trained with a sufficient amount of data, it may be updated with a small quantity of additional data in a very short time, without compromising its accuracy [5]. Thus, DTL is suitable for solving problems involving small amounts of data.

Mat Jizat *et al.* [4] evaluated four machine classifiers for wafer defect detection on a small dataset with less than 1000 images, using InceptionV3 Transfer Learning. According to their reports, logistic regression and stochastic gradient descent (SGD) exhibit better classification accuracy in the range of 85–88%, in comparison with the two remaining classifiers. The use of more image samples and further optimization aiming to increase the accuracy rate are predicted, but no details on the training parameters are provided to support this suggestion.

Imoto *et al.* [7] compared DL with the existing automatic defect classification (ADC) approach used for detecting defects in semiconductor manufacturing. The comparison showed a significantly higher detection accuracy of DL compared to ADC. Kudo *et al.* [8] applied transfer learning in CNN to solve the issue of dislocation clusters, i.e. crystallographic defects in a photoluminescence (PL) image of multi-crystalline silicon wafers. Transfer learning of a convolutional neural network (CNN) was applied to solve the issue. The input image is a sub-region image of a whole PL image, and the CNN evaluates whether the dislocation cluster regions are detected in the upper wafer image, by using the images of dislocation clusters in lower wafers as positive examples. The experiment was carried out under three conditions: negative examples using images of some depth wafer, randomly selected images, and images from both types of condition. Then, the accuracy and Youden's J statistics were used to evaluate two cases, which are predictions of occurrences of dislocation clusters at ten or twenty upper wafers. Results from the investigation show that accuracy and Youden's J were better than the "bag of features" approach in predicting the dislocation cluster regions.

Lee and Lee [9] evaluated the use of DTL for learning new defect patterns in wafer images. They found DTL may be used as effectively as a fully trained DL model (with the accuracy difference equaling 2%). The advantage of DTL is that it learns the defects faster. It also enabled the researchers to obtain a reliable model by updating the model as needed.

### 3. Classification of Silicon Wafer Defects using DTL

The conceptual framework for classifying silicon wafer defects is presented in Fig. 2. Firstly, wafer defect images are collected with manually inspected ground truth data by industrial experts. Then, a suitable DTL architecture is identified based on the available models in the Top-1 results (based on GPU architecture) which is adopted to classify monocrystalline silicon wafer defects [10]. The next step consists in building the input pipeline tasked with reading all the collected sample images from the wafer defect data sets. After that, experiments are conducted to build the DTL-MobileNetV2 model by adding additional layers that learn the six different defect classes using the training set. The model built was saved and tested by performing a prediction with the use of the testing set. To improve the performance of the model obtained further training sessions were performed by unfreezing the parameters in the network layer.

#### 3.1. Data Collection

The sample images of the defective wafers were randomly selected from the existing database compiled by a production expert from LONGI. These images were automatically collected by running the defective wafers through an AOI machine. Manual classifications performed by industrial experts are collected as ground truth data. Examples of images in the dataset may be seen in Fig. 1. The entire dataset contains 6,000 images, with each defect class being shown in 1,000 pictures. For each defect class, the images are randomly divided into three subsets, i.e. training (70%), validation (15%), and testing (15%) sets. The resolution of each image is  $224 \times 224 \times 3$ . The training set is used to build the DTL models, while the validation set is used to provide an unbiased evaluation of the built models and to refine their parameters. The testing set is used to ensure an equitable evaluation of the best model built based on the training set.

#### 3.2. DTL Architecture

The DTL architecture used in this work was based on MobileNetV2 [2]. We used the pre-trained version of MobileNetV2 trained using the ImageNet dataset which contains 14 million images of 22 thousand visual categories [11]. Based on the learned feature maps of the MobileNetV2 pre-trained DL algorithm, significant features were extracted from silicon wafer defect images.

The advantage of using the DTL architecture consists in the fact that we do not need to use random initialization for building a new deep learning model. Instead, the model for classifying the wafer defects shares the same initialization parameters that were identified as effective during the learning process, using the ImageNet dataset. To achieve

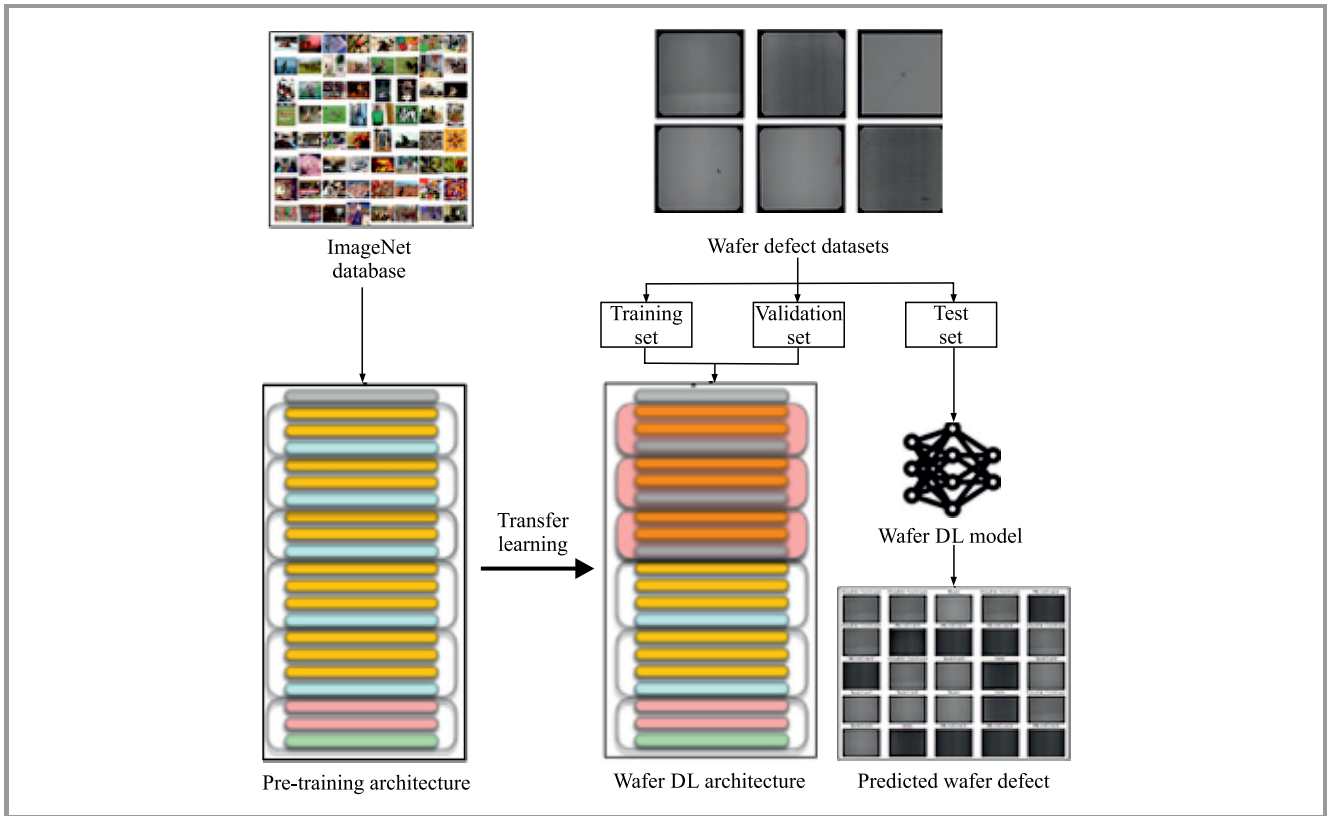


Fig. 2. Silicon wafer defect classification framework using DTL.

Table 2  
DTL training parameters

Variables	Description	Values
Base learning rate	Initial learning rate	0.001
Learning rate decay	Rate decay coefficient after every fifth epoch	0.5
Training epoch	Total training iterations	100
Optimizer	Optimization method for updating parameters based on training data (we used ADAM)	$\beta_1 = 0.9, \beta_2 = 0.999$
DropBlock	Convolution regularization technique	0.8
Learning strategy	Strategy for changing the learning rate	Step

a high classification accuracy rate, we refined the model’s parameters for identifying silicon wafer defects by unfreezing the network layers.

3.3. Experiment Design

The algorithm learned to recognize defects in silicon wafers by analyzing images of defective silicon wafers. This was done by feeding the images from the training set into the DTL architecture. The experiment was designed to assess the accuracy of using MobileNetV2 as a DL model to classify silicon wafers into correct defect categories. In addition, we also evaluated the effects of freezing and unfreezing the DL model’s parameters during the training process. The training parameters used to conduct the experiments

are listed in Table 2. We refine the training process by unfreezing the trained network layers using the step learning strategy. Initially, the learning rate equals 0.001 and decreases by a factor of 0.5 every five epochs. During the training process, the regularized DropBlock method was used to reduce parameter calculations in the fully connected layer. This allows to avoid network over-fitting and boosts the accuracy of the process of classifying silicon defects. The silicon wafer defect features obtained during the training phase with the use of MobileNetV2 were fed into a new Softmax layer to obtain the output probability for each silicon wafer image and its respective defect class. The model built was then used to classify the images from the testing set.

## 4. Analysis and Discussion of Results

We evaluated the effectiveness of the DTL model using the standard evaluation measures, namely accuracy and loss. Accuracy is the percentage of correct predictions made by the model. It is calculated by dividing the sum of correct predictions (true positive + true negative) by the total number of predictions (true positive + true negative + false positive + false negative). The model loss reflects the error rate between two probability distributions of the true defect class and the predicted defect class. It is measured using cross-entropy, where a higher value indicates that the predicted defect class diverges from the true defect class.

### 4.1. DTL Training Accuracy

Due to the stochastic nature of DL, the models can be built several times using the same set of training data to assess the accuracy and the compare each model against its counterparts. No standard number of models that need to be built has been defined. Most research relied on one model only, due to time- and resource-related limitations encountered while building the models [12]. In our experiment, we chose to build three models and to evaluate their mean and standard deviation [13]. The accuracy of the DTL-MobileNetV2 model (trained using the training set and validated using the validation set) for three iterations is shown in Table 3.

Table 3  
Model accuracy results for three iterations  
of building the DTL wafer model

Build iteration	Accuracy [%]
1	96.70
2	96.05
3	97.20
Mean	96.65
Std dev	0.47

The mean accuracy and standard deviation accuracy of the DTL MobileNetV2 model are 96.59% and 0.49%, respectively. The best accuracy of DTL MobileNetV2 equals 97.02%, while its lowest accuracy amounts to 96.05%. As the MobileNetV2 model was designed to shorten the calculation time and reduce model size, we found that it took 182.46 s to train one epoch and that the generated model size was 12.5 MB. The accuracy obtained is considerably high. This indicates that the DTL MobileNetV2 model offers good potential and ensures favorable classification performance, thus helping in the classification of wafer defects.

### 4.2. Batch Size (32 vs. 64)

The impact of different batch sizes on the accuracy of the model was investigated as well. Masters and Luschi [14]

reported that best performance in their experiments was achieved with batch sizes of 16, 32 and 64 for an ImageNet dataset. In this paper, models of batch sizes 32 and 64 were trained and results obtained before and after their fine tuning were combined to conduct a more comprehensive comparison analysis. The batch size of 16 was excluded from the experiment as it is computationally and time intensive. We added two additional layers on top of the existing MobileNetV2 that will classify wafer defects into the six respective classes.

In order to compare the effectiveness of using DTL without fine tuning the model (all network layers frozen), we conducted the training phase for 100 epochs. We further executed another 100 epochs by unfreezing the network layers to optimize the model for monocrystalline silicon wafer defects. This process updates the weights of ImageNet feature maps to features specifically associated with the dataset. The detailed results from before and after fine tuning for the batch sizes of 32 and 64 are shown in Table 4. From the experiment using batch size 32, the built model's training accuracy equals 91.32%, and validation accuracy amount to 91.78% before fine tuning. When the model was fine tuned, the training accuracy improved to 97.68%, and validation accuracy was 97.2%. Figure 3 shows the accuracy and loss versus the epoch during training for the two different batch sizes.

Using the batch size of 64, the built model achieved a training accuracy of 91.52% and a validation accuracy of 91.80% before being fine tuned. After the model was fine tuned, the result improved to 98.05% in terms of training accuracy and 97.67% in terms of validation accuracy.

The results of the experiments have shown that the larger the batch, the faster the deep learning algorithm converges, and the shorter the time required to achieve better training accuracy. On top of that, from the visual and table results, it is safe to say that with the increase of the batch size, the accuracy of the model prediction will be improved to a certain extent, and the mean accuracy and mean loss are better than outcomes specified in the literature.

Upon performing the optimization, the DTL model learned more features and classified the wafer defects better. This can be clearly seen on the right side of the graph in Fig. 3. The improvement stemmed from the fact that the optimized model was allowed to learn new features, update its weights and biases from the data that was different from the ImageNet data. Although there are two declining spikes, the accuracy was still better than the frozen results. The two declining spikes may be caused by the sample data in that validation batch which is harder to classify by the DTL model. Overall, the findings prove that unfreezing the network layers during the model training phase produces a better result than when the layers are frozen. We speculate that the same model parameters could be adopted when using other DL algorithms, such as DenseNet201.

Table 4  
Accuracy and loss of the DTL MobileNetV2 model training and validation for batch sizes of 32 and 64

Models	Batch size	Mean of training accuracy [%]	Mean of training loss [%]	Mean of validation accuracy [%]	Mean of validation loss [%]
Freeze	32	91.32	4.50	91.78	4.35
	64	<b>91.52</b>	<b>4.17</b>	<b>91.80</b>	<b>4.08</b>
Unfreeze	32	97.68	1.34	97.20	1.95
	64	<b>98.05</b>	<b>0.81</b>	<b>97.67</b>	<b>0.94</b>

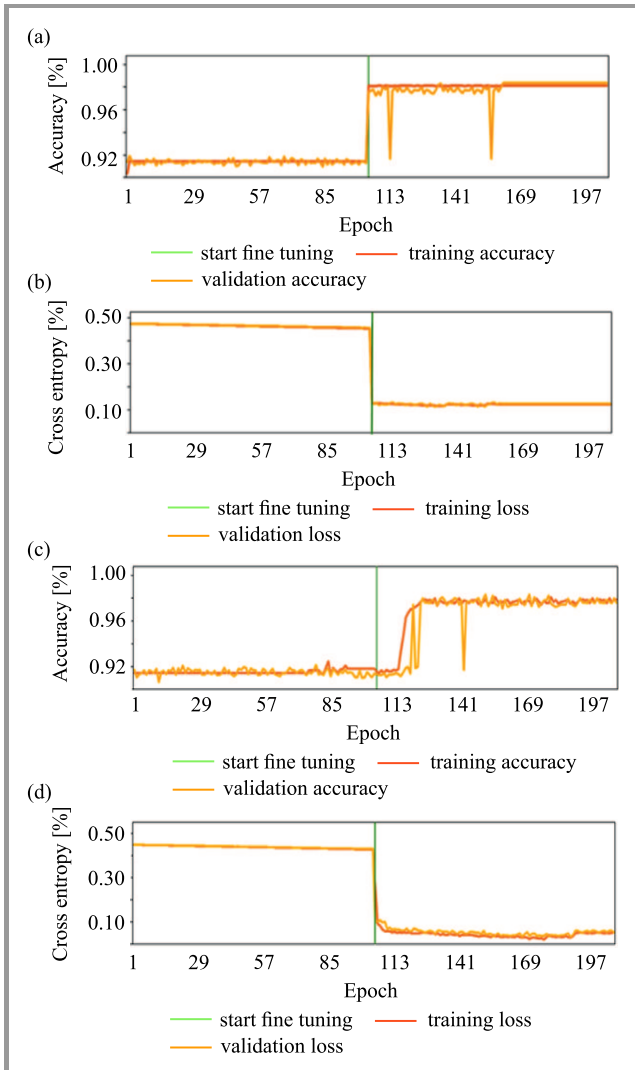


Fig. 3. Training and validation accuracy of batch sizes 32 (a)–(b) and 64 (c)–(d) versus epoch during model training.

4.3. Classification Accuracy

To evaluate the DTL MobileNetV2 model built for classifying silicon wafer defects, a classification prediction was performed with new sample images of wafer defects from the testing set. The model evaluation accuracy against the testing set is at 98.99%. As we do not compare different DTL architectures in this work, we have not performed a significant test for the results. The visualization of the

defect classification confusion matrix into six types is shown Fig. 4a which depicts the number of correct and incorrect classifications, and the corresponding percentage is presented in Fig. 4b. Examples of images and their corresponding classifications performed using the DTL model are illustrated in Fig. 5. Based on the confusion matrix, the model successfully classified the double contrast de-

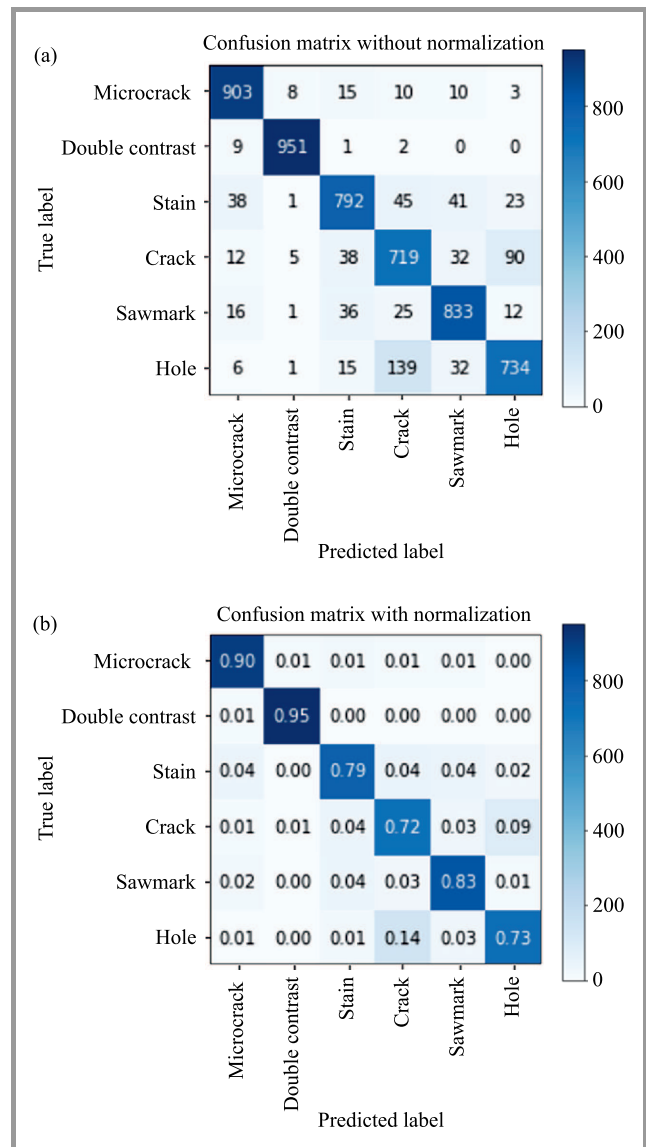


Fig. 4. Confusion matrix using (a) the exact number of predicted images and (b) accuracy percentage.



Fig. 5. Sample of defect classification prediction results of 25 images from the testing set.

fect (with the accuracy rate of 95%). More training and customization of the DL is needed to recognize the crack defect, as the classification accuracy for this class was the lowest.

### 5. Conclusion

In this work, we present a solution allowing to classify monocrystalline silicon wafer defects using deep transfer learning. The experiments were carried out using a real-world dataset from a production plant. We found that DTL MobileNetV2 was capable of accurately identifying certain defects with limited training sample size. It was also determined that batch size influenced the results as well, both in terms of accuracy and loss percentage. We also showed that a batch size of 64 offered higher accuracy (before and after fine tuning) than a smaller batch size of 32.

Despite the success in training the model and classifying wafer defects, several limitations have been encountered.

Firstly, the dataset could be improved by adding perfect wafers that had passed AOI defect inspection. Secondly, the methodology relied upon in this work was not designed for real-time classification. Prospects for future work include collection of perfect and defective wafer samples from diversified production facilities to expand the dataset, further customization of the DTL MobileNetV2 solution using other new deep learning models, and integration with a real time mobile terminal.

### Acknowledgements

This research would not have been possible without the exceptional support from Universiti Malaysia Sarawak and LONGi (Kch) Sdn. Bhd.

### References

[1] A. Ganum, "Improve wafer defects detection using deep learning approach", Master thesis, Universiti Malaysia Sarawak (UNIMAS), 2021.

- [2] A. G. Howard *et al.*, “MobileNets: efficient convolutional neural networks for mobile vision applications”, *Computing Research Repository*, arXiv:1704.04861, 2017 [Online]. Available: <https://arxiv.org/pdf/1704.04861.pdf>
- [3] M. Sandler, A. Howard, M. Zhu, A. Zhmoginov, and L.-C. Chen, “MobileNetV2: Inverted Residuals and Linear Bottlenecks”, in *Proc. of the IEEE Conf. on Computer Vision and Pattern Recognition (CVPR)*, Salt Lake City, UT, USA, 2018, pp. 4510–4520 (DOI: 10.1109/CVPR.2018.00474).
- [4] J. A. Mat Jizat, A. P. P. Abdul Majeed, A. F. Ab. Nasir, Z. Taha, and E. Yuen, “Evaluation of the machine learning classifier in wafer defects classification”, *JCT Express* (in Press), 2021 (DOI: 10.1016/j.icte.2021.04.007).
- [5] C. Tan *et al.*, “A Survey on Deep Transfer Learning”, in *Artificial Neural Networks and Machine Learning – ICANN*, Rhodes, Greece, 2018, pp. 270–279 (DOI: 10.1007/978-3-030-01424-7\_27).
- [6] P. Gavali and J. S. Banu, “Deep convolutional neural network for image classification on CUDA platform”, in *Deep Learning and Parallel Computing Environment for Bioengineering Systems*, A. K. Sangaiah, Ed. USA: Academic Press, 2019, pp. 99–122 (DOI: 10.1016/B978-0-12-816718-2.00013-0).
- [7] K. Imoto, T. Nakai, T. Ike, K. Haruki, and Y. Sato, “A CNN-based transfer learning method for defect classification in semiconductor manufacturing”, *IEEE Trans. on Semiconductor Manufacturing*, vol. 32, no. 4, pp. 455–459, 2019 (DOI: 10.1109/TSM.2019.2941752).
- [8] H. Kudo, T. Matsumoto, K. Kutsukake, and N. Usami, “Occurrence prediction of dislocation regions in photoluminescence image of multicrystalline silicon wafers using transfer learning of convolutional neural network”, *IEICE Trans. on Fundamentals of Electronics, Commun. and Computer Sci.*, vol. E104A, no. 6, pp. 857–865, 2020 (DOI: 10.1587/transfun.2020IMP0010).
- [9] J.-H. Lee and J.-H. Lee, “A reliable defect detection method for patterned wafer image using convolutional neural networks with the transfer learning”, in *4th Int. Conf. on Adv. Materials Res. and Manufacturing Technol. (AMRMT)*, Oxford, United Kingdom, vol. 647, 2019 (DOI: 10.1088/1757-899X/647/1/012010).
- [10] Keras Applications, [Online]. Available: <https://keras.io/api/applications/> (accessed on 30.08.2021).
- [11] O. Russakovsky *et al.*, “ImageNet large scale visual recognition challenge”, *Int. J. Comput. Vis.*, vol. 115, no. 3, pp. 211–252, 2015 (DOI: 10.1007/s11263-015-0816-y).
- [12] C. Chen *et al.*, “Deep learning on computational-resource-limited platforms: A survey”, *Mobile Information Systems*, vol. 2020, Article ID 8454327, 19 pages, 2020 (DOI: 10.1155/2020/8454327).
- [13] J. Brownlee, “Estimate the number of experiment repeats for stochastic machine learning algorithms”, 2020 [Online]. Available: <https://machinelearningmastery.com/estimate-number-experiment-repeats-stochastic-machine-learning-algorithms/>
- [14] D. Masters and C. Lusch, “Revisiting small batch training for deep neural networks”, arXiv:1804.07612, 2018.



**Adriana Ganum** is an executive engineer at LONGi Kuching Sdn Bhd. She received her Bachelor’s degree (Hons) in Information Technology from UKM. She has recently received her Master’s degree in Advanced Information Technology from UNIMAS, with her final year project focus-

ing deep learning studies and experiments.

E-mail: [adrianaganum0307@gmail.com](mailto:adrianaganum0307@gmail.com)  
 LONGi (Kch) Sdn Bhd, 1072  
 Persiaran Elektronik 2  
 93350 Kuching  
 Sarawak, Malaysia



**Dayang NurFatimah Awang Iskandar** is an Associate Professor at the Faculty of Computer Science and Information Technology (FCSIT), UNIMAS, Sarawak. She obtained her Bachelor degree (Hons) in Information Technology (majoring in Computational Science) from UNIMAS. She holds a Master’s degree in Multimedia

Computing from Monash University, Australia and a Ph.D. degree in Computer Science from Royal Melbourne Institute of Technology (RMIT), Australia. She pursued her postdoctoral studies with the Biomedical Informatics Systems Engineering Laboratory (BISEL), Heriot-Watt University, UK, working under the EU funded project – Combining and Uniting Business Intelligence with Semantic Technologies (CUBIST). Recently, she was attached as a researcher at Jodrell Bank Centre for Astrophysics, Department of Physics and Astronomy, the University of Manchester, UK. Dayang has expertise in spatio-temporal image analysis, semantic representation and retrieval. Her research focuses on minimizing the gap between image features and high-level semantics in the domain of medicine, agriculture and astronomy.

 <https://orcid.org/0000-0002-0909-5670>

E-mail: [dnfaiz@unimas.my](mailto:dnfaiz@unimas.my)

Faculty of Computer Science and Information Technology  
 Universiti Malaysia Sarawak (UNIMAS)  
 94300 Kota Samarahan  
 Sarawak, Malaysia



**Lim Phei Chin** received her Ph.D. in Text and Data Mining and M.Sc. in Information Technology from Universiti Malaysia Sarawak, Malaysia in 2016 and 2008, respectively. She is currently a lecturer at Universiti Malaysia Sarawak. Her research interests include image processing, statistical analysis, and machine learning.

 <https://orcid.org/0000-0002-9987-0481>

E-mail: [pclim@unimas.my](mailto:pclim@unimas.my)

Faculty of Computer Science and Information Technology  
 Universiti Malaysia Sarawak (UNIMAS)  
 94300 Kota Samarahan  
 Sarawak, Malaysia



**Ahmad Hadinata Fauzi** is presently working as a senior lecturer at the Faculty of Computer Science and Information Technology, Universiti Malaysia Sarawak (UNIMAS). He received his Master's degree in Network Computing from Monash University, Australia. His area of interests includes

the Internet of Things (IoT), network security and network administration.

 <https://orcid.org/0000-0003-0702-0074>

E-mail: [hadinata@unimas.my](mailto:hadinata@unimas.my)

Faculty of Computer Science  
and Information Technology  
Universiti Malaysia Sarawak (UNIMAS)  
94300 Kota Samarahan  
Sarawak, Malaysia

# Preliminary Evaluation of Convolutional Neural Network Acoustic Model for Iban Language Using NVIDIA NeMo

Steve Olsen Michael, Sarah Samson Juan, and Edwin Mit

*Universiti Malaysia Sarawak, Kota Samarahan, Sarawak, Malaysia*

<https://doi.org/10.26636/jtit.2022.156121>

**Abstract**—For the past few years, artificial neural networks (ANNs) have been one of the most common solutions relied upon while developing automated speech recognition (ASR) acoustic models. There are several variants of ANNs, such as deep neural networks (DNNs), recurrent neural networks (RNNs), and convolutional neural networks (CNNs). A CNN model is widely used as a method for improving image processing performance. In recent years, CNNs have also been utilized in ASR techniques, and this paper investigates the preliminary result of an end-to-end CNN-based ASR using NVIDIA NeMo on the Iban corpus, an under-resourced language. Studies have shown that CNNs have also managed to produce excellent word error (WER) rates for the acoustic model on ASR for speech data. Conversely, results and studies concerned with under-resourced languages remain unsatisfactory. Hence, by using NVIDIA NeMo, a new ASR engine developed by NVIDIA, the viability and the potential of this alternative approach are evaluated in this paper. Two experiments were conducted: the number of resources used in the works of our ASR's training was manipulated, as was the internal parameter of the engine used, namely the epochs. The results of those experiments are then analyzed and compared with the results shown in existing papers.

**Keywords**—*acoustic modeling, automated speech recognition, convolutional neural network, CNN, under-resourced language, NVIDIA NeMo.*

## 1. Introduction

Acoustic models are one of the most important components of automated speech recognition (ASR) systems. Acoustic model functions represent the relationship between an audio signal and the phonemes or other linguistic units that make up speech in an ASR. A good acoustic model will help an ASR recognize speech inputs accurately and will produce excellent training data. Current state-of-the-art (SOTA) acoustic models rely primarily on end-to-end artificial neural model's algorithm [1] which helps simplify the conventional module-based ASR system into a single deep learning framework.

In the case of low-resourced languages, the ability to transcribe the language accurately is much more critical, since low-resourced languages have limited amounts of speech data available. As mentioned by Chuangsuwanich *et al.* [2], a speech recognizer typically requires the following: thousands of hours of transcribed speech for the statistical learning of the acoustic model, a phonetic pronunciation dictionary that determines how words of the language are decomposed into smaller phone-like units, and a large collection of texts to create the language model. For limited-resourced languages, these items are expensive and time-consuming to obtain [3]. Hence, an acoustic model is required to be able to perform excellently, although with limited resources only in the case of low-resourced languages.

The first objective of this paper is to investigate how an end-to-end CNN-based ASR model performs on the Iban corpus, an under-resourced language. Experiments have been conducted using different amounts of resources on a CNN model to identify whether this architecture has the means to overcome the problem of the lack of training data of an under-resourced language. The second objective is to perform sensitivity analysis concerning the selected architecture parameters, in order to investigate their impact on the word error rate (WER) produced. A further experiment is conducted after the most optimal amount of resources to be used for model training has been identified, with one of the parameters used in the training phase being manipulated.

## 2. Literature Review

### 2.1. Neural Network and Under-resourced Languages

Over the past few years, artificial neural networks (ANNs) have been among the most well-known options for developing an ASR's acoustic model [4]. There are several variants of ANNs in existence, including deep neural network (DNNs), recurrent neural networks (RNNs), and convolutional neural networks (CNNs). Currently, many re-

searchers are looking into the capabilities of CNN when working on ASR technologies, because this approach has shown some promising results in terms of performance, with a WER of 0.0295 using a beam search decoder with an external neural language model [5] and of 0.019/0.041 using ContextNet, a fully convolutional encoder that incorporates global context information into convolution layers by adding squeeze-and-excitation modules, with language model [6]. Several research projects have already been conducted to investigate how to further enhance the performance of an ASR using a neural network by experimenting with the acoustic model for under-resourced languages.

Implementation of a multilingual neural network ASR architecture for an under-resourced language is a popular method for achieving better accuracy. Biswas *et al.* has implemented this to improve the performance of their ASR for the native language of South Africa, isiZulu, which has an issue of “code switching”, i.e. a method of combining their native language with different languages in their everyday conversations [7]. Researches implemented three types of acoustic models, with two of them implemented as multilingual methods, in order to alternatively solve this matter. They were able to enhance the performance of their ASR reaching an overall WER of  $\geq 0.55$  from the initial baseline of 0.63, which is an increase of roughly 0.08 in terms of reduced error rate, for each experiment they conducted. Their acoustic model was a variant of the Gaussian hidden Markov model (GMM/HMM), multilingual DNNs and multilingual time delay-long short-term memory neural networks (TDNN-LSTMs). This effort was a good improvement for their ASR in terms of WER performance, although their results are still scaled as a “high-error rate” ASR performance. They concluded that a higher amount of monolingual data for training is necessary to achieve very good WER performance for their under-resourced language.

Furthermore, He *et al.* also conducted a research experiment on improving the WER of an ASR for an under-resourced language, Iban, by adopting the multi-task learning (MLT) and acoustic landmark method for the purpose of ASR training [8]. The authors used an ASR trained with the TIMIT corpus using the MLT method and then further trained it for detection and classification landmarks. The same ASR was then cross-lingually adapted to the Iban corpus as a secondary task. From their experiment, they were able to increase the performance of an ASR trained with very few resources, “Iban 10%”, meaning that ASR was trained with as little as 40 min of Iban data, to a reduced WER of 0.087 on a mono-phone and 0.0617 on a tri-phone ASR. Conversely, although a cross-language landmark detector provides useful information complementary to orthographic transcription, visual inspection indicates that a cross-language landmark detector is not as accurate as a same-language landmark detector. They later suggested training a more accurate landmark detector using RNN methods that could be applied to multilingual trained corpora as a means to overcome the aforementioned belief as their future work.

## 2.2. CNN as the Chosen Architecture

Although producing an ASR for low-resourced language has proven to be quite a challenge, past research has shown that an ASR with a single deep learning framework acoustic model, such as CNN, was able to produce promising results using only raw unprocessed speech data in estimating phonemes [9] and ASR with an excellent WER (in comparison with other ANNs), such as the DNN model architecture [10].

Palaz in [9] has proven that CNN was able to outperform or produce a similar result when compared with an ANN-based system that takes standard cepstral features as inputs. He was able to prove that contrary to his previous findings, in which poor ASR performance was attained using raw speech signal as input to DNN, his study on large vocabulary speech recognition (LVCSR) indicates that CNNs have an edge over DNNs in modeling raw speech signals. From his study, he was able to get a WER of 6.7 using a neural model of three CNN layers with one max pooling layer plus a hidden layer and HMM as decoder, but taking only a raw speech signal as its input, in comparison with HMM-ANN with one hidden layer and using mel-frequency cepstrum (MFCC) to preprocess its input with a WER of 7.0. Both were tested and trained on the Wall Street Journal corpus. As the number of layers increases to three hidden layers for each model, Palaza’s CNN model achieving a WER of 5.6 outperforms the ANN model even further, as the latter achieved a value of 6.4. It is known that under-resourced languages lack the resources needed for training. Furthermore, even without the need of data pre-processing, having only raw speech data as a requirement for an ANN to train its model, would serve as a potential step in perhaps not eliminating, but reducing the difficulties faced while producing well-performing ASR for under-resourced languages. This may be achieved by allowing only raw speech data as a necessity to train an ASR, eliminating the need for an abundant resource for preprocessing and accurate transcribing.

Moreover, much research has been conducted recently showing that CNN outperforms several other architectures, including the famous speech recognition neural network architecture, RNN, in building ASR for low-resourced languages. In papers [11]–[14], Reyes *et al.*, Thai *et al.*, Mon, and Lekshmi and Sherly stated that CNN offers a truly exceptional feature extraction capability. These authors were conducting experiments on their respective under-resourced languages using the CNN architecture. Since CNN is a SOTA architecture for image and graphic classification, it is not surprising that this NN would be able to perform better in terms of feature extraction. Taking raw speech signal as a spectrogram, CNN was able to distinguish even the smallest differences in features, leading to an accurate prediction of spoken words. Mon in [13] also mentioned that optimization of the hyperparameter in CNN architecture was capable of producing better performance than other ANNs, as well as greatly impacted the perfor-

mance of ASR through the setting of the number of feature maps and pooling the sizes of the CNN. Conversely, Thai *et al.* stated that both deep RNN and GMM/HMM models were outperformed by their fully convolutional acoustic model which yields significant accuracy improvements [12]. The same authors further mentioned that CNN mitigates the issue of incompatibility in parallelization on modern hardware, as cited by Collobert *et al.*, and is advantageous as it requires only a few parameters to collect sufficient important features for an accurate prediction that leads to the reduction of computational cost [15]. Furthermore, Lekshmi *et al.* implored that CNN is a better deep learning model because of its capability to reduce spectral variations [14] and to model spectral correlations between signals, as reported in Rabiner and Juang [16]. All the results and benefits mentioned above further support the choice of CNN.

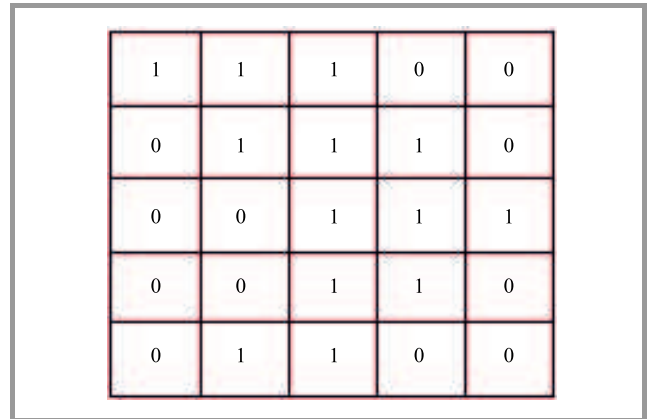
Finally, another reason why CNN was chosen is due to the Iban language being relatively unexplored as a CNN-ASR model. There are not many works on CNN for Iban. One of the most recognizable ones was that by Juan who experimented on the Iban language using the DNN architecture and GMM/HMM [17]. Hence, this also serves as a motivation for CNN to be studied to address this research gap. Focusing on the manipulation of data amount and the parameters that exist in the CNN architecture, this study aims to look into the architecture's performance on the basis of the two factors that were highlighted earlier when dealing with the same under-resourced situation in the case of the Iban language.

The rest of this paper is organized as follows. Section 3 discusses the architecture of CNN. Section 4 presents the methodology used for the experiment. Section 5 describes the protocol used in the setup, as well as the results that were obtained. Sections 6 and 7 discuss the findings and constraints of this experiment, while Section 8 concludes the research.

### 3. CNN Model Architecture

Rather than using fully linked hidden layers, as its comparable variant, i.e. DNN does, CNN uses a unique network structure that comprises alternating convolution and pooling layers. The idea behind the CNN architecture was adopted from the pattern of connections between neurons in the human brain and from the arrangement of the visual cortex [18]. In the case of a CNN, the main purpose of convolution is to extract features from visual inputs. Such an approach is highly useful in image processing and identification. Through the learning of image features using small squares of input data, convolution is capable of preserving the spatial relationship between pixels, as an image is basically a matrix of pixel values [19]. Essentially, a matrix of pixel values can be used to represent every image as well as waveforms. Typically, CNN comprises four major operations: (1) convolution, (2) non-linearity – rectified linear unit (ReLU), (3) pooling step, and (4) classification (fully connected layer).

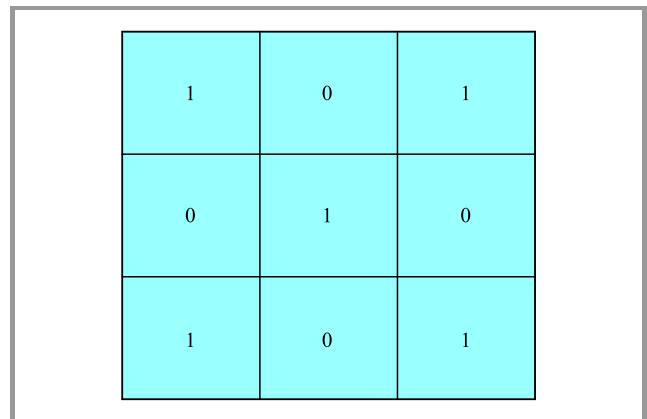
For the first operation (convolution), let us begin by considering a 5-image matrix with pixel values assuming, in a special case, values of 0 and 1 only, as shown in Fig. 1.



1	1	1	0	0
0	1	1	1	0
0	0	1	1	1
0	0	1	1	0
0	1	1	0	0

Fig. 1. Original  $5 \times 5$  matrix.

We shall also consider another 3 matrix as shown in Fig. 2. This small matrix is known as a “kernel”, “filter” or “feature detector”.



1	0	1
0	1	0
1	0	1

Fig. 2.  $3 \times 3$  Kernel matrix.

As shown in Figs. 3–5, imagine that our  $3 \times 3$  matrix (blue selected cells) slides over the  $5 \times 5$  image matrix, moving by one pixel at a time. This process is known as a “stride”. As the slide takes place, element-wise multiplication is computed between the two matrices and its multiplication outputs are added to obtain the final integer, which forms a single element of the output matrix (green cells).

The output matrix (green highlights) was formed by sliding the  $3 \times 3$  kernel matrix over the original  $5 \times 5$  matrix. The computation of the dot product is a process called “convolved feature” or “activation map” or the “feature map”. Note that the kernels detect features from the original input image ( $5 \times 5$  matrix). On the same input matrix (image), different feature maps are produced by various values of the kernel matrix. During implementation, the values of these kernels are learned by the CNN throughout the training process. However, parameters such as the number of

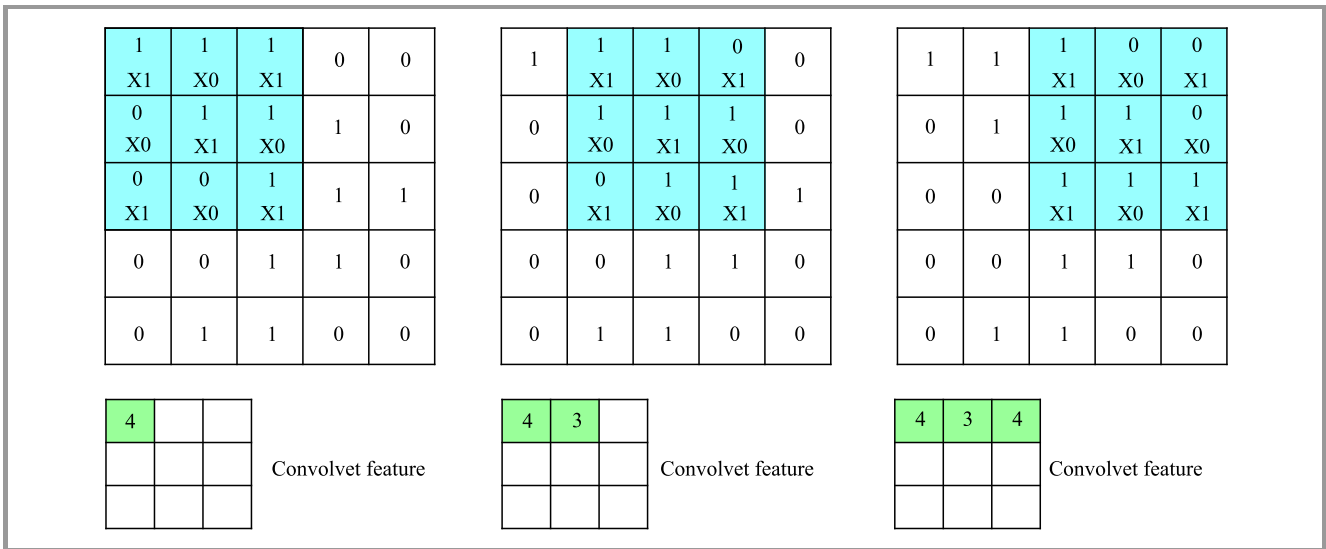


Fig. 3. First to third strides of the kernel matrix.

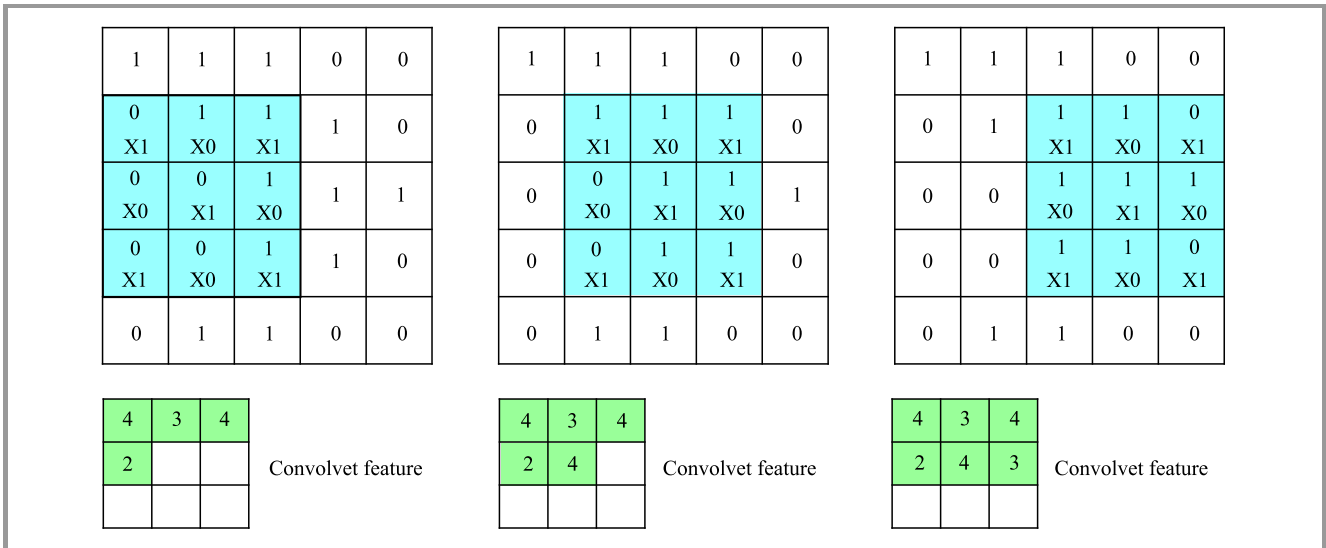


Fig. 4. Fourth to sixth strides of the kernel matrix.

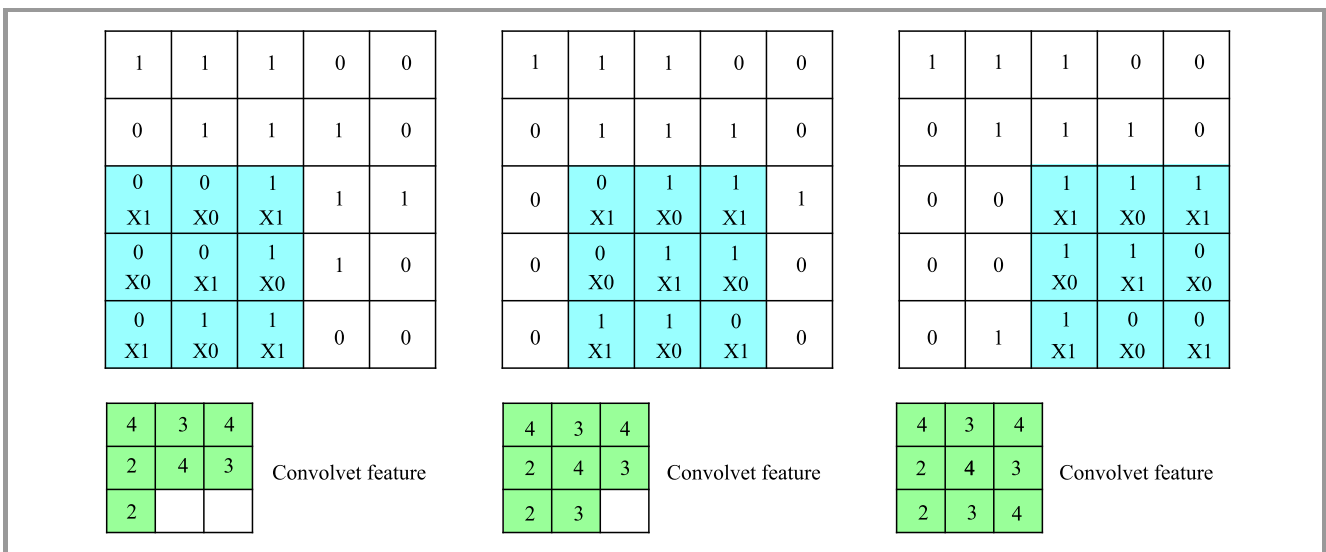


Fig. 5. Seventh to ninth strides of the kernel matrix.

kernels, kernel size, and architecture of the network still need to be specified before the training process. Moreover, before the convolution step is performed, three parameters have to be specified, as they control the size of the convolved feature. These include: depth, which represents the number of kernels used in convolution; stride, representing the number of pixels that were slid over the input matrix by our kernel matrix; and zero-padding, which involves zeros that pad around the border of the input matrix, allowing the application of the kernels to the bordering elements of the input matrix. A higher number of kernels corresponds to extraction of a higher number of image features and to the network's better recognition of patterns in unseen images. Next, while proceeding with the second operation (non-linearity – ReLU of CNN), non-linearity should be applied to CNN, since convolution is a linear operation but most real-world data are non-linear. The purpose of the activation function is to transform the summed weighted input from the node into the activation of the node or output for that input of a neural network [20]. For CNN, ReLU is the most commonly used activation function, as it has been found to perform better in most situations when compared with the other non-linear functions such as tanh or sigmoid. Also, ReLU has become a common activation function for several types of neural networks, as it offers ease of the training process and often ensures better performance. It is a piece-wise linear function that outputs the input directly if it is positive, and the 0, if it is negative [20]. From the previous example, when an image was formed from the output feature map, it would be a mixture of black and white shades since it is a result of black = negative values and white = positive values. By applying ReLU to CNN, we would be removing all negative values from the feature map and would only be taking the non-negative values. This allows the CNN to identify the image of a feature map, as there are only non-negative values to indicate the differences of layers in the feature map. A feature map to which ReLU has been applied is also called a "rectified" feature map.

The third operation, namely the pooling step (spatial pooling), also known as sub-sampling, is to reduce each feature map's dimensionality while simultaneously retaining important key information. Usually, the pooling layer comes after finishing the convolutional layer. It serves as a layer for reducing the input volume's spatial dimensions (width  $\times$  height) for the next convolutional layer, although the depth dimension of the volume is not affected. This operation is also known as subsampling because the loss of information occurs as well, alongside the reduction of dimensions. This loss however is more beneficial to CNN, mainly because of the following:

- the next layers in the network will suffer from lower computational overheads,
- overfitting will be prevented.

Similarly to convolution, the pooling layer takes a sliding window in which serves as a another newly defined ma-

trix window that is to be striding along with the rectified feature map. In this operation, the window will be transforming the values from the feature map by taking either the maximum value or the average value, as observed under the window known as "max pooling". Because of its better performance characteristics, max pooling has been preferred in most situations. Figure 6 depicts the operation of max pooling on a rectified feature map using a  $2 \times 2$  window.

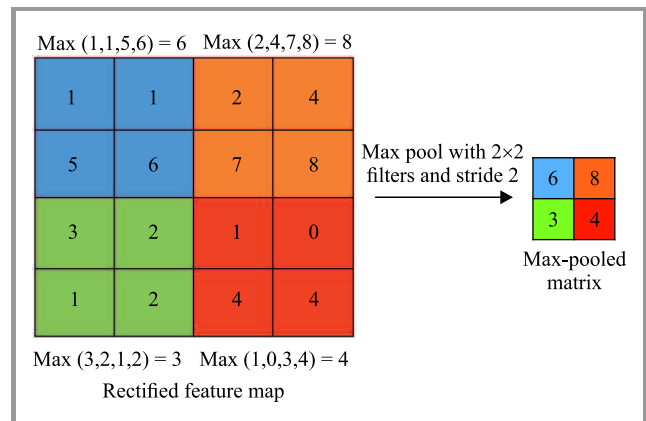


Fig. 6. Max pooling of a rectified feature map.

Max pooling can be deduced as an operation of applying a function over the input values. No new parameters were introduced during this phase and it uses fixed-sized portions at a time, with a size configurable as a parameter. Note that although CNN may undergo max pooling, pooling operations are excluded in most CNN architectures. Thus far, the operations have reduced the size of the original matrix making it even smaller than it was before, since it was divided into smaller-sized feature maps. As the first operation progresses further to the second convolution, the second pooling step, and then onward to the third convolution and also the third pooling step and so on, the size of the matrix will be reduced further and more feature maps will be produced, until the network can finally conclude one or more possible outputs for the original image.

Finally, as mentioned earlier in this section, the fourth operation (classification or a fully connected layer) is just as what its name implies – the CNN layers are all fully interconnected with each other. In other words, each neuron in the preceding layer is connected to each neuron in the next. Outputs from the second and third operations represent high-level features of the original image. The fully connected layer uses these features for classifying the input image into various classes on the basis of the training dataset [19]. Furthermore, implementation of fully connected layers enhances the learning of non-linear combinations of those features. A combination of the features gained through the convolution and pooling step would be very helpful in classifying the image. Through the use of the Softmax function, the sum of the output probabilities is ensured to be equal to 1. Softmax, as an activation function in the output layer of a fully connected layered

network, takes a vector of arbitrary real-valued scores and compresses it to a vector of values between 0 and 1 that sums to 1.

## 4. Methodology

### 4.1. Architecture of CNN Used

The ASR experiment involving an under-resourced language and the CNN architecture is performed using the NVIDIA Neural Module (NeMo) in Google Colab. NeMo is a flexible Python toolkit that allows building SOTA speech and language deep learning models by using reusable building blocks that can be safely connected together for conversational AI applications [21]. NeMo allows the configuration of the architecture to be laid out by specifying the model using a Yet Another Markup Language (YAML) file. This allows us to have flexibility in designing our CNN architecture. The content of the YAML config file has an entry labeled as “encoder” with a field called “jasper”, with parameters that specify the criteria of one block, as such:

```
filters = 128, repeat = 1
kernel = [11]
stride = 2
dilation = 1
dropout = 0.2
residual = false
separable = true
```

```
se = true
se_context_size = -1.
```

Our configuration follows the Jasper\_4x1 model, which comprises ( $K = 4$ ) blocks of single ( $R = 1$ ) sub-blocks and a greedy connectionist temporal classification (CTC) decoder. A total of seven blocks was used, with the first six of them consisting of pointwise and one-dimensional time channel separable convolutional layers, followed by batch normalization, and then the ReLU layer. Two subsequent invariants of  $K \times R$  blocks have 256 and 1024 filters each, respectively, and both were also repeated once. Moreover, NeMo works closely with libraries from Pytorch Lightning (PTL), in which the training and saving of models and checkpoints had relied heavily upon PTL functions to complete.

The framework is shown in Fig. 7. Typically, the experiment requires us to include raw audio data files together with a manifest file that comprises metadata of our audio files as inputs. NeMo requires a standardized manifest file in which it is shown that each line in the file corresponds to one audio sample, such that the number of lines in the manifest is equal to that of samples that are represented by that manifest. Moreover, NeMo specifies that a line must contain the path to the audio file, the corresponding transcript or path to the transcript file, and the duration of the audio sample.

The CNN model then produces an output of text files that hold the details and the WER of the trained dataset that was calculated using a third-party plugin, the speech recognition scoring toolkit (SCTK).

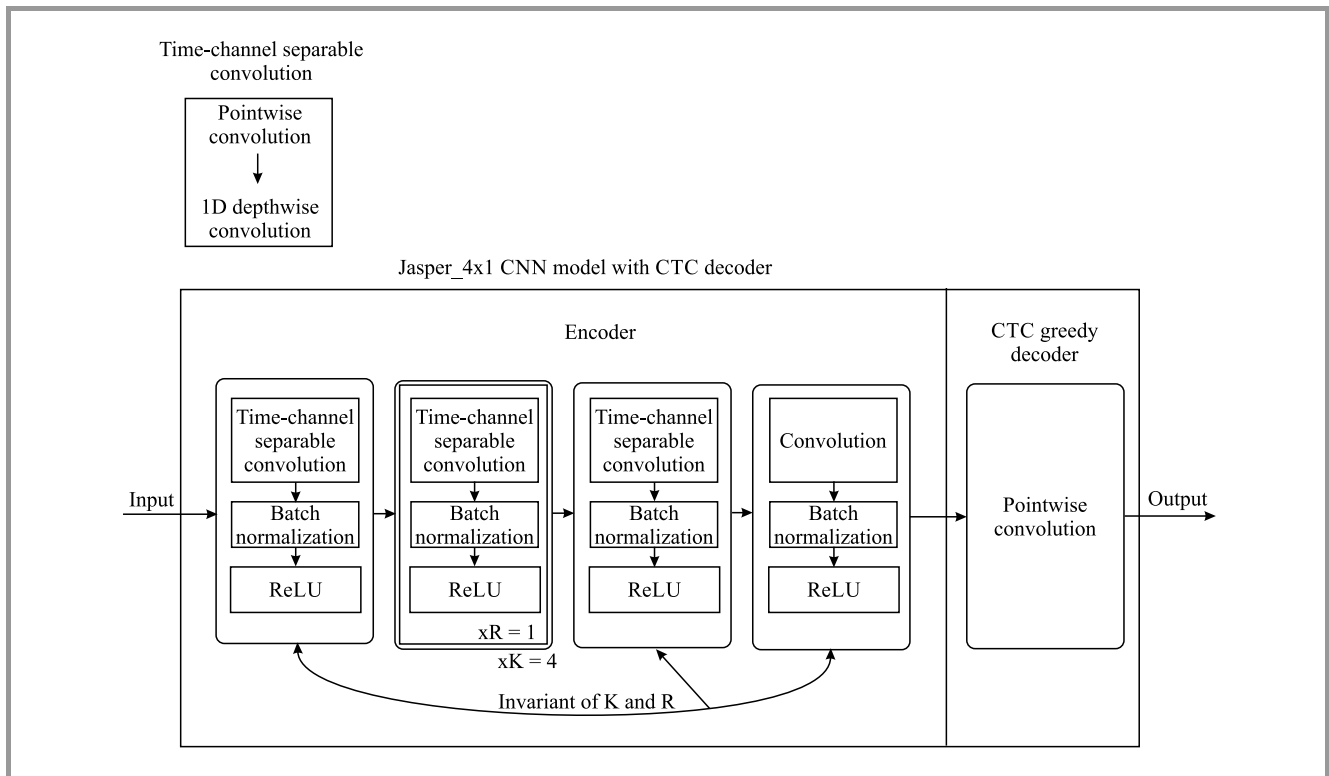


Fig. 7. Framework model of the CNN architecture used.

#### 4.2. Iban as an Under-resourced Language

The under-resourced language that was used is the Iban language, a native language from Sarawak, Malaysia which is still widely used by local people for communication and official procedures. A total of 400 lines of Iban sentences have been used for testing, whereas another 2000 lines of sentences taken from the original corpus dataset are used for training. The resources were previously gathered by Juan *et al.* who used them to investigate the resourcefulness of closely related languages for automatic speech recognition in low-resource languages from Malaysia [22].

The corpus was composed of news gathered after receiving the permission to collect data from a local news station in Malaysia, Radio Televisyen Malaysia Berhad. A total of 3 GB of audio data was received for pre-processing, but only 1.1 GB could be relied upon, as the rest turned out to be of poor quality. The news data were transcribed into text during a data collection workshop organized at the Faculty of Computer Science and Technology, Universiti Malaysia Sarawak, which was aimed to have users with basic skills in using a transcriber application to annotate speech signals [17]. Eight native speakers were hired to produce the transcription data.

The Iban corpus has a total speaker of 6, a male-to-female ratio of 1:2, 473 sentences, 11,000 words, and a total of 71 min of audio data for its test set. For its train set, there were 17 speakers in total, with a male-to-female ratio of 7:10, 2659 sentences, 61,000 of words, and a total of 408 min audio data. In total, 3000 sentences uttered by 23 speakers in 8 h of clean speech were gathered during the workshop [17].

## 5. Experiment Setup and Results

To investigate the authors' first objective, i.e. how an end-to-end CNN-based ASR model performs on the Iban language, using a different number of lines of sentences for

Table 1  
Protocol for the training lines experiment

No. of training lines	Total speakers	Total female speakers	Total male speakers	Total lines spoken by female	Total lines spoken by male
200	10	5	5	100	100
400	10	5	5	200	200
600	10	5	5	300	300
800	11	6	5	400	400
1000	13	7	6	500	500
1200	13	7	6	600	600
1400	15	8	7	700	700
1600	16	9	7	800	800
1800	16	9	7	900	900
2000	17	10	7	1000	1000

testing and training, this experiment evaluates the number of resources needed for a CNN architecture to perform well on an under-resourced language such as Iban, since mostly, resources are lacking. Experiment 1 comprises two rounds. The first round of the experiment was conducted to identify the most optimal number of training lines to be used in order to train our model to get the best WER performance on an under-resourced language. With just 10 testing lines, Table 1 shows the summary of the first round of the experiment.

#### 5.1. Experiment 1

The 10 testing lines used for this experiment were spoken by a total of five speakers, of whom three were female and two were male. Five lines were spoken by both male and female speakers. The number of lines was distributed randomly among the speakers, but the total lines spoken by the two genders were kept equal. Table 2 shows the protocol of the testing line used in the training line experiment. Table 3 shows the WER result achieved by a range of 200-2000 training lines with 10 test lines only.

Table 2  
Protocol for the testing line used in the training lines experiment

No. of testing lines	No. of female speakers	No. of male speakers	No. of lines spoken by female	No. of lines spoken by male
10	3	2	5	5

Table 5 shows the WER result achieved by a range of 100-400 testing lines with 2000 training lines.

We found that the most optimal number of training lines to be used to get the best WER performance would be 2000 lines for training with a WER of 0.832. Subsequently, the second round of Experiment 1 was conducted to obtain baseline results for an increasing number of testing lines. As obtained from the previous round, using 2000 training lines as the most optimal number of training lines to get the best WER, Table 4 shows the protocol of the second round of the experiment. Table 5 shows the resulting WER. Results showed that the best WER performance is 0.868 when tested on 400 lines.

#### 5.2. Experiment 2

To fulfill the second objective of this paper, namely to verify sensitivity of the architecture to selected parameters in order to investigate their effects on WER produced, we further analyze the selected parameter that affects the performance of the CNN-based ASR model. We used the most optimal setup obtained from the previous experiment, with 2000 and 400 training and testing lines. We fine-tune the number of epochs for each setup. This is done to ana-

Table 3  
WER result for the training lines experiment with 10 testing lines only

Training lines	200	400	600	800	1000	1200	1400	1600	1800	2000
Test lines	10	10	10	10	10	10	10	10	10	10
Epochs	100	100	100	100	100	100	100	100	100	100
WER	1.00	1.00	0.94	0.95	0.94	0.94	0.91	0.90	0.89	0.83

Table 4  
Protocol for testing lines experiment

No. of testing lines	No. of female speakers	No. of male speakers	No. of lines spoken by female	No. of lines spoken by male
100	4	2	50	50
200	4	2	100	100
300	4	2	150	150
400	4	2	200	200

Table 5  
WER result for the testing lines experiment with 2000 training lines

Test lines	100	200	300	400
Training lines	2000	2000	2000	2000
WER	0.88	0.87	0.91	0.87

lyze whether CNN models are capable of further improving performance of the ASR model on under-resourced languages by adjusting its parameters. The setup focuses on manipulating the number of epochs from 500 to 5500, and the models will be tested by measuring WER.

The numbers for both testing and training line protocols were maintained the same as in Experiment 1 – 400 testing lines and 2000 training lines.

Table 6 shows the result of WER achieved by the model under the epochs of 500–5500, using 400 and 1000 testing and training lines, respectively. The table shows that the lowest WER achieved is 0.67, which was attained using the ASR model when the epoch was set at 5500.

As for the time taken for the training process to finish, we discover that each increase of the number of epochs by 500 is equivalent to 3–4 h of training. Let us assume that 500 epochs take 3 h to complete the training process. Then, 1000 epochs, i.e. double the original amount, will take 6 h to complete. Therefore, it is estimated that the longest time taken for training was 44 h with the setup for 5500 epochs.

Table 6  
WER results for Experiment 2

Epoch	500	1000	1500	2000	2500	3000	3500	4000	4500	5000	5500
WER	0.85	0.81	0.78	0.75	0.73	0.71	0.70	0.69	0.68	0.68	0.67

## 6. Discussion

### 6.1. Analysis of Results

Table 3 shows that as the number of the training lines increases, the performance of ASR evaluated based on its WER increases as well. This is also true for the increase in the number of testing lines used, as shown in Table 5. This indicates that even an end-to-end CNN architecture is limited by the requirement of the resourcefulness of a given language. The resourcefulness of the language still plays a vital role in training a CNN ASR to perform well on an under-resourced language. The number of lines for testing and training in both setups clearly shows that it is not enough for the ASR to perform excellently, as WER remains above 0.8 in both setups. Nonetheless, the results show that they could be further improved with more training data. This proves that the resourcefulness of the setup with a higher number of lines of sentences used for training the ASR using CNN on an under-resourced language helps achieve better performance in terms of accurate audio transcription. Under-resourced languages have small amounts of data for training, and it seems that even CNN could not overcome this problem. This answers the first objective of this experiment.

Furthermore, the data presented in Table 6 shows that an increase in the number of epochs also increases performance, as WER improves. An epoch is the number of passes of the entire training dataset that the deep learning algorithm has completed. The experiment batches comprise iterations. As such, an epoch is not the number of iterations completed, but the number of batches that have been completed from the entire training session. Table 6 shows that there is a pattern related to the performance of the training process. The early stage of Experiment 2, starting from an epoch setup of 500, shows the minimum performance of an outstanding WER of 0.85, which then started to decrease gradually at a rate of  $-0.2$  to  $-0.4$  WER, until it reached the epoch setup of 2500. At the epoch setup of 3000, performance of the experiment starts to increase very slightly, at a rate of  $-0.01$  WER only, leading us to conclude that the effort to manipulate the number

epochs for a performance upgrade may have reached its limit.

The peak performance of the ASR has been achieved when the epoch count was set at 5500 with a WER of 0.67. At this stage, the results showed that we were going in the direction of overtraining the model, although this claim must be investigated further. This may also be affected by the number of resources used to train the model, as it limits the increase in performance of the proposed ASR model. Hence, for a CNN architecture, a high number of epochs may help, for the betterment of WER, it may not be the most effective variable to optimize the model's performance. The CNN architecture still relies on the amount of resources to be trained in order to produce a very good ASR for under-resourced languages.

### 6.2. Comparison of Results with a Similar Study on Iban ASR

Juan has also researched the Iban language using DNN, one of the most commonly applied ANN algorithms when generating ASRs [17]. Using DNN, the author was able to get a WER performance of 0.184 on a 7 h speech audio data, which is a much better results for an ASR model than the one achieved with a CNN model. This may be caused by integrating a pronunciation dictionary developed during in the course of the research project, and by a language model that was trained on 2 the 2 million-word Iban news data using the SRI language modelling toolkit (SRILM) to their ASR model. Our CNN model was an end-to-end variant, where neither the usage of a pronunciation dictionary nor language model is a necessity, in contrast to the traditional method of ASR development.

The absence of a pronunciation dictionary may have affected the performance of the developed model, as the difference of 0.486 WER exists when one compares the CNN end-to-end model without a pronunciation dictionary with Juan's DNN model with both a pronunciation dictionary and a language model [17]. Her pronunciation dictionary was developed using the Malay grapheme-to-phoneme (G2P) model, which helped them to produce an Iban G2P. The method subsequently enabled them to produce a hybrid G2P as well – a model that incorporates pronunciation rules from Malay and Iban. The G2P was used to produce a pronunciation dictionary for the architecture of their Iban ASR.

The existing pronunciation dictionary may help the model recognize specifically the phonetic structure of Iban language, thus increasing its WER performance, whereas our CNN model depends wholly on the performance of the CNN-based acoustic model ASR and on the learning of phonetics through convolutions of frames.

## 7. Limitations of Experiments

An obvious hindrance that we have been struggling with while conducting this research experiment was the vague-

ness and ambiguity in understanding how the NVIDIA NeMo ASR engine works. Although it is intended to serve as a toolkit for building new SOTA conversational AI models, we believe that this new engine also has a high potential of becoming a “go-to” engine as an ASR development toolkit. Unfortunately, to date, its documentation is limited, and we are unable to fully benefit from this tool. For example, the technique for integrating the language model and pronunciation dictionary, the process of saving and loading checkpoints, and the method for obtaining output transcripts and WER files are still lacking and incomplete. This may be due to the fact that this engine remains rather new, as it was only released in 2019. Thus, it is still undergoing development, fortunately at a rapid rate. Nonetheless, this has placed upon us a blockade that limits us from fully configuring our setup the way we have planned it initially. However, we still encourage the usage of this engine to help its developer gain more feedback for improvement purposes.

## 8. Conclusion and Future Work

This paper has shown how an end-to-end CNN architecture using the NVIDIA NeMo engine and the Google Colab toolkit performs on raw under-resourced language data (Iban), with a WER of 0.67, using only 2000 lines of sentences for training and without the help of a pronunciation dictionary and a language model. The CNN architecture may not be able to eliminate the lack of resources that is faced by under-resourced languages, but with the integration of other tools, such as language models, this architecture may also be able to achieve an excellent WER. This paper presents also the results and a discussion on gradually increasing the performance of the model with different configurations on its number of epochs.

Future work should include the training of the model using a more considerable amount of data, since it will be interesting to see what the minimum amount of data is, needed for the model to train in order to be able to achieve a very good WER performance, under the same setup and weights. Moreover, an increase in the number of filters or blocks in the CNN architecture may yield different, possibly better results. Also, it would be desirable to identify whether the performance of the model upon exceeding 5500 epochs would help the ASR increase its performance, would keep it stagnant or maybe would even lead to the production of a negative output, namely to an increase in WER caused by overtraining. Furthermore, other parameters such as the learning rate, which would help increase the WER of the model when configured to a certain state, must be identified. Finally, the integration of language models and/or pronunciation dictionaries with the model should be investigated to learn whether it could help increase the transcription accuracy of the CNN ASR model on the Iban language.

## Acknowledgement

This work was supported by the Malaysia Comprehensive University Network (Grant number: GL/F08/MCUN/11/2020). We are grateful for the support enabling us to complete the project.

## References

- [1] V. Passricha and R. Aggarwal, "Convolutional neural networks for raw speech recognition", *IntechOpen.*, vol. 32, pp. 137–144, 2013 (DOI:10.5772/intechopen.80026).
- [2] E. Chuangsuwanich, "Multilingual techniques for low resource automatic speech recognition", Ph.D. thesis, Massachusetts Institute of Technology, Department of Electrical Engineering and Computer Science, 2016 [Online]. Available: <http://hdl.handle.net/1721.1/105571>
- [3] B. Pulugundla *et al.*, "BUT system for low resource Indian language ASR", in *Proc. 19th Ann. Conf. of the Int. Speech Commun. Assoc. Interspeech 2018*, Hyderabad, India, 2018, pp. 3182–3186 (ISSN: 1990-9772).
- [4] O. Mamyrbayev *et al.*, "Voice identification using classification algorithms", in *Intelligent System and Computing*, Yang Yi, Ed. IntechOpen, 2020 (DOI: 10.5772/intechopen.88239).
- [5] J. Li *et al.*, "Jasper: An end-to-end convolutional neural acoustic model", in *Proc. of the Ann. Conf. of the Int. Speech Commun. Assoc., Interspeech 2019*, Graz, Austria, 2019, pp. 71–75, 2019 (DOI:10.21437/Interspeech.2019-1819).
- [6] W. Han *et al.*, "ContextNet: Improving convolutional neural networks for automatic speech recognition with global context", in *Proc. of the Ann. Conf. of the Int. Speech Commun. Assoc., Interspeech 2020*, vol. 2020-October, pp. 3610–3614, 2020 (DOI: 10.21437/interspeech.2020-2059) [Online]. Available: <https://arxiv.org/pdf/2005.03191.pdf>
- [7] A. Biswas, F. D. Wet, E. V. D. Weisthuizen, E. Yilmaz, and T. Niessler, "Multilingual neural network acoustic modelling for ASR of under-resourced English-Isizulu code-switched speech", in *Proc. of the Ann. Conf. of the Int. Speech Commun. Assoc., Interspeech 2018*, Hyderabad, India, 2018, pp. 2603–2607 (DOI: 10.21437/Interspeech.2018-1711).
- [8] D. He, B. P. Lim, X. Yang, M. Hagesawa-Johnson, and D. Chen, "Improved ASR for under-resourced languages through multi-task learning with acoustic landmarks", *Proc. of the Ann. Conf. of the Int. Speech Commun. Assoc., Interspeech 2018*, Hyderabad, India, 2018, pp. 2618–2622 (DOI:10.21437/Interspeech.2018-1124).
- [9] D. Palaz, R. Collobert, and M. Magimai-Doss, "Estimating phoneme class conditional probabilities from raw speech signal using convolutional neural networks", in *Proc. of the Ann. Conf. of the Int. Speech Commun. Assoc., Interspeech 2013*, Lyon, France, 2013, pp. 1766–1770 [Online]. Available: <https://arxiv.org/pdf/1304.1018>
- [10] D. Palaz, M. Magimai-Doss, and R. Collobert, "Convolutional neural networks-based continuous speech recognition using raw speech signal", in *Proc. IEEE Int. Con. on Acoust., Speech and Sig. Process. ICASSP 2015*, South Brisbane, QLD, Australia, 2015, pp. 4295–4299 (DOI: 10.1109/ICASSP.2015.7178781).
- [11] F. Reyes, A. Fajardo, and A. Hernandez, "Convolutional neural network for automatic speech recognition of Filipino language", *Int. J. of Adv. Trends in Comp. Sci. and Engin.*, vol. 9, no. 1.1, pp. 34–40, 2020 (DOI:10.30534/ijatcse/2020/0791.12020).
- [12] B. Thai, R. Jimerson, R. Ptucha, and E. Prud'hommeaux, "Fully convolutional ASR for less-resourced endangered languages", in *Proc. of the 1st Joint Worksh. on Spok. Language Technol. for Under-res. Lang. (SLTU) and Collab. and Comput. for Under-Resourced Lang. (CCURL)*, Marseille, France, 2020, pp. 126–130 [Online]. Available: <https://aclanthology.org/2020.sltu-1.17.pdf>
- [13] A. N. Mon, "Myanmar language continuous speech recognition using convolutional neural network (CNN)", Ph.D. thesis, University of Computer Studies, Yangon, 2019, pp. 87–88 [Online]. Available: <https://meral.edu.mm/record/4316/files/AyeNyeinMonThesisBook.pdf>
- [14] K. R. Lekshmi and E. Sherly, "An acoustic model and linguistic analysis for Malayalam disyllabic words: a low resource language", *Int. J. of Speech Technol.*, vol. 24, pp. 483–495, 2021 (DOI: 10.1007/s10772-021-09807-1).
- [15] R. Collobert, C. Puhersch, and G. Synnaeve, "Wav2Letter: an End-to-End ConvNet-based Speech Recognition System", arXiv:1609.03193v2, 2016.
- [16] L. Rabiner and B. H. Juang, *Fundamentals of Speech Recognition*. Upper Saddle River, NJ: Prentice-Hall, 1993 (ISSN: 9780130151575).
- [17] S. S. Juan, "Exploiting resources from closely-related languages for automatic speech recognition in low-resource languages from Malaysia", Ph.D. thesis, Université Grenoble Alpes, France, 2015, pp. 115–118 [Online]. Available: <https://tel.archives-ouvertes.fr/tel-01314120/document>
- [18] S. Saha, "A Comprehensive Guide to Convolutional Neural Networks – the ELI5 way", Towards Data Science, 2018 [Online]. Available: <https://towardsdatascience.com/a-comprehensive-guide-to-convolutional-neural-networks-the-eli5-way-3bd2b1164a53>
- [19] Ujjwal Karn, "An intuitive explanation of convolutional neural networks", the data science blog, 2016 [Online]. Available: <https://ujjwalkarn.me/2016/08/11/intuitive-explanation-convnets>
- [20] J. Brownlee, "A gentle introduction to the rectified linear unit (ReLU)", Machine Learning Mastery, 2010 [Online]. Available: <https://machinelearningmastery.com/rectified-linear-activation-function-for-deep-learning-neural-networks/>, 2020.
- [21] "NVIDIA Deep Learning NeMo Documentation", Nvidia website, 2021 [Online]. Available: <https://docs.nvidia.com/deeplearning/nemo/index.html>
- [22] S. S. Juan, L. Besacier, B. Lecouteux, and M. Dyab, "Using resources from a closely-related language to develop ASR for a very under-resourced language: A case study for Iban", in *Proc. of the Ann. Conf. of the Int. Speech Commun. Assoc., Interspeech 2015*, Dresden, Germany, 2015 (DOI: 10.21437/Interspeech.2015-318).



**Steve Olsen Michael** received his B.Sc. in Computer Science and Information Technology (Software Engineering) from Universiti Malaysia Sarawak, Malaysia in 2019. Since 2021, he has been a M.Sc. student focusing on speech technology, automated speech recognition (ASR) systems, convolutional neural network (CNN) models,

and acoustic modeling, working at the Faculty of Computer Science and Information Technology (FCSIT), UNIMAS. His current research interests are in acoustic modeling techniques using CNN, ASR for under-resourced languages, and speech recognition toolkits.

 <https://orcid.org/0000-0002-2510-5736>

E-mail: [steveolsen.ms@gmail.com](mailto:steveolsen.ms@gmail.com)

Universiti Malaysia Sarawak

94300 Kota Samarahan

Sarawak, Malaysia



**Sarah Samson Juan** presently works at the Faculty of Computer Science and Information Technology at Universiti Malaysia Sarawak. She received her Ph.D. from Grenoble-Alpes University, France, after completing her thesis on automatic speech recognition systems for under-resourced language in Malaysia. Her research

interests focus primarily on natural language processing techniques and machine learning approaches relied upon to develop acoustic models, language models and pronunciation dictionaries.

 <https://orcid.org/0000-0002-9590-1666>

E-mail: [sjsflora@unimas.my](mailto:sjsflora@unimas.my)  
Universiti Malaysia Sarawak  
94300 Kota Samarahan  
Sarawak, Malaysia



**Edwin Mit** is an Associate Professor at the Faculty of Computer Science and Information Technology, Universiti Malaysia Sarawak. He received his Ph.D. in Software Engineering from the University of Salford, UK. His research interests is focus on modeling quality software and the formal approach.

 <https://orcid.org/0000-0002-1670-8586>

E-mail: [edwin@unimas.my](mailto:edwin@unimas.my)  
Universiti Malaysia Sarawak  
94300 Kota Samarahan  
Sarawak, Malaysia

# How to Model an Engaging Online Quiz? The Emotion Modeling Approach

Syazwanie Filzah binti Zulkifli, Cheah Waishiang, Muhammad Asyraf bin Khairuddin, Nurfaeza binti Jali, and Yanti Rosmunie binti Bujang

*Universiti Malaysia Sarawak, Kota Samarahan, Sarawak, Malaysia*

<https://doi.org/10.26636/jtit.2022.156221>

**Abstract**—The article focuses on software technology used to provide a more engaging and exciting learning environment for students by introducing a variety of quizzes. Presently, quiz development can range from simple multiple-choice questions, true or false, drag-and-drop, dropdown menu selections, to 3D interactive techniques. This study introduces a systematic way of creating an engaging application using emotion modeling. Emotion models are being introduced in order to collect and model the systems' meaningful emotional needs. According to the findings, agent-oriented modeling is capable of modeling the emotional requirements of a system and of transforming these into a specific solution enabling to rapidly prototype an engaging system. A quantitative study has been performed on the novel approach to determine the feasibility of the proposed methodology in terms of analyzing, designing, and developing engaging applications.

**Keywords**—*emotion modeling, agent-oriented modeling, learning technology.*

## 1. Introduction

Learning methods such as online quizzes and massive open online courses (MOOCs) are being introduced to create a more engaging learning environments relied upon in teaching students [1]. Engagement a core principle of motivating learners, as it allows them to select a suitable topic [2], [3]. Without engagement, it will be difficult to absorb knowledge and complete courses relying on MOOCs or other similar applications [4]. The primary domains of learner engagement are cognitive, behavioral, and emotional [5]. Seeking additional information concerning the materials, preparing for completing quizzes, and a desire to learn are all indicators of cognitive engagement [6].

The level of contribution demonstrated by students performing classroom activities is referred to as behavioral engagement [5]. Emotional engagement refers to the students' emotional connections with institutions, teachers, peers, and MOOC material [7]. Positive and negative feelings are included in the emotional component.

To date, quizzes have evolved from simple multiple-choice questions [8], true or false, drag-and-drop [9], dropdown menu selections [9], to 3D interactive techniques [10]. Al-

though lots of online quizzes have been introduced back in the days, those of the text-based or multimedia variety failed to engage the students.

How to develop an engaging online quiz? A technique for eliciting user emotional goals has yet to be found [11]. This may be due to the fact that emotion is a subjective and complex notion. Despite of that, in order for the application to be successful, the software developer must address the emotional needs of the users. Emotion modeling is necessary to capture what the users desire to feel, to ensure that all user concerns are addressed, to discover new requirements, to improve the system, and to reduce application failure and rejection rates [11], [12]. As a result, the suggested research was driven by a desire to incorporate emotion thinking into all phases of the development process, in order to reduce the complexity of designing an emotion-oriented application. Emotional modeling was chosen over other methodologies because it is utilized to address gaps in the original unified modeling language (UML), by extending agent-oriented modeling (AOM). The reason for this is that conventional software development approaches were primarily concerned with functional requirements in order to demonstrate system behavior. Unlike UML, which is excellent for modeling functional requirements, UML is incapable of dealing with the human factor.

AOM is an agent-oriented methodology that employs the concept of an agent at all stages of its execution via modeling steps [13]. In AOM, the interaction diagram depicts the interactions of agents (human or artificial) with the system [12]. AOM is useful for modeling a socio-technical system. AOM has been used in the Mauritius smart parking system [14], project-based ICT4D Education in the Field [15], and Digital Media Design [16].

This paper presents preliminary results of modeling an engaging online quiz through the agent-oriented approach. A systematic approach is introduced to create an engaging application through emotion modeling. A quantitative analysis of the novel approach is conducted to understand the feasibility of the proposed methodology. From the findings, AOM is able to model a non-functional requirement of a system and to transform it into a concrete model for rapid prototyping of an engaging system.

## 2. Emotion Modeling

Student engagement refers to the degree of attention, curiosity, interest, optimism, and passion that learners show while learning [17]. Engagement is defined as “energy in action” and symbolizes the connection between a person and the specific activity [18]. In addition, engagement can be defined as the user’s focus on the application [19]. There are four aspects that need to be taken into consideration in terms of maintaining the users’ involvement in online courses. These include skills engagement (keeping up with readings), emotional engagement (making the course fascinating), interaction engagement (having fun while participating in small group discussions), and performance engagement (performing well during tests, receiving a decent grade) [20].

The learning engagement has the potential to increase the performance of a user completing an online course [21], [22]. For example, when a person receives feedback from their tutor on their work, it helps them improve their learning process [22]. Meanwhile, when guided by the instructor, students may develop cognitive abilities and enhance their understanding of the topic. As a result, such an approach improves the student’s achievement [22]. In addition, engagement can help address the problem of user isolation and dropout in online learning. Learner engagement has been bolstered through discussion and interaction with peers and the instructor. Sharing an idea encourages students to remain involved and to enjoy their learning experience [23].

A comparison of the findings and functionalities of the proposed system reveals similarities with those found in the existing literature [11], [12], [24]–[26]. These similarities include taking into account emotion models which are introduced in order to capture and represent the systems’ meaningful emotional demands. Those emotion models are the qualities of individuals that are tied to the roles and to the system as such [12]. Furthermore, emotional goals should be given the same weight as functional and quality goals [11]. In addition, an emotional goal derived based on the emotion model is associated with its functional counterpart and is expressed as the third goal, after functional and qualitative goals.

Recent studies fail to fully cover the process of including emotional goals in the software development cycle. In the context of software engineering, emotional goals are usually regarded as non-functional requirements.

There are two kinds of emotional goals. Positive emotions that the user wishes to feel while interacting with the application are classified as emotional goals [12]. Positive emotions include the feelings of joy, trust, interest, curiosity, calm, and surprise. Emotion goals are linked to a goal model representing how the functional goal could deliver what the user needs. An emotional threat refers to negative feelings that represent emotions the user does not desire or that must be avoided in the application [12], i.e. boredom, grief, distraction, fear, rage, and frustration.

In a case study involving an emergency alarm system for orderly persons [12], the emotional goal has been used. Such a system is developed to keep elderly people safe at home while they live alone. They may experience emergency situations that require the assistance of emergency services [11]. Thanks to such a system, an elderly person can raise an alarm. If the older person requires assistance, the service provider will contact them. Meanwhile, the persons rely on a well-being check to show that they are doing fine, by pressing a button on a regular basis. This, however, fails to address the emotional needs of consumers. As a result, their independence is threatened. They feel less independent, because they assume the emergency alarm system would stigmatize them as incapable of taking care of themselves. Furthermore, users lack control over the emergency system because they must hit the well-being button within a specific time frame. If they fail to press the button, the service provider will contact them with a reminder message. Consequently, people feel burdened because they must check-in on a daily basis.

Emotion modeling is used in smart homes, but according to studies, this technology is focused on the system’s functionality rather than the on the user’s feelings and emotions [25].

Personal and context-specific emotions have been added to the emotional goal [26]. A personal emotion is defined as an emotion that a person wants to feel regardless of whether the system is well designed or not. The context-specific emotional goal is defined as emotions that a person feels or desires to feel about the system. A process model is used for emotion-led requirement modeling. A process model is introduced to help with emotion modeling in AOM.

The process model begins with determining the activities that need to be completed. Following that, an activity that will be investigated is chosen. The next step is to collect information on the activity. Such data may be obtained through a combination of interviews, observations, technology probes, surveys, brainstorming sessions, domain research, and user feedback. Once data is collected, the fourth step is to extract roles and primary emotional goals. Next, key functional goals, i.e. quality, and context-specific emotional goals are extracted. In parallel, the modeler defines the motivational scenarios and the role models that have not yet been identified together with the personal emotional goals.

## 3. An Agent Oriented Approach

AOM modeling takes place at three distinct layers: motivation layer, system design layer, as well as platform specific design and implementation layer. The motivation layer is on the top and was used to discuss the issue and try to understand what people wanted. This involves the use of an emotion model, a goal model, determination of the role and organization, identification of a domain model, and the Tropos goal model [13].

The system design layer is located in the middle of the system. It shows how the system is designed. The motivation

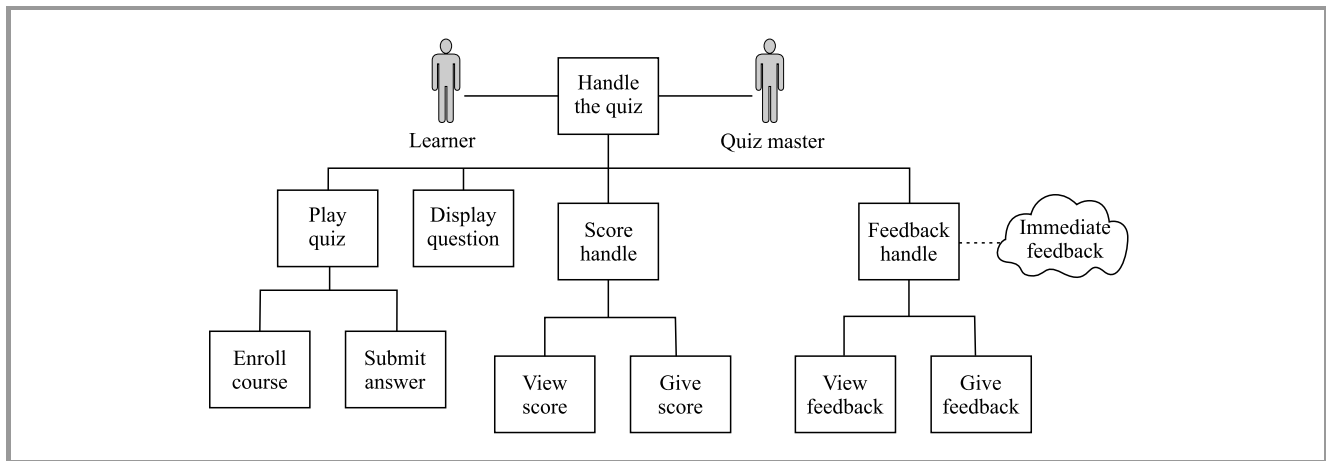


Fig. 1. Example of an overall goal model of the QuizMAster application.

layer is transformed into system design layer models. It introduces interaction, scenarios, and behavior models to illustrate the system’s design.

The system’s lower-level component has the form of the platform-specific design and implementation layer. It expresses how the system deploys the design models conceptually in order to construct a valuable solution by utilizing a programming platform, technology, and architecture.

**3.1. Model Goal, Decide Roles and Organization**

In this study, an online quiz called QuizMAster is designed. It is an educational game-based learning system that is integrated with an intelligent software agent to provide the learner with suitable feedback [10].

The entire goal model of the QuizMAster is depicted in Fig. 1. It illustrates the goals (functional, quality, and emotional) and the corresponding roles [25]. A goal model is a model that specifies which components of a problem the roles are capable of solving in a hierarchical manner.

It is made up of several components, including functional quality and emotional goals, as well as roles. All of them are organized and structured by the goal model [12] being the primary tool for discussing the issue with all stakeholders [12]. They assist in getting an overview of the overall system but do not provide a sufficient amount of development-related details.

Furthermore, the goal model enables the stakeholders to understand the problem, purpose, and requirements of the system at an early stage. It also uses a simple notation to improve understanding and communication between the development team and non-technical personnel [12].

The main goal of QuizMAster is to “handle the quiz”. Several system purposes have been translated into functional goals in order to achieve the main functional aim (sub-goals), i.e. play quiz, display question, score handle, and feedback. The learner is responsible for achieving the play quiz’s functional goal and then enrolling in the course and submitting the answer.

The quiz master is responsible of accomplishing the display question’s functional goal. After the learner enrolls in the

course, the quiz master will display the question. The score handle is made up of the view score and give score sub-goals. The learner is responsible for achieving view score. This includes the sub-goals of high score and low score. The learner will see the top score if he or she submits the correct answer. If the learner provides a wrong answer, they will see the low score.

Feedback handles are made up of two sub-goals: view feedback and give feedback. The learner is responsible of achieving view feedback. If the student provides the correct answer, the positive feedback will be displayed and negative feedback will be shown in response to a bad answer. The feedback handle functional goal is linked to the “immediate feedback” quality goal [9].

**3.2. Emotion Modeling Through Extended Goal Model**

The emotional model has two elements: emotional goal and emotional threat, as seen in Fig. 2.

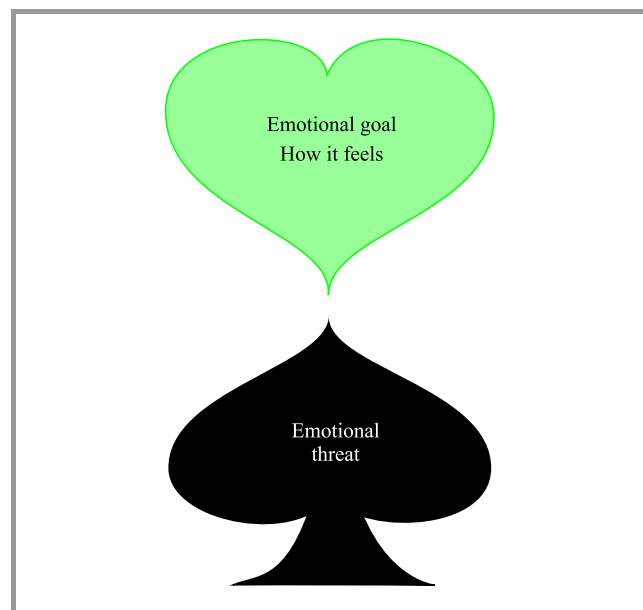


Fig. 2. Notation for emotional goals and threats.

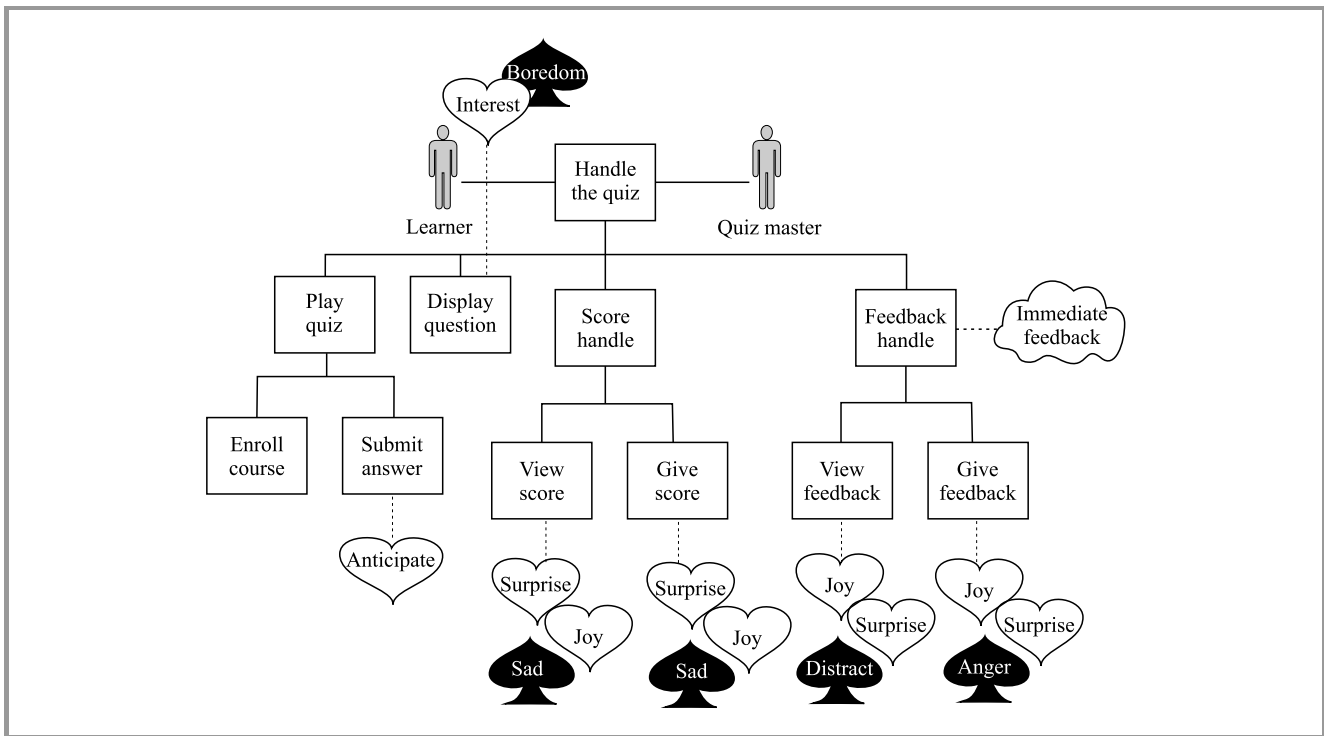


Fig. 3. Example of emotion-oriented goal model for QuizMaster application.

The emotional goal is a non-functional aim that captures, supports or improves the emotional need, or a goal describing what the user desires to feel and how people feel about a specific software application. The emotional goal does represent a positive emotion (heart shape) in order to capture or support the user's good feeling.

The emotional threat is a negative emotion (spades) capturing what the user does not desire or what needs to be avoided. All negative emotions should be addressed to ensure all user concerns are taken into consideration. By including the negative emotion in the model, the developer can maintain the traceability of negative emotions throughout the model. Emotional goals help remind the developer of the need to prioritize requirements by counteracting or eliminating negative emotions. However, it is up to the stakeholders to decide whether a given emotion is mapped as positive or negative.

Figure 3 shows an example of an emotion-oriented goal model for QuizMaster. The feeling is based on responses obtained during the requirement study. The learner wishes to feel anticipation when submitting an answer. They enjoy imagining and planning what is going to happen once they submit their answer. The quiz master wishes to capture the learner's interest while displaying the question and the answer affects the score and result in feedback. When displaying questions, boredom is regarded as a bad emotion that the quiz master does not want to experience, particularly while displaying the question [27]. Following the learner's response to the question, the quiz master will assign a score and provide feedback. If the learner provides the correct answer, they wish to experience joy during the process.

If the student provides a wrong answer, the learner only wants to be surprised by the low score and negative feedback. The student does not want to be sad when viewing a low score or distracted and then unable to realize their mistake. The quiz master, on the other hand, wants to be surprised when giving a low score and does not want to be angry while providing negative comments.

### 3.3. Define Emotion Dependency Analysis Through Tropos Model

From the emotion-oriented goal model shown in Fig. 3, we can develop the Tropos goal model to define how the interaction of a given role can influence the feeling of another individual role. A dependency may be described as a situation in which one actor (the depender) depends on another actor (the dependee) for gaining some dependum [13]. In general, the depender would be able to achieve a goal by depending on the dependee for the dependum. If the dependee fails to deliver the dependum, the depender would be unable to achieve its goals on its own, or would not be able to do that easily. Since emotion is an interactive mechanism, a model is needed capable of modeling the interaction between the emotion's elements. The main actors are the learner and the quiz master.

The quiz master is relying on the learner to display the question. When displaying the question, the quiz master wants the learner to be interested, and not bored. The quiz master is counting on the learner to provide an answer. When submitting the answer, the learner wishes to feel a sense of anticipation. The learner relies on the quiz master to provide the score. When the learner views a high score, he wants to feel joy. In case of a low score,

he wants to feel surprised and do not want to feel surprised, but not sad. The quiz master wants to feel joy when the learner receives a high score. The quiz master wants to feel surprised when the learner receives a low score. The quiz master does not want to feel sad when giving a low score to the learner.

**3.4. Define the Emotion Handling Strategy Through Extended Goal Model and Domain Models**

Once the emotion linked with goal achievement has been identified, we can continue to identify the strategy for dealing with the emotion as well as the knowledge entities that will be influenced by the emotion. This is accomplished using the goal and the domain models. Figures 4 and 5 show examples of an emotion-oriented goal model for the expression of joy and a domain model to be applied by the quiz master. Joy is expressed through the use of a simple and natural method of notation. The quiz master aims to demonstrate joy by smiling, giving the student a thumbs up, playing a clap sound, complimenting the learner, displaying motivational images, a bright color background, and unlocking a new level.

Though several approaches have been developed to measure and detect emotions, our research focuses on how to model emotion-oriented applications. Emotions are subjective and complex, hence there is no guarantee that users will feel

happy using the software. However, it all depends on how the learner perceives the application [11].

A domain model consists of domain entities and their relationships. It represents the knowledge that the program is expected to handle. An object type can be used to represent such entities. In a system, a domain entity is a modular unit of knowledge. These include the environments, services, and types of resources produced and stored by roles and role connections. Domain entities in our model correspond to the course, question, answer, score/answer, and feedback. We will transform the goal model and the domain model into the design phase.

This includes modeling the emotion component using a scenario model, an interaction model, and a behavior model.

**3.5. Designing Emotion-Oriented Application Through Scenario, Interaction and Behavior Model**

Once the approach for dealing with emotion and knowledge entities has been determined, we may proceed to designing an emotion-oriented application using scenario, knowledge, interaction, and behavior models. A scenario model consists of collective activities that must achieve functional goals. The activities are based on the functionalities described in the motivation layer. It provides functionality-related information by specifying the number, aim, initiator, trigger, failure, condition, constituent stages, set of activi-

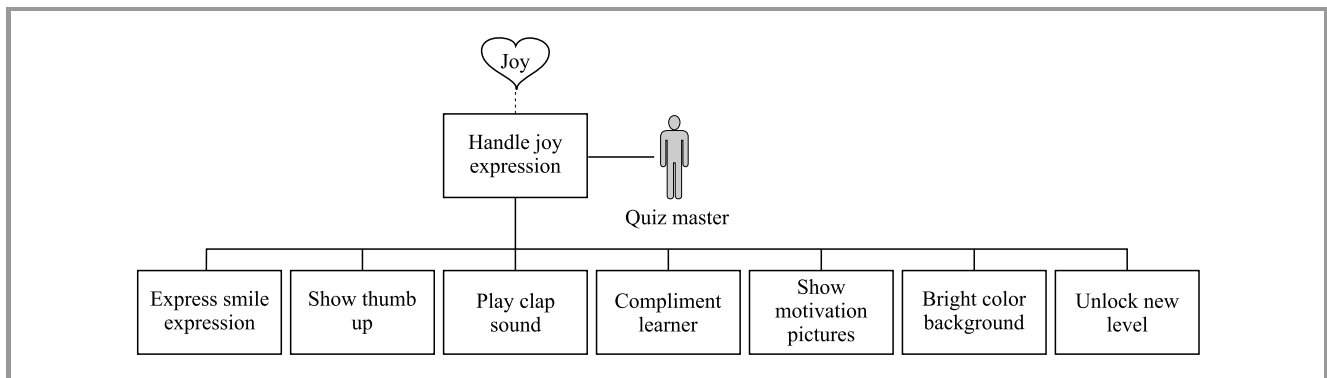


Fig. 4. Example of an emotion-oriented goal model to handle the expression of joy.

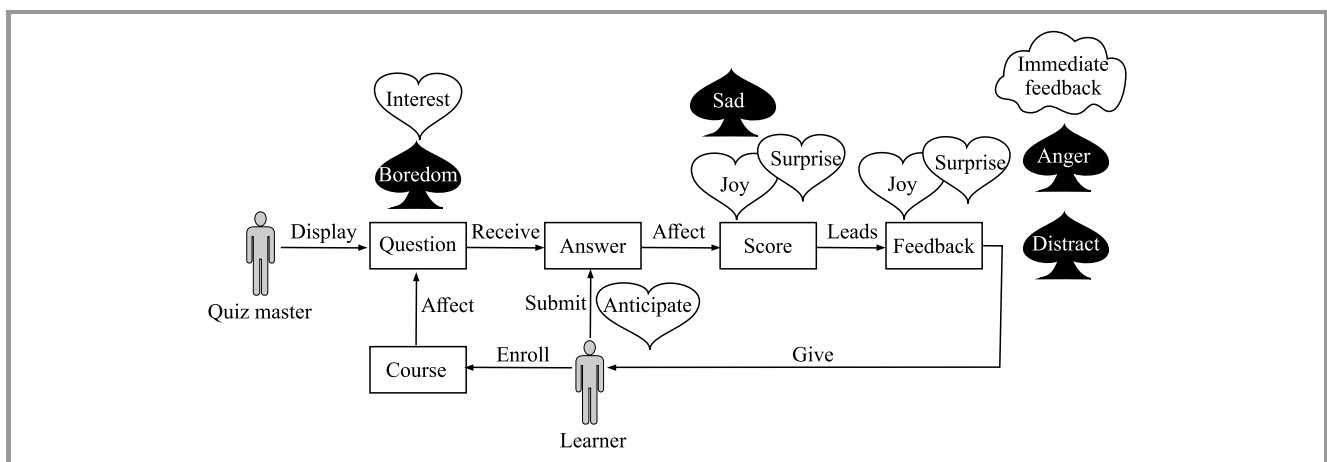


Fig. 5. Example of an emotion-oriented interaction model applied by the quiz master.

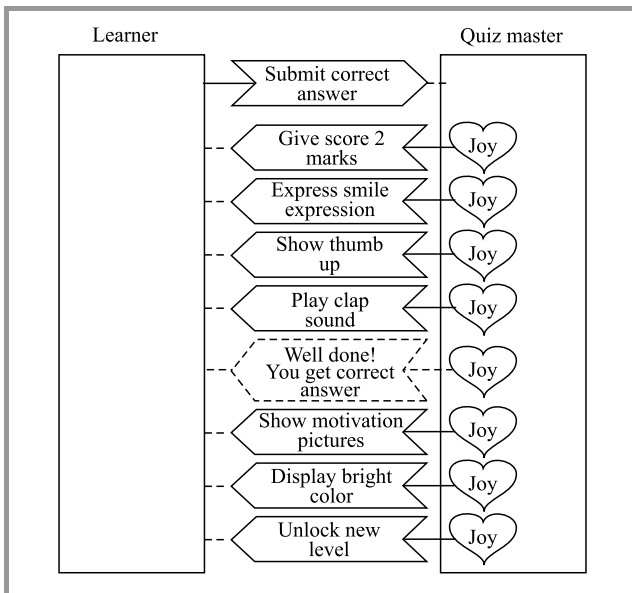


Fig. 6. Example of emotion-oriented interaction model for quiz master.

ties, agent types/roles, as well as quality [13] and emotional goals [26].

An interaction model can be designed from the scenario model. An example thereof is shown in Fig. 6.

An interaction model represents a set of interactions between the application agents. Interaction is defined as actions in which people exchange information through communication or physical action. The interaction model notation has been expanded by incorporating the applicable emotional threat in each emotional goal for the specific activities, triggers, and situations. The quiz master is the perceiving agent and the learner is the acting agent. This is due to the fact that the student starts the exercise by virtually submitting the correct response. When the student provides the correct answer, the quiz master awards two points to the student.

In the meantime, the quiz master wants to be happy when the student gets the right answer. As a result, the quiz master expresses joy by smiling, showing a thumbs up, and playing a clap sound.

After that, a new level will be unlocked. Furthermore, the quiz master wishes to share their satisfaction by displaying motivational images, such as graduation pictures, study groups at the library, or employment-related achievements. The final step in the process of designing an emotion-oriented application is to model the behavior model. It describes the internal behavior of a specific individual agent within the system by triggering rules and messages in this final step of designing an emotion-oriented application.

### 3.6. Build Emotion-oriented Quiz MASTer Application

Once the modeling is finalized, we will proceed to implementing the QuizMAStEr. Figure 7 depicts the evolution of the application. A 3D character is created to serve as the game host. Thanks to this feature, the learner will be greeted at the start of the quiz session, so that they feel motivated and not bored.

## 4. Evaluating Emotion Modeling

### 4.1. Evaluation Through an AOM Survey

A survey of 30 students at FCSIT, Unimas was performed. 28 respondents were studying software engineering, one computer science, and one network computing. 28 students with no prior knowledge of or experience with AOM participated in the session.

All participants are familiar with programming concepts, the software development cycle, and UML. The survey’s goal is to better understand the learner’s function in respect to each of the AOM model types and to learn how novices may understand the feasibility of the emotion modeling ap-

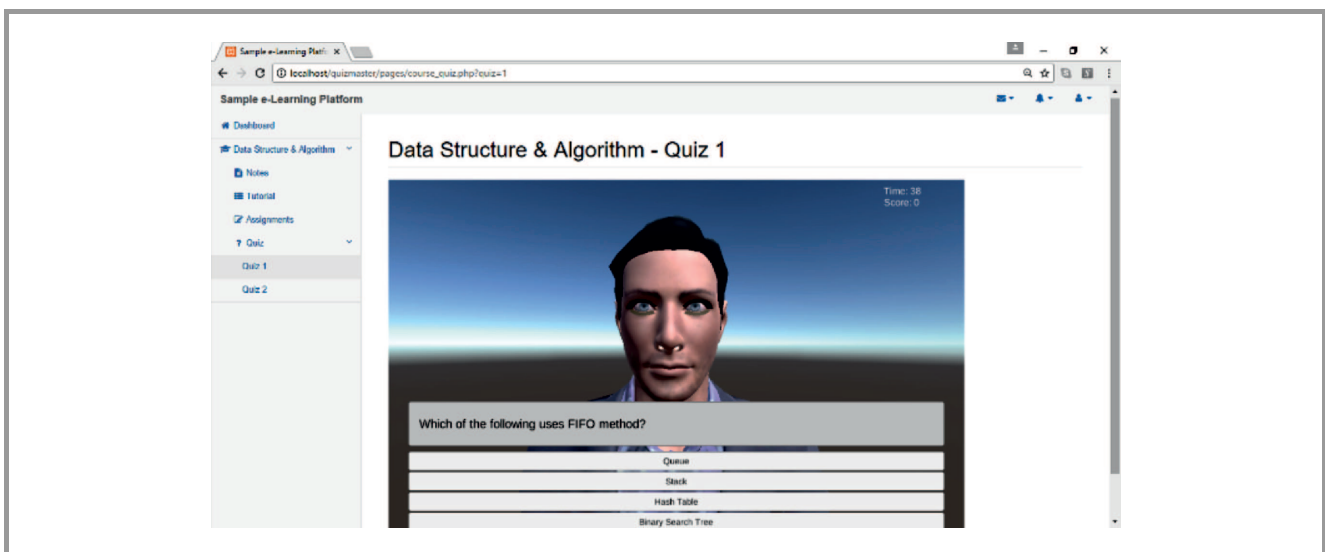


Fig. 7. Exported objects: base, happy, worried, and mouth opened.

proach being analyzed and how to develop an engaging application. The survey participants used three dimensions of the AOM model. The first question involves understanding the role of agent models in emotion-oriented applications. These include client validation, implementation, documentation, and clarification [28].

In other words, the questions verify whether AOM is capable of managing specific modeling requirements in collaboration with the client’s representatives being on the project team, to specify the system’s implementation-related needs. We asked if AOM may be used as a potential communication tool or an understandable artifact among programmers. The second set of questions examines the user’s functionalities in connection with each of the agent models in an emotion-oriented application. These involve creation, evaluation, and approval.

The final set of questions explores the rationale behind not employing any or all agent models in the emotion-oriented application.

**4.2. Evaluation of AOM Survey Data**

Figure 8 depicts the findings of a survey concerned with agent models in emotion-oriented modeling. Clearly, the majority of students (22 and 21, respectively) believe that the goal model may be employed for client validation and clarification. Meanwhile, implementation has been selected by 19 people asked. Only 16 students believe the goal model can be utilized for documentation. The domain model can be used for clarification and client validation, according to 19 and 18 students, respectively. Only 16 students agreed that the domain model could be utilized for documentation. According to the findings, 17 students agreed that the objective of the Tropos model is clarification.

This is followed by client validation, which is agreed upon by 14 persons.

Only 12 of the surveyed believe the Tropos model can be used for implementation and documentation. It is clear that clarification was the primary goal of employing the interaction model. This answer was chosen by 22 pupils.

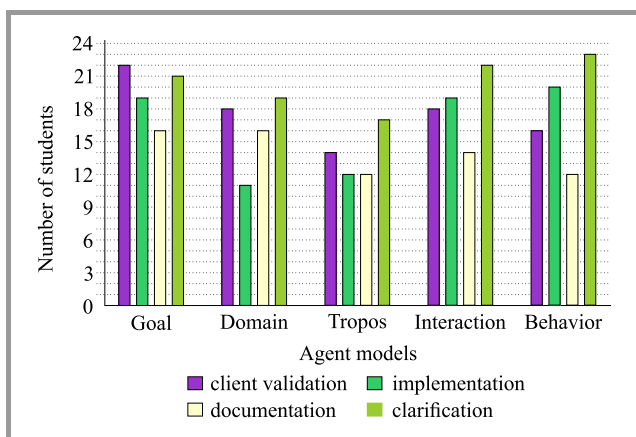


Fig. 8. Survey results in regards to the purpose of agent models.

This is followed by implementation, on which 19 participants agreed. The interaction model can be used for client validation, according to 18 votes. Only 14 students believe the interaction model can be applied for the purpose of documentation. According to the chart, clarification is the ultimate goal of the behavior model. Client validation and clarification received a relatively low number of votes (16 and 12, respectively).

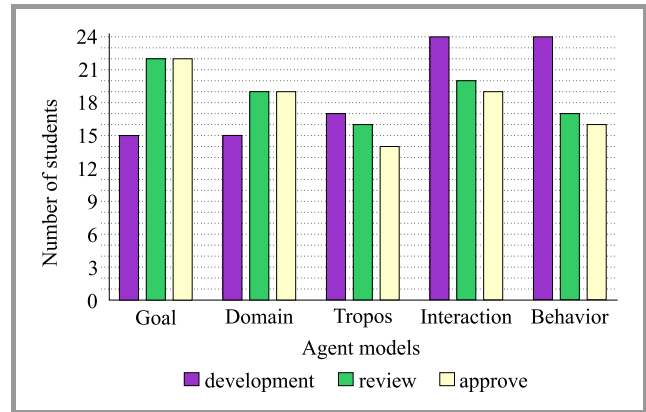


Fig. 9. Survey results regarding the user’s role in relation to each of the agent models.

Figure 9 shows the findings regarding the user’s involvement in respect to each of the agent models in emotion-oriented modeling.

It can be concluded that 22 students agreed the user was most likely to be involved in reviewing and approving the goal model.

While users were less likely to assist in the development of the goal model, only 15 students agreed with such a choice. The same is true for the domain model. The user, according to 19 students, is most likely to be active in reviewing and approving the domain model.

This is followed by the development option which was selected by 15 pupils only. According to the findings, the majority of participants (17 and 16, respectively) agreed that users were most likely to be involved in the development and review of the Tropos model. Approval was a relatively minor reason, with only 14 persons agreeing thereon. The user was most likely to be involved in the development of the interaction model, according to 24 of the surveyed. Review and approval were very minor reasons, with 20 and 19 students selecting them, respectively. According to the graph, it was development that was the most popular user role. This was followed by review and approval as the user’s role, selected by 17 and 16 participants, respectively.

Figure 10 shows the survey responses in relation to the various reasons for not employing agent models in emotion-based modeling. Among other things, the most plausible reasons include the fact that analysis is not well understood, that there is insufficient value to justify the cost, and that it is not useful for most projects.

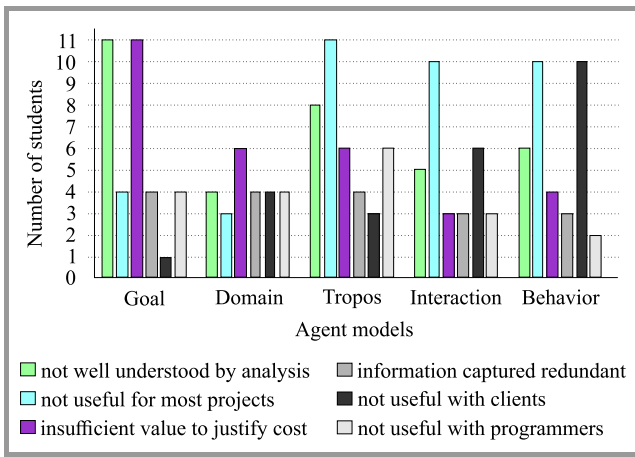


Fig. 10. Number of students selecting the reasons for not using some or all of the agent models.

It is reasonable to conclude that improper understanding based on an analysis, and inadequate value to justify the expense were both equally valid arguments for not implementing the goal model. These options were selected by 11 survey participants. The score is seven times greater than the one for the following options: not useful for most projects, information captured is redundant, and not beneficial for programmers. Not useful for clients was a reason that was selected relatively seldom, with only one person asked agreeing with it. Six persons agreed that the most important reason for not using the domain model is the lack of value justifying the expenditure borne. Analysis not well understood, information captured redundant, and not useful for clients and programmers were all equally popular as reasons for not adopting the domain model (selected by 4 respondents). Not useful for most projects, meanwhile, was a relatively unpopular reason, with only three students choosing this option.

According to the findings, 11 students agreed that being not useful for the majority of projects is the most important reason for not using the Tropos model. This choice was followed by a poorly understood analysis, on which just 8 peoples agreed. Inadequate value to justify expense and redundant nature of the information acquired were both plausible reasons for not implementing the Tropos paradigm. Redundant nature of the information obtained and lack of usefulness for customers were modest contributors, as these answers were selected by 4 and 3 users, respectively.

One may notice that the most obvious cause for not using the interaction model was that it was not useful for most projects. This reason was selected by 10 of the surveyed. This score is four times greater than that related to the model not being useful for clients. Only 5 students agreed that one of the possible reasons for not employing the interaction model was that it was not well understood based on the analysis conducted. Inadequate value to justify the expense, information acquired being redundant and unusable with programmers were all equally minor reasons for not implementing the interaction model and were ranked third.

According to Fig. 10, the most common reasons for not adopting the behavior model included statements that it was not beneficial for most projects and that the information obtained was redundant. This was followed by insufficient value to justify expense, information acquired being redundant and useless for programmers, which were all relatively minor contributors. A usability test, on the other hand, was conducted among 13 students enrolled in the "data structure and algorithm" course. They were instructed to experiment with the quiz application and answer a few questions using the provided questionnaire, with an emphasis on rating the amount of usage challenges, understanding the questions after taking part in the quiz, interactivity, assessing its interactivity, engagement, and usefulness. The rating scale varied from 1 to 5, with 1 being the lowest and 5 being the highest score. The students were asked to rate these elements for text-based quizzes, which are currently employed in FC-SIT, as well as for the emotion-oriented QuizMAster application that was developed as part of this research.

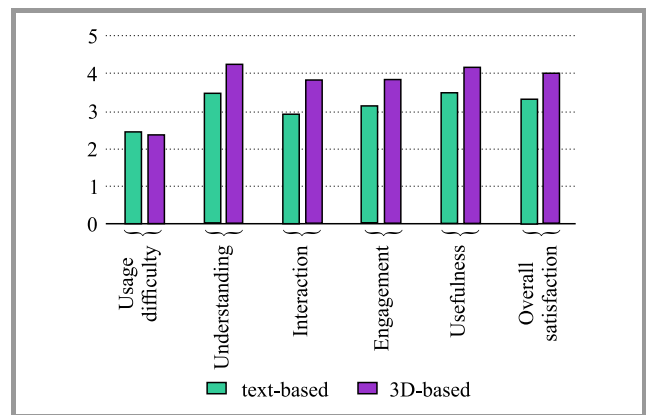


Fig. 11. Average rating of text-based and emotion-oriented quiz.

Figure 11 shows the average rating of a text-based quiz and of the emotion-oriented QuizMAster. The rating for the emotion-oriented QuizMAster is superior to that of the text-based quiz, in every way. Difficulties related to using the emotion-oriented QuizMAster are slightly less prominent than in the case of the text-based quiz, with the score equaling 2.38 for the emotion-oriented variety and 2.46 for the text-based quiz. Students believed that after taking the quiz, they had a better understanding of the questions in the emotion-oriented (4.23) than in the text-based (3.46) quiz. The amount of involvement for the emotion-oriented quiz is also greater than for text-based variety, with the score amounting to 3.85 and 2.92, respectively. While the level of engagement for the emotion-oriented quiz is evaluated at 3.85, it is greater than the level of engagement for the text-based quiz, with its score equaling 3.15. Additionally, usefulness of the emotion-oriented quiz is ranked higher than that of its text-based counterpart (with the scores amounting to 4.15 and 3.46, respectively). The overall level of satisfaction with the emotion-oriented quiz is rated at 4.00, while it equals 3.31 for the text-based quiz.

## 5. Conclusion

Creating an emotionally engaging learning application is not an easy task. The emotional anticipation of the user is a major predictor of the application's acceptance level. However, not much study has been conducted into incorporating user's emotional expectations into the software development cycle. We tried to help by suggesting a systematic strategy for creating an emotionally engaging application which would require more validation and verification in the course of future research.

## Acknowledgements

Thanks to Unimas University to support on this research.

## References

- [1] S. Y. Wai, C. W. Shiang, S. F. Zulkifli, N. B. Jali, and M. A. Khairuddin, "Requirement engineering meets emotion: A case study of Quiz MASTer", *Int. J. of Adv. Sci. and Technol.*, vol. 28, no. 2, pp. 215–222, 2019.
- [2] C. A. Courtad, "Making your classroom smart: Universal design for learning and technology", in *Smart Education and e-Learning 2019*, V. Uskov, R. Howlett, and L. Jain, Eds. *Smart Innovation, Systems and Technologies*, vol. 144, pp. 501–510. Springer, 2019 (DOI: 10.1007/978-981-13-8260-4\_44).
- [3] A. Khan, O. Egbue, B. Palkie, and J. Madden, "Active learning: Engaging students to maximize learning in an online course", *The Electron. J. of e-Learn.*, vol. 15, no. 2, pp. 107–115, 2017 [Online]. Available: <https://files.eric.ed.gov/fulltext/EJ1141876.pdf>
- [4] R. Deng, P. Benckendorff, and D. Gannaway, "Learner engagement in MOOCs: Scale development and validation", *British J. of Educ. Technol.*, vol. 51, pp. 245–262, 2019 (DOI: 10.1111/bjet.12810).
- [5] T. D. Nguyen, M. Cannata, and J. Miller, "Understanding student behavioral engagement: Importance of student interaction with peers and teachers", *J. of Educ. Res.*, vol. 111, no. 2, pp. 163–174, 2016 (DOI: 10.1080/00220671.2016.1220359).
- [6] L. M. Daniels, C. Adams, and A. McCaffrey, "Emotional and social engagement in a massive open online course: An examination of Dino 101", *Emotion, Technol. and Learn.*, in *Emotions, Technology, and Learning*, S. Tettegah and M. P. McCreery, Eds. Elsevier, 2016, pp. 25–41 (DOI:10.1016/B978-0-12-800649-8.00004-3).
- [7] S. R. Jimerson, E. Campos, and J. L. Greif, "Toward an understanding of definitions and measures of school engagement and related terms", *The California School Psychologist*, vol. 8, no. 1, pp. 7–27, 2003 (DOI:10.1007/BF03340893).
- [8] F. Zhao, "Using quizzz to integrate fun multiplayer activity in the accounting classroom", *Int. J. of Higher Educ.*, vol. 8, no. 1, pp. 37–43, 2019 [Online]. Available: <http://files.eric.ed.gov/fulltext/EJ1203198.pdf>
- [9] S. H. Gamage, J. R. Ayres, M. B. Behrend, and E. J. Smith, "Optimising moodle quizzes for online assessments", *Int. J. of STEM Educ.*, vol. 6, no. 1, 2019 (DOI:10.1186/s40594-019-0181-4).
- [10] S. Leung, S. Virwaney, F. Lin, A. Armstrong, and A. Dubbelboer, "TSL-enhanced pedagogical agents to engage learners in virtual worlds", *Int. J. of Distance Educ. Technol.*, vol. 11, no. 1, pp. 1–13, 2013 (DOI: 10.4018/jdet.2013010101).
- [11] M. Kissoon Curumsing, "Emotion-oriented requirements engineering", Ph.D. thesis, Swinburne University of Technology, Melbourne, Australia, 2017 [Online]. Available: <https://nzjohng.github.io/publications/theses/anju2017.pdf>
- [12] A. A. Lopez-Lorca, T. Miller, S. Pedell, L. Sterling, and M. Kissoon Curumsing, "Modelling Emotional Requirements", 2014 [Online]. Available: <https://people.eng.unimelb.edu.au/tmiller/pubs/modelling-emotional-requirements.pdf>
- [13] L. Sterling and K. Taveter, *The Art of Agent-Oriented Modeling*. London, England: The MIT Press, 2009 (ISBN: 9780262013116).
- [14] H. Dargaye, B. Gobin-Rahimbux, and N. G. Sahib-Kaudeer, "Agent-based modeling for a smart parking system for Mauritius", in *Information Systems Design and Intelligent Applications. Proceedings of Fifth International Conference INDIA 2018, Volume 2*, S. C. Satapathy et al., Eds. *AISC*, vol. 863, pp. 367–377. Springer, 2019 (DOI: 10.1007/978-981-13-3338-5\_34).
- [15] A. Bon et al., "Community-centered, project-based ICT4D education in the field", in *Proc. of 15th Int. Conf. on Social Implic. of Comp. in Develop. Countr.*, Warsaw, Poland, 2019, pp. 386–397 (DOI: 10.1007/978-3-030-19115-3\_32).
- [16] J. Marshall, "Agent-based modeling of emotional goals in digital media design projects", in *Innovative Methods, User-Friendly Tools, Coding, and Design Approaches in People-Oriented Programming*, S. Goschnick, Ed. Publisher IGI Global, 2018, pp. 262–284 (ISBN: 9781522559696).
- [17] "Student Engagement", *The Glossary of Education Reform*, 2016 [Online]. Available: <https://www.edglossary.org/student-engagement/>
- [18] V. Sagayadevan and S. Jeyaraj, "The role of emotional engagement in lecturer-student interaction and the impact on academic outcomes of student achievement and learning", *J. of the Scholarship of Teach. and Learn.*, vol. 12, no. 3, pp. 1–30, 2012 [Online]. Available: <https://files.eric.ed.gov/fulltext/EJ992115.pdf>
- [19] A. Dirin and T. H. Laine, "User experience in mobile augmented reality: Emotions, challenges, opportunities and best practices", *Computers*, vol. 7, no. 2, pp. 215–222, 2018 (DOI: 10.3390/computers7020033).
- [20] M. D. Dixon, "Creating effective student engagement in online courses: What do students find engaging?", *J. of the Scholar. of Teach. and Learning*, vol. 10, no. 2, pp. 1–13, 2010 [Online]. Available: <http://files.eric.ed.gov/fulltext/EJ890707.pdf>
- [21] C. Taylor et al., "Student engagement: A framework for on-demand performance assessment tasks", *Stanford Center for Opportunity Policy in Education*, 2016 [Online]. Available: <https://edpolicy.stanford.edu/sites/default/files/publications/student-engagement-framework.pdf>
- [22] F. Martin and D. U. Bolliger, "Engagement matters: Student perceptions on the importance of engagement strategies in the online learning environment", *Online Learning J.*, vol. 22, no. 1, pp. 205–222, 2018 [Online]. Available: <https://files.eric.ed.gov/fulltext/EJ1179659.pdf>
- [23] J. Banna, M. F. G. Lin, M. Stewart, and M. K. Fialkowski, "Interaction matters: Strategies to promote engaged learning in an online introductory nutrition course", *J. of Online Learn. and Teach.*, vol. 11, no. 2, pp. 249–261, 2015 [Online]. Available: <https://pdfs.semanticscholar.org/65c7/0b42305630dc9da07d2cdd2d9b3939d6b971.pdf>
- [24] M. Sherkat, A. Mendoza, T. Miller, and R. Burrows, "Emotional Attachment Framework for People-Oriented Software", *Online Learn. J.*, vol. 22, no. 1, pp. 205–222, 2018 [Online]. Available: <https://arxiv.org/pdf/1803.08171.pdf>
- [25] D. Curumsing, M. K. Fernando, M. Abdelrazek, R. Vasa, K. Mouzakis, and J. Grundy, "Emotion-oriented requirements engineering: A case study in developing a smart home system for the elderly", *J. of Syst. and Softw.*, vol. 147, pp. 215–229, 2019 (DOI: 10.1016/j.jss.2018.06.077).
- [26] T. Miller et al., "Emotion-led modeling for people-oriented requirements engineering: The case study of emergency systems", *J. of Syst. and Softw.*, vol. 22, no. 1, 105, pp. 54–71, 2015 (DOI: 10.1016/j.jss.2015.03.044).
- [27] R. S. J. D. Baker, S. K. D'Mello, M. M. T. Rodrigo, and A. C. Graesser, "Better to be frustrated than bored: The incidence, persistence, and impact of learners' cognitive-affective states during interactions with three different computer-based learning environments", *Int. J. of Human-Comp. Stud.*, vol. 68, no. 4, pp. 223–241, 2010 (DOI: 10.1016/j.ijhcs.2009.12.003).
- [28] B. Dohing and J. Parsons, "Dimensions of UML diagram use: A survey of practitioners", *J. of Database Manag.*, vol. 19, no. 1, pp. 1–18, 2008 (DOI: :10.4018/jdm.2008010101).



**Syazwanie Filzah binti Zulkifli** earned her M.Sc. in Software Engineering from Universiti Malaysia Sarawak. Her primary research interests focus on modeling and creating engaging AI games used in education. She plans to commence, in the future, additional research on requirement engineering used in sociotechnical systems.

 <https://orcid.org/0000-0003-3736-5516>

E-mail: waniefilzah@yahoo.com  
 Faculty of Computer Science and Information Technology  
 Universiti Malaysia Sarawak (UNIMAS)  
 94300 Kota Samarahan  
 Sarawak, Malaysia



**Cheah Wai Shiang** is a senior lecturer at the Faculty of Computer Science and Information Technology, Universiti Malaysia Sarawak. His main research interests are in agent technologies used in real time environments, with a particular emphasis placed on AI games and on validating agent-oriented modelling (AOM). He

is also interested in analyzing sustainability of ICT4D projects through e3Value.

 <https://orcid.org/0000-0002-1647-6703>

E-mail: wscheah@unimas.my  
 Faculty of Computer Science and Information Technology  
 Universiti Malaysia Sarawak (UNIMAS)  
 94300 Kota Samarahan  
 Sarawak, Malaysia



**Muhammad Asyraf bin Khairuddin** is a senior lecturer at the Faculty of Computer Science and Information Technology, Universiti Malaysia Sarawak (UNIMAS). He received his B.Sc. and M.Sc. degrees in Computer Science from Universiti Teknologi Malaysia, Johor, Malaysia in

2003 and 2007, respectively. His research interests include security in requirement engineering and requirement elicitation.

 <https://orcid.org/0000-0001-9837-4438>

E-mail: kmasyraf@unimas.my  
 Faculty of Computer Science and Information Technology  
 Universiti Malaysia Sarawak (UNIMAS)  
 94300 Kota Samarahan  
 Sarawak, Malaysia



**Nurfaeza binti Jali** is a lecturer at the Faculty of Computer Science and Information Technology, Universiti Malaysia Sarawak (UNIMAS). She received her M.Sc. degree in Computer Science (Real Time Software Engineering) from Universiti Teknologi Malaysia (UTM). Her research interests focus on requirement

engineering, software design patterns and object oriented design.

 <https://orcid.org/0000-0002-7789-8168>

E-mail: jnurfaeza@unimas.my  
 Faculty of Computer Science and Information Technology  
 Universiti Malaysia Sarawak (UNIMAS)  
 94300 Kota Samarahan  
 Sarawak, Malaysia



**Yanti Rosmunie binti Bujang** is a lecturer at the Department of Software Engineering, Faculty of Computer Science and Information Technology, Universiti Malaysia Sarawak (UNIMAS). Her research interests focus on software testing, community services, ethics in information technology and Internet security.

E-mail: byanti@unimas.my  
 Faculty of Computer Science and Information Technology  
 Universiti Malaysia Sarawak (UNIMAS)  
 94300 Kota Samarahan  
 Sarawak, Malaysia

# Implementation of a Malicious Traffic Filter Using Snort and Wireshark as a Proof of Concept to Enhance Mobile Network Security

Rafia Afzal and Raja Kumar Murugesan

*School of Computer Science and Engineering, Taylor's University, Malaysia*

<https://doi.org/10.26636/jtit.2022.155821>

**Abstract**—In the 1970s, roaming interconnections for cellular networks were designed for a few trusted parties. Hence, security was not a major concern. Today, the SS7 (Signaling System no. 7) solution that is several decades old is still used for many roaming interconnections. SS7 has been proven vulnerable to serious threats due to deregulation, expansion, and convergence with IP-based Long Term Evolution (LTE) networks. The limitations of the SS7 network that it is unable to check the subscriber's authentic location, verify their identity and filter illegitimate messages, makes the system vulnerable to attacks. Adversaries taking advantage of these shortcomings can inflict threats such as interception of calls and text messages, subscriber tracking and denial of service attacks. Although LTE and Diameter signaling protocols promise enhanced security keeping up with the latest attack vectors, their inherent flaws related to roaming interconnections are still there and continue to make the networks vulnerable. Hence, a highly secure signaling network is required to protect the operators and the subscribers from a diverse range of security attacks. SS7 network protocol layers, such as signaling connection control part (SCCP), transaction capabilities application part (TCAP), and global system for mobile Communications – mobile application part (GSM MAP), manage connectivity between networks and subscribers. An analysis of the parameters of these layers may provide a clear insight into any anomalies present. Unfortunately, these parameters are not validated and verified at the network's edge. The major contribution of this research is a methodology for detecting anomalies by checking malformed parameters and intra-layer parameter discrepancies at the abovementioned protocol layers. This paper provides an insight into the severity of SS7 network security vulnerabilities. Furthermore, it provides a proof of concept for the analysis of SS7 network traffic using the Wireshark packet capture tool and the Snort intrusion detection system (IDS) capable of detecting malicious traffic patterns.

**Keywords**—mobile network, signaling network security, SS7.

## 1. Introduction

In telecommunication networks, a signaling system is used to manage call set-up and termination processes in order

to connect and manage both ends. SS7 was designed five decades ago, in the 1970s, when only a few operators were providing telecommunication services and had access to the core network [1]. Since then, SS7 has been used for call establishment/termination, mobility management, user security information, billing information, and access/service authorization [2]. As it was considered that mutual trust existed between operators, no inherent security controls were incorporated in the SS7 core network. Operators being national or multinational corporations were assumed to be trustworthy, making the SS7 network a walled garden [3], [4]. The merger of packet-switched IP networks and circuit-switched telephone networks attracted more subscribers, resulting in an increase level of competition and in the expansion of coverage, thus creating high demand and allowing new competitors to enter the market. The number of core network entry points increased due to the introduction of new technologies and interfaces with the legacy SS7 network, boosting the number of operators accessing the system [5].

Network exposure results from the design and the architecture of the solution that needs to support the roaming of peers, making the system vulnerable to attacks. Vulnerabilities faced by users may be grouped into five major categories: obtaining information on the subscriber's location, spying or snooping, monetary mugging, account fraud, and interruption and denial of service [3]. Liberalization of the telecommunications domain and shifting to IP based communications exposed SS7 to severe threats, such as interference between calls and text messages, tracking the location of subscribers, deception/spamming, denial of service, and subscriber account frauds [6]. Several commercial signaling firewalls are currently available and much effort has been taken by the Global System for Mobile Association (GSMA) to mitigate such attacks. However, the commercial firewalls are not fully secure, as they focus solely on home public land mobile network level protection to mitigate the risks faced. They are still not adequate and are hardly accepted by telcos, since there are several ways in which the security measures may be evaded. This issue arises mainly

because of the lack of protection while the subscribers are roaming, and due to the possibility of spoofing messages in the SS7 signaling connection control part (SCCP) and in the Diameter protocols. Taking into consideration the fact that present defensive procedures, such as the use of firewalls, filtering and blacklisting, regrettably are not capable of ensuring satisfactory levels of safety for SS7 [4], a rule-based intrusion detection system has been proposed. In this research, the proof of concept for the rule-based intrusion detection system is provided to demonstrate that it improves detection accuracy and reduces the false alarm rate.

This paper is organized into the following sections. Section 2 highlights the causes of security vulnerabilities affecting the SS7 network. Section 3 presents the proof of concept for the rule-based intrusion detection system, and Section 4 concludes the paper and specifies future directions.

## 2. Related Work

### 2.1. Causes that Lead to SS7 Network Vulnerability

SS7 firewalls are currently breached and exposed to a wide range of vulnerabilities and threats that jeopardize the security of the telecommunications networks. Liberalization of the telecommunications sector has resulted in relaxation of the rules and regulations that are applied to manage the SS7 network. The deregulation has resulted in the SS7 network being more easily accessible to network providers and users alike.

In the early twenty-first century, a series of signaling transport protocols, known as SIGTRAN, was established to meet the new requirements for mobile connections and to support the emerging services. SIGTRAN is an SS7 extension that enables messages to be transmitted over IP networks. Because of this advancement, the signaling network is no longer isolated. Many entry points to the network were formed due to attempts to integrate the SS7 network with other solutions, for interoperability purposes. The emergence of numerous entry points to the SS7 network has become a major source of weakness. This helps attackers write, intercept and change SS7 posts via multiple mobile network and subscriber attacks [1], [2].

### 2.2. How Vulnerable is the SS7 Network?

Stealthy attacks made possible by the vulnerabilities of the SS7 system are discussed by Puzankov [7]. He feared that due to misconfiguration errors, SMS home routing may be by-passed and the IMSI of the subscriber may be disclosed, thus helping in the launch of further sophisticated security attacks. In his study, he also examines how an intruder can connect using a bogus MSC, while VLR remains legal. Although genuine MSC is used for voice calls and short messages, fake MSC will be used to intercept incoming messages [7]. In their research, Savadatti and Sharma explain signaling system no. 7 with a brief discussion of

SS7 attacks [8]. Holtmanns demonstrates that SS7 vulnerabilities endanger LTE users as well as GSM/UMTS subscribers. Because of their internet-working capabilities, the attacker can monitor LTE subscribers through the Diameter protocol, taking advantage of SS7 vulnerabilities [9]. In [10], Jensen gave a summary of SS7 attacks, including a section on entry points to the SS7 core network. Such attacks relied on the use of machine learning algorithms to detect SS7 attacks. His most significant contribution to SS7 research was the development of an open-source simulator called “SS7 Attack Simulator” that generates simulated SS7 regular and abnormal traffic.

Similarly, experts at Positive Security explained the entry points to SS7 and explained or demonstrated some attack plots [2]. A white paper released by the SANS Institute gives an insight into potential SS7 attacks. It also proposes how essential security monitoring may be deployed to secure the SS7 network more effectively [2]. Exploiting MAP messages can lead to several security attacks and research done by Rao *et al.* explains the methods relied upon to accomplish such attacks [11]. In another research, Rao *et al.* demonstrate SS7 location tracking attacks exposing vulnerabilities linked to the network’s entry points. They also provide recommendations on how to secure such entry points [12]. Engel gave a live demonstration of location monitoring and DoS attacks at the Chaos Communication Congress. He also described a wide range of other attacks [13]. Karsten Nohl from Security Research Labs showed how access to the SS7 network makes the calls and SMS interceptions possible, at the Chaos Communication Congress mentioned in [14]. At the Hackito Ergo Summit, security experts from P1 labs demonstrated user location tracking and showed how spoofed messages may be used as a security exploit [15].

Keeping in view the current cyber threat environment and the known SS7 vulnerabilities, further studies on this topic are needed to help protect the public’s privacy and to ensure personal protection. Attackers may cause billions in losses suffered by network operators. Hence, it is equally important for operators to help close these gaps in the fence of what once used to be a “walled garden”. It is the need of the hour to gear up against signaling vulnerabilities by understanding the major attacks that were recently carried out using these exploits, and by grasping their severity. This would help us develop methods to safeguard mobile networks from adversaries before any catastrophic security attacks take place.

## 3. Proposed Proof of Concept

### 3.1. Intrusion Detection Systems

A software system that detects malicious activities and behaviors is known as the Intrusion Detection System (IDS). An IDS usually detects data-driven attacks against applications, network-based attacks on vulnerable services, attacks against hosts, such as unauthorized logins, privilege escalation, and access to sensitive data files.

### 3.1.1. Types of Intrusion Detection Systems

Intrusion detection relies on two fundamental techniques, namely anomaly detection and signature detection. In the former method, the normal working conditions or the standard profile of a system is defined, meaning that any deviations from that profile may be detected [16]. In other words, the desired action is defined, and unwanted or undesired behaviors are identified using this technique. Stored data sets and behaviors are two different things. In the case of stored data, a single bit altered may be detected easily, whereas differentiating anomalous behaviors from those that are acceptable is not an easy task [16]. The method relying on characterizing the known ways of penetrating a system is called misuse detection and constitutes another approach to intrusion detection. These known ways are termed patterns. Unambiguous patterns are monitored by a misuse detection system. Patterns may vary from a static bit string to a suspected set of actions. Although both techniques have their advantages, some systems rely on both of these approaches, taking advantage of a hybrid intrusion detection system.

### 3.1.2. Anomaly-Based Detection

Anomaly-based detection is also well-known as statistical or profile-based intrusion detection. In this approach, a “regularity” is defined and any irregular or abnormal traffic deviating from that regularity profile is declared as intrusive [17]. Whatever differs from the normal profile can be comfortably considered as intrusive. Classifying a normal activity as intrusive or abnormal is considered false positive, whereas classification of an abnormal activity as normal is known as false negative. False negative identifications are considered more harmful than their false positive counterparts, as they involve a failure to detect harmful activities. What makes anomaly-based intrusion detection systems hard to implement is the requirement of not only complying with protocols and understanding the inner workings of an application, but also added with expert level users with their preferences, and date and time [17]. Anomaly-based IDS requires computationally intensive behavioral models for construction and tuning [18].

### 3.1.3. Snort-IDS

Snort is one of the most famous, free, and well-known open-source network IDS solutions. It utilizes a rule-based language combined with signature, protocol, and anomaly verification techniques to detect malicious activities, such as denial of service (DOS) attacks and stealth port scan attacks. The best thing about the program is the flexibility of its rule language. It is also suitable for writing rules concerning new attacks, meaning that the creation of new rules is reasonably simple. Rules are the major entities on which Snort relies to differentiate between regular Internet activities and malicious behaviors. In comparison with Wireshark, the program lacks a good GUI and is terminal-based.

### 3.2. Packet Sniffing and Analysis using Wireshark

Wireshark is a network packet analyzer. It has the form of data capturing software that understands the abstraction (structure) of different networking protocols. It captures live packet data from a network interface, or from a file of the packets already collected. It can parse and view fields and their definitions defined by various networking protocols. Data from various types of networks can be read in real-time and stored for later use. The program can export some or all the packets in many file formats available. It helps search the saved packets based on numerous criteria. The GUI version or terminal (command line) version of the utility, TShark, can be used to search the network data captured. A display filter may help refine the captured data. Wireshark is capable of color marking the code packets displayed, based on filters. It also helps create various statistics. Filtering wireless connections is also possible if they move through the controlled Ethernet network. Other options, such as timers and filters, may be used to aid in the filtering of output traffic.

### 3.3. SS7 Attack Simulation

Due to privacy and ethical considerations, using real SS7 network data is not plausible. As such, a simulation setup was realized using the open-source SS7 Attack Simulator [10] to produce the required data set that reflects a practical scenario of an SS7 network in operation. This tool can be used to produce both normal and attack traffic to study SS7 security vulnerabilities. Network traffic is created using MAP in the SS7 stack, according to 3GPP-defined MAP technical specifications.

The simulator generates both normal and anomalous traffic that is used to detect abnormalities. Three network operators, namely A, B and C, are built using the SS7 network simulator’s complex mode. The first network operator (A) is a victim, the second network operator (B) is a roaming network, and the third network operator (C) is an adversary. These operators communicate with one another through thirteen common messages. In addition to the usual communications, call/SMS intercept and location tracking attacks are carried out using anyTimeInterrogation (ATI), sendRoutingInfo (SRI) (-SM, -LCS) and ProvideSubscriberInfo (PSI). An attacker who is a subscriber of network operator C will imitate the attacks.

In this research, the two most debated and critical attacks, namely location tracking and interception attacks [2], are simulated. To demonstrate these attacks, one type of a message request from each category of SS7 MAP messages has been selected. Home network messages are categorized as category 1, inbound roamers’ messages as category 2, and outbound roamers’ messages as category 3. An ATI from category 1 was selected, as it could only be used within the home network. Similarly, a PSI message could only be sent by the home location register (HLR) to the current visitor location register (VLR). However, the attacker can bypass the HLR and can send this PSI message request di-

rectly to VLR through its MSC/VLR. In order to do this, the attacker needs to have international mobile subscriber identity (IMSI) and current VLR address information of the target. Therefore, the attacker performs another attack by sending SRI-SM to HLR which sends, without verifying and validating the requires, all crucial information to the attacker. This SRI-SM message request is a category 3 message and needs to be verified and validated at network borders or edges. An SRI-SM message request can also be used for other types of attacks, such as SMS interception attacks. The selected attack messages are marked in bold in Table 1.

Table 1  
SS7 MAP messages with attack types

Category	Message	Attack
1	provideSubscriber Location (PSL)	Tracking
1	<b>anyTime Interrogation (ATI)</b>	<b>Tracking and interception</b>
2	insertSubscriber Data (ISD)	Interception, DoS
2	<b>provideSubscriber Info (PSI)</b>	<b>Tracking</b>
3	updateLocation (UL)	Interception, DoS
3	<b>sendRoutingInfo (SRI)(-SM, -LCS)</b>	Multiple attacks i.e. <b>IMSI disclosure, SMS interception</b>
3	sendAuthentication Info (SAI)	Interception

3.4. Proposed Anomaly Detection Scheme

To demonstrate location tracking and interception attacks, three types of map message requests: ATI, PSI and SRI-

SM are used. The simulator generates a data set for attacks and for normal traffic. This traffic is then captured on the loopback interface (lo) using the Wireshark packet capturing tool that generates pcap files. Anomalies are detected using Snort and customized SS7 anomaly detection rules. The proof-of-concept is presented, in the form of a flow diagram, in Fig. 1, and the model or the template of the anomaly detection rules is given in Fig. 2.

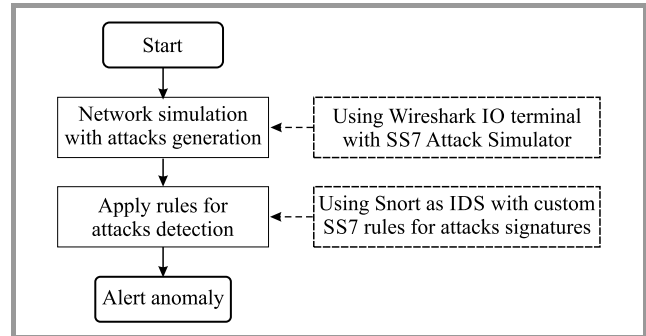


Fig. 1. Anomaly detection and alert generation flow.

3.5. Anomaly Detection and Alert Generation

As shown in Fig. 4, the first or the upper window shows live packet capturing. The middle or the second window shows the protocols underneath. The lower or the third window is the one that offers the information in “hexadecimal” form – a direct translation of the “bits” circulating through the communication channel. This tool’s window is crucial, as it helps collect signatures of traffic patterns in the form of hexadecimal figures. Bits are the deepest level of signatures, as any other form of analysis in the higher-level protocols will always be more densely packaged. Information circulating at the lowest level, in the form of bits, cannot avoid detection. During this experiment, Wireshark was helpful in identifying and analyzing attack packets from the captured traffic. Differentiating at-

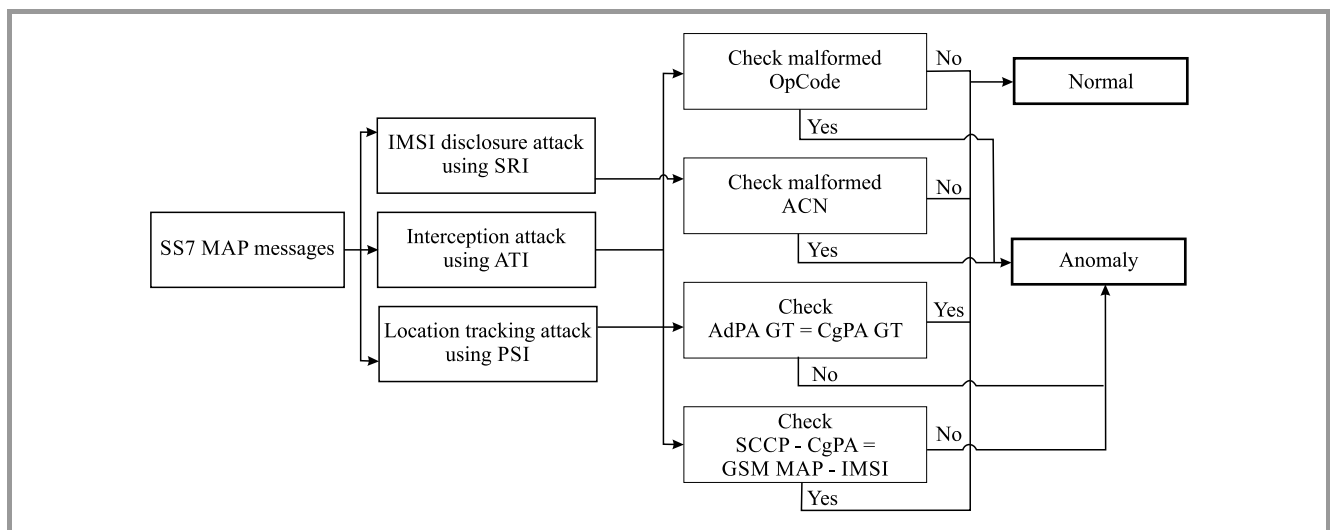


Fig. 2. Model of SS7 anomaly detection rules.

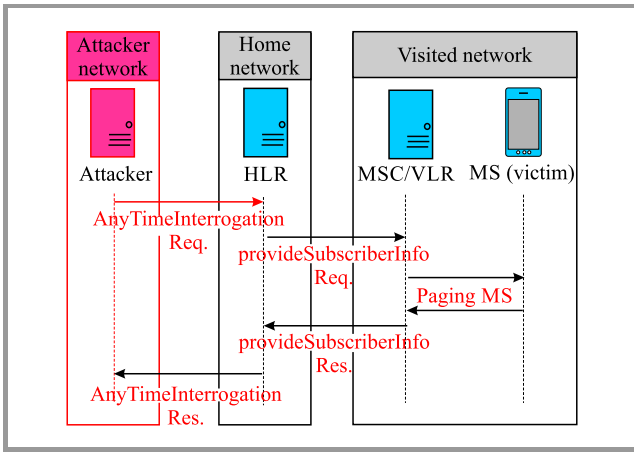


Fig. 3. SS7 attack using a MAP ATI message request.

tack packets manually by analyzing each packet is difficult and is not a recommended approach.

**Attack using anyTimeInterrogation (ATI) request.** The use of SS7 MAP ATI messages to perform a location tracking attack is presented in Figs. 3 and 4.

**Attack using provideSubscriberInfo (PSI) request.** Figures 5 and 6 show how SS7 MAP PSI message exploitation is carried out to perform location tracking attacks. Unfortunately, only the HLR could send the MAP PSI message to the current VLR. However, the attacker can send this MAP PSI message request straight to VLR via its MSC/VLR,

bypassing the HLR. To do so, the attacker will require the target’s IMSI and current VLR address information. As a result, the attacker launches a new attack by sending MAP SRI-SM to HLR, which provides all the critical information to the attacker without checking or validating it. This SRI-SM message request belongs to the category 3 message type and must be inspected and validated at the network node. This SRI-SM message request can potentially be exploited for other attacks, such as SMS interception.

Wireshark supports the SCCP protocol, and the tool offers the option of applying visualization filters for SCCP elements. It allocates different subsystem numbers (SSNs) to each entity, making it easier to use them as a filter. It helps

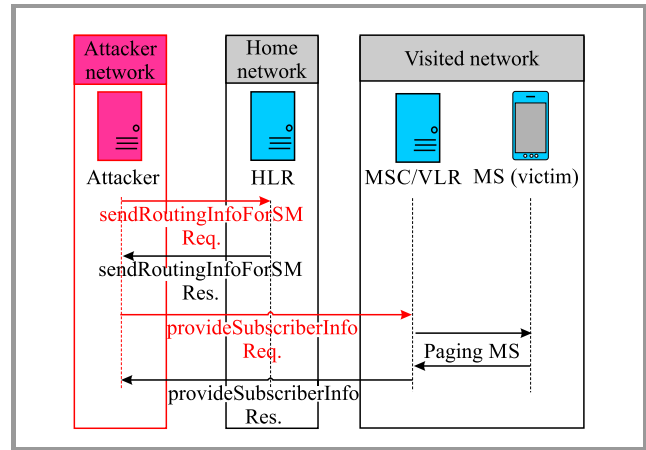


Fig. 5. Example of a PSI signaling message being exploited.

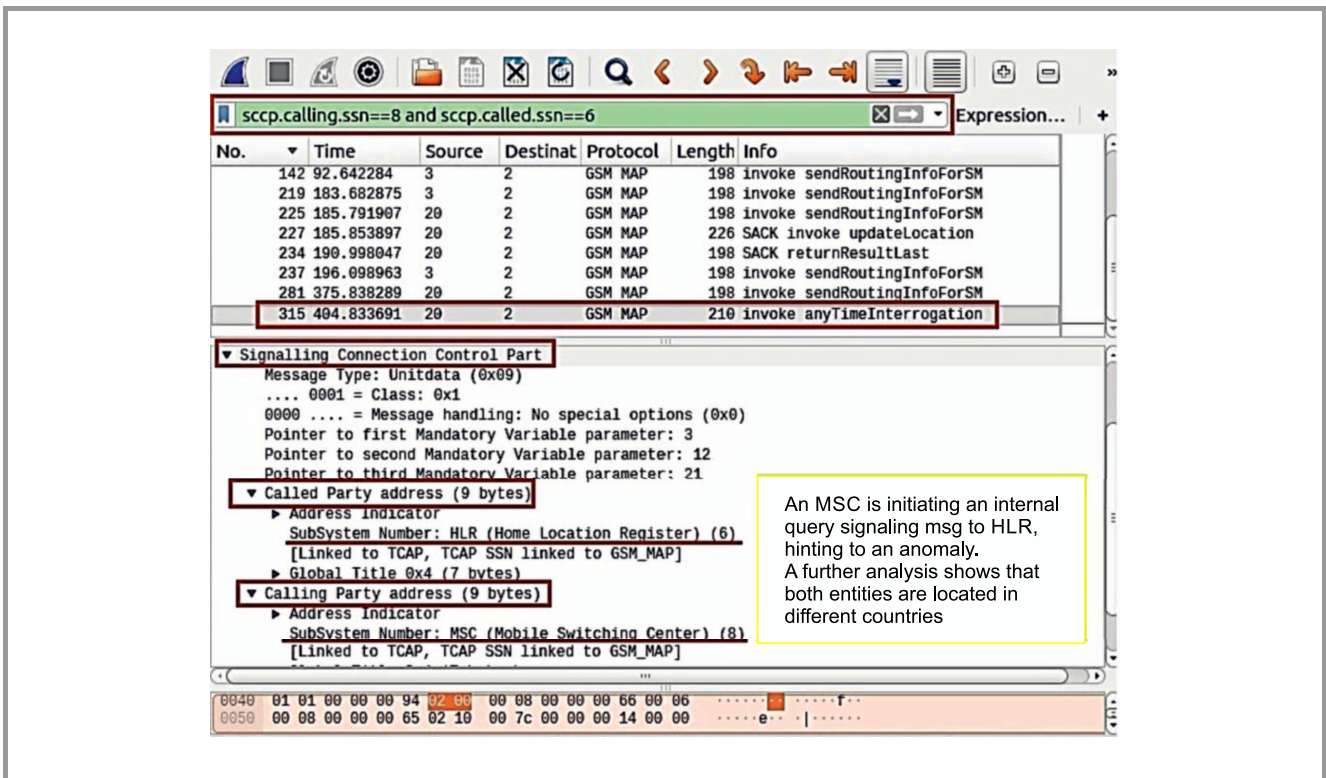


Fig. 4. Identification and analysis of attack packets captured in Wireshark

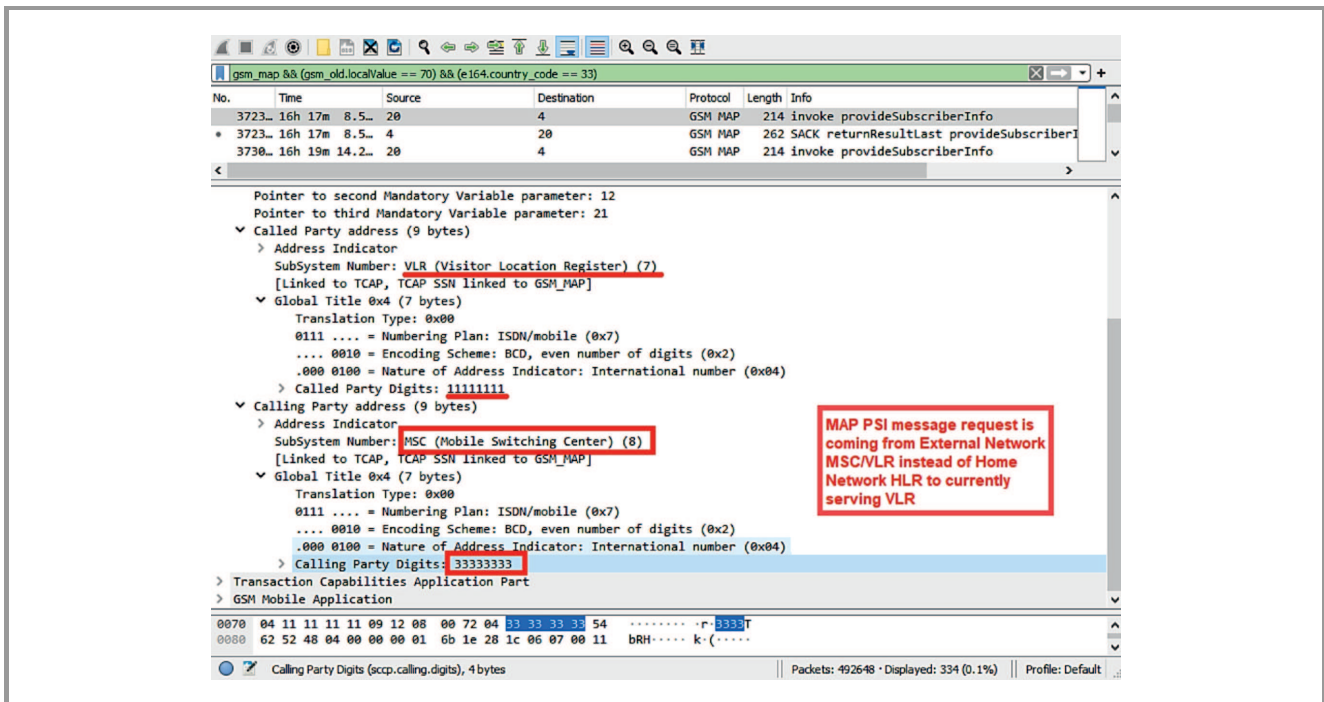


Fig. 6. SS7 attack using a MAP PSI message request.

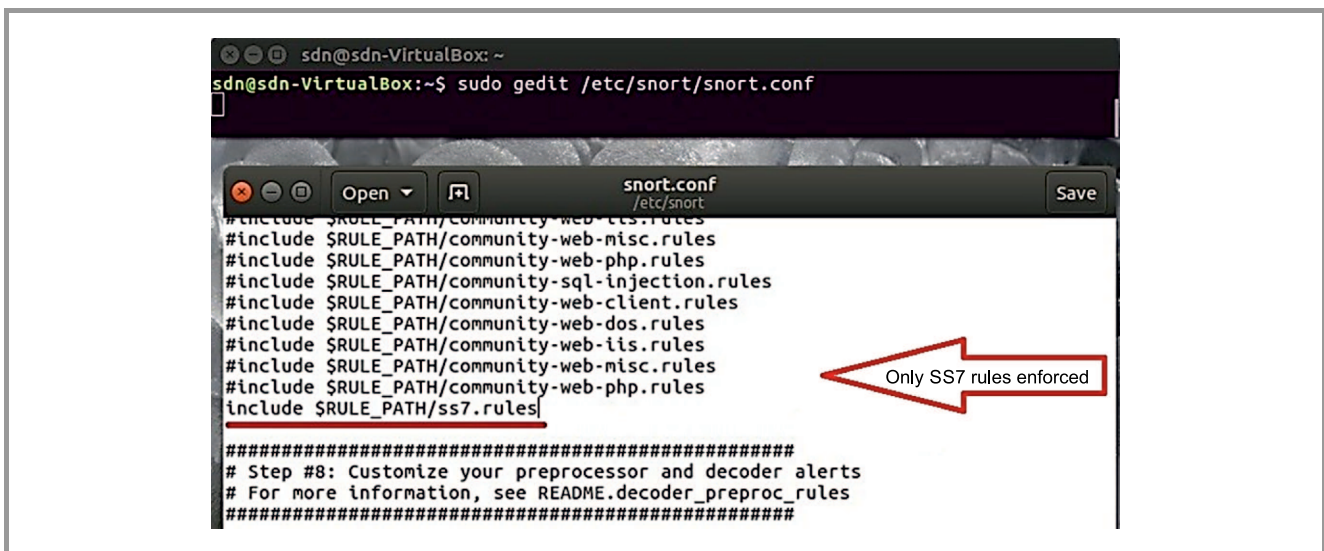


Fig. 7. Snort using an SS7 rules file.

deduce that if this attack packet is provided as an input to a detection tool, then all attack-related packets can be detected live or during the attack, should it reoccur. The data is presented in hexadecimal form, which is the primary representation of the packet's bits circulating across the communication channel. These bits could be helpful for the detection of signatures if provided as an input to some content-matching tool that is capable of matching all the packets against these bits to help detect all attack-related packets.

Acting in the capacity of an IDS, Snort provides hundreds of pre-loaded rules classified into different families, such

as HTTP, telnet, ssh, etc. All these rules, if enforced, can help detect hundreds of attacks. However, the tool must be kept up to date for standard usage, as new rules are published and regularized on a regular basis. With its great flexibility, Snort allows the addition of custom rules in its configuration file.

In this research, as shown in Fig. 7, custom rules named SS7 rules were added to the configuration file of Snort. This rules file contains all three types of rules covering all simulated attacks, with hexadecimal bits from the third window of Wireshark added as content matching information. After adding these rules, all other rules were disabled

using the hash symbol. The generated pcap file is given as input to Snort to test the SS7 rules. The tool detected the attacks without any false negatives.

## 4. Results

The results demonstrate that by relying on the knowledge of the SS7 network and its operation, traffic anomalies can easily be detected and, hence, attacks can be mitigated. Furthermore, from the results shown in Table 2, one may infer that filtering SS7 data with the use of a rule-based algorithm should be performed as the first defensive layer for all MAP SS7 messages.

Table 2  
Confusion matrix for MAP UL, MAP PSI, SRI-SM,  
and ATI

	MAP PSI		MAP SRI		MAP ATI	
	TP	TN	TP	TN	TP	TN
Predicted positive	96	4	10	2	10	4
Predicted negative	0	4605	0	2946	0	4600
Accuracy	0.9998		0.9997		0.9998	
Detection rate	99.980%		99.997%		99.998%	
False positive	1		1		1	
False discovery	0.04		0.1667		0.2857	
False negative	0.9796		0.9966		0.9978	
Sensitivity	0.0204		0.0034		0.0022	
Specificity	0.9998		0.9997		0.9998	
Precision	0.96		0.833		0.7143	

A dataset of 12,279 samples was generated using the SS7 attack simulator. Out of these samples, 16 were detected as anomalies related to a MAP anyTimeInterrogation (ATI) message request, and 100 were detected as anomalies related to MAP provideSubscriberInfo (PSI) message requests. Similarly, for the MAP sendRoutingInfoSM (SRI-SM) message request, 12 samples were detected as anomalies. Based on the dataset for a particular MAP ATI message request, 10 of the detected anomalies were actual attacks, i.e. true positives, leaving 6 false positives. Similarly, for the MAP PSI message request, 96 of the detected anomalies were actual attacks, i.e. true positives, leaving 4 to be false positives. Likewise, in the case of MAP SRI-SM message requests, 10 of the detected anomalies were actual attacks, i.e. true positives, leaving 2 to be false positives. As shown in Table 2, the overall anomaly detection accuracy (related to all three types of message requests) is 99.98%.

### 4.1. Evaluation Matrix

The anomaly detection model is evaluated using the following metrics:

- True positive (TP), the number of instances correctly predicted as attacks.
- False positive (FP), the number of instances incorrectly predicted as attacks.
- True negative (TN), the number of instances correctly predicted as non-attacks.
- False negative (FN), the number of cases incorrectly predicted as non-attacks.
- Accuracy =  $\frac{TP + TN}{TP + FP + FN + TN}$ .
- False alarm rate =  $\frac{FP}{FP + TN}$ .
- Detection rate = DR =  $\frac{TP}{TP + FN}$  is the ratio between the total number of attacks detected by the proposed model and the total number of attacks present in the dataset.

## 5. Conclusion

SS7 networks have become open and exposed to a multitude of vulnerabilities, degrading the level of security of telecommunication systems. Relaxation in the rules and regulations that governed the telecommunications market has rendered the networks vulnerable. Interoperability-driven attempts to merge networks have added additional concerns regarding breaches of SS7 security measures. The addition of new signaling messages for telephone mobility and advanced telecommunication services has led to further abuses and attacks, such as subscriber tracking, call interception, SMS spamming, and denial of service. Although the advantages of Diameter, a new protocol gradually replacing the SS7 signaling protocol in the next generation telecommunication networks are numerous, the default level of security provided by Diameter is not sufficient to make LTE an attack-resistant solution.

It is worth mentioning that traffic analysis is a useful tool for monitoring networks and detecting anomalies, and it has been relied upon for a long time now. In order to enable the adoption of this approach for detecting SS7 attacks, Snort and Wireshark tools were deployed on a simulated SS7 attack traffic data set to show that the deployment of Snort is a feasible solution mitigating the problem of network security. The approach adopted analyses SS7 attack traffic using Wireshark (a packet capture tool), as well as identifies malicious patterns and signatures to create Snort IDS rules allowing to detect common types of attacks. Test results related to the proposed intrusion detection method show that Snort detects all 3 types of attacks that the simulator can generate, relying on rule-determining signatures stored in its configuration file. This method allows us to analyze and identify the flow of bits that circulate through the network during a simulated attack, and to detect such potential traffic patterns. This scheme uses tools with open-source licenses to avoid the huge costs of custom development. It will be useful for small- and medium-sized networks with manageable volumes of traffic to filter.

## Acknowledgment

This research project was supported by Taylor's University, Malaysia, through Taylor's Ph.D. Scholarship Program.

## References

- [1] "5G-ready next-generation signaling firewall", Positive Technologies, 2019 [Online]. Available: <https://positive-tech.com/storage/Signaling-NgFW.pdf>
- [2] S. P. Rao, S. Holtmanns, and T. Aura, "Threat modeling framework for mobile communication systems", arXiv:2005.05110, 2020.
- [3] B. Welch, "Exploiting the weaknesses of SS7", *Network Secur.*, vol. 2017, no. 1, pp. 17–19 (DOI: 10.1016/S1353-4858(17)30008-9).
- [4] K. Ullah *et al.*, "SS7 vulnerabilities – a survey and implementation of machine learning vs rule based filtering for detection of SS7 network attacks", *IEEE Commun. Surv. and Tutor.*, vol. 22, no. 2, pp. 1337–1371, 2020 (DOI: 10.1109/COMST.2020.2971757).
- [5] I. Ahmad *et al.*, "Security for 5G and beyond", *IEEE Commun. Surv. and Tutor.*, vol. 21, no. 4, pp. 3682–3722, 2019 (DOI: 10.1109/COMST.2019.2916180).
- [6] H. Zhang and L. Dai, "Mobility prediction: A survey on state-of-the-art schemes and future applications", *IEEE Access*, vol. 7, pp. 802–822, 2019 (DOI: 10.1109/ACCESS.2018.2885821).
- [7] S. Puzankov, "Stealthy SS7 attacks", *J. of ICT Standard.*, vol. 5, no. 1, pp. 39–52, 2017 (DOI: 10.13052/jicts2245-800X.512).
- [8] M. B. Savadatti and D. Sharma, "SS7 network and its vulnerabilities: An elementary review", *Imperial J. of Interdiscip. Res. (IJIR)*, vol. 3, no. 3, pp. 911–916, 2017 [Online]. Available: <http://www.onlinejournal.in/IJIRV3I3/153.pdf>
- [9] S. Holtmanns, I. Oliver, and Y. Míche, "Mobile subscriber profile data privacy breach via 4G diameter interconnection", *J. of ICT Standard.*, vol. 6, no. 3, pp. 245–262, 2018 (DOI: 10.13052/jicts2245-800X.634).
- [10] K. Jensen, H. T. Nguyen, T. V. Do, and A. Arnes, "A big data analytics approach to combat telecommunication vulnerabilities", *Cluster Comput.*, vol. 20, no. 3, pp. 2363–2374, 2017 (DOI: 10.1007/s10586-017-0811-x).
- [11] S. P. Rao, B. T. Kotte, and S. Holtmanns, "Privacy in LTE networks", in *Proc. 2nd Int. Worksh. on 5G Secur. – 9th EAI Int. Conf. on Mob. Multimed. Commun. MOBIMEDIA 2016*, Xi'an, China, 2016, pp. 176–183 (DOI: 10.4108/eai.18-6-2016.2264393).
- [12] S. P. Rao, I. Oliver, S. Holtmanns, and T. Aura, "We know where you are!", in *Proc. 18th Int. Conf. on Cyber Conflict CyCon 2016*, Tallinn, Estonia, 2016, pp. 277–293 (DOI: 10.1109/CYCON.2016.7529440).
- [13] T. Engel, "SS7: Locate. Track. Manipulate", in *Proc. 31th Chaos Commun. Congr. 31C3 2014*, Hamburg, Germany [Online]. Available: <https://berlin.ccc.de/~tobias/31c3-ss7-locate-track-manipulate.pdf>
- [14] S. R. Hussain, M. Echeverria, A. Singla, O. Chowdhury, and E. Bertino, "Insecure connection bootstrapping in cellular networks: the root of all evil", in *Proc. of the 12th Conf. on Secur. and Priv. in Wirel. and Mob. Netw. WiSec 2019*, Miami Florida, USA, 2019, pp. 1–11 (DOI: 10.1145/3317549.3323402).
- [15] A. D. Oliveira and C. D. Nguyen, "Tids: A framework for detecting threats in telecom networks", Hack.lu 2017, 2017 [Online]. Available: [http://archive.hack.lu/2017/Hacklu\\_POST.TIDS\\_framework.pdf](http://archive.hack.lu/2017/Hacklu_POST.TIDS_framework.pdf)
- [16] R. Panigrahi, S. Borah, A. K. Bhoi, and P. K. Mallick, "Intrusion detection systems (IDS) – an overview with a generalized framework", in *Cognitive Informatics and Soft Computing*, P. Mallick, V. Balas, A. Bhoi, and G. S. Chae, Eds. *AISC*, vol. 1040, pp. 107–117. Springer, 2020 (DOI: 10.1007/978-981-15-1451-7.11).
- [17] M. Pawlicki, M. Choraś, and R. Kozik, "Defending network intrusion detection systems against adversarial evasion attacks", *Future Gener. Com. Syst.*, vol. 110, pp. 148–154, 2020 (DOI: 10.1016/j.future.2020.04.013).
- [18] H. Hindy *et al.*, "A taxonomy of network threats and the effect of current datasets on intrusion detection systems", *IEEE Access*, vol. 8, pp. 104650–104675, 2020 (DOI: 10.1109/ACCESS.2020.3000179).



**Rafia Afzal** received her B.Sc. in Computer Science in 2012 and M.Sc. in Computer Science in 2016 from COMSATS University (CU), Islamabad. She is currently pursuing a Ph.D. degree in Computer Science at Taylor's University Lake Side Campus, Subang Jaya, Malaysia. Between 2015 and 2018 she worked as a Teaching

Associate with the COMSATS University Islamabad, Campus, Pakistan. She also worked as Senior Computer Teacher at F. G. Model High School For Girls I/8-1 Islamabad, Pakistan from Jan 2018 to Dec 2018. Her research interests include artificial intelligence, machine learning and mobile network security.

 <https://orcid.org/0000-0002-5299-1366>

E-mail: [afzalrafia@sd.taylors.edu.my](mailto:afzalrafia@sd.taylors.edu.my)

School of Computer Science and Engineering

Taylor's University

47500 Subang Jaya

Selangor, Malaysia



**Raja Kumar Murugesan** is an Associate Professor of Computer Science, and Head of Research for the Faculty of Innovation and Technology at Taylor's University, Malaysia. He holds a Ph.D. in Advanced Computer Networks from the Universiti Sains Malaysia. His research interests include IPv6, future of Internet, Internet governance,

computer networks, network security, IoT, blockchain, and machine learning. He is a member of the IEEE and IEEE Communications Society, Internet Society (ISOC), and is associated with IPv6 Forum, Asia Pacific Advanced Network Group (APAN), Internet 2, and Malaysia Network Operator Group (MyNOC) member's community.

 <https://orcid.org/0000-0001-9500-1361>

E-mail: [rajakumar.murugesan@taylors.edu.my](mailto:rajakumar.murugesan@taylors.edu.my)

School of Computer Science and Engineering

Taylor's University

47500 Subang Jaya

Selangor, Malaysia

# A DFT-based Low Complexity LMMSE Channel Estimation Technique for OFDM Systems

Jyoti P. Patra<sup>1</sup>, Bibhuti Bhusan Pradhan<sup>1</sup>, and Poonam Singh<sup>2</sup>

<sup>1</sup> Madanapalle Institute of Technology and Science, Madanapalle Andhra Pradesh, India

<sup>2</sup> National Institute of Technology, Rourkela Odisha, India

<https://doi.org/10.26636/jtit.2022.148720>

**Abstract**—The linear minimum mean square error (LMMSE) channel estimation technique is often employed in orthogonal frequency division multiplexing (OFDM) systems because of its optimal performance in the mean square error (MSE) performance. However, the LMMSE method requires cubic complexity of order  $O(N_p^3)$ , where  $N_p$  is the number of pilot sub-carriers. To reduce the computational complexity, a discrete Fourier transform (DFT) based LMMSE method is proposed in this paper for OFDM systems in the frequency selective channel. To validate the proposed method, the closed form mean square error (MSE) expression is also derived. Finally, a computer simulation is carried out to compare the performance of the proposed LMMSE method with the classical LS and LMMSE methods in terms of bit error rate (BER) and computational complexity. Results of the simulation show that the proposed LMMSE method achieves exactly the same performance as the conventional LMMSE method, with much lower computational complexity.

**Keywords**—channel estimation, LMMSE, mean square error, OFDM.

## 1. Introduction

Orthogonal frequency division multiplexing (OFDM) has been attracting a lot of attention due to its high spectrum efficiency, as well as fast and easy implementation using the fast Fourier transformation (FFT) approach. It is also resilient to inter symbol interference (ISI) which occurs due to the frequency selective nature of the fading channel [1]. However, high peak-to-average power ratio (PAPR) [2] and channel estimation accuracy [3] are the major challenges for OFDM systems. The equalization of the OFDM system solely depends solely on the accuracy of channel estimation [4].

Generally, there are two schemes that may be relied upon to estimate the channel, namely non-blind or pilot-aided and blind schemes. When compared to pilot-aided channel estimation, the blind channel estimation approach is limited to slow time varying channels and also has a higher

level of complexity and is characterized by poorer performance. Hence, pilot-aided channel estimation is preferred over blind channel estimation. Based on the comb-type pilot, the least square (LS) and the minimum mean square error (MMSE) based channel estimation methods have been investigated in [5]. LS estimation has low computational complexity but its mean square error (MSE) is high due to the noise enhancement problem. To obtain better performance of the LS based estimation method, several denoising strategies have been proposed in [6]–[9].

Eigen-select denoising threshold [6], linear filtering least square method [7], AdaBoost [8] and singular spectrum analysis (SSA) [9] based channel estimation techniques are proposed for channel estimation in OFDM systems.

In [10], the authors proposed an adaptive SSA based channel estimation method. In adaptive SSA, additional noise reduction is performed at a singular value level and, therefore, it provides better performance as compared to the SSA algorithm-based channel estimation method. However, all these channel estimation methods provide a trade-off between performance and computational complexity. If the power delay profile (PDP) of the channel is known to the receiver a priori, the LMMSE channel estimation method is typically implemented. However, it requires cubic complexity due to matrix inversion operation.

To reduce the complexity of LMMSE estimation, the low rank approximation-based singular value decomposition (SVD) approach is proposed in [11]. Based on the SVD method [11], the authors proposed two efficient channel estimation methods for OFDM/OQAM systems in [12]. However, these SVD-based estimation methods are still characterized by high computational complexity, as decomposing the  $R_{HH}$  matrix using the SVD method itself requires cubic complexity [13].

In [14], the authors approximate the LMMSE method using the law of large numbers to reduce the computational complexity of the channel to  $O(N \log N)$ . However, its performance is poor at high SNR values. In [15], the authors proposed a dual-diagonal LMMSE (DD-LMMSE) channel estimation method with  $O(N \log N)$  and also derive

the closed form expression of the asymptotic MSE of the DD-LMMSE.

In [16], the author proposed a low complexity LMMSE channel estimation method based on  $K$  terms Neumann series expansion method to avoid the matrix inversion. A joint low complexity channel estimation and symbol detection approach is proposed in [17], based on a message passing algorithm. In this method, the Sherman-Morrison formula is applied which transforms cubic matrix inversion into a series of diagonal matrix inversions, thus reducing computational complexity.

In [18], the authors proposed a conjugant gradient (CG)-based channel estimation method to achieve similar performance as that of the LMMSE method. This method performs the channel estimation process in an iterative manner and requires computational complexity of the order  $O[(N_p \log N_p)G]$ , where  $G$  is the number of iterations. Typically, a high value of  $G$  is required to achieve optimal performance. A structure-based LMMSE estimation method was proposed in [19] by assuming that the number of pilots is an exact integer multiple of channel length. This method depends on prior information regarding the channel's impulse response and on the appropriate placement of pilots across the OFDM subcarriers. Although the length of CIR can be obtained from the knowledge of the channel auto-correlation function by using the adaptive guard interval (GI) as given in [20], the length of the channel may not be guaranteed to be equal to exact integer multiples of the number of pilot subcarriers.

A compressed sensing (CS) algorithm based MMSE channel estimation is proposed in [21]. This method offers similar performance to that of LMMSE, with much lower computational complexity. However, this method assumes that the channel coefficients are sparse while estimating the channel. Recently, an LMMSE algorithm based on the vector quantization approach was proposed in [22] for OFDM systems. In this method, LMMSE filtering matrices corresponding to wireless channel parameters are calculated offline in the first phase. Subsequently, an appropriate LMMSE filtering matrix is selected according to the MSE criterion while estimating the channel in the online mode. Therefore, this method does not require the PDP to be known at the receiver and, hence, is characterized by negligible performance degradation with much lower computational complexity.

In this paper, a simple but efficient LMMSE channel estimation technique is proposed by exploiting discrete Fourier transformation (DFT) and circulant properties of the channel frequency autocorrelation matrix ( $R_{HH}$ ) for OFDM systems in a frequency selective fading channel.

The symbols associated with the matrices and vectors are denoted with the use of boldface and underlined characters, respectively. Notations  $(\cdot)^H$ ,  $(\cdot)^{-1}$  denote the Hermitian and inverse operation, respectively. Similarly,  $(\cdot)_p$  denotes the position of the pilot signal and  $E[\cdot]$  symbolizes the expectation operator.

## 2. System Model

Let us consider an OFDM system with  $N$  number of subcarriers. After some signal manipulation consisting in addition of a cyclic prefix (CP), removal of CP, inverse fast Fourier transformation (IFFT) and FFT operation, the received signal vector in the frequency domain is given by:

$$\underline{Y} = \underline{X}\underline{H} + \underline{W}, \quad (1)$$

where  $\underline{Y} = [Y(0), Y(1), \dots, Y(N-1)]^T$ .

The transmitted signal  $\underline{X} = \text{diag}[X(0), X(1), \dots, X(N-1)]$  is an  $N \times N$  diagonal matrix. Symbols  $\underline{H} = [H(0), H(1), \dots, H(N-1)]^T$  and  $\underline{W} = [W(0), W(1), \dots, W(N-1)]^T$  are the  $N \times 1$  channel frequency response (CFR) and additive white Gaussian noise (AWGN) vector, respectively. In this paper, the comb-type pilot pattern is adopted for channel estimation purposes. After extraction of the pilot symbol at the receiver side, the received signal vector at the pilot position can be written as:

$$\underline{Y}_p = \underline{X}_p \underline{H}_p + \underline{W}_p. \quad (2)$$

Parameters  $\underline{Y}_p$ ,  $\underline{X}_p$  and  $\underline{H}_p$  are the frequency domain received signal, transmitted signal and CFR at the pilot position, respectively. The CFR vector at the pilot subcarrier can be represented as:

$$\underline{H}_p = \underline{F}_p \underline{h}, \quad (3)$$

where  $\underline{F}_p$  is an  $N \times L$  unitary FFT matrix with  $\underline{F}_p(k, l) = e^{-j2\pi \frac{kl}{N}}$ ,  $k = 0 : p_s : (N_p - 1)p_s$ ,  $l = 0 : L - 1$ .

The IFFT matrix is defined as  $\underline{F}_p^H = \frac{1}{N_p} (\underline{F}_p)^H$ . The channel impulse response (CIR) vector is defined as  $\underline{h} = [h(0), h(1), \dots, h(L-1)]$ , where  $L$  is the total number of multipath channels. It is assumed that each multipath channel  $h(l)$  is independent and identically distributed (i.i.d.) with a zero mean complex Gaussian random variable. The corresponding autocorrelation of the CIR  $\underline{h}$  is given by  $E[\underline{h}\underline{h}^H] = \Delta$  with  $\Delta = \text{diag}[\Lambda(0), \Lambda(1), \dots, \Lambda(L-1)]$  is the diagonal PDP matrix and  $\Lambda(l)$  denotes the average power of the  $l$ -th delay path. The total power of the PDP  $\text{tr}(\Delta) = 1$  where  $\text{tr}(\cdot)$  denotes the trace operation. The power delay profile (PDP) of the multipath is known to the receiver *a priori* or may be calculated using the method given in [23] with a computational complexity of  $O(L^2)$ . Channel estimation using the LS criterion is given by:

$$\tilde{\underline{H}}_{p,ls} = (\underline{X}_p)^{-1} \underline{Y}_p. \quad (4)$$

In order to obtain the channel at all data subcarriers, the interpolation methods are to be deployed, such as linear interpolation, low pass interpolation, discrete Fourier transform (DFT)-based interpolation and so on [24]. In this paper, the DFT-based interpolation is adopted to obtain the CFR at all data subcarriers. After estimating the channel at all data subcarriers, one tap zero forcing equalization is performed to obtain the desired transmitted data signal at the receiver side. The LS method suffers from high MSE and

thus the LMMSE channel estimation method is typically adopted, as it is optimal in terms of MSE. From [5], the LMMSE channel estimation method at pilot positions can be written as:

$$\tilde{\mathbf{H}}_{p,lmmse} = \mathbf{R}_{\mathbf{H}_p\mathbf{H}_p} \left( \mathbf{R}_{\mathbf{H}_p\mathbf{H}_p} + \frac{\beta}{SNR} \mathbf{I}_{N_p} \right)^{-1} \tilde{\mathbf{H}}_{p,ls}. \quad (5)$$

The signal to noise ratio (SNR) is defined as:

$$SNR = \frac{E[|\mathbf{X}_p|^2]}{\sigma_w^2}.$$

Symbol  $\beta = \frac{E[|\mathbf{X}_p|^2]}{E[|1/|\mathbf{X}_p|^2]}$  is a constant depending on the constellation. For QPSK and 16QAM modulation, the values of  $\beta$  are 1 and 17/9, respectively. The LMMSE method experiences high computational complexity of the order  $O(N_p^3)$  due to the matrix inversion operations, as given in Eq. (5).

### 3. Proposed Low Complexity LMMSE Method

In this section, a low complexity LMMSE method is proposed that exploits the DFT technique. The channel frequency autocorrelation matrix is the Fourier transformation of the PDP and is given as:

$$\mathbf{R}_{\mathbf{H}_p\mathbf{H}_p} = E[\mathbf{H}_p\mathbf{H}_p^H] = N_p \mathbf{F}_p \Delta \mathbf{F}_p^H. \quad (6)$$

As  $\mathbf{R}_{\mathbf{H}_p\mathbf{H}_p}$  and  $\mathbf{R}_{\mathbf{H}_p\mathbf{H}_p} + \frac{\beta}{SNR} \mathbf{I}_{N_p}$  are circulant matrices, hence they are commutative [25]. Thus, the LMMSE method can be rewritten as:

$$\tilde{\mathbf{H}}_{p,lmmse} = \left( \mathbf{R}_{\mathbf{H}_p\mathbf{H}_p} + \frac{\beta}{SNR} \mathbf{I}_{N_p} \right)^{-1} \mathbf{R}_{\mathbf{H}_p\mathbf{H}_p} \tilde{\mathbf{H}}_{p,ls}. \quad (7)$$

Multiplying both sides of Eq. (7) with  $(\mathbf{R}_{\mathbf{H}_p\mathbf{H}_p} + \frac{\beta}{SNR} \mathbf{I}_{N_p})$  matrix, we have:

$$\left( \mathbf{R}_{\mathbf{H}_p\mathbf{H}_p} + \frac{\beta}{SNR} \mathbf{I}_{N_p} \right) \tilde{\mathbf{H}}_{p,lmmse} = \mathbf{R}_{\mathbf{H}_p\mathbf{H}_p} \tilde{\mathbf{H}}_{p,ls}. \quad (8)$$

As  $\frac{\beta}{SNR}$  is a scalar quantity, then  $\frac{\beta}{SNR} \mathbf{I}_{N_p}$  can be written as  $N_p F_p \left( \frac{1}{N_p} \frac{\beta}{SNR} \mathbf{I}_L \right) F_p^H$  and Eq. (8) can be simplified to:

$$\begin{aligned} \left[ N_p F_p \Delta F_p^H + N_p F_p \left( \frac{1}{N_p} \frac{\beta}{SNR} \mathbf{I}_L \right) F_p^H \right] \tilde{\mathbf{H}}_{p,lmmse} &= \\ N_p F_p \Delta F_p^H \tilde{\mathbf{H}}_{p,ls} & \\ \Rightarrow N_p F_p \left( \Delta + \frac{1}{N_p} \frac{\beta}{SNR} \mathbf{I}_L \right) F_p^H \tilde{\mathbf{H}}_{p,lmmse} &= \\ N_p F_p \Delta F_p^H \tilde{\mathbf{H}}_{p,ls} & \\ \Rightarrow \left( \Delta + \frac{1}{N_p} \frac{\beta}{SNR} \mathbf{I}_L \right) \tilde{\mathbf{H}}_{lmmse} &= \Delta \tilde{\mathbf{H}}_{ls} \\ \Rightarrow \tilde{\mathbf{H}}_{lmmse} &= \delta \tilde{\mathbf{H}}_{ls}, \end{aligned} \quad (9)$$

where  $\delta = \text{diag} \left[ \frac{\Lambda(0)}{\Lambda(0) + \frac{1}{N_p} \frac{\beta}{SNR}}, \dots, \frac{\Lambda(L-1)}{\Lambda(L-1) + \frac{1}{N_p} \frac{\beta}{SNR}} \right]$ . The parameters  $\tilde{\mathbf{h}}_{ls}$  and  $\tilde{\mathbf{H}}_{lmmse}$  are the estimated channel in the time

domain using LS and MMSE criterion, respectively. The estimated channel frequency response is given as  $\tilde{\mathbf{H}}_{lmmse} = \mathbf{F}_l \tilde{\mathbf{H}}_{lmmse}$ , where  $\mathbf{F}_l$  is an  $N \times L$  FFT unitary matrix.

## 4. Performance Analysis

In this section, the mean square error of the proposed DFT-based LMMSE channel estimation method is derived. The time domain LS method is given by  $\tilde{\mathbf{h}}_{ls} = \mathbf{F}_p^H \tilde{\mathbf{H}}_{p,ls} = \mathbf{h} + \mathbf{F}_p^H (\mathbf{X}_p)^{-1} \mathbf{W}_p$ . The mean square error of the proposed channel estimation method can be written as:

$$\begin{aligned} \text{mse} &= \frac{1}{L} \text{tr} E [ |\mathbf{h} - \tilde{\mathbf{h}}_{lmmse}|^2 ] = \\ &= \frac{1}{L} \text{tr} E [ |\mathbf{h} - \delta (\mathbf{h} + \mathbf{F}_p^H (\mathbf{X}_p)^{-1} \mathbf{W}_p)|^2 ] = \\ &= \frac{1}{L} \text{tr} E [ \mathbf{h}\mathbf{h}^H - \mathbf{h}\mathbf{h}^H \delta^H - \delta \mathbf{h}\mathbf{h}^H + \\ &\quad \delta \mathbf{h}\mathbf{h}^H \delta^H + \delta \mathbf{F}_p^H \frac{\beta}{SNR} \mathbf{I}_{N_p} \mathbf{F}_p \delta^H ] = \\ &= \frac{1}{L} \left( \sum_{l=0}^{L-1} \delta(l) [1 - \delta(l)]^2 + \delta(l)^2 \frac{1}{N_p} \frac{\beta}{SNR} \right), \end{aligned} \quad (10)$$

where  $\delta(l) = \frac{\Lambda(l)}{\Lambda(l) + \frac{1}{N_p} \frac{\beta}{SNR}}$  and the parameter  $\Lambda(l)$  is power of the  $l$ -th multipath channel.

## 5. Computational Complexity

The efficacy of LS, LMMSE and the proposed method can be compared by evaluating the computational complexity related to obtaining CFR at all subcarriers. The LS estimation technique at the pilot positions given in Eq. (4) requires  $N_p$  number of complex multiplications. In order to obtain the CFR at for all subcarriers, the DFT interpolation is used. This requires  $N_p$  numbers of IFFT and  $N$  number of FFT operations. Therefore, the overall computational complexity of the LS estimation approach requires  $N_p + N_p \log_2 N_p + N \log_2 N$ . The conventional LMMSE channel estimation at the pilot positions, as given in Eq. (5), requires multiplication and inversion of the CFR autocorrelation matrix  $\mathbf{R}_{\mathbf{H}_p\mathbf{H}_p}$  of size  $N_p \times N_p$ . In order to determine the  $\mathbf{R}_{\mathbf{H}_p\mathbf{H}_p}$  matrix in Eq. (6),  $N_p$  point FFT/IFFT operations of the diagonal channel autocorrelation matrix  $E[\mathbf{h}\mathbf{h}^H]$  are required. As a result, the computation complexity of  $\mathbf{R}_{\mathbf{H}_p\mathbf{H}_p}$  is  $N_p \log_2 N_p$ . Thus, the LMMSE channel estimation at the pilot positions requires computational complexity of  $N_p^2 + N_p^3 + N_p \log N_p$ .

Similarly, CFR at all subcarriers, as discussed in the previous paragraph, requires  $N_p \log N_p + N \log N$  operations. The overall computational complexity of obtaining CFR using the LMMSE technique requires  $N_p^2 + N_p^3 + 2N_p \log_2 N_p + N \log_2 N$ . The proposed DFT-based low complexity LMMSE method is given in Eq. (9). The  $\delta$  in Eq. (9) requires a diagonal matrix inversion of size  $L \times L$ . Therefore, the calculation of the  $\delta$  parameter needs an  $L$  number of complex multiplications. CFR at all subcarriers

can be obtained by  $N$  point FFT operations. Therefore, the overall computational complexity of the proposed low complexity LMMSE method requires  $L + N \log_2 N$  operations. The overall computational complexities of various channel estimation methods are compared and is listed in Table 1.

Table 1  
Computational complexity

Methods	Computational complexity
LS	$N_p + N_p \log_2 N_p + N \log_2 N$
Classical LMMSE	$N_p^2 + N_p^3 + 2N_p \log_2 N_p + N \log_2 N$
Proposed LMMSE	$L + N \log_2 N$

## 6. Simulation Results

In this section, the performance of the proposed LMMSE method is compared with classical LS and LMMSE channel estimation methods in terms of MSE and BER. The following parameters are considered for an OFDM system model: the number of subcarriers  $N = 128$ , length of cyclic prefix  $N_{CP} = 16$ , system bandwidth  $B = 1$  MHz and QPSK/16QAM modulation. If no modulation scheme is specified in the simulation, it is considered to be the 16QAM variety. The channel is assumed to be of the exponential decaying power delay profile (PDP) [26] with power of the  $l$ -th path given as  $\Lambda(l) = \Lambda(0)e^{-\frac{l}{d}}$  where:

$$\Lambda(0) = \frac{1 - e^{-\frac{1}{d}}}{1 - e^{-\frac{L}{d}}}$$

is the power of the first multipath channel. Parameter  $d = \frac{\tau_{rms}}{T_s}$  is the normalized delay spread, where  $T_s$  is the sampling period and  $\tau_{rms}$  is the root mean squared (rms) delay of the channel. The number of multipaths is given by  $L = \frac{\tau_{max}}{T_s}$  where  $\tau_{max}$  is the maximum excess delay and is defined as  $\tau_{max} = \tau_{rms} \ln A$  with  $A$  being the ratio of non-negligible path power to first path power. In this paper, the value of  $A$  is taken as  $A = -40$  dB and normalized delay spread  $d = 1.5$ , giving the total number of multipaths of

Table 2  
Simulation parameters

Parameters	Value
Number of subcarriers	128
Number of FFT	128
Number of CP	16
Modulation type	QPSK/16QAM
System bandwidth	1 MHz
Subcarrier spacing	7.8125 kHz
Channel type	Exponential decaying PDP
Pilot spacing	8
Normalized delay spread	1.5
Number of multipath	14

$L = 14$ . The total number of pilots is considered as  $N_p = 16$  with pilot spacing of  $p_s = 1:8$ . All simulation parameters are listed in the Table 2. Perfect time and frequency synchronizations are assumed at the receiver side.

Figure 1 shows MSE performance with respect to SNR for the proposed LMMSE, classical LS and LMMSE methods with a normalized delay spread of  $d = 1.5$  and  $L = 14$ . The simulation results show that the LS method offers poorer MSE performance than the LMMSE method, due to the noise enhancement problem. It is observed that the MSE performance of the proposed LMMSE estimation method exactly matches that of the classical LMMSE method. This is due to the fact that, the proposed method is directly derived from the classical LMMSE method, without any approximations.

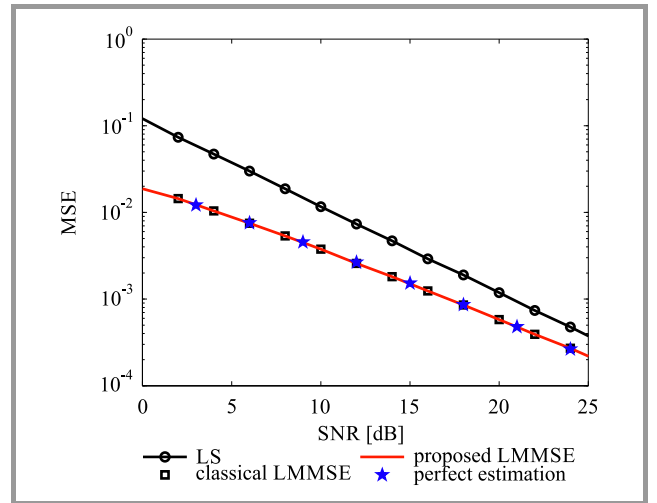


Fig. 1. Comparison of MSE vs SNR performance between the proposed LMMSE, classical LS and LMMSE channel estimation methods.

In order to analyze the effect of normalized delay spread  $d$  on the performance of various channel estimation methods, multiple values of  $d$  are taken into considerations, e.g.  $d = [0.3 \ 0.6 \ 0.9 \ 1.2 \ 1.5 \ 1.8]$ . This leads to the total number of multipath channels equaling  $L = [3 \ 6 \ 8 \ 12 \ 14 \ 16]$ . The MSE vs. normalized delay spread ( $d$ ) for various channel estimation methods is shown in Fig. 2. The result is obtained for pilot spacing of  $p_s = 8$  at 25 dB SNR. The simulation result shows that the performance of the proposed LMMSE approach exactly matches that of LMMSE, irrespective of the value of normalized delay spread  $d$ . It is also noticed that the performance of LS is close to that of the LMMSE method for low values of  $d$ . However, the performance gap increases with an increase in normalized delay spread value.

BER performance comparison of the proposed LMMSE, classical LS, LMMSE and perfect channel estimation methods for pilot spacing of  $p_s = 8$  is shown in the Fig. 3. The simulation results show that BER performance of the LS estimation method is poorer when compared with the LMMSE estimation method. Figure 3 that performance of the proposed LMMSE method is very close to that of

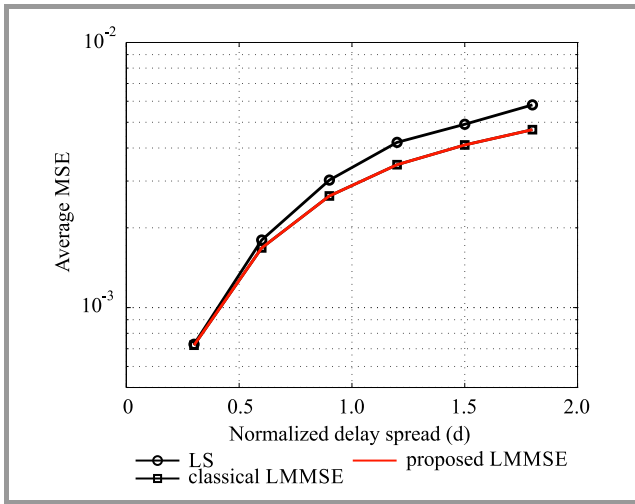


Fig. 2. MSE vs. normalized delay spread of the proposed LMMSE, classical LS and LMMSE channel estimation methods.

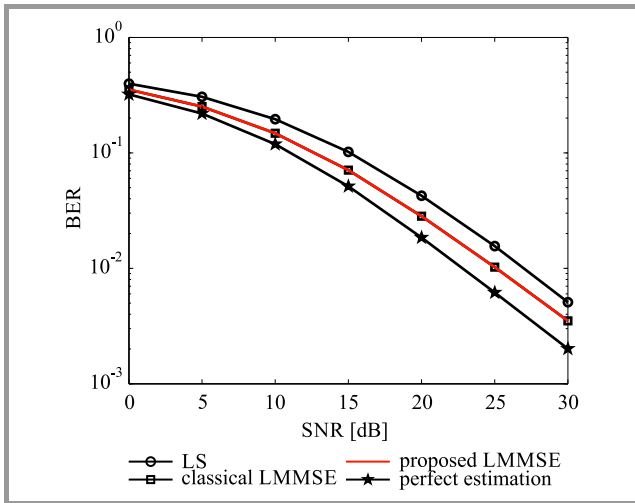


Fig. 3. BER vs. SNR performance comparison of the proposed LMMSE, classical LS, and LMMSE channel estimation methods for pilot spacing of  $p_s = 8$ .

the perfect estimation method, where it is assumed that complete channel state information (CSI) is known at the receiver side.

Comparison of BER vs. SNR performance of the various channel estimation methods with QPSK and 16QAM modulation for pilot spacing of  $p_s = 8$  is shown in Fig. 4. The simulation results show that the performance of QPSK modulated channel estimation methods outperforms that of the 16QAM modulated channel estimation methods. It is also observed that the performance gap between LMMSE and perfect estimation with QPSK modulation is narrower than compared with 16QAM modulation.

## 7. Conclusion

In this paper, an optimal low complexity DFT-based LMMSE channel estimation method is proposed for an

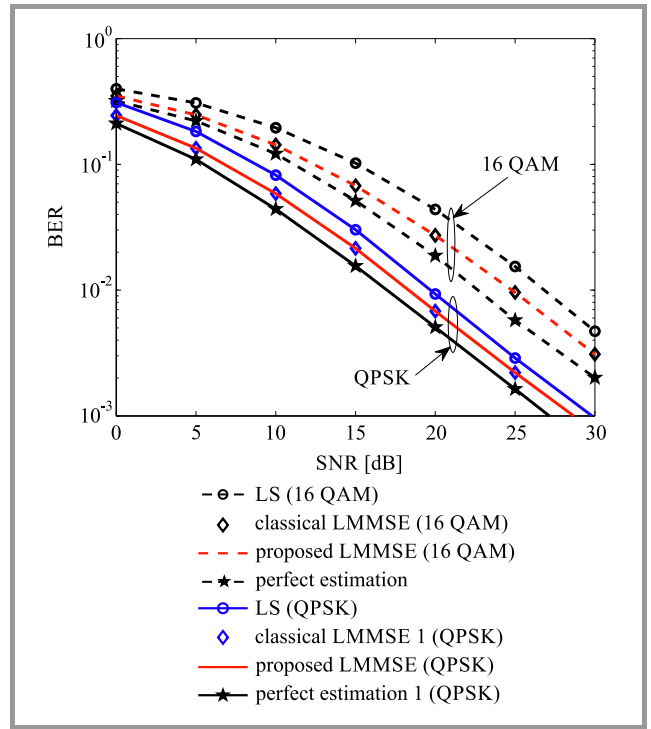


Fig. 4. BER vs. SNR performance comparison of the proposed LMMSE, LS, and LMMSE channel estimation methods with QPSK and 16QAM modulation for pilot spacing of  $p_s = 8$ .

OFDM system in the frequency selective channel. The closed form MSE expression is also derived to validate the proposed method. The proposed LMMSE method is compared with conventional channel estimation methods in terms of performance and computational complexity. Simulation results show that the proposed LMMSE channel estimation approach exactly matches the theoretical assumptions and achieves the same performance as the classical LMMSE channel estimation method, with computational complexity of  $L + N \log_2 N$  only. The limitation of the proposed LMMSE channel estimation technique is that it is not applicable to non-sample spaced channels, as it utilizes the DFT technique to estimate the channel.

## References

- [1] T. Hwang, C. Yang, G. Wu, S. Li, and G. Ye Li, "OFDM and its wireless applications: A survey", *IEEE Trans. on Veh. Technol.*, vol. 58, no. 4, pp. 1673–1694, 2009 (DOI: 10.1109/TVT.2008.2004555).
- [2] S. B. Y. Aimer, B. S. Bouazza, and C. Duvanaud, "Interleaving technique implementation to reduce PAPR of OFDM signal in presence of nonlinear amplification with memory effects", *J. of Telecommun. and Inform. Technol.*, no. 3, pp. 14–22, 2018 (DOI: 10.26636/jtit.2018.123517).
- [3] P. Vimala and G. Yamuna, "Pilot design for sparse channel estimation in orthogonal frequency division multiplexing systems", *J. of Telecommun. and Inform. Technol.*, no. 2, pp. 60–68, 2018 (DOI: 10.26636/jtit.2018.113817).
- [4] J.-J. Van De Beek, O. Edfors, M. Sandell, S. K. Wilson, and P. O. Borjesson, "On channel estimation in OFDM systems", in *Proc. of IEEE 45th Veh. Technol. Conf. Count. to the Wirel. Twenty-First Cent.*, Chicago, IL, USA, 1995, pp. 815–819 (DOI: 10.1109/VETEC.1995.504981).

- [5] M.-H. Hsieh and C.-H. Wei, "Channel estimation for OFDM systems based on comb-type pilot arrangement in frequency selective fading channels", *IEEE Trans. on Consumer Electron.*, vol. 44, no. 1, pp. 217–225, 1998 (DOI: 10.1109/30.663750).
- [6] C. M. B. P. Sure, "A survey on OFDM channel estimation techniques based on denoising strategies", *Int. J. of Engin. Sci. and Technol.*, vol. 20, no. 2, pp. 629–636, 2017 (DOI: 10.1016/j.jestch.2016.09.011).
- [7] X. L. Xiao Zhou, Zhun Ye, and C. Wang, "Channel estimation based on linear filtering least square in OFDM systems", *J. of Commun.*, vol. 11, no. 11, pp. 1005–1011, 2016 (DOI: 10.12720/jcm.11.11.1005-1011).
- [8] P. K. Pradhan, O. Faust, S. K. Patra, and B. K. Chua, "Channel estimation algorithms for OFDM systems", *Int. J. of Sig. and Imag. Syst. Engin.*, vol. 5, no. 4, pp. 267–273, 2012 (DOI: 10.1504/IJSISE.2012.050324).
- [9] E. Hari Krishna, K. Sivani, and K. A. Reddy, "New channel estimation method using singular spectrum analysis for OFDM systems", *Wirel. Pers. Commun.*, vol. 101, no. 4, p. 2193–2207, 2018 (DOI: 10.1007/s11277-018-5811-5).
- [10] V. Vasylyshyn, "Channel estimation method for OFDM communication system using adaptive singular spectrum analysis", in *Proc. IEEE 40th Int. Conf. on Electron. and Nanotechnol. ELNANO 2020*, Kyiv, Ukraine, 2020, pp. 884–887 (DOI: 10.1109/ELNANO50318.2020.9088787).
- [11] O. Edfors, M. Sandell, J.-J. Van de Beek, S. K. Wilson, and P. O. Borjesson, "OFDM channel estimation by singular value decomposition", *IEEE Trans. on Commun.*, vol. 46, no. 7, pp. 931–939, 1998 (DOI: 10.1109/26.701321).
- [12] V. Savaux, Y. Louët, and F. Bader, "Low-complexity approximations for LMMSE channel estimation in OFDM/OQAM", in *Proc. 23rd Int. Conf. on Telecommun. ICT 2016* Thessaloniki, Greece, 2016 (DOI: 10.1109/ICT.2016.7500464).
- [13] G. H. Golub and C. F. Van Loan, *Matrix Computations*, 3rd ed. The Johns Hopkins University Press, 1996 (ISBN: 9780801854149).
- [14] S. Ohno, S. Munesada, and E. Manasseh, "Low-complexity approximate LMMSE channel estimation for OFDM systems", in *Proc. of the 2012 Asia-Pacific Sign. and Inform. Process. Assoc. Ann. Summit and Conf. APSIPA 2012*, Hollywood, CA, USA, 2012 [Online]. Available: <https://ieeexplore.ieee.org/document/6411093>
- [15] N. Geng, X. Yuan, and L. Ping, "Dual-diagonal LMMSE channel estimation for OFDM systems", *IEEE Trans. on Sig. Process.*, vol. 60, no. 9, pp. 4734–4746, 2012 (DOI: 10.1109/TSP.2012.2202112).
- [16] L. Fang and D. Huang, "Neumann series expansion based LMMSE channel estimation for OFDM systems", *IEEE Communications Letters*, vol. 20, no. 4, pp. 748–751, 2016 (DOI: 10.1109/TSP.2012.2202112).
- [17] R. Xin, Z. Ni, S. Wu, L. Kuang, and C. Jiang, "Low-complexity joint channel estimation and symbol detection for OFDMA systems", *China Commun.*, vol. 16, no. 7, pp. 49–60, 2019 (DOI: 10.23919/JCC.2019.07.004).
- [18] A. Khelifi and R. Bouallegue, "An accurate and very low complexity LMMSE channel estimation technique for OFDM systems", *Wirel. Pers. Commun.*, vol. 88, no. 4, pp. 911–922, 2016 (DOI: 10.1007/s11277-016-3219-7).
- [19] A. Zaib and S. Khattak, "Structure-based low complexity MMSE channel estimator for OFDM wireless systems", *Wirel. Pers. Commun.*, vol. 97, no. 4, pp. 5657–5674, 2017 (DOI: 10.1007/s11277-017-4800-4).
- [20] K. Kavitha and S. Manikandan, "LMMSE channel estimation algorithm based on channel autocorrelation minimization for LTE-Advanced with adaptive guard interval", *Wirel. Pers. Commun.*, vol. 81, no. 3, pp. 1233–1241, 2015 (DOI: 10.1007/s11277-014-2181-5).
- [21] A. Munshi and S. Unnikrishnan, "Performance analysis of compressive sensing based LS and MMSE channel estimation algorithm", *J. of Commun. Softw. and Syst.*, vol. 17, no. 1, pp. 13–19, 2021 (DOI: 10.24138/jcomss.v17i1.1084).
- [22] H. Wu, "LMMSE channel estimation in OFDM systems: A vector quantization approach", *IEEE Commun. Lett.*, vol. 25, no. 6, pp. 1994–1998, 2021 (DOI: 10.1109/LCOMM.2021.3059776).
- [23] Y.-J. Kim and G.-H. Im, "Pilot-symbol assisted power delay profile estimation for MIMO-OFDM systems", *IEEE Commun. Lett.*, vol. 16, no. 1, pp. 68–71, 2012 (DOI: 10.1109/LCOMM.2011.110711.112047).
- [24] S. Coleri, M. Ergen, A. Puri, and A. Bahai, "Channel estimation techniques based on pilot arrangement in OFDM systems", *IEEE Trans. on Broadcast.*, vol. 48, no. 3, pp. 223–229, 2002 (DOI: 10.1109/TBC.2002.804034).
- [25] R. M. Gray, *Toeplitz and Circulant Matrices: A Review. Foundations and Trends in Communications and Information Theory*. Now Publishers Inc, 2006 (ISBN-13: 9781933019239).
- [26] Y. S. Cho, J. Kim, W. Y. Yang, and C. G. Kang, *MIMO-OFDM Wireless Communications with MATLAB*. Wiley, 2010 (DOI: 10.1002/9780470825631, ISBN: 9780470825617).



**Jyoti Prasanna Patra** received his Ph.D. and M.Tech. degrees from the National Institute of Technology Rourkela, India, in 2018 and 2012, respectively. He has completed his B.Tech. degree from BPUT University, Odisha, India, in 2008. He is currently working as an Associate Professor at the Department of Electronics and Com-

munication Engineering at Madanapalle Institute of Technology and Science, Madanapalle, Andhra Pradesh, India. His research interests focus on signal processing for wireless communication.

 <https://orcid.org/0000-0002-6470-2728>

E-mail: [jyotiprasannapatra@gmail.com](mailto:jyotiprasannapatra@gmail.com)

Madanapalle Institute of Technology and Science  
Madanapalle  
Andhra Pradesh, India



**Bibhuti Bhusan Pradhan** received his Ph.D. and M.Tech. degrees from the National Institute of Technology Rourkela, India, in 2018 and 2012, respectively. He has completed his B.Tech. degree from BPUT University, Odisha, India, in 2007. He is currently working as a Senior Assistant Professor at the Department of Electron-

ics and Communication Engineering at Madanapalle Institute of Technology and Science, Madanapalle, Andhra Pradesh, India. His research interests concentrate on performance analysis of wireless communication systems over fading channels.

 <https://orcid.org/0000-0001-6817-7505>

E-mail: [bibhutibhusanpradhan@gmail.com](mailto:bibhutibhusanpradhan@gmail.com)

Madanapalle Institute of Technology and Science  
Madanapalle  
Andhra Pradesh, India



**Poonam Singh** received her B.Tech. degree from University College of Engineering Burla, Odisha, India, in 1988 and M.Tech. degree from Regional Engineering College, Rourkela, India, in 1991. She completed her Ph.D. from the Indian Institute of Technology, Kharagpur, India. She is pres-

ently working as a Professor at the National Institute of Technology, Rourkela, India. She is a senior member of IEEE and a life member of ISTE. Her teaching and research interests focus on wireless communication systems, spread spectrum modulation, multicarrier systems, etc.

E-mail: [psingh@nitrkl.ac.in](mailto:psingh@nitrkl.ac.in)  
National Institute of Technology  
Rourkela  
Odisha, India

# An Investigation of the MIMO Space Time Block Code Based Selective Decode and Forward Relaying Network over $\eta$ - $\mu$ Fading Channel Conditions

Ravi Shankar<sup>1</sup>, V. V. Raghava Raman<sup>2</sup>, Kantilal Pitamber Rane<sup>3</sup>, Sarojini B. K.<sup>4</sup>, and Rahul Neware<sup>5</sup>

<sup>1</sup> Madanapalle Institute of Technology and Science, Madanapalle, India

<sup>2</sup> Aurora's Degree and PG College, Chikkadapally, Hyderabad, India

<sup>3</sup> Department of Electronics and Communication, K L University, Hyderabad, India

<sup>4</sup> Basaveshwar Engineering College, Bagalkot, Karnataka, India

<sup>5</sup> Høgskulen på Vestlandet, Bergen, Norway

<https://doi.org/10.26636/jtit.2022.150421>

**Abstract**—In this paper, we examine the end-to-end average pairwise error probability (PEP) and output probability (OP) performance of the maximum ratio combining (MRC) based selective decode and forward (S-DF) system over an  $\eta$ - $\mu$  scattering environment considering additive white Gaussian noise (AWGN). The probability distribution function (PDF) and cumulative distribution function (CDF) expressions have been derived for the received signal-to-noise (SNR) ratio and the moment generating function (MGF) technique is used to derive the novel closed-form (CF) average PEP and OP expressions. The analytical results have been further simplified and are presented in terms of the Lauricella function for coherent complex modulation schemes. The asymptotic PEP expressions are also derived in terms of the Lauricella function, and a convex optimization (CO) framework has been developed for obtaining optimal power allocation (OPA) factors. Through simulations, it is also proven that, depending on the number of multi-path clusters and the modulation scheme used, the optimized power allocation system was essentially independent of the power relation scattered waves from the source node (SN) to the destination node (DN). The graphs show that asymptotic and accurate formulations are closely matched for moderate and high SNR regimes. PEP performance significantly improves with an increase in the value of  $\eta$  for a fixed value of  $\mu$ . The analytical and simulation curves are in close agreement for medium-to-high SNR values.

**Keywords**—5G, MIMO, MRC, non-homogeneous fading channel, PEP, S-DF, SNR.

## 1. Introduction

With the explosive growth of cellular traffic, researchers are increasingly interested in improving performance of wireless networks in real-time propagation conditions. Therefore, they focus on the different systems, including massive multiple-input multiple-output (m-MIMO), device-to-

device (D2D) communication, spatial modulation (SM) techniques, machine-to-machine (M2M) communication, non-orthogonal multiple access (NOMA) systems, and cooperative wireless communications over real-time propagation environments [1]–[4].

The use of multiple-input-multiple-output (MIMO) networks over multipath fading links can significantly increase spectral efficiency (SE) and quality of service (QoS). However, installation of multiple antennas is not possible in the case of some wireless devices. As a result, space time block code (STBC) introduces the cooperative diversity (virtual MIMO) approach to mitigate multipath fading and to increase diversity gains (DGs). In a  $\frac{1}{2}$  transmit diversity system, Alamouti suggested in [4] that orthogonal space-time codes achieve DG levels that are comparable to those of MRC systems.

The increasing popularity of smartphones and tablets has recently accelerated the use of wireless local area networks (LAN). This means that a dense network of access points exists in apartments, buildings and public places, causing signal interference and increasing the time needed to transmit and receive data.

Cooperative communication is a very recent idea and stimulates the emergence of popular modern wireless communication systems, especially those characterized by high data rates or the fifth generation (5G) wireless communication systems. In 5G and beyond 5G wireless communication networks, cooperative communication schemes are seen as a practicable technique to expand network coverage while maintaining a high data rate [5]–[6]. Several developing applications have been implemented, including M2M networks, D2D networks, wireless sensor networks (WSNs) and vehicle-to-vehicle (V2V) 5G networks, to relay wireless networking. In a relaying network, the relay node (RN) receives the signal from the SN, manipulates it by

performing specific operations, e.g. some basic processing operations or complex and advanced signal processing operations that depend on the nature of the RN, and then it relays or forwards this signal to the DN.

In cooperative communication, the networks are divided into three popular categories: amplify-and-forward (AF), decode-and-forward (DF), and compress-and-forward (COF). The RNs decrypt incoming signals in DF systems and then forward the decoded signals back to the next RN, preventing noise spread. The AF protocol only amplifies the signal that is later forwarded to the next node. COF compresses, encodes and transmits received data to the next-hop device. However, the main drawbacks of the DF and AF approaches include noise amplification and erroneous signal propagation, respectively [7]–[8].

To fix the error propagation and noise amplification problem, the S-DF relaying protocol is considered in [9]–[11], under various fading channel conditions. In the case of S-DF relaying, the RN compares the threshold SNR with instantaneous SNR. If the threshold SNR is greater than instantaneous SNR, then the RN will remain idle. The authors examined a MIMO-STBC S-DF cooperative network under Rayleigh fading channel circumstances in [9]. The performance of the system is examined for OPA and equal power allocation (EPA) factors. The AF and S-DF protocols are compared, and the curves reveal that the S-DF protocol performs significantly better than the AF protocol. The line of sight (LOS) scenario was not considered in the Rayleigh fading channel conditions. In the case of wireless channels, both fast fading and shadowing, sometimes also known as small-scale fading and large-scale fading, have been observed. Statistical distributions, such as Rayleigh, Nakagami-m, and Weibull, have been proposed in the literature to characterize small-scale variations in the fading channel envelope [10]–[11]. The average PEP analysis of the MIMO-STBC S-DF relaying network across the extended Nakagami-m fading channel conditions was explored in [12]. Both LOS and non-line of sight (NLOS) propagation scenarios were considered by the authors. In [13], the authors examined the S-DF relaying technique under keyhole fading channel conditions. Performance under keyhole Nakagami-m and Nakagami-m fading channel circumstances is compared. Symbol error rate (SER) performance under keyhole Nakagami-m fading channel conditions is worse than that under Nakagami-m fading channel circumstances, as shown by the simulation curves. However, whereas articles [10]–[13] looked at MIMO-S-DF performance under frequency flat time-invariant fading, in real-time propagation conditions, the channel becomes frequency selective, owing to multipath fading, and time selective due to movement between the communicating nodes.

The authors of paper [14] examined PEP and OP performance of the S-DF relaying protocol under time selective fading channel circumstances. In their study, the authors of [15]–[16] considered poor channel state information (CSI) and calculated the OPA factors. The authors of [15]

examined OP and PEP performance of the MIMO STBC S-DF relaying network under time selective Nakagami-m fading channel circumstances, while accounting for poor CSI and node mobility. The results demonstrate that when node mobility increases, SER decreases considerably. The authors of [16] obtained the OP expression of the MIMO OSTBC and found the OPA factors under the time selective fading connections, while accounting for poor CSI. The PDF of the sum of i.i.d. gamma RVs and CDF is obtained and utilized for investigating performance of the cooperative communication system. To acquire the OPA factors, a mathematical framework is obtained. The results show that SN mobility has a higher influence than DN mobility on the average OP performance. As a result, cooperative systems are limited by an asymptotic error floor with a higher SNR value in other node mobility conditions. Simulation results show that the only ideal approach to distributing the power equally between the SN and RNs is possible when the SR fading link is stronger than the RD link.

However, none of those analyses considered non-homogeneous fading channel environments. Nonetheless, the documented performance and OPA experiments were conducted using Rician, Nakagami-m, and Nakagami-m fading channels. These fading channel models, as described in [9]–[15], are based on the concept of homogeneous scattering environments, which is not practical in most radio propagation scenarios, because the surfaces in the majority of spatial radio propagation environments are spatially correlated, as proven by previous research. The  $\eta$ - $\mu$  distribution, a generalized fading model used to give an especially precise fitting to genuine measurement data while also encompassing the well-known Rayleigh, Nakagami-m, and Hoyt distributions as specific instances, was proposed to solve this issue in [17]. The distribution was proven to have properly accommodated small-scale variations in the NLOS communication situations, where the two parameters designated  $\eta$  and  $\mu$  are defined and valid for two distinct forms which correspond to two physical models, as described in paper [17]. In addition, work [18] gives the PDF of the immediate SNR.

## 2. Related Work

In 5G networks, stochastic modeling and characterization of the wireless fading channel have a significant impact on bit error rate (BER) and OP performance. So, precise channel modeling is necessary for identifying 5G communication protocols and techniques that are efficient and cost-effective. However, the fading distributions described in the literature fail to take into consideration non-linearity of the medium.

Under non-homogeneous circumstances, such as  $\alpha$ - $\mu$ ,  $\kappa$ - $\mu$ , and  $\eta$ - $\mu$ , an exact OP calculation for diversity receivers was provided in [17]. Yacoub proposed  $\eta$ - $\mu$  fading in [17] as a generalized distribution to describe diverse fading situations. The  $\eta$ - $\mu$  distribution may also be used

to represent non-LOS situations. For the study of wireless communication networks, several researchers utilize the  $\eta$ - $\mu$  fading distribution.  $\eta$ - $\mu$  distribution also simulates generalized fading, such as Nakagami-m fading.

The MRC approach was chosen as one of the diversity receivers in [18], and a detailed performance study of the L-branch system over  $\eta$ - $\mu$  fading channels considering imperfect CSI was presented. The authors have investigated the OP and SER performance under  $\alpha$ - $\mu$  fading channel scenarios, considering 4-quadrature amplitude modulation (QAM) techniques. For mmWave fluctuating two-ray fading links, an SER investigation was performed in [19]. In [20], the authors derived the CF expression of the average SER and BER for M-ary cross QAM symbols with MRC diversity reception over i.i.d.  $\eta$ - $\mu$  fading links. Rectangular and cross QAM methods were also investigated in a similar manner in [21]. In [22], the net throughput for relaying users in a NOMA network over  $\kappa$ - $\mu$  shadowed fading channels was analytically evaluated.

In [23], the authors investigated OP and SER for  $\kappa$ - $\mu$  shadowing distribution, in an interference-limited scenario. In [24], the authors studied spatial modulation techniques over  $\alpha$ - $\mu$ ,  $\kappa$ - $\mu$ , and  $\eta$ - $\mu$  fading channel models. Using non-homogeneous channel distributions, the research conducted in [25]–[29] examined physical layer security and secrecy capacities for various system models. In [25], the authors examined secrecy capacity over  $\kappa$ - $\mu$  fading channels. In [26], the authors examine the secrecy capacity performance over  $\kappa$ - $\mu$  fading connections for MIMO networks [26]. To significantly improve on the results of the analysis performed in [26], a complete physical layer security study for MIMO networks was given in article [27], under the  $\eta$ - $\mu$  and  $\lambda$ - $\mu$  fading scenarios.

As an alternative, in [28], the authors investigated secrecy capacity for wireless communication networks under  $\alpha$ - $\mu$  fading conditions. As it was the case in [25]–[29], they also examined physical layer security for a  $\alpha$ - $\kappa$ - $\mu$  and  $\alpha$ - $\eta$ - $\mu$  fading scenarios, with SISO fading links. Three parameters of the fading models were examined as well, namely  $\alpha$ ,  $\eta$ ,  $\mu$  or  $\alpha$ ,  $\eta$ ,  $\mu$ .

In papers [30]–[33], the authors examined AF, best relay selection (BRS) DF, and cognitive AF (CAF) relaying networks. In [30], the authors verified SER performance of dual hop (DH) CAF relaying networks over  $\eta$ - $\mu$  fading channels. Under mixed  $\kappa$ - $\mu$  and  $\eta$ - $\mu$  circumstances, in [31], the authors investigated  $\alpha$ - $\mu$  fading channels. Mixed-fading links were utilized to evaluate performance of the BRS approach for D2D wireless networks [32].

In the literature, only the well-known AWGN noise was taken into account when evaluating the performance of different system models across non-homogeneous fading channels. The  $\alpha$ - $\eta$ - $\mu$  distribution is a fading distribution used in N-LOS communications to characterize small-scale variations in a faded signal. In the  $\alpha$ - $\eta$ - $\mu$  distribution, the fading signal is composed of numerous multipath clusters traveling across a non-homogeneous medium. Non-linearity of the propagation medium and the number of

clusters are represented by the exponents  $\alpha$  and  $\mu$ , respectively. The  $\alpha$ - $\mu$  distribution may be used to produce Rayleigh, Nakagami-m, and Weibull fading channel distributions. To assess performance of the system through multiple fading models, the  $\alpha$ - $\mu$  model can be employed. Paper [34] indicates that several common decaying distributions are generated in a precise manner by  $\alpha$ - $\mu$ ,  $\alpha$ - $\mu$ , and  $\mu$  values, including  $\eta$ - $\mu$ ,  $\alpha$ - $\mu$ ,  $\lambda$ - $\mu$ , Nakagami-m, exponential, Weibull, one-sided Gaussian, Hoyt, and Rayleigh. The  $\alpha$ - $\eta$ - $\mu$  distribution may also be used to approximate the Rice and lognormal distributions. The authors of [34] looked at BER performance of the DF relaying network under  $\alpha$ - $\mu$  fading channel conditions. The end-to-end SNR's PDF, CDF, and MGF were calculated in this work. CF expressions for the system's average OP, net throughput, and average BER were calculated as well. The resulting expressions may be used to compare the performance of multi-hop relaying networks with other well-known fading channel models, by simply inserting the relevant values for the  $\alpha$  and  $\mu$  parameters. In [35], the authors looked at BER performance of a DH AF beamforming network with multiple antennas, only at the DN and SNs and with both hops subjected to  $\kappa$ - $\mu$  fading channel circumstances.

The  $\kappa$ - $\mu$  fading channel model is of the generalized variety and may properly represent realistic fast fading in LOS scenarios. It also includes specific cases for Rayleigh, Rician, and Nakagami-m scenarios. In article [36], the authors derived the CF expressions of the OP, average BER, and net throughput for a MIMO STBC S-DF relaying network over  $\kappa$ - $\mu$  fading channel conditions. They analyzed those fading links that are subjected to i.i.d.  $\kappa$ - $\mu$  fading conditions. According to simulation results, the stronger LOS component increases BER performance. It has been demonstrated that the in the case of LOS scenarios, MIMO STBC S-DF relaying systems can function effectively, and BER performance improves significantly. Through MC simulations, it was determined that theoretical findings closely matched the actual results, thus validating the derivations produced. In [37], the authors investigated 5G heterogeneous cellular systems operating over  $\kappa$ - $\mu$  shadowed fading channels. Furthermore, asymptotic outcomes for BER, net throughput and OP were obtained in simpler forms of fundamental functions, making the system's behavior and the influence of channel parameters understandable. These theoretical outcomes are general and they may be used to simulate a variety of asymmetric and symmetric fading scenarios, including Nakagami-m, Rayleigh, Rician, and mixed  $\kappa$ - $\mu$  fading connections. In [38], the authors researched a DH AF cooperative communications system, where RD and SR fading links are subject to mixed  $\eta$ - $\mu$  and  $\kappa$ - $\mu$  fading channel conditions. The RN is assumed to be fixed gain and perfect CSI conditions are considered. The modeling of realistic DH transmissions is enabled by the use of such mixed  $\eta$ - $\mu$  and  $\kappa$ - $\mu$  fading channels. It is possible to obtain accurate theoretical expressions for OP and for average BER of various complex modulation techniques, in the form of fast converging infinite series. In [39], the

authors derived a mathematical framework for investigating BER and channel capacity of the relaying network over an inverse gamma shadowing fading channel. Firstly, the paper examined the advantages of inverse gamma over gamma fading and log-normal fading models. Novel PDF and CDF expressions were derived and the analytical results for BER and channel capacity of selection combining diversity are presented.

In [40], the authors investigated channel capacity over the inverse gamma and  $\eta$ - $\mu$  composite fading channels. To achieve that aim, precise theoretical expressions for net throughput were derived, along with simple tight-bound representations. Additionally, simple approximation formulas for the high SNR regime were presented. Next, net throughput was examined under various shadowing, multipath fading, and delay constraints scenarios. The simulation results show that as the multipath fading and shadowing parameters decrease, or the delay restriction rises, the attainable SE decreases significantly. The authors of [41] derived the CDF of the sum of the  $\alpha$ - $\mu$ ,  $\kappa$ - $\mu$ , and  $\eta$ - $\mu$  RVs in the context of rare event Monte Carlo simulations. A less complex and extremely efficient sampling scheme was proposed to obtain higher diversity gains. The main consequence of this approach is the relative BER of the suggested estimators that are constrained by certain limits. The authors estimated the OP of multibranch MRC and equal gain diversity receivers over  $\alpha$ - $\mu$ ,  $\kappa$ - $\mu$ , and  $\eta$ - $\mu$  faded links of the kind articles [36]–[41] with great accuracy.

In [42], the authors derived PDF of the instantaneous SNR at the receiver side and investigated BER and asymptotic BER performance of uplink SIMO networks with AWGN noise over the non-homogeneous fading conditions, such as  $\eta$ - $\mu$ ,  $\lambda$ - $\mu$ , and  $\kappa$ - $\mu$ . The OP and BER performances is shown for several fading parameter settings, receiver antenna counts, modulation methods, and noise type combinations to illustrate these points. These simulations are then used to verify correctness of the analytical frameworks suggested for the systems concerned.

In [43], the authors investigated a DF-based MIMO network over the  $\kappa$ - $\mu$ ,  $\eta$ - $\mu$ , and mixed  $\kappa$ - $\mu$  and  $\eta$ - $\mu$  fading scenarios. After applying the MGF scheme, they derived novel expressions of BER, considering the M-ary PSK modulation symbols. Additionally, for high SNR, asymptotic BER expressions were examined to obtain OPA factors at the SN and RNs. The DO expression is derived for various types of non-homogeneous fading channel distributions. As far as OPAs are concerned, the impact of the SD distance on the performance of a fixed-relay network was analyzed.

In earlier studies concerned with the performance of different system models over non-homogeneous fading channels, including those cited above, the well-known AWGN type of channel was investigated only. Many outdoor, indoor, and underwater applications make the AWGN distribution problematic. Also, it is not taken advantage of in ultra-wideband wireless networks to reduce impulsive noise and multiuser interference [44]–[45]. However, as far as we

know, no work has been devoted to PEP performance of the MIMO STBC network over  $\eta$ - $\mu$ .

Against this background we propose, in this paper, some novel expressions of PEP for the MIMO STBC network by considering non-homogeneous channels – not only to eliminate the disadvantages of the AWGN model but also to present PEP performance of the MIMO STBC network with AWGN over  $\eta$ - $\mu$  fading channels.

The main contributions of our paper include the following:

- performance of the MIMO STBC network over  $\eta$ - $\mu$  fading channels is theoretically analyzed in terms of PEP;
- approximate CF average PEP is derived, using MGF, are derived for the  $\eta$ - $\mu$  fading conditions under consideration;
- asymptotic PEP expressions of MIMO STBC networks over non-homogeneous channels are analyzed and compared with approximate results;
- CO framework is developed for finding DO and for identifying optimal source-relay power allocation factors;
- in order to validate the theoretical analysis, extensive computer simulations are performed. Simulations fully agree with our numerical results obtained in the course of the proposed analysis.

The mathematical expressions discussed in this work are denoted by the following notations. The Lauricella function and the Euclidean norm are represented by  $F_A^{(1)}$  and  $\|X\|_F$ , respectively. The conjugate transpose, absolute value, and trace of matrix  $X$  are represented by  $X^H$ ,  $|X|$ , and  $\text{trace}(X)$ , respectively.  $E\{\cdot\}$  is the expectation operator, and  $J_0\{\cdot\}$  denotes the 1st kind and 0th order Bessel function. The gamma function and the lower incomplete gamma function are represented by  $\Gamma(\cdot)$  and  $\gamma(\cdot, \cdot)$ , respectively.  $P(X > u)$  denotes the chance that a given value of a standard normal random variable  $X$  is larger than a specified value  $u$ .

The rest of the paper is organized as follows. The model of a MIMO-STBC-based S-DF relaying system over  $\eta$ - $\mu$  fading channel conditions is presented in Section 2. Section 3 derives the per-block average PEP, OP, asymptotic error floor, and asymptotic PEP expressions for the MIMO-STBC over  $\eta$ - $\mu$  fading channel conditions. Section 4 presents simulation outcomes, while Section 5 concludes the paper.

### 3. System Model

Consider a MIMO-STBC S-DF relaying network and let  $S \in C^{K \times \phi}$  denote the Alamouti STBC code-word matrix transmitted from the SN. The MIMO-STBC-based S-DF network is equipped with  $K$  number of antennas over the  $\phi$  time slots. The SN transmits the  $S \in C^{K \times \phi}$  codeword to the DN and RN simultaneously. The codewords received at

the DN and RN are represented as  $B_{SD} \in \mathbb{C}^{K_D \times \varphi}$  and  $B_{SR} \in \mathbb{C}^{K \times \varphi}$ , respectively. Figure 1 is a schematic representation of the S-DF relaying protocol over  $\eta$ - $\mu$  fading channel conditions.

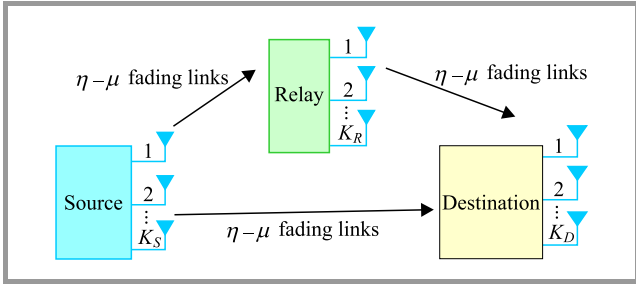


Fig. 1. Schematic representation of the S-DF relaying protocol over  $\eta$ - $\mu$  fading channel conditions.

Since the Alamouti STBC codeword is considered at both the RN and SN, the corresponding data rate will be the same and, hence, we are considering  $K_S = K_R = K$ . The received  $B_{SD} \in \mathbb{C}^{K_D \times \varphi}$  and  $B_{SR} \in \mathbb{C}^{K \times \varphi}$  codewords can be expressed as [18]–[20]:

$$B_{SD} = \sqrt{\frac{\Phi_0}{K}} Z_{SD} S + \Pi_{SD}, \quad (1)$$

$$B_{SR} = \sqrt{\frac{\Phi_0}{K}} Z_{SR} S + \Pi_{SR}, \quad (2)$$

where  $Z_{SD} \in \mathbb{C}^{K_D \times K}$  and  $Z_{SR} \in \mathbb{C}^{K \times K}$  represent the fading channel matrices between the SD and SR fading links, respectively.  $\Phi_0$  represents the power transmitted from the SN. Matrices  $\Pi_{SD}$  and  $\Pi_{SR}$  consist of AWGN noise samples at the DN and RN, respectively. Each noise sample is modeled as  $CN(0, N_0)$ , i.e. complex circularly symmetric AWGN with zero mean and  $K_0$  variance. These channel matrices consist of the  $\eta$ - $\mu$  faded channel coefficients with PDF [20]–[22]:

$$pdf_{\kappa_i}(\kappa_i) = \frac{2\sqrt{\pi}\mu_i^{\mu_i+\frac{1}{2}}z_i^{\mu_i}\bar{\kappa}_i^{\mu_i-\frac{1}{2}}}{\Gamma(\mu_i)Z_i^{\mu_i-\frac{1}{2}}\bar{\kappa}_i^{\mu_i+\frac{1}{2}}} e^{-\frac{2\mu_i z_i \kappa_i}{\bar{\kappa}_i}} \times I_{\mu_i-\frac{1}{2}}\left(\frac{2\mu_i Z_i \kappa_i}{\bar{\kappa}_i}\right) \in \{SD, SR\}, \quad (3)$$

where  $\kappa_i$  is the instantaneous SNR and  $\bar{\kappa}_i = \frac{\Phi_0 v_{jn}^2 \delta_i^2}{4KK_0}$  denotes the average SNR. The average channel gain is represented as  $\delta_i^2$ ,  $Z_i$  and  $z_i$  are the functions of fading parameters  $\eta_i$  defined in [22] and  $\mu_i$  is the fading parameter.  $v_{jn}$  denotes the singular values (SVs) obtained after performing the singular value decomposition (SVD) of the codeword difference matrix  $S_0 - S_j$  and  $I_x(\cdot)$  is the modified Bessel function of the first kind and order  $x$ . At the RN, S-DF protocol is employed and the RN will forward the signal received from the SN when the received instantaneous SNR will be greater than the threshold SNR. The codeword

forwarded from the RN to the DN, denoted by  $B_{RD} \in \mathbb{C}^{K_D \times \varphi}$  is expressed as:

$$B_{RD} = \sqrt{\frac{\Phi_1}{K}} Z_{RD} S + \Pi_{RD}, \quad (4)$$

where  $\Phi_1$  represents the power transmitted at the RN. The MIMO channel matrix  $Z_{RD}$  consists of  $\eta$ - $\mu$  distributed fading channel coefficients with PDF as:

$$pdf_{\kappa_{RD}}(\kappa_{RD}) = \frac{2\sqrt{\pi}\mu_{RD}^{\mu_{RD}+\frac{1}{2}}z_{RD}^{\mu_{RD}}\bar{\kappa}_{RD}^{\mu_{RD}-\frac{1}{2}}}{\Gamma(\mu_{RD})Z_{RD}^{\mu_{RD}-\frac{1}{2}}\bar{\kappa}_{RD}^{\mu_{RD}+\frac{1}{2}}} e^{-\frac{2\mu_{RD}z_{RD}\kappa_{RD}}{\bar{\kappa}_{RD}}} \times I_{\mu_{RD}-\frac{1}{2}}\left(\frac{2\mu_{RD}Z_{RD}\kappa_{RD}}{\bar{\kappa}_{RD}}\right), \quad (5)$$

where  $Z_{RD}$  and  $z_{RD}$  are the functions of fading parameters  $\eta_{RD}$  defined in [22] and  $\mu_{RD} > 0$  is the fading parameter.  $\Pi_{RD}$  matrices at the destination corresponding to the transmission from RN, consist of noise samples with zero mean and variance equal to  $\frac{K_0}{2}$  (per dimension).

## 4. PEP Analysis of MIMO-STBC S-DF Relaying Protocol

### 4.1. PEP Analysis

We commence our analysis by deriving the average PEP expression for the MIMO-STBC (single relay system), as shown in Fig. 1. Let  $C = \{S_j\}$  represent the codeword set, where codeword matrix  $S_j \in \mathbb{C}^{K \times \varphi}$  and  $1 \leq j \leq |C|$ , where  $|C|$ , represents the number of elements of the codeword set  $C$ . The end-to-end PEP of the erroneous event corresponding to  $S_0 \in \mathbb{C}^{K \times \varphi}$  being confused for the codeword  $S_j \in \mathbb{C}^{K \times \varphi}$  at the RN, where  $j \neq 0$ , conditioned on the channel matrix  $Z_{SR}$ , is expressed as [23]:

$$P_{S \rightarrow R}(S_0 \rightarrow \frac{S_j}{Z_{SR}}) = Q(\sqrt{\kappa_{SR}}), \quad (6)$$

where  $\kappa_{SR} = \frac{\Phi_0 \|Z_{SR}(S_0 - S_j)\|_F^2}{2KK_0}$  denotes the instantaneous SNR for SR fading link,  $S_0 \rightarrow S_j$  represents the erroneous event and  $P_{S \rightarrow R}$  represents the error probability for the SN to RN transmission. Let the SVD of the codeword difference matrix  $S_0 - S_j$  be represented as  $S_0 - S_j = U_j \Lambda_j V_j^H$ , where  $U_j \in \mathbb{C}^{K \times K} = I_K$ , and the diagonal matrix  $\Lambda_j \in \mathbb{R}^{K \times K}$  be represented as [23]:

$$\Lambda_j = \begin{bmatrix} v_{j,1} & 0 & 0 & \dots & 0 \\ 0 & v_{j,2} & 0 & \dots & 0 \\ 0 & 0 & v_{j,3} & \dots & 0 \\ \dots & \dots & \dots & \dots & \dots \\ 0 & 0 & 0 & \dots & v_{j,K} \end{bmatrix}_{K \times K}. \quad (7)$$

It contains the positive SVs  $v_{j,1}, v_{j,2}, \dots, v_{j,K}$  of the codeword difference matrix. The  $V_j^H \in \mathbb{C}^{\varphi \times K}$  matrix contains orthogonal row vectors which form a basis for the row space of the difference matrix  $S_0 - S_j$ , and satisfying the property  $V_j V_j^H = I_K$ . The Frobenius norm  $\|Z_{SR}(S_0 - S_j)\|_F^2$  can therefore be simplified as [23]:

Using  $S_0 - S_j = U_j \Lambda_j V_j^H$  in the above expression, the  $\|Z_{SR}(S_0 - S_j)\|_F^2$  can be expressed as:

$$\begin{aligned} \|Z_{SR}(S_0 - S_j)\|_F^2 &= \text{Tr} \{ Z_{SR} U_j \Lambda_j V_j^H V_j \Lambda_j U_j^H Z_{SR}^H \} = \\ &= \text{Tr} \{ Z_{SR} U_j \Lambda_j^2 U_j^H Z_{SR}^H \} = \text{Tr} \{ \Lambda_j^2 \tilde{Z}_{SR} \tilde{Z}_{SR}^H \} = \\ &= \sum_{n=1}^K v_{jn}^2 \sum_{\tilde{n}=1}^K |\tilde{z}_{\tilde{n},n}|^2, \end{aligned} \quad (8)$$

where coefficient  $\tilde{z}_{\tilde{n},n}$  is the  $(\tilde{n}, n)$  entry of matrix  $\tilde{Z}_{SR} = Z_{SR} U_j$  for  $1 \leq \tilde{n}, n \leq K$ . Therefore, the above expression for the PEP conditioned on the  $Z_{SR}$  can be simplified by substituting this expression for  $\|Z_{SR}(S_0 - S_j)\|_F^2$  as [20]:

$$P_{S \rightarrow R}(S_0 \rightarrow S_j) = Q \left( \sqrt{\frac{\Phi_0 \sum_{n=1}^K v_{jn}^2 \sum_{\tilde{n}=1}^K |\tilde{z}_{\tilde{n},n}|^2}{2KK_0}} \right). \quad (9)$$

Further, it can be readily seen that the gain  $|\tilde{z}_{\tilde{n},n}|^2$  is  $\eta - \mu$  distributed. The MGF is expressed as [20]–[22]:

$$\begin{aligned} MGF_{\kappa_{\eta-\mu}} \left( \frac{g_{PSK}}{\sin^2(\theta)} \right) &= \\ &= \left( \frac{4\mu_{SR}^2 z_{SR}}{\left[ 2(z_{SR} - Z_{SR})\mu_{SR} + \frac{g_{PSK} \bar{\kappa}_{SR}}{\sin^2(\theta)} \right] \left[ 2(z_{SR} + Z_{SR})\mu_{SR} + \frac{g_{PSK} \bar{\kappa}_{SR}}{\sin^2(\theta)} \right]} \right)^{\mu_{SR}}, \end{aligned} \quad (10)$$

where  $\bar{\kappa}_{SR} = \frac{\Phi_0 v_{jn}^2 \delta_{SR}^2}{4KK_0}$  denotes the average SNR and  $g_{PSK} = \sin^2(\frac{\pi}{M})$ .

$$\begin{aligned} P_{S \rightarrow R}(S_0 \rightarrow S_j) &= \\ &= \frac{1}{\pi} \int_0^{\frac{\pi}{2}} \frac{(4\mu_{SR}^2 z_{SR})^{\mu_{SR}} \left[ 2(z_{SR} - Z_{SR})\mu_{SR} + \frac{g_{PSK} \bar{\kappa}_{SR}}{\sin^2(\theta)} \right]^{-\mu_{SR}}}{\left[ 2(z_{SR} + Z_{SR})\mu_{SR} + \frac{g_{PSK} \bar{\kappa}_{SR}}{\sin^2(\theta)} \right]^{\mu_{SR}}} d\theta, \end{aligned} \quad (11)$$

The solution of  $P_{S \rightarrow R}(S_0 \rightarrow S_j)$  is as follows. Let  $\cos^2(\theta) = t$ . This will yield:

$$\sin^2(\theta) = 1 - \cos^2(\theta) = 1 - t, \quad (12)$$

$$-2 \cos(\theta) \sin(\theta) d\theta = dt, \quad (13)$$

The upper and lower limits of the integral will become 0 and 1, respectively. Also,  $d\theta$  will become:

$$d\theta = \frac{-dt}{2\sqrt{t}\sqrt{1-t}}. \quad (14)$$

Then  $P_{S \rightarrow R}(S_0 \rightarrow S_j)$  can be expressed as:

$$\begin{aligned} P_{S \rightarrow R}(S_0 \rightarrow S_j) &= \\ &= \frac{2^{2\mu_{SR}} (4\mu_{SR}^2 z_{SR})^{\mu_{SR}}}{2\pi \left[ 4(z_{SR} - Z_{SR})\mu_{SR} + 2\bar{\kappa}_{SR} \right]^{\mu_{SR}} \left[ 4(z_{SR} + Z_{SR})\mu_{SR} + 2\bar{\kappa}_{SR} \right]^{\mu_{SR}}} \times \\ &= \int_0^1 \frac{t^{-\frac{1}{2}} (1-t)^{2\mu_{SR}-\frac{1}{2}} dt}{\left[ 1 - \frac{4(z_{SR} - Z_{SR})\mu_{SR} t}{4(z_{SR} - Z_{SR}) + 2\bar{\kappa}_{SR}} \right]^{\mu_{SR}} \left[ 1 - \frac{4(z_{SR} + Z_{SR})\mu_{SR} t}{4(z_{SR} + Z_{SR}) + 2\bar{\kappa}_{SR}} \right]^{\mu_{SR}}}, \end{aligned} \quad (15)$$

$$\begin{aligned} P_{S \rightarrow R}(S_0 \rightarrow S_j) &= \\ &= M_{\kappa_{SR}}(1) \int_0^1 \frac{t^{-\frac{1}{2}} (1-t)^{2\mu_{SR}-\frac{1}{2}} dt}{\left[ 1 - \frac{4(z_{SR} - Z_{SR})\mu_{SR} t}{4(z_{SR} - Z_{SR}) + 2\bar{\kappa}_{SR}} \right]^{\mu_{SR}} \left[ 1 - \frac{4(z_{SR} + Z_{SR})\mu_{SR} t}{4(z_{SR} + Z_{SR}) + 2\bar{\kappa}_{SR}} \right]^{\mu_{SR}}}, \end{aligned} \quad (16)$$

where

$$MGF_{\kappa_{SR}}(s) = \frac{(4\mu_{SR}^2 z_{SR})^{\mu_{SR}}}{\left[ 2(z_{SR} - Z_{SR})\mu_{SR} + s\bar{\kappa}_{SR} \right]^{\mu_{SR}} \left[ 2(z_{SR} + Z_{SR})\mu_{SR} + s\bar{\kappa}_{SR} \right]^{\mu_{SR}}}. \quad (17)$$

The Appell hypergeometric function of two variables is expressed as [29]:

$$\begin{aligned} F_A^{(1)}(\tau; \vartheta, \vartheta'; \Xi; \dagger; \diamond) &= \\ &= \frac{\Gamma(\Xi)}{\Gamma(\tau)\Gamma(\Xi-\tau)} \int_0^1 t^{\tau-1-\frac{1}{2}} (1-t)^{\Xi-\tau-1} (1-tx)^{-\vartheta} (1-ty)^{-\vartheta'} dt. \end{aligned} \quad (18)$$

Comparing Eq. (17) with Eq. (18) we get:

$$\tau = \frac{1}{2}, \quad \vartheta = 1, \quad \vartheta' = 1, \quad \Xi = 2\mu_{SR} + 1, \quad (19)$$

$$\dagger = \frac{4(z_{SR} - Z_{SR})\mu_{SR}}{4(z_{SR} + Z_{SR})\mu_{SR} + 2\bar{\kappa}_{SR}}, \quad (20)$$

and

$$\diamond = \frac{4(z_{SR} + Z_{SR})\mu_{SR}}{4(z_{SR} + Z_{SR})\mu_{SR} + 2\bar{\kappa}_{SR}}. \quad (21)$$

Therefore,  $P_{S \rightarrow R}(S_0 \rightarrow S_j)$  can be expressed as:

$$\begin{aligned} P_{S \rightarrow R}(S_0 \rightarrow S_j) &= \\ &= \frac{1}{2\pi} MGF_{\kappa_{SR}}(1) \frac{\Gamma(\frac{1}{2})\Gamma(2\mu_{SR} + \frac{1}{2})}{\Gamma(2\mu_{SR} + 1)} \times \\ &= F_A^{(1)} \left( \frac{1}{2}; 1, 2\mu_{SR} + 1; \frac{4(z_{SR} - Z_{SR})\mu_{SR}}{4(z_{SR} - Z_{SR})\mu_{SR} + 2\bar{\kappa}_{SR}}; \right. \\ &\quad \left. \frac{4(z_{SR} + Z_{SR})\mu_{SR}}{4(z_{SR} + Z_{SR})\mu_{SR} + 2\bar{\kappa}_{SR}} \right). \end{aligned} \quad (22)$$

The overall possible space-time block-code codeword's  $S_j \in C$ , the upper bound of  $P_{S \rightarrow R}(S_0 \rightarrow S_j)$  is expressed as:

$$\bar{P}_{S \rightarrow R} \leq \sum_{S_j \in C, S_j \neq X_0} P_{S \rightarrow R}(S_0 \rightarrow S_j). \quad (23)$$

With a similar procedure applied, the average PEP for the SD fading link is expressed as:

$$\begin{aligned} \bar{P}_{S \rightarrow D} &= \frac{1}{2\pi} MGF_{\kappa_{SD}}(1) \frac{\Gamma(\frac{1}{2})\Gamma(2\mu_{SD} + \frac{1}{2})}{\Gamma(2\mu_{SD} + 1)} \times \\ &= F_A^{(1)} \left( \frac{1}{2}; 1, 2\mu_{SD} + 1; \frac{4(z_{SD} - Z_{SD})\mu_{SD}}{4(z_{SD} - Z_{SD})\mu_{SD} + 2\bar{\kappa}_{SD}}; \right. \\ &\quad \left. \frac{4(z_{SD} + Z_{SD})\mu_{SD}}{4(z_{SD} + Z_{SD})\mu_{SD} + 2\bar{\kappa}_{SD}} \right). \end{aligned} \quad (24)$$

Let  $\tilde{z}_{in}^{(SD)}, \tilde{z}_{in}^{(RD)}$  represent the  $\eta$ - $\mu$  fading channel coefficients corresponding to the effective SD and RD matrices  $\tilde{Z}_{SD} = Z_{SD}U_i$  and  $\tilde{Z}_{RD} = Z_{RD}U_i$ , respectively. For erroneous event  $S_0 \rightarrow S_i$  at the DN, when the RN decodes all the data symbols transmitted by the SN during the first signaling phase successfully, conditioned on the SD and RD channel matrices  $\tilde{Z}_{SD}, \tilde{Z}_{RD}$ ,  $P_S$  is expressed below:

$$P_{S \rightarrow D, R \rightarrow D}(S_0 \rightarrow S_i, \tilde{Z}_{SD}) = Q \left( \sqrt{\frac{\Phi_0 \sum_{n=1}^K v_{in}^2 \sum_{l=1}^{K_D} |\tilde{z}_{l,n}^{(SD)}|^2}{2KK_0} + \frac{\Phi_1 \sum_{n=1}^K v_{in}^2 \sum_{l=1}^{K_D} |\tilde{z}_{l,n}^{(RD)}|^2}{2KK_0}} \right). \quad (25)$$

The average PEP for the cooperation mode is:

$$\tilde{E}_{\tilde{Z}_{SD}, \tilde{Z}_{RD}} \left\{ Q \left( \sqrt{\frac{\Phi_0 \sum_{n=1}^K v_{in}^2 \sum_{l=1}^{K_D} |\tilde{z}_{l,n}^{(SD)}|^2}{2KK_0} + \frac{\Phi_1 \sum_{n=1}^K v_{in}^2 \sum_{l=1}^{K_D} |\tilde{z}_{l,n}^{(RD)}|^2}{2KK_0}} \right) \right\} = \frac{1}{\pi} \int_0^{\frac{\pi}{2}} \left( \frac{4\mu_{SD}^2 z_{SD} (2(z_{SD} + Z_{SD})\mu_{SD} + g_{PSK} \bar{\kappa}_{SD} / \sin^2(\theta))^{-1}}{(2(z_{SD} - Z_{SD})\mu_{SD} + g_{PSK} \frac{\bar{\kappa}_{SD}}{\sin^2(\theta)})} \right)^{\mu_{SD}} \times \left( \frac{4\mu_{RD}^2 z_{RD} (2(z_{RD} + Z_{RD})\mu_{RD} + g_{PSK} \frac{\bar{\kappa}_{RD}}{\sin^2(\theta)})^{-1}}{(2(z_{RD} - Z_{RD})\mu_{RD} + g_{PSK} \frac{\bar{\kappa}_{RD}}{\sin^2(\theta)})} \right)^{\mu_{RD}} d\theta. \quad (26)$$

After performing some algebraic manipulations, the expression can be represented in terms of a generalized Lauricella hypergeometric function  $F_D^{(n)}(\cdot)$  of  $n$  variables [24] as:

$$P_{S \rightarrow D, R \rightarrow D}(S_0 \rightarrow S_i) = \frac{\nabla_{MRC}(g_{PSK})\Gamma(2\mu_{SD} + 2\mu_{RD} + \frac{1}{2})}{2\sqrt{\pi}\Gamma(2\mu_{SD} + 2\mu_{RD} + \frac{1}{2})} \times F_D^{(4)} \left[ 2\mu_{SD} + 2\mu_{RD} + \frac{1}{2}; \mu_{SD}, \mu_{SD}, \mu_{RD}; \mu_{RD}; 2\mu_{SD} + 2\mu_{RD} + 1; \frac{1}{A_1}, \frac{1}{A_2}, \frac{1}{B_1}, \frac{1}{B_2} \right], \quad (27)$$

where

$$\nabla_{MRC}(g_{PSK}) = \left[ \frac{4\mu_{SD}^2 (z_{SD}^2 - Z_{SD}^2)}{g^2_{PSK} \bar{\kappa}_{SD}^2} \right]^{\mu_{SD}} \times \left[ \frac{4\mu_{RD}^2 (z_{RD}^2 - Z_{RD}^2)}{g^2_{PSK} \bar{\kappa}_{RD}^2} \right]^{\mu_{RD}}, \quad \left\{ \begin{matrix} A_1 \\ A_2 \end{matrix} \right\} = \frac{\bar{\kappa}_{SD} g_{PSK}}{2 \left[ z_{SD} \left\{ \begin{matrix} - \\ + \end{matrix} \right\} Z_{SD} \right] \mu_{SD}} \quad (28)$$

and

$$\left\{ \begin{matrix} B_1 \\ B_2 \end{matrix} \right\} = \frac{\bar{\kappa}_{RD} g_{PSK}}{2 \left[ z_{RD} \left\{ \begin{matrix} - \\ + \end{matrix} \right\} Z_{RD} \right] \mu_{RD}}. \quad (29)$$

Finally, the average PEP  $\bar{P}_e(S_0 \rightarrow S_i)$  is:

$$\bar{P}_e(S_0 \rightarrow S_i) = \bar{P}_{S \rightarrow D}(S_0 \rightarrow S_i) \times \bar{P}_{S \rightarrow R} + \bar{P}_{S \rightarrow D, R \rightarrow D}(S_0 \rightarrow S_i) \times (1 - \bar{P}_{S \rightarrow R}). \quad (30)$$

At high SNR,  $1 - \bar{P}_{S \rightarrow R} \approx 1$  and Eq. (30) is:

$$\bar{P}_e(S_0 \rightarrow S_i) = \bar{P}_{S \rightarrow D}(S_0 \rightarrow S_i) \times \bar{P}_{S \rightarrow R} + \bar{P}_{S \rightarrow D, R \rightarrow D}(S_0 \rightarrow S_i). \quad (31)$$

The union bound of  $\bar{P}_e(S_0 \rightarrow S_i)$  is:

$$\bar{P}_e \leq \sum_{i=1}^{|C|} P_e(S_0 \rightarrow S_i). \quad (32)$$

#### 4.2. Asymptotic PEP Expression

Here, we derive the asymptotic PEP expression which provides significant understandings of the effect of the participating parameters on the end-to-end network performance. The asymptotic PEP is investigated for higher SNR values. For higher SNR values, the approximate MGF for the  $\eta$ - $\mu$  fading channel can be expressed as:

$$MGF_{\kappa\eta-\mu} \left[ \frac{g}{\sin^2(\theta)} \right] = \left[ \frac{4\mu^2 z}{\left( 2(z - Z)\mu + \frac{g\bar{\kappa}}{\sin^2(\theta)} \right) \left( 2(z + Z)\mu + \frac{g\bar{\kappa}}{\sin^2(\theta)} \right)} \right]^\mu \approx \left( \frac{4\mu^2 z}{g_{PSK} \bar{\kappa}^2} \right)^\mu \sin^{4\mu}(\theta). \quad (33)$$

Based on this, the conditional error probability  $\bar{P}_e$  can be approximated as:

$$\bar{P}_e^{ASY} \approx \left( \frac{4\mu_{SD}^2 z_{SD}}{g_{PSK}^2 \bar{\kappa}_{SD}^2} \right)^{\mu_{SD}} \sum_{z=0}^1 A_{RD} \left( \frac{4\mu_{RD}^2 z_{RD}}{g_{PSK}^2 \bar{\kappa}_{RD}^2} \right)^{\mu_{RD}} \times A_{SR} \left( \frac{4\mu_{SR}^2 z_{SR}}{g_{PSK}^2 \bar{\kappa}_{SR}^2} \right)^{\mu_{SR}}, \quad (34)$$

where  $g_{PSK}$ ,  $A_{RD}$  and  $A_{SR}$  for the M-ary-phase shift keying (PSK) constellations is:

$$g_{PSK} = \sin^2 \left( \frac{\pi}{M} \right), \quad (35)$$

$$A_{RD} = \frac{1}{\pi} \int_0^{(M-1)\frac{\pi}{M}} \sin^{4(\mu_{SD} + \mu_{RD})}(\theta) d\theta, \quad (36)$$

$$A_{SR} = \frac{1}{\pi} \int_0^{(M-1)\frac{\pi}{M}} \sin^{4\mu_{SR}}(\theta) d\theta, \quad (37)$$

Equation (34) can be expressed, in terms of coding gain  $G_c$  and DG  $G_d$ , as [25, Eq. (13)]:

$$G_d = 2\mu_{SD} + 2\min(\mu_{SR}, \mu_{RD}) \quad (38)$$

$$G_c = \left( \left[ \frac{4\mu_{SD}^2 z_{SD}}{g_{PSK}^2 \bar{\omega}_0^2 \delta_{SD}^2} \right]^{\mu_{SD}} \sum_{z=0}^1 A_{RD} \left[ \frac{4\mu_{RD}^2 z_{RD}}{g_{PSK}^2 \bar{\omega}_1^2 \delta_{RD}^2} \right]^{\mu_{RD}} \times A_{SR} \left[ \frac{4\mu_{SR}^2 z_{SR}}{g_{PSK}^2 \bar{\omega}_0^2 \delta_{SR}^2} \right]^{\mu_{SR}} \right)^{\frac{1}{G_d}}. \quad (39)$$

The power ratios  $\bar{\omega}_0$  and  $\bar{\omega}_1$  are expressed as  $\bar{\omega}_0 = \frac{\Phi_0}{\Phi}$  and  $\bar{\omega}_1 = \frac{\Phi_1}{\Phi}$ , respectively. It can be readily seen that the DO does not depend on the fading parameters, but it affects  $G_c$ . Also, it is important to note that for  $\mu_{SD} = \mu_{SR} = \mu_{RD} = 0.50$  the value of  $G_d = 2$  (Rayleigh fading case), which confirms the results provided in [26].

### 4.3. Amount of Fading

Amount of fading (AOF) is a parameter that is useful for evaluating the fading severity of a wireless communication system, and it is given in [27, Eq. (1.27)] as:

$$\text{AOF} = \frac{\text{Variance}(\kappa_{MRC})}{E(\kappa_{MRC})^2} = \frac{E(\kappa_{MRC}^2) - E(\kappa_{MRC})^2}{E(\kappa_{MRC})^2}. \quad (40)$$

The order moment of the  $\kappa_{MRC}$  in the considered set up can be obtained by [27], [28], giving:

$$\mu_n = (-1)^n \left[ \frac{d^n}{ds^n} (MGF_{\kappa_{SD}}(s) MGF_{\kappa_{RD}}(s)) \right]_{s=0}. \quad (41)$$

Based on this, the first two moments in Eq. (41) are obtained for  $n = 1$  and  $n = 2$ , namely:

$$E(\kappa_{MRC}) = \frac{\partial MGF_{\kappa_{MRC}}(s)}{\partial s} \Big|_{s=0}, \quad (42)$$

$$E(\kappa_{MRC}^2) = \frac{\partial^2 MGF_{\kappa_{MRC}}(s)}{\partial s^2} \Big|_{s=0}. \quad (43)$$

In the case of i.i.d. fading links and when the RN decodes successfully, the minimum value of the AOF can be calculated after performing some manipulations, such as:

$$\text{AOF} = \frac{\mu_{SD}(\mu_{SD} + 1)\bar{h}_1^2 - 2\bar{h}_2\mu_{SD} - 2\bar{h}_3\mu_{RD}}{(\bar{h}_1\mu_{SD} + \bar{h}_4\mu_{RD})^2} + \frac{\mu_{RD}(\mu_{RD} + 1)\bar{h}_4^2 + 2\bar{\delta}_{RD}\mu_{SD}\bar{h}_1\bar{h}_4}{(\bar{h}_1\mu_{SD} + \bar{h}_4\mu_{RD})} - 1, \quad (44)$$

$$\bar{h}_1 = \frac{\bar{\kappa}_{SD} z_{SD}}{\mu_{SD}(z_{SD}^2 - Z_{SD}^2)}, \quad (45)$$

$$\bar{h}_2 = \frac{\bar{\kappa}_{SD}^2}{4\mu_{SD}^2(z_{SD}^2 - Z_{SD}^2)}, \quad (46)$$

$$\bar{h}_3 = \frac{\bar{\kappa}_{RD}^2}{4\mu_{RD}^2(z_{RD}^2 - Z_{RD}^2)}, \quad (47)$$

$$\bar{h}_4 = \frac{\bar{\kappa}_{RD} z_{RD}}{\mu_{RD}(z_{RD}^2 - Z_{RD}^2)}. \quad (48)$$

By remembering that the  $\eta$ - $\mu$  fading includes Rayleigh distributions as well as Hoyt and Nakagami- $m$  distributions, the fading severity of these distributions can be calculated by the modification described in [29]–[33].

### 4.4. Analysis of OPA Factors

To obtain OPA, EPA is not the preferable choice. When SR and RD channel gains are different, EPA is not going to improve the system's performance. In this section, we compare the end-to-end system performance for both EPA and OPA schemes considering the total available power constraints over the  $\eta$ - $\mu$  fading channel conditions [33]–[38]. The Karush-Kuhn-Tucker (KKT)-based non-linear optimization problem is:

$$\bar{\omega}_{opt} = \arg \min_{\bar{\omega}} P_{SER}, \quad (49)$$

$$\text{s.t. } \bar{\omega}_0 + \bar{\omega}_1 = 1, \quad (50)$$

$$\bar{\omega}_0 \geq 0; \bar{\omega}_1 \geq 0, \quad (51)$$

where the power allocation matrix is represented as  $\bar{\omega} = [\bar{\omega}_0, \bar{\omega}_1]$ . A careful investigation of Eq. (49) shows that it is convex in nature, with parameters  $\bar{\omega}_0$  and  $\bar{\omega}_1$ . The Lagrangian of this KKT problem is [38]:

$$P_{SER} + \lambda(\bar{\omega}_0 + \bar{\omega}_1 - 1) - \epsilon_0 \bar{\omega}_0 - \mathfrak{R}_1 \bar{\omega}_1, \quad (52)$$

where the Lagrangian multiplier is represented as  $\lambda$  and  $\epsilon_0$  and  $\mathfrak{R}_1$  represents the slack variables. Taking the derivative of expression (52) with respect to  $\bar{\omega}_0$  and  $\bar{\omega}_1$  and combining both equations, we have:

$$\frac{\partial P_{SER}}{\partial \bar{\omega}_0} = \frac{\partial P_{SER}}{\partial \bar{\omega}_1}. \quad (53)$$

In order to obtain the OPA factors, asymptotic PEP given in Eq. (34) can be expressed in terms of power allocation factors as:

$$P_{SER} \approx \left[ \frac{4\mu_{SD}^2 z_{SD} N_0^2}{g_{PSK}^2 \bar{\omega}_0^2 \lambda_{jn}^2 \delta_{SD}^2 \Phi^2} \right]^{\mu_{SD}} \sum_{z=0}^1 A_{RD} \left[ \frac{4\mu_{RD}^2 z_{RD} N_0^2}{g_{PSK}^2 \bar{\omega}_1^2 \lambda_{jn}^2 \delta_{RD}^2 \Phi^2} \right]^{\mu_{RD}} \times A_{SR} \left[ \frac{4\mu_{SR}^2 z_{SR} N_0^2}{g_{PSK}^2 \bar{\omega}_0^2 \lambda_{jn}^2 \delta_{SR}^2 \Phi^2} \right]^{\mu_{SR}}. \quad (54)$$

Equation (54) can be written in terms of the CO problem as [39]:

$$\min \left[ \frac{\psi_1}{\bar{\omega}_0^{2(\mu_{SD} + \mu_{SR})}} + \frac{\psi_2}{\bar{\omega}_0^{2\mu_{SD}} \bar{\omega}_1^{2\mu_{RD}}} \right] \quad (55)$$

s.t.  $\bar{\omega}_0 + \bar{\omega}_1 = 1,$

where

$$\psi_1 = A_{SD} A_{SR} \left[ \frac{4\mu_{SR}^2 z_{SR} N_0^2}{g_{PSK}^2 \bar{\omega}_0^2 \lambda_{jn}^2 \delta_{SR}^2 \Phi^2} \right]^{\mu_{SR}}, \quad (56)$$

$$\psi_2 = A_{RD} \left[ \frac{4\mu_{RD}^2 z_{RD} N_0^2}{g_{PSK}^2 \varpi_1^2 \lambda_{jm}^2 \delta_{RD}^2 \Phi^2} \right]^{\mu_{RD}} \quad (57)$$

Differentiating  $P_{SER}$  with respect to  $\varpi_0$  and  $\varpi_1$  as:

$$\frac{\partial P_{SER}}{\partial \varpi_0} = \frac{-2(\mu_{SD} + \mu_{SR})\psi_1}{\varpi_0^{2(\mu_{SD} + \mu_{SR}) + 1}} - \frac{2\mu_{SD}\psi_2}{\varpi_0^{2\mu_{SD} + 1} \varpi_1^{2\mu_{RD}}}, \quad (58)$$

$$\frac{\partial P_{SER}}{\partial \varpi_1} = -\frac{2\mu_{RD}\psi_2}{\varpi_0^{2\mu_{SD}} \varpi_1^{2\mu_{RD} + 1}}. \quad (59)$$

Using the relation given in Eq. (53), we get:

$$\frac{(\mu_{SD} + \mu_{SR})\psi_1}{\psi_2} = \frac{\varpi_0^{2\mu_{SR} + 1}}{\varpi_1^{2\mu_{RD}}} \left( \frac{\mu_{RD}}{\varpi_1} - \frac{\mu_{SD}}{\varpi_0} \right). \quad (60)$$

It can be readily seen that the left-hand side of Eq. (60) depends solely on the fading channel's parameters, so this side will always be positive, and it yields to:

$$\varpi_0 \mu_{RD} \geq \varpi_1 \mu_{SD}. \quad (61)$$

By applying the constraint  $\varpi_0 + \varpi_1 = 1$ , the following conditions are obtained:

$$\frac{\mu_{SD}}{\mu_{SD} + \mu_{RD}} \Phi < \Phi_S < \Phi \quad (62)$$

and

$$0 < \Phi_1 < \frac{\mu_{RD}}{\mu_{SD} + \mu_{RD}} \Phi. \quad (63)$$

For simplicity,  $\mu_{SR} = \mu_{RD} = \mu$  and by substituting  $Q = \frac{\varpi_0}{\varpi_1}$ , Eq. (60) can be expressed as:

$$Q^{2\mu + 1} - \frac{\mu_{SD}}{\mu} Q^{2\mu} - \left(1 + \frac{\mu_{SD}}{\mu}\right) \frac{\psi_1}{\psi_2} = 0. \quad (64)$$

For  $2\mu = 1$  the power allocated for the source and relay can be given as:

$$\Phi_0 = \frac{\mu_{SD} + \sqrt{\mu_{SD}^2 + (1 + 2\mu_{SD}) \frac{\psi_1}{\psi_2}}}{1 + \mu_{SD} + \sqrt{\mu_{SD}^2 + (1 + 2\mu_{SD}) \frac{\psi_1}{\psi_2}}} \Phi \quad (65)$$

and

$$\Phi_1 = \frac{1}{1 + \mu_{SD} + \sqrt{\mu_{SD}^2 + (1 + 2\mu_{SD}) \frac{\psi_1}{\psi_2}}} \Phi. \quad (66)$$

### 5. Average OP Analysis of a MIMO-STBC-based S-DF Relaying Network

In this section, we investigate the average OP of a MIMO-STBC-based S-DF relaying network over  $\eta-\mu$  fading channel conditions. The channel is in outage when the instantaneous SNR  $\kappa_{SR}$  is lower than the SNR  $\gamma_0$ -threshold.

Let  $P_r(\bar{\Phi})$  represent the probability of the event  $\bar{\Phi}$  corresponding to the instantaneous SNR  $\kappa_{SR}(k)$  of the SR fading link being lower than the SNR outage threshold  $\gamma_0$ , and  $P_r(\Phi) = 1 - P_r(\bar{\Phi})$  represent the probability of the complementary event  $\bar{\Phi}$ , when  $\kappa_{SR}(k)$  is larger than  $\gamma_0$ . The per-frame average OP  $\bar{P}_{OUT}(\gamma_0)$  at the destination system for the selective DF based MIMO-OSTBC cooperative system can be written as:

$$\bar{P}_{OUT}(\gamma_0) = E_{\hat{\kappa}} [P_r(\kappa_{SD} \leq \gamma_0) P_r(\bar{\Phi}) + P_r(\kappa_{SD} + \kappa_{RD} \leq \gamma_0) P_r(\Phi)], \quad (67)$$

where  $\hat{\kappa} = [\kappa_{SD}, \kappa_{SR}, \text{ and } \kappa_{RD}]$  and  $P_r(\kappa_{SD} \leq \gamma_0)$  are the probabilities of outage at the destination for the events  $\bar{\Phi}$  and  $\Phi$ , respectively. Since the SR, SD and RD links fade independently, can be simplified as:

$$\begin{aligned} \bar{P}_{OUT}(\gamma_0) = & E_{\kappa_{SD}} [P_r(\kappa_{SD} \leq \gamma_0)] \times E_{\kappa_{SR}} [P_r(\bar{\Phi})] + \\ & E_{\kappa_{SD} + \kappa_{RD}} [P_r(\kappa_{SD} + \kappa_{RD} \leq \gamma_0)] \times \{1 - E_{\kappa_{SR}} [P_r(\bar{\Phi})]\}, \end{aligned} \quad (68)$$

$$\begin{aligned} \bar{P}_{OUT}(\gamma_0) = & \bar{F}_{\kappa_{SD}}(\gamma_0) \times \bar{F}_{\kappa_{SR}}(\gamma_0) + \\ & \bar{F}_{\kappa_{SD} + \kappa_{RD}}(\gamma_0) \times (1 - \bar{F}_{\kappa_{SR}}(\gamma_0)), \end{aligned} \quad (69)$$

where  $\bar{F}_{\kappa_{SR}}(\gamma_0)$ ,  $\bar{F}_{\kappa_{SD}}(\gamma_0)$  are provided in Eqs. (72), (74) and  $\bar{F}_{\kappa_{SD} + \kappa_{RD}}(\gamma_0)$  is the CDF of the sum of the two independent gamma RVs which can be evaluated in Eq. (75). The instantaneous OP of the SR fading link is:

$$\bar{F}_{\kappa_{SR}}(\bar{\kappa}_{SR}, \gamma_0) = P(\bar{\kappa}_{SR} \| Z_{SR} \|_F^2 < \gamma_0). \quad (70)$$

The average OP can be evaluated by substituting Eq. (3) in the above expression as:

$$\begin{aligned} \bar{F}_{\kappa_{SR}}(\bar{\kappa}_{SR}, \gamma_0) = & \int_0^{\gamma_0} \frac{2\sqrt{\pi} \mu_{SR}^{\mu_{SR} + \frac{1}{2}} z_{SR}^{\mu_{SR}} \bar{\kappa}_{SR}^{\mu_{SR} - \frac{1}{2}} \times}{\Gamma(\mu_{SR}) Z_{SR}^{\mu_{SR} - \frac{1}{2}} \bar{\kappa}_{SR}^{\mu_{SR} + \frac{1}{2}}} \\ & e^{-\frac{2\mu_{SR} z_{SR} \bar{\kappa}_{SR}}{\bar{\kappa}_{SR}}} \times I_{\mu_{SR} - \frac{1}{2}} \left( \frac{2\mu_{SR} Z_{SR} \bar{\kappa}_{SR}}{\bar{\kappa}_{SR}} \right) d\bar{\kappa}_{SR}. \end{aligned} \quad (71)$$

OP is the CDF of the received instantaneous SNR, as mentioned earlier and as seen above. Thus, the CDF of  $\eta-\mu$  distributed instantaneous SNR, given below, may be used to compute the OP of MIMO-STBC systems over  $\eta-\mu$  fading channels.

$$\bar{F}_{\kappa_{SR}}(\bar{\kappa}_{SR}, \gamma_0) = 1 - Y_{\mu_{SR}} \left( \frac{Z_{SR}}{z_{SR}}, \sqrt{\frac{2\mu_{SR} z_{SR} \gamma_0}{\bar{\kappa}_{SR}}} \right), \quad (72)$$

where

$$Y_{\mu}(\omega, \phi)$$

is called the Yacoub's integral [17]–[19]. It is defined as:

$$Y_\mu(\omega, \phi) = \sqrt{\frac{\pi(1-\omega^2)^\mu 2^{\frac{3}{2}-\mu}}{\Gamma(\mu)\omega^{\mu-\frac{1}{2}}}} \times \int_\phi^\infty e^{-\frac{t^2}{2}} t^{2\mu} I_{\mu-\frac{1}{2}}(t\omega^2) dt, \quad (73)$$

where

$$-1 < \omega < 1$$

and

$$\phi \geq 0.$$

Using Yacoub's integral the  $\bar{F}_{\kappa_{SD}}(\gamma_0)$  and  $\bar{F}_{\kappa_{SD}+\kappa_{RD}}(\gamma_0)$  are:

$$\bar{F}_{\kappa_{SD}}(\bar{\kappa}_{SD}, \gamma_0) = 1 - Y_{\mu_{SD}} \left[ \frac{Z_{SD}}{z_{SD}}, \sqrt{\frac{2\mu_{SD}z_{SD}\gamma_0}{\bar{\kappa}_{SD}}} \right], \quad (74)$$

$$\begin{aligned} \bar{F}_{\kappa_{SD}+\kappa_{RD}}(\gamma_0) = & \\ & \left\{ 1 - Y_{\mu_{SD}} \left( \frac{Z_{SD}}{z_{SD}}, \sqrt{\frac{2\mu_{SD}z_{SD}\gamma_0}{\bar{\kappa}_{SD}}} \right) \right\} \times \\ & \left\{ 1 - Y_{\mu_{RD}} \left( \frac{Z_{RD}}{z_{RD}}, \sqrt{\frac{2\mu_{RD}z_{RD}\gamma_0}{\bar{\kappa}_{RD}}} \right) \right\}. \quad (75) \end{aligned}$$

## 6. Simulation Results

In this section, the end-to-end performance and OPA of MIMO-STBC-based S-DF relaying networks is investigated over the  $\eta-\mu$  fading channel conditions. Over i.i.d. and i.n.i.d. channels, exact and asymptotic formulas for the end-to-end PEP, assuming MPSK modulated signals, is obtained. The analytic expressions obtained are then employed to gain insight into the various fading parameters in the  $\eta-\mu$  fading channel scenarios, as well as to assess their impact on end-to-end PEP and OP performance. To that aim, performance curves depicting average PEP versus SNR in dB for M-ary QAM modulation symbols are shown,

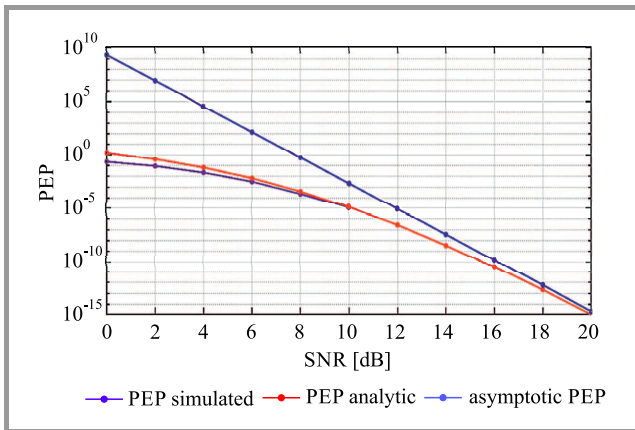


**Fig. 2.** PEP versus SNR performance, in dB, for 4-PSK symbols over i.i.d.  $\eta-\mu$  fading channel conditions considering  $\mu_{SD} = \mu_{SR} = \mu_{RD} = 0.50$ ,  $\eta_{SD} = \eta_{SR} = \eta_{RD} = 0.50$ , and average channel gains of the SD, SR and RD links are:  $\delta_{SD}^2 = \delta_{RD}^2 = \delta_{SR}^2 = 0$  dB.

with the overall transmit power being assigned equally or optimally to the SN and RN using the power strategy developed in Section 3. Figure 2 demonstrates the average PEP performance as a function of SNR for MIMO STBC-based S-DF cooperative systems utilizing EPA factors, i.e.  $\Phi_0 = \Phi_1 = \Phi/2$ , for symmetric and balanced  $\eta-\mu$  fading channels considering the 4-PSK constellations.

Furthermore, the  $\eta-\mu$  fading parameters are:  $\mu_{SD} = \mu_{SR} = \mu_{RD} = 0.50$ ,  $\eta_{SD} = \eta_{SR} = \eta_{RD} = 0.50$ , and the average channel gains of the SD, SR and RD links are:  $\delta_{SD}^2 = \delta_{RD}^2 = \delta_{SR}^2 = 0$  dB. Because of the good agreement between the exact outcomes of PEP and OP expressions and the results of corresponding computer simulations, their validity has been shown. A complete diversity order of 2 can be attained, with the exact results being firmly limited by asymptotic curves in the spectrum from low SNR values to high SNR regimes. The DG (exact), DG (asympt.) and DG Eq. (39) – are given as 1.95, 2 and 2, respectively, where it is assumed that  $\Phi_0 = \Phi$ . MIMO-STBC-based S-DF systems outperform direct transmission (SD transmission) scenarios by roughly 15 dB and 21.5 dB, respectively, at  $10^4$  target PEP.

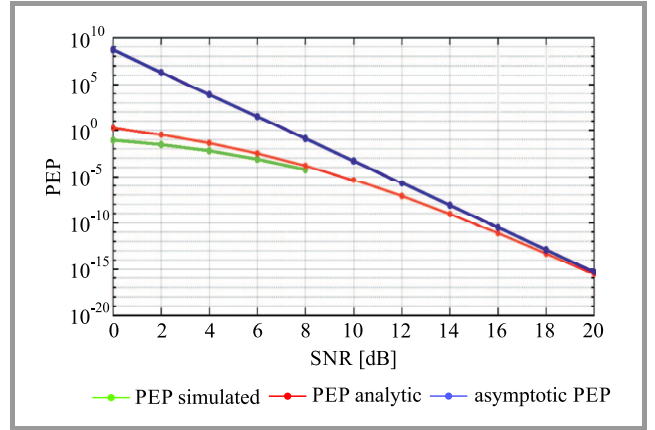


**Fig. 3.** PEP versus SNR performance, in dB, for 16-QAM symbols over i.i.d.  $\eta-\mu$  fading channel conditions considering with  $\mu_{SD} = \mu_{SR} = \mu_{RD} = 1.50$  and  $\eta_{SD} = \eta_{SR} = \eta_{RD} = 1$  as well as balanced links, i.e. average channel gains of the SD, SR and RD links are:  $\delta_{SD}^2 = \delta_{RD}^2 = \delta_{SR}^2 = 0$  dB.

In the same context, Fig. 3 shows the average PEP performance as a function of SNR for 16-QAM modulation symbols for a single relay MIMO STBC-based S-DF network considering the EPS factors over symmetric  $\eta-\mu$  fading channels with  $\mu_{SD} = \mu_{SR} = \mu_{RD} = 1.50$  and  $\eta_{SD} = \eta_{SR} = \eta_{RD} = 1$  as well as balanced links, i.e. average channel gains of the SD, SR and RD links are:  $\delta_{SD}^2 = \delta_{RD}^2 = \delta_{SR}^2 = 0$  dB. It is further demonstrated that the exact analytical PEP curves closely match the simulation curves for medium and high SNR values, and that the asymptotic curves tend to be nearly the exact copies of those for PEP lower than  $10^4$ . As a result, in actual S-DF relaying system designs with high SNR, the provided asymptotic formulas might provide important system performance insights.

In Fig. 4, a MIMO STBC S-DF single relay network is considered with QPSK symbols and EPA factors taken into account. The simulation parameters are given as:  $\mu_{SD} = \mu_{SR} = \mu_{RD} = \{1, 2, 3\}$  and the average channel gains of the SD, SR and RD links are:  $\delta_{SD}^2 = \delta_{RD}^2 = \delta_{SR}^2 = 0$  dB. It is evident that the Hoyt distribution is equal to the  $\eta$ - $\mu$  fading distribution when  $\mu_{SD} = \mu_{SR} = \mu_{RD} = 0.50$ . We can see the impact of the scattered-wave power ratio on the average PEP of the proposed MIMO-STBCD-based S-DF network by changing the value of  $\eta$ . This proves that PEP is inversely proportional to  $\eta$ , since when  $\eta$  increases from 1 to 3 for all values of  $\mu$ , an average gain of 2 dB is observed for the target average PEP of  $10^{-5}$ . Furthermore, when  $\mu$  increases from 1 to 3 and  $\mu$  increases from 2 to 3, average improvements of 3.89 dB and 1.65 dB are attained.

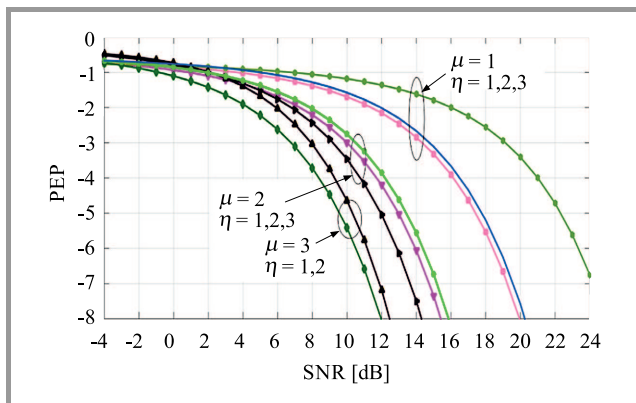


**Fig. 4.** PEP vs. SNR, in dB, with  $\mu_{SD} = \mu_{SR} = \mu_{RD} = \{1, 2, 3\}$ ,  $\eta$  increases from 1 to 3 QPSK and EPA factors.

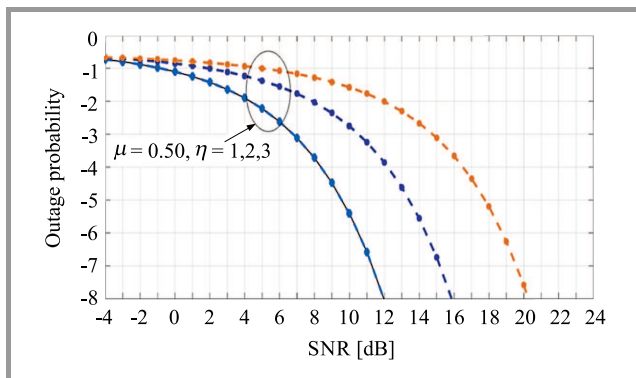


**Fig. 5.** SER vs. SNR with  $\mu_{SD} = \mu_{SR} = \mu_{RD} = \mu = \{0.50\}$  with  $\eta$  increasing from 1 to 3 for 4-PSK considering the EPA factors.

In the similar manner, Fig. 5 demonstrates the average OP performance for 4-PSK modulation symbols under the independent and non-identically distributed  $\eta$ - $\mu$  fading channels, for single relays with EPA factors. The simulation parameters are:  $\delta_{SD}^2 = \delta_{SR}^2 = 1$ ,  $\delta_{RD}^2 = 10$  dB,  $\mu_{SD} = \mu_{SR} = \mu_{RD} = \mu = \{0.50\}$  dB, with  $\eta$  increasing from 1 to 3. When the values of  $\eta$  change from 1 to 3 for  $\delta_{RD}^2 = 10$  dB, for the considered values of  $\mu_{SD} = \mu_{SR} = \mu_{RD} =$

$\mu = \{0.50\}$ , the system's performance improves significantly. At OP of nearly 1.25 dB and 1.75 dB, gains are achieved when the values of  $\eta_{SR}$  and  $\eta_{RD}$  change from 1 to 3 for the considered values of  $\eta$ .

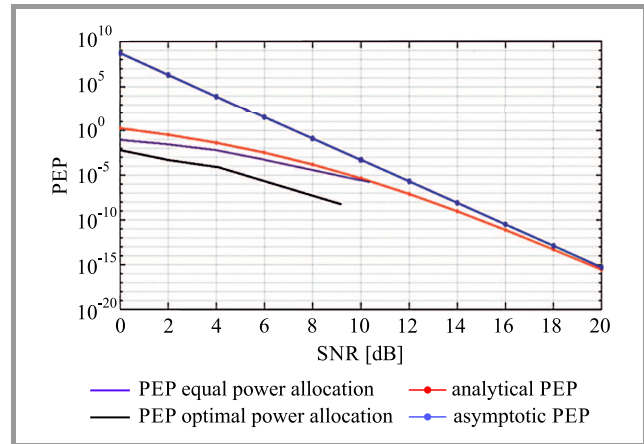


**Fig. 6.** PEP vs. SNR performance, in dB, for quadrature PSK symbols over i.i.d. fading channel conditions for OPA factors.

Figure 6 shows PEP performance of the proposed OPA scheme and assumes a greater channel variance from the RNs to the DN, with a constant scattered-wave power ratio for single relays and QPSK constellations. The simulation parameters are:  $\mu_{SD} = \mu_{SR} = \mu_{RD} = \mu = 0.50$ ,  $\delta_{SD}^2 = \delta_{SR}^2 = 0$  dB,  $\delta_{RD}^2 = 100$  dB and  $\eta = 0.50$ . The OPA factors are  $\omega_0 = 0.90$  and  $\omega_0 + \omega_1 = 1 - 0.98$ . It has been assumed that when  $\mu$  is small, such as  $\mu = 0.50$ , the proposed OPA scheme creates a cooperation mechanism offering minor benefits which, however, grow as  $\mu$  increases. Indicatively, the optimal method surpasses the EPA scenario by at least 1.5 dB when  $\mu = 0.50$  for a PEP of  $10^{-4}$ .

## 7. Conclusion

In this paper, we have investigated end-to-end PEP and average OP performance of MIMO-STBC-based S-DF relaying networks under  $\eta$ - $\mu$  fading channel conditions. The exact and asymptotic end-to-end PEP expression, assuming modulated M-ary-PSK and M-ary-QAM complex modulated symbols, have been produced on i.i.d. fading links. The analytical expressions acquired were then used to obtain insights into different fading factors and their effect on end-to-end system performance under non-homogeneous fading channel conditions. The data given were then used in the development of an asymptotically optimal power distribution system, within a total sum power limit, which showed that the standard EPA technique was substantially outperformed. The OPA system is also demonstrated to be virtually separate from the power ratio parameter dispersed waves from SN to DN, depending upon the number of multipath clusters and on the chosen modulating system. The curves demonstrate that for moderate and high SNR regimes, the asymptotic and exact expressions are closely

matching. PEP performance is noticeably increased as and increase as with a PEP of plots show that the OPA schemes outperform the EPA schemes.

## References

- [1] M. K. Beuria, R. Shankar, and S. S. Singh, "Analysis of the energy harvesting non-orthogonal multiple access technique for defense applications over Rayleigh fading channel conditions", *The J. of Defense Model. and Simulation*, 2021 (DOI: 10.1177/15485129211021168).
- [2] S. N. Swain, R. Thakur, and S. R. M. Chebiyyam, "Coverage and rate analysis for facilitating machine-to-machine communication in LTE-A networks using device-to-device communication", *IEEE Trans. on Mob. Comput.*, vol. 16, no. 11, pp. 3014–3027, 2017 (DOI: 10.1109/TMC.2017.2684162).
- [3] S. Pandya, M. A. Wakchaure, R. Shankar, and J. R. Annam, "Analysis of NOMA-OFDM 5G wireless system using deep neural network", *The J. of Defense Model. and Simul.*, 2021 (DOI: 10.1177/1548512921999108).
- [4] R. Shankar, "Examination of a non-orthogonal multiple access scheme for next generation wireless networks", *The J. of Defense Model. and Simul.*, 2020 (DOI: 10.1177/1548512920951277).
- [5] R. Shankar, K. N. Pandey, A. Kumari, V. Sachan, and R. K. Mishra, "C(0) protocol based cooperative wireless communication over Nakagami-m fading channels: PEP and SER analysis at optimal power", in *Proc. IEEE 7th Ann. Comput. and Commun. Worksh. and Conf. CCWC 2017*, Las Vegas, NV, USA, 2017 (DOI: 10.1109/CCWC.2017.7868399).
- [6] N. Varshney, A. V. Krishna, and A. K. Jagannatham, "Selective DF protocol for MIMO STBC based single/multiple relay cooperative communication: end-to-end performance and optimal power allocation", *IEEE Trans. on Commun.*, vol. 63, no. 7, pp. 2458–2474, 2015 (DOI: 10.1109/TCOMM.2015.2436912).
- [7] N. Varshney, A. K. Jagannatham, and P. K. Varshney, "Cognitive MIMO-RF/FSO cooperative relay communication with mobile nodes and imperfect channel state information", *IEEE Trans. on Cognitive Commun. and Network.*, vol. 4, no. 3, pp. 544–555, 2018 (DOI: 10.1109/TCCN.2018.2844827).
- [8] K. Eltira, N. Jibreel, A. Younis, and R. Mesleh, "Capacity analysis of cooperative amplify and forward multiple-input multiple-output systems", *Trans. on Emerg. Telecommun. Technol.*, vol. 32, no. 10 (DOI: 10.1002/ett.4290).
- [9] H. K. Boddapati, R. B. Manav, and P. Shankar, "Performance of cooperative multi-hop cognitive radio networks with selective decode-and-forward relays", *IET Commun.*, vol. 12, no. 20, pp. 2538–2545, 2018 (DOI: 10.1049/iet-com.2018.5328).
- [10] A. Z. Afify, A. Shawky, and N. Mazen, "A new inverse Weibull distribution: properties, classical and Bayesian estimation with applications", *Kuwait J. of Sci.*, vol. 48, no. 3, 2021 (DOI: 10.48129/kjs.v48i3.9896).
- [11] E. M. Almetwally *et al.*, "Marshall-Olkin alpha power Weibull distribution: Different methods of estimation based on type-I and type-II censoring", *Complexity*, vol. 2021, article ID 5533799, 2021 (DOI: 10.1155/2021/5533799).
- [12] R. Shankar, I. Kumar, A. Kumari, K. N. Pandey, and R. K. Mishra, "Pairwise error probability analysis and optimal power allocation for selective decode-forward protocol over Nakagami-m fading channels", in *Proc. Int. Conf. on Algor., Methodol., Models and Appl. in Emerg. Technol. ICAMMAET 2017*, Chennai, India, 2017 (DOI: 10.1109/ICAMMAET.2017.8186700).
- [13] R. Shankar and R. K. Mishra, "An investigation of S-DF cooperative communication protocol over keyhole fading channel", *Phys. Commun.*, vol. 29, pp. 120–140, 2018 (DOI: 10.1016/j.phycom.2018.04.027).
- [14] R. Shankar and R. K. Mishra, "EP and OP examination of relaying network over time-selective fading channel", *SN Appl. Sci.*, vol. 2, article ID: 1329, 2020 (DOI: 10.1007/s42452-020-3077-5).
- [15] R. Shankar and R. K. Mishra, "S-DF cooperative communication system over time selective fading channel", *J. of Inform. Sci. and Engin.*, vol. 35, no. 6, pp. 1223–1248, 2019 (DOI: 10.6688/JISE.201911\_35(6).0004).
- [16] R. Shankar and R. K. Mishra, "Outage probability analysis of selective-decode and forward cooperative wireless network over time varying fading channels with node mobility and imperfect CSI condition", in *Proc. TENCON 2018 — 2018 IEEE Region 10 Conf.*, Jeju, South Korea, 2018, pp. 0508–0513 (DOI: 10.1109/TENCON.2018.8650275).
- [17] C. B. Issaid, M.-S. Alouini, and R. Tempone, "On the fast and precise evaluation of the outage probability of diversity receivers over  $\eta$ - $\mu$ ,  $\kappa$ - $\mu$ , and  $\eta$ - $\mu$  fading channels", *IEEE Trans. Wirel. Commun.*, vol. 17, no. 2, pp. 1255–1268, 2018 (DOI: 10.1109/TENCON.2018.8650275).
- [18] O. S. Badarneh and F. S. Almeahmadi, "Performance analysis of L-branch maximal ratio combining over generalized  $\eta$ - $\mu$  fading channels with imperfect channel estimation", *IET Commun.*, vol. 10, no. 10, pp. 1175–1182, 2016 (DOI: 10.1049/iet-com.2015.1015).
- [19] F. S. Almeahmadi and O. S. Badarneh, "Performance analysis of outage probability and error rate of square M-QAM in mobile wireless communication systems over generalized  $\alpha$ - $\mu$  fading channels with non-Gaussian noise", *China Commun.*, vol. 15, no. 1, pp. 62–71, 2018 (DOI: 10.1109/CC.2018.8290806).
- [20] H. Yu, G. Wei, F. Ji, and X. Zhang, "On the error probability of cross-QAM with MRC reception over generalized  $\eta$ - $\mu$  fading channels", *IEEE Trans. on Veh. Technol.*, vol. 60, no. 6, pp. 2631–2643, 2011, (DOI: 10.1109/TVT.2011.2154347).
- [21] M. Bilim, "QAM signaling over  $\kappa$ - $\mu$  shadowed fading channels", *Phys. Commun.*, vol. 34, pp. 261–271, 2019 (DOI: 10.1016/j.phycom.2019.04.005).
- [22] M. Bilim and N. Kapucu, "On the analysis of achievable rate for NOMA networks with cooperative users over  $\kappa$ - $\mu$  shadowed fading channels", *Int. J. Commun. Syst.*, vol. 32, no. 12, 2019 (DOI: 10.1002/dac.4001).
- [23] S. Kumar and S. Kalyani, "Outage probability and rate for  $\kappa$ - $\mu$  shadowed fading in interference limited scenario", *IEEE Trans. Wirel. Commun.*, vol. 16, no. 12, pp. 8289–8304, 2017 (DOI: 10.1109/TWC.2017.2760822).
- [24] O. S. Badarneh and R. Mesleh, "A comprehensive framework for quadrature spatial modulation in generalized fading scenarios", *IEEE Trans. Commun.*, vol. 64, no. 7, pp. 2961–2970, 2016 (DOI: 10.1109/TCOMM.2016.2571285).
- [25] N. Bhargav, S. L. Cotton, and E. David Simmons, "Secrecy capacity analysis over  $\kappa$ - $\mu$  fading channels: theory and applications", *IEEE Trans. Commun.*, vol. 64, no. 7, pp. 3011–3024, 2016 (DOI: 10.1109/TCOMM.2016.2565580).
- [26] J. M. Moualeu and W. Hamouda, "On the secrecy performance analysis of SIMO systems over  $\kappa$ - $\mu$  fading channels", *IEEE Commun. Lett.*, vol. 21, no. 11, pp. 2544–2547, 2017 (DOI: 10.1109/LCOMM.2017.2741458).
- [27] J. M. Moualeu *et al.*, "Physical-layer security of SIMO communications systems over multipath fading conditions", *IEEE Trans. on Sustain. Comput.*, vol. 6, no. 1, pp. 105–118, 2019 (DOI: 10.1109/TSUSC.2019.2915547).
- [28] H. Lei, I. S. Ansari, G. Pan, B. Alomair, and M.-S. Alouini, "Secrecy capacity analysis over  $\alpha$ - $\mu$  fading channels", *IEEE Commun. Lett.*, vol. 21, no. 6, pp. 1445–1448, 2017 (DOI: 10.1109/LCOMM.2017.2669976).
- [29] J. M. Moualeu, D. B. da Costa, W. Hamouda, U. S. Dias, and R. A. A. de Souza, "Physical layer security over  $\alpha$ - $\kappa$ - $\mu$  and  $\alpha$ - $\eta$ - $\mu$  fading channels", *IEEE Trans. on Veh. Technol.*, vol. 68, no. 1, pp. 1025–1029, 2019 (DOI: 10.1109/TVT.2018.2884832).
- [30] J. Yang, L. Chen, X. Lei, K. P. Peppas, and T. Q. Duong, "Dual-hop cognitive amplify-and-forward relaying networks over  $\eta$ - $\mu$  fading channels", *IEEE Trans. on Veh. Technol.*, vol. 65, no. 8, pp. 6290–6300, 2015 (DOI: 10.1109/TVT.2015.2480968).

- [31] S. H. Alvi, S. Wyne, and D. B. da Costa, "Performance analysis of dual-hop AF relaying over  $\alpha$ - $\mu$  fading channels", *AEU-Int. J. of Electron. and Commun.*, vol. 108, pp. 221–225, 2019 (DOI: 10.1016/j.aeue.2019.06.013).
- [32] J. M. Moualeu, T. M. N. Ngatched, and D. B. da Costa, "Sequential relay selection in D2D-enabled cellular networks with outdated CSI over mixed fading channels", *IEEE Wirel. Commun. Lett.*, vol. 8, no. 1, pp. 245–248, 2019 (DOI: 10.1109/LWC.2018.2868645).
- [33] S. Kumar *et al.*, "Energy detection based spectrum sensing for gamma shadowed  $\alpha$ - $\eta$ - $\mu$  and  $\alpha$ - $\kappa$ - $\mu$  fading channels", *AEU-Int. J. of Electron. and Commun.*, vol. 93, pp. 26–31, 2018 (DOI: 10.1016/j.aeue.2018.05.031).
- [34] T. F. Hailat, H. B. Salameh, and T. Aldalgamouni. "Performance study of multi-hop communication systems with decode-and-forward relays over  $\alpha$ - $\mu$  fading channels", *IET Commun.*, vol. 11, no. 10, pp. 1641–1648, 2017 (DOI: 10.1049/iet-com.2016.1220).
- [35] A. Hussain, A. K. Lee, S.-H. Kim, S.-H. Chang, and D. I. Kim, "Performance analysis of dual-hop variable-gain relaying with beamforming over  $\kappa$ - $\mu$  fading channels", *IET Commun.*, vol. 11, no. 10, pp. 1587–1593, 2017 (DOI: 10.1049/iet-com.2016.1102).
- [36] R. Shankar, L. Bhardwaj, and R. K. Mishra, "Analysis of selective-decode and forward relaying protocol over  $\kappa$ - $\mu$  fading channel distribution", *J. of Telecommun. and Inform. Technol.*, no. 1, pp. 21–30, 2020 (DOI: 10.26636/jit.2020.135919).
- [37] Y. J. Chun *et al.*, "A Comprehensive analysis of 5G heterogeneous cellular systems operating over  $\kappa$ - $\mu$  shadowed fading channels", *IEEE Trans. on Wirel. Commun.*, vol. 16, no. 11, pp. 6995–7010, 2017 (DOI: 10.1109/TWC.2017.2734080).
- [38] K. P. Peppas, G. C. Alexandropoulos, and P. T. Mathiopoulos, "Performance analysis of dual-hop AF relaying systems over mixed  $\eta$ - $\mu$  and  $\kappa$ - $\mu$  fading channels", *IEEE Trans. on Veh. Technol.*, vol. 62, no. 7, pp. 3149–3163, 2013 (DOI: 10.1109/TVT.2013.2251026).
- [39] D. Pant, P. S. Chauhan, S. K. Soni, and S. Naithani, "Channel capacity analysis of wireless system under ORA scheme over  $\kappa$ - $\mu$  inverse gamma and  $\eta$ - $\mu$ / inverse gamma composite fading models", in *Proc. of Int. Conf. on Elec. and Electron. Engin. ICE3 2020*, Gorakhpur, India, 2020, pp. 425–430 (DOI: 10.1109/ICE348803.2020.9122938).
- [40] S. K. Yoo, S. L. Cotton, P. C. Sofotasios, S. Muhaidat, and G. K. Karagiannidis, "Effective capacity analysis over generalized composite fading channels", *IEEE Access*, vol. 8, pp. 123756–123764, 2020 (DOI: 10.1109/ACCESS.2020.3003207).
- [41] C. Ben Issaid, M. Alouini, and R. Tempone, "On the fast and precise evaluation of the outage probability of diversity receivers over  $\alpha$ - $\mu$ , and  $\eta$ - $\mu$  fading channels", *IEEE Trans. on Wirel. Commun.*, vol. 17, no. 2, pp. 1255–1268, 2018 (DOI: 10.1109/TWC.2017.2777465).
- [42] M. Bilim, "Uplink communication with AWGN over non-homogeneous fading channels", *Phys. Commun.*, vol. 39, no. C, 2020 (DOI: 10.1016/j.phycom.2020.101047).
- [43] P. Kumar and K. Dhaka, "Performance analysis of a decode-and-forward relay system in  $\kappa$ - $\mu$  and  $\eta$ - $\mu$  fading channels", *IEEE Trans. on Veh. Technol.*, vol. 65, no. 4, pp. 2768–2775, 2016 (DOI: 10.1109/TVT.2015.2418211).
- [44] K. Papazafeiropoulos and S. A. Kotsopoulos, "Second-order statistics for the envelope of  $\alpha$ - $\kappa$ - $\mu$  fading channels", *IEEE Commun. Lett.*, vol. 14, no. 4, pp. 291–293, 2010 (DOI: 10.1109/LCOMM.2010.04.092265).
- [45] B. Samudhyatha, S. Gurugopinath, and K. Saraswathi, "Maximum eigenvalue-based spectrum sensing over  $\alpha$ - $\kappa$ - $\mu$  and  $\alpha$ - $\eta$ - $\mu$  fading channels", in *Proc. of IEEE 28th Ann. Int. Symp. on Pers., Indoor, and Mob. Radio Commun. PIMRC 2017*, Montreal, QC, Canada, 2017 (DOI: 10.1109/PIMRC.2017.8292575).



**Ravi Shankar** received his B.E. in Electronics and Communication Engineering from Jiwaji University, Gwalior, India, in 2006. He received his M.Tech. degree in Electronics and Communication Engineering from GGSIPU, New Delhi, India, in 2012. He received a Ph.D. in Wireless Communication from the National Institute of Technology Patna, Patna, India, in 2019. From 2013 to 2014 he was an Assistant Professor at MRCE Faridabad, where he was engaged in researching wireless communication networks. He is presently an assistant professor at MITS Madanapalle, Madanapalle, India. His current research interests cover cooperative communication, D2D communication, IoT/M2M networks and networks protocols. He is a student member of IEEE.

 <https://orcid.org/0000-0001-7532-3275>

E-mail: ravishankar.nitp@gmail.com

Department of Electronics and Communication Engineering  
Madanapalle Institute of Technology and Science  
Andhra Pradesh  
517325, India

**V. V. Raghava Raman** holds a Ph.D. in Computer Science and Engineering. He has over two decades of experience in teaching at national and international levels. He has guided research scholars in the area of the Internet of Things. His areas of interest cover data warehousing, data mining, programming languages, AI and IoT.  
Department of Computer Science  
Aurora's Degree and PG College  
Chikkadapally  
Hyderabad, India



**Kantilal P. Rane** is presently working as a Professor at Department of Electronics and Communication, K L University, Hyderabad. He completed his Ph.D. in 2013 from North Maharashtra University, Jalgaon. His areas of research includes antennas, wave propagation, electromagnetic field theory, VLSI and embedded system design, as well as networking.

E-mail: kantiprane@rediffmail.com

Department of Electronics and Communication  
K L University  
Hyderabad, India



**Sarojini B. K.** received her Ph.D. in Computer and Information Engineering from Vishweshwaraya Technological University (VTU) Belagavi, Karnataka. She completed her M.Tech. at the ECE Department of the Indian Institute of Technology Kharagpur and B.E. in Electronics and Communication Engineering from Mysore Uni-

versity. Currently, she is a professor at the Department of Electronics and Communication Engineering, Basaveshwar Engineering College, Bagalkot, Karnataka. Her research interests include signal processing, machine learning and communication.

E-mail: srjnsarojini@gmail.com

Department of ECE

Basaveshwar Engineering College

Bagalkot-587103, Karnataka, India



**Rahul Neware** received his B.E. in Information Technology from RTM Nagpur University India, in 2015, and M.Tech. in Computer Science and Engineering from G. H. Rasoni College of Engineering, Nagpur, India, in 2018. He is currently pursuing a Ph.D. in Computing from Western Norway University of Applied Sciences,

Bergen campus, Norway. His interests focus on cybersecurity, cloud and fog computing, advanced image processing and remote sensing.

E-mail: rane@hvl.no

Høgskulen på Vestlandet

Bergen, Norway

# Improved CSE with DLS-MMSE Criteria in TH-UWB System

Ali Djebbari and Sid Ahmed Elahmar

University of Sidi Bel Abbas, Sidi Bel Abbas, Algeria

<https://doi.org/10.26636/jtit.2022.151421>

**Abstract**—This article presents a study on the use of deterministic least squares criteria combined with the minimum mean square error method for the purpose of computing filter coefficients of the channel shortening equalizer. This method is well known to alleviate inter-symbol interference in time hopping UWB systems. The validity of this method is applied to shorten the impulse response of the effective UWB channels and, therefore, reduce the complexity of the rake receiver. Results show a very promising advantage compared to partial-rake (P-Rake), selective-rake (S-Rake) and optimal maximum shortening signal-to-noise ratio methods.

**Keywords**—channel shortening equalizer, inter-symbols interference, rake receiver, time hopping, ultra-wide-band, ZF-MMSE.

## 1. Introduction

Time hopping ultra-wideband (TH-UWB) modulation evokes a great deal of interest as it may be used for transmitting in high data rate, low-power communication applications [1], [2]. However, TH-UWB suffers from drawbacks related to inter-symbol interference (ISI), due to the very long impulse channel response compared to the pulse duration used in time hopping [3]–[5]. On the other hand, the channel shortening equalizer (CSE) is used to combat the negative impact of ISI by shortening the response of the multipath channel and, consequently, by increasing the system's performance due to the reduction in the complexity of the rake receiver [6]–[13].

In the literature, the maximum shortening signal-to-noise ratio (MSSNR) criterion is well-known and is widely relied upon in CSE implementations [11]. Another technique proposed in [12] consists in dividing the CSE filter into a concept concentrating energy in the desired window, and the tail suppression parts. However, these techniques can suffer from an increase in noise in certain deep fading situations. In this article, we propose a CSE algorithm designed by modifying the first part of the energy concentration criterion proposed in [12] to improve the bit error rate (BER) performance of the system.

The first part of the proposed CSE filter design is based on deterministic least squares (DLS) criteria combined with the minimum mean square error algorithm (MMSE) [13]–[15], to concentrate all energy within a small

desired window and, hence, to achieve a shortened effective channel and lower noise.

The second part of the filter is exploited to satisfy the other criterion, namely to minimize the amount of energy outside the desired window. The proposed CSE approach offers good BER performance compared to the conventional MSSNR CSE and Ragoubi's CSE [12], as these methods fail to take into account a noisy channel when designing the CSE.

The paper is organized as follows. In Section 2, a model of the TH-UWB system with CSE is presented. In Section 3, the proposed algorithm is shown. Section 4 is devoted to the simulation results with the comparison between several methods and the MSSNR algorithm.

## 2. TH-UWB System Model

In the binary pulse position modulation (BPPM) scheme, the expression of the signal transmitted by the single user TH-UWB system is:

$$s(t) = \sum_{i=0}^{N_s-1} \sqrt{E_s} p(t - iT_s - c_i T_c - a_i \varepsilon), \quad (1)$$

where  $E_s$  is the pulse energy,  $p(t)$  is the pulse waveform with the duration of  $T_p$ .  $N_s$  is the number of pulse repetitions (frames),  $T_s$  is the pulse repetition time,  $T_c$  is the chip duration such that there are  $N_c$  chips within  $T_s$ ,  $c_i \in \{0, 1, \dots, N_c - 1\}$  is the  $i$ -th coefficient of time-hopping (TH) pseudo-random sequence of the user, and  $a_i \varepsilon$  is the time delay produced by the signal modulation with  $\varepsilon$  PPM offset and  $a_i$  data bit.

In this work, we use the channel models proposed by the IEEE 802.15.3a Study Group, known as CM1 to CM4 [3]. The simplified form of these channel models is:

$$h(t) = \sum_{m=0}^{M-1} h_m \delta(t - \tau_m), \quad (2)$$

where  $h_m$  and  $\tau_m$  are the multipath gain coefficients and their arrival times, respectively, with  $\delta(t)$  being the Dirac delta function. The received signal, in the presence of additive thermal noise  $n(t)$ , at the channel's UWB output, is modeled as:

$$r(t) = s(t) * h(t) + n(t), \quad (3)$$

where  $*$  is the convolution operator.

In UWB systems, in order to keep the rake receiver design simple, a large number of channel taps must be suppressed. A CSE filter present at the receiver's front end (Fig. 1) combats inter-symbol interference (ISI) of the multipath channel and reduces the complexity of the rake receiver. To achieve that, the pulse waveform width  $T_p$  should be less than the multipath arrival delay bin, i.e. only resolvable multipaths should be considered. The temporal response of the CSE filter of length  $N$  is given by:

$$w(t) = \sum_{n=0}^{N-1} w_n \delta(t - \tau_n) \quad N \ll M, \quad (4)$$

with  $N$  very small to channel model length  $M$ , and where  $w_n$  is the  $n$ -th filter coefficient and  $\tau_n$  is the temporal spacing between any two consecutive filter taps.

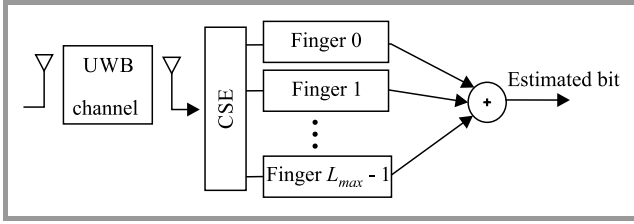


Fig. 1. UWB system model with a channel shortening equalizer.

The received signal will experience an effective channel effect  $c(t)$ :

$$c(t) = h(t) * w(t) = \sum_{m=0}^{M'-1} c_m \delta(t - \tau_m), \quad (5)$$

where  $c_m$  and  $\tau_m$  are the effective channel multipath gains and the arrival times, with  $M' = M + N - 1$ .

### 3. CSE Design Method

#### 3.1. Channel Shortening Decomposition

Besides the decomposition of the coefficients into two parts, as in [12], the proposed method uses an optimization based on ZF-MMSE, which leads to a reduction of the undesirable noise amplification effect. The effective discrete channel model is given by the convolution operation in a matrix form as:

$$\mathbf{c} = \mathbf{H}\mathbf{w}, \quad (6)$$

where  $\mathbf{H}$  is the  $(M + N - 1)N$  Toeplitz convolution matrix corresponding to the channel  $h$  (see Appendix) and  $\mathbf{w} = \{w_0 w_1 \dots w_{N-1}\}^T$  is the vector of the equalization coefficients (CSE).

Next, we have decomposed the CSE coefficients vector adopted in [12], [16]:

$$\mathbf{w} = [\mathbf{w}_{\max} \quad \mathbf{w}_{\min}]^T, \quad (7)$$

where:

$$\begin{cases} \mathbf{w}_{\max} = [w_0 & \dots & w_{L_{\max}}] \\ \mathbf{w}_{\min} = [w_{L_{\max}+1} & \dots & w_{N-1}] \end{cases} \quad (8)$$

and  $L_{\max}$  is the length of the desired window for the effective channel.

Similarly, the resulting effective channel  $\mathbf{c}$  of length  $M + N - 1$  will be divided into two matrices as follows:

$$\mathbf{c} = [\mathbf{c}_{\max} \quad \mathbf{c}_{\min}]^T, \quad (9)$$

where:

$$\begin{cases} \mathbf{c}_{\max} = [c_0 & \dots & c_{L_{\max}}] \\ \mathbf{c}_{\min} = [c_{L_{\max}+1} & \dots & c_{M+N-2}] \end{cases} \quad (10)$$

Taking into account the previous decomposition in the Eq. (6), we reformulate the matrix convolution as:

$$\begin{bmatrix} \mathbf{c}_{\max} \\ \mathbf{c}_{\min} \end{bmatrix} = \begin{bmatrix} \mathbf{P} & \mathbf{O} \\ \mathbf{Q} & \mathbf{R} \end{bmatrix} \begin{bmatrix} \mathbf{w}_{\max}^T \\ \mathbf{w}_{\min}^T \end{bmatrix}, \quad (11)$$

where  $\mathbf{P}$ ,  $\mathbf{Q}$  and  $\mathbf{R}$  are the Toeplitz channel matrix with size  $(L_{\max} + 1) \times (L_{\max} + 1)$ ,  $(M + N - 2 - L_{\max}) \times (L_{\max} + 1)$ ,  $(M + N - 2 - L_{\max}) \times (N - L_{\max} - 1)$ , respectively (see Appendix).  $\mathbf{O}$  is the zeros matrix with size  $(L_{\max} + 1) \times (N - L_{\max} - 1)$ .

From Eq. (11), we obtain:

$$\mathbf{c}_{\max}^T - \mathbf{P}\mathbf{w}_{\max}^T, \quad (12)$$

$$\mathbf{c}_{\min}^T - \mathbf{Q}\mathbf{w}_{\max}^T + \mathbf{R}\mathbf{w}_{\min}^T. \quad (13)$$

The shortening of  $\mathbf{c}$  in the  $\mathbf{c}_{\max}$  format is depends solely on  $\mathbf{w}_{\max}$  coefficients, while minimizing energy in  $\mathbf{c}_{\min}$  depends on the  $\mathbf{Q}$ ,  $\mathbf{R}$  matrix and also on  $\mathbf{w}_{\min}$  coefficients, assuming a given  $\mathbf{w}_{\max}$  initialization.

#### 3.2. Energy Concentration

##### 3.2.1. Review of the MSSNR Algorithm

The maximum shortening SNR (MSSNR) [11] method involves minimizing the energy outside the desired window of the effective channel response while maintaining a constant amount of energy within it. From Eq. (6), we divide the effective channel into two consecutive parts:

$$\mathbf{c} = \begin{bmatrix} \mathbf{H}_{\max} \mathbf{w} \\ \mathbf{H}_{\min} \mathbf{w} \end{bmatrix}, \quad (14)$$

where  $\mathbf{H}_{\max}$  is the sub-matrix of  $\mathbf{H}$  corresponding to the first  $L_{\max} + 1$  rows and  $\mathbf{H}_{\min}$  is the remaining rows of the matrix  $\mathbf{H}$  up to  $(M + N - 1)$ . The optimal MSSNR CSE coefficients vector is given by:

$$\mathbf{w}_{opt} = \arg \max_{\mathbf{w}} \left\{ \frac{\mathbf{w}^T \mathbf{A} \mathbf{w}}{\mathbf{w}^T \mathbf{B} \mathbf{w}} \right\}, \quad (15)$$

with  $\mathbf{A} = \mathbf{H}_{\max}^T \mathbf{H}_{\max}$  and  $\mathbf{B} = \mathbf{H}_{\min}^T \mathbf{H}_{\min}$ .

The solution will be to minimize  $\mathbf{w}^T \mathbf{B} \mathbf{w}$  while setting  $\mathbf{w}^T \mathbf{A} \mathbf{w} = 1$ . That is:

$$\mathbf{w}_{opt} = (\sqrt{\mathbf{A}^T})^{-1} \hat{\mathbf{b}}_{\min}, \quad (16)$$

where  $\hat{\mathbf{b}}_{\min}$  is given by the eigenvector corresponding to the minimum eigenvalue of  $(\sqrt{\mathbf{A}})^{-1} \mathbf{B} (\sqrt{\mathbf{A}^T})^{-1}$  and  $\sqrt{\mathbf{A}}$  is the Cholesky factor of  $\mathbf{A}$ .

### 3.2.2. Review of the Ragoubi's Algorithm

The Ragoubi's method [12] is mainly based on concentrating energy using the discrete cosine transform (DCT), where  $w_{\max}$  can be computed as:

$$w_{\max}(i) = \text{DCT}(i) \quad 0 \leq i \leq L_{\max}, \quad (17)$$

with

$$\begin{cases} \sqrt{\frac{1}{L_{\max}}} \cos \left[ \frac{\pi(2i+1)}{2L_{\max}} \right] & 0 \leq i \leq L_{\max} \\ \sqrt{\frac{2}{L_{\max}}} & i = 0 \end{cases}. \quad (18)$$

Optionally,  $w_{\max}$  can be calculated simply by using a Dirac delta:

$$w_{\max}(i) = \delta_{0,i} \quad 0 \leq i \leq L_{\max}, \quad (19)$$

where  $\delta_{0,k}$  is the Kronecker symbol.

The second part of the Ragoubi's method was to calculate the CSE coefficients  $w_{\min}$  by minimizing the energy outside the window of size  $L_{\max}$ , i.e. by simply imposing null taps in the window going from  $L_{\max} + 1$  to  $N - 1$ , as detailed later on in our proposed algorithm.

### 3.2.3. Proposed Method

In the proposed method, we explore zero-forcing based on the deterministic least squares (DLS) criteria [13] combined with the MMSE method for  $w_{\max}$  initialization. To shorten the channel, we use the zero-forcing method, so a given  $c_{\max}$  becomes the desired  $c_r$  setting as:

$$\mathbf{P}w_{\max}^T = c_r, \quad (20)$$

$$\text{where } c_r(k) = \begin{cases} 1 & k = 0 \\ 0 & k > 0 \end{cases}.$$

The  $w_{\max}$  vector of the CSE coefficients has been computed based on minimizing the error given by:

$$\mathbf{e} = \mathbf{P}w_{\max}^T - c_r. \quad (21)$$

Thus, the resolution of Eq. (20) is obtained in the sense of MMSE as follows:

$$w_{\max\_opt} = (\mathbf{P} * \mathbf{P})^{-1} \mathbf{P} * c_r. \quad (22)$$

From Eq. (22) it appears that in order to compute CSE equalizer coefficients, only the channel knowledge needed to create  $\mathbf{P}$  and the trivial destination vector  $c_r$  are required. In the case of additional white Gaussian noise (AWGN), the vector of CSE coefficients will be deduced by the optimal MMSE solution [15] with consideration of the effective signal to noise ratio (SNR) given by:

$$w_{\max\_opt} = (\mathbf{P} * \mathbf{P} + \gamma_{pe}^2 \mathbf{I})^{-1} \mathbf{P} * c_r, \quad (23)$$

where  $\gamma_{pe}^2 = \frac{1}{SNR}$  and  $\mathbf{I}$  is identity matrix.

The second task of the CSE design is the one used in [12], based on minimizing energy outside the desired window of

size  $L_{\max}$ . The  $w_{\min}$  coefficients are then calculated using the original CIR  $\mathbf{h}$ , the first part of the CSE  $w_{\max}$  and considering null taps outside the window of size  $L_{\max}$  [12]. The elements of convolution vectors obtained respectively from the column-wise summation of  $\mathbf{Q}w_{\max}^T$  and  $\mathbf{R}w_{\min}^T$  of (13) are, respectively:

$$q(k) = \sum_{j=0}^{L_{\max}} w_{\max}(j)h(k-j) + L_{\max} + 1, \quad (24)$$

$$r(k) = \sum_{j=0}^k w_{\min}(j)h(k-j) = w_{\min}(k) * h(k), \quad (25)$$

with  $0 \leq k \leq N - L_{\max} - 1$ .

Then, substituting  $c_{\min}^T$  with zero in order to have a null taps outside the desired window of size  $L_{\max}$ , we obtain:

$$w_{\min}(k) * h(k) = -q(k). \quad (26)$$

Finally, using the classical Fourier quotient method, Eq. (26) becomes:

$$w_{\min}(k) = F^{-1} \left\{ \frac{F\{-q(k)\}}{f\{h(k)\}} \right\}, \quad (27)$$

where  $F$  and  $F^{-1}$  denote the fast Fourier transform and its inverse transform, respectively.

### 3.3. Complexity

Here, we present the computational complexities of all the discussed algorithms. The proposed algorithm using the CSE calculated according to the DLS/MMSE method in the first symbols of  $L_{\max}$ , the Ragoubi's method using the DCT decomposition in the useful window of  $L_{\max}$  and, finally, the MSSNR is also cited as a reference algorithm. Computations are performed in the following steps:

The calculation of  $w_{\max}$  using Eq. (23), requires:  $\frac{L_{\max}^3}{3} + 3L_{\max}^2 + \frac{8L_{\max}}{3}$  [17].

First, we have to compute  $q(k)$  using Eq. (24) with [12]:

- $(M - L_{\max})L_{\max} + N + \sum_{i=1}^{L_{\max}-1} i - 1$  additions,
- $(M - L_{\max})L_{\max} + \sum_{i=1}^{L_{\max}-1} i$  multiplications.

The computation of  $w_{\min}$  requires 2 FFTs with a maximum complexity of order  $M \log M$  operations, one IFFT with  $N \log N$  operations and  $N$  dividing operations. This brings the total complexity to:

$$2(M - L_{\max})L_{\max} + 2N + 2 \left( \sum_{i=1}^{L_{\max}-1} i \right) + 2M \log M + N \log N - 1 + \frac{L_{\max}^3}{3} + 3L_{\max}r + \frac{8L_{\max}}{3}.$$

The Ragoubi’s method [12] requires a global computation of:

$$L_{\max} \log(L_{\max}) + 2(M - L_{\max})L_{\max} + 2N + 2\left(\sum_{i=1}^{L_{\max}-1}\right) + 2M \log M + N \log N - 1 .$$

The complexity for  $N_d$  iterations of MSSNR is given by (see pp. 61–63 of [17]):  $N^4 + \frac{5N^3}{3} + N^2\left(N_d + M + \frac{1}{2}\right) + \frac{11N}{6}$ . The comparison of the complexity of each design scheme mentioned above shows that the method presented by Ragoubi *et al.* [12] is characterized by the lowest complexity, with a difference of  $O(L_{\max} \log L_{\max})$  compared to our  $O\left(\frac{L_{\max}^3}{3}\right)$ , but this can be neglected as it only concerns a few useful window samples of  $L_{\max}$  independently of the other parameters. The MSSNR algorithm is more complex because it needs an iterative search for the optimal delay of the effective channel. However, as discussed in the next section, it is important to note that BER-related performance of the proposed method is significantly better.

### 4. Simulation Results

In this section, the simulation results show the BER-related performance of the proposed CSE, the conventional MSSNR and different rake structures, compared with the average SNR. The PPM TH-UWB waveform  $p(t)$  is chosen as the second derivative of Gaussian pulse with the duration of  $T_p = 0.15$  ns with the following parameters of transmission:  $T_s = 8$  ns,  $\varepsilon = 0.15$  ns,  $T_c = 0.9$  ns. We use channel models from [1], namely CM1 and CM4. There is a line of sight (LOS) signal in the CM1 channel, whereas the CM4 channel has a long distance in non-line of sight (NLOS) and is characterized by high dispersion. The length of  $L_{\max}$  is 10 taps in all of the cases.  $N = 50$  in CM1 and  $N = 75$  in CM4.

The overall receiver can be viewed as a CSE followed by P-Rake. It is worth noting that P-Rake has negligible complexity compared to CSE [4]. Thus, the complexity of S-Rake is greater than that of P-Rake, because it scans all multipaths in the  $M$  channel in order to correctly select the strongest paths that may be used. However, P-Rake combines the first  $L_{\max}$  arriving paths, which are not necessarily the best. Thus, it does need to sort the multipath components by the magnitude of their instantaneous path gains.

Figures 2 and 3 compare the performance of the proposed method with the conventional MSSNR, the Ragoubi CSE method and all rake receivers (A-Rake) using the CM1 and CM4 channels, respectively. The proposed method shows better performance, except for the comparison with the A-Rake receiver, where the totality of multipath contribution are processed but this last method is more. However, the number of path components that can be utilized in

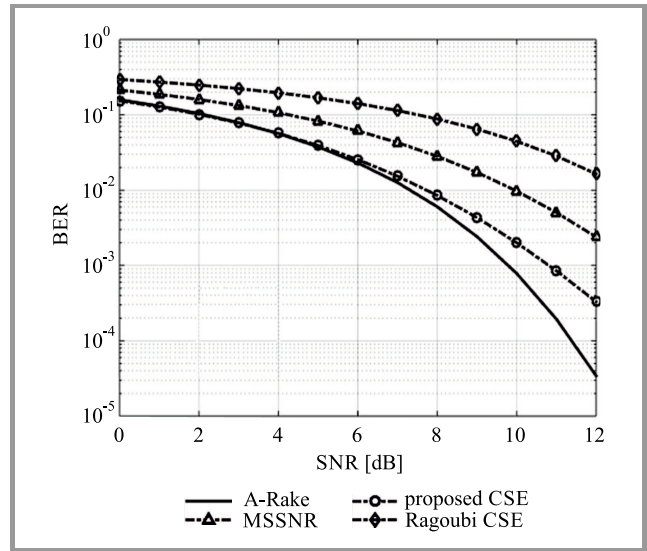


Fig. 2. BER comparison for different CSEs with 10-tap effective window of CM1.

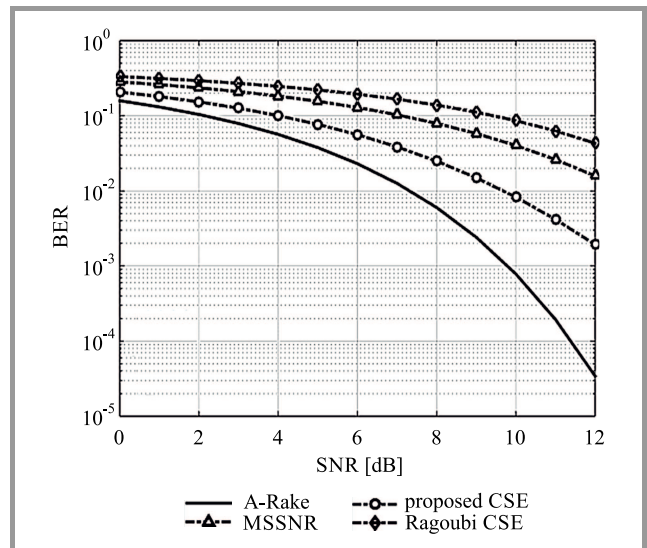
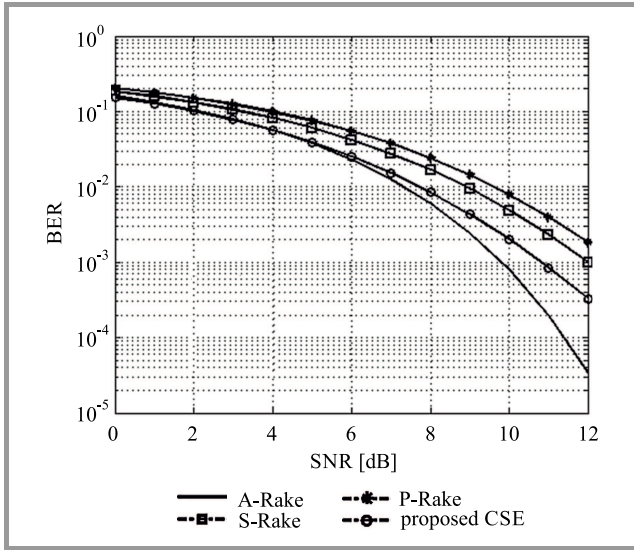


Fig. 3. BER comparison for the proposed CSE, MSSNR, Ragoubi CSE and A-Rake in CM4 channel with 10-tap effective window.

the A-Rake receiver is limited by power consumption constraints and complexity considerations (i.e. memory usage). Thus, we consider the A-Rake receiver only as a benchmark that provides an upper limit of achievable performance. Note that for a BER of  $10^{-2}$  in the case of channel CM1, there is a major improvement in the SNR gain, of 2 dB, obtained by the proposed CSE compared to MSSNR, and of approx. 4.5 dB compared to the Ragoubi’s method. The reason is obvious, as the DLS-MMSE method is favored for ISI and noise reduction by minimizing the majority of the signal energy outside the desired multipath window and minimizing noise throughout the effective channel response. While the MSSNR and Ragoubi’s CSE methods maximize the energy of the channel in the desired window,

they do not cancel the large amount of ISI and noise outside this window. Performance decreases slightly for CM4, because this channel is more severe and contains more multipaths than CM1.



**Fig. 4.** BER comparison of CM1 channel for proposed CSE, A-Rake, S-Rake and P-Rake.

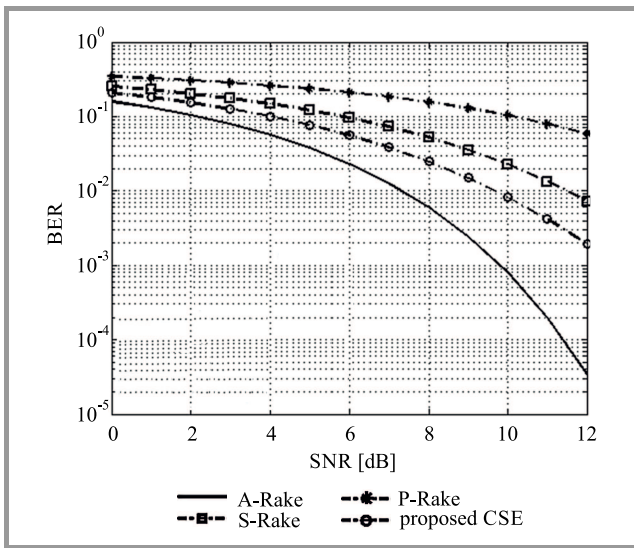


**Fig. 5.** BER comparison for proposed CSE, A-Rake, S-Rake and P-Rake in a CM4 channel with 10-tap effective window.

Performance of the proposed DLS CSE and the different rake receivers (A-Rake, S-Rake and P-Rake) for channel models CM1 and CM4 is compared in Figs. 4 and 5, respectively. One may notice that the proposed CSE has the best BER except when compared with A-Rake. The P-Rake receiver only processes part of the useful signal energy present in the first incoming multipath  $L_{\max}$ . In the case of S-Rake, it processes the strongest  $L_{\max}$  multipaths but the ISI increases, which leads to self-interference and decreases the output SNR. The performance of S-Rake may be improved at the expense of a reduced data rate.

## 5. Conclusion

In this paper, we proposed a CSE technique for TH-UWB systems using the zero-forcing and MMSE methods to have a shortened effective channel through the DLS algorithm. Channel energy is concentrated within the desired window containing several multipaths and simultaneously canceling the majority of the effective channel energy outside this desired window. Therefore, the rake receiver becomes less complex and is characterized by the strongest multipath. By examining performance, one may conclude that the use of the proposed CSE at the reception of the signal, just prior the receiver rake, is a better solution in terms of BER than P-Rake and S-Rake. Simulation results also show that the proposed CSE surpasses performance of the optimal MSSNR design.

## Appendix

Matrices **H**, **P**, **Q** and **R** are given by:

$$\mathbf{H} = \begin{bmatrix} h_0 & 0 & \dots & \dots & 0 \\ h_1 & h_0 & \ddots & & \vdots \\ \vdots & \vdots & & & \\ h_{M-1} & h_{M-2} & \dots & h_{M-N+1} & h_{M-N} \\ 0 & h_{M-1} & \dots & & h_{M-N+1} \\ \vdots & \ddots & & & \vdots \\ 0 & \dots & 0 & h_{M-1} & \end{bmatrix}_{(M+N-1) \times (N)}$$

$$\mathbf{P} = \begin{bmatrix} h_0 & 0 & \dots & 0 \\ h_1 & h_0 & \dots & 0 \\ \vdots & \vdots & \ddots & 0 \\ h_{L_{\max}} & h_{L_{\max}-1} & \dots & h_0 \end{bmatrix}_{(M+N-2-L_{\max}) \times (L_{\max}+1)}$$

$$\mathbf{Q} = \begin{bmatrix} L_{\max}+1 & h_{L_{\max}} & \dots & h_1 \\ \vdots & \vdots & \ddots & \vdots \\ h_{M-1} & h_{M-2} & \dots & h_{M-L_{\max}-1} \\ 0 & h_{M-1} & \dots & h_{M-L_{\max}} \\ \vdots & \ddots & \vdots & \vdots \\ 0 & 0 & \dots & 0 \end{bmatrix}_{(M+N-2-L_{\max}) \times (L_{\max}+1)}$$

$$\mathbf{R} = \begin{bmatrix} h_0 & 0 & 0 \\ \vdots & \vdots & \vdots \\ h_{M-L_{\max}-2} & \dots & h_{M-N} \\ h_{M-L_{\max}-1} & \dots & h_{M-N+1} \\ \vdots & \ddots & \vdots \\ 0 & \dots & h_{M-1} \end{bmatrix}_{(M+N-2-L_{\max}) \times (N-L_{\max}-1)}$$

## References

- [1] M. Z. Win and R. A. Scholtz, "Ultra-wide bandwidth time-hopping spread-spectrum impulse radio for wireless multiple-access communications", *IEEE Trans. on Commun.*, vol. 48, no. 4, pp. 679–691, 2000 (DOI: 10.1109/26.843135).
- [2] L. Fang and H. Zailu, "Low complexity multi-user detectors of TH-PPM UWB system", in *Proc. of Int. Conf. on Wirel. Commun., Network. and Mob. Comput.*, Wuhan, China, 2005 (DOI: 10.1109/WCNM.2005.1544041).
- [3] A. F. Molisch, "Channel models for ultra-wide band personal area networks", *IEEE Wirel. Commun.*, vol. 10, no. 6, pp. 14–21, 2003 (DOI: 10.1109/MWC.2003.1265848).
- [4] Z. Ahmadian and L. Lampe, "Robust design of widely linear pre-equalization filters for pre-rake UWB systems", *IEEE Trans. Commun.*, vol. 61, no. 10, pp. 4206–4217, 2013 (DOI: 10.1109/TCOMM.2013.0828131.120920).
- [5] A. Rajeswaran, Somayazulu, and V. S. Foerster, "Rake performance for a pulse based UWB system in a realistic UWB indoor channel", in *Proc. Int. Conf. on Commun. ICC'03*, Anchorage, AK, USA, 2003 (DOI: 10.1109/ICC.2003.1204551).
- [6] N. Benotmane, S. A. Elahmar, I. Dayoub, and W. A. Hamouda, "Improved eigenfilter design method for channel shortening equalizer in TH-UWB", *IEEE Trans. Veh. Technol.*, vol. 67, no. 8, pp. 7749–7753, 2018 (DOI: 10.1109/TVT.2018.2822178).
- [7] S. I. Husain, J. Yuan, and J. Zhang, "Rake performance after channel shortening by decay factor optimization in UWB channels", in *Proc. IEEE 66th Veh. Technol. Conf. VTC-2007 Fall*, Baltimore, MD, USA, 2007 (DOI: 10.1109/VETECF.2007.259).
- [8] L. Zhang and C. Y. Yang, "Performance analysis of channel shortening of Rake receiver in ultra-wideband systems", in *Proc. IEEE Veh. Technol. Conf. VTC*, Montreal, QC, Canada, 2006 (DOI: 10.1109/VTTCF.2006.166).
- [9] N. Benotmane and S. A. Elahmar, "Channel shortening equalizer for multi-access TH-UWB in the presence of multipath and multiuser interferences", *Radioelectron. and Commun. Syst.*, vol. 60, no. 8, pp. 339–349, 2017 (DOI: 10.3103/S0735272717080027).
- [10] S. I. Husain and J. Choi, "Single correlator based UWB receiver implementation through channel shortening equalizer", in *Proc. Asia Pacific Conf. on Commun. APCC 2005*, Perth, WA, Australia, 2005, pp. 610–614, 2005 (DOI: 10.1109/APCC.2005.1554134).
- [11] P. J. Melsa, R. C. Younce, and C. E. Rohrs, "Impulse response shortening for discrete multitone transceivers", *IEEE Trans. on Commun.*, vol. 44, no. 12, pp. 1662–1672, 1996 (DOI: 10.1109/26.545896).
- [12] K. Ragoubi, M. Hélar, and M. Crussière, "Low complexity channel shortening technique applied to MB-OFDM UWB systems", in *Proc. 4th Int. Conf. on Sig. Process. and Commun. Syst.*, Gold Coast, QLD, Australia, 2010 (DOI: 10.1109/ICSPCS.2010.5709684).
- [13] A. Mohan and K. V. S. Haris, "Low complexity adaptation for SISO channel shortening equalizers", *Int. J. of Electron. and Commun. (AEU)*, vol. 66, no 8, pp. 600–604, 2012 (DOI: 10.1016/j.aeue.2012.03.011).
- [14] B. Das and S. Das, "RAKE-MMSE Time domain equalizer for high data rate UWB communication system", in *Proc. Ann. IEEE India Conf.*, Ahmedabad, India, 2009 (DOI: 10.1109/INDCON.2009.5409346).
- [15] S. Sparrer and R. F. H. Fischer, "MMSE-based version of OMP for recovery of discrete-valued sparse signals", *Electron. Lett.*, vol. 52, no. 1, pp. 75–77, 2016 (DOI: 10.1049/el.2015.0924).
- [16] P. M. Ndao, M. Hélar, M. Crussière, and F. Yven, "Channel shortening for OFDM systems: An improved algorithm in noisy environments", in *Proc. IEEE Int. Conf. on Ultra-Wide-Band ICUWB 2014*, Paris, France, 2014, pp. 228–233 (DOI: 10.1109/ICUWB.2014.6958983).
- [17] N. Yuan, "An equalisation technique for high rate OFDM systems", M.Sc. thesis, Department of Electrical Engineering, University of Saskatchewan, Saskatoon, Canada, 2003 [Online]. Available: <https://www.collectionscanada.gc.ca/obj/s4/f2/dsk3/SSU/TC-SSU-12022003213031.pdf>



**Ali Djebbari** received his B.Sc. degree in Electronics from the University of Djillali Liabes, Sidi Bel Abbes (UDL), Algeria, in 1993, and the M.Sc. degree from the University of Sciences and Technology of Oran (USTO), Algeria, in 1995. Currently he is working as an Assistant Professor of Communications Engineering, Department of Telecommunications at the University of Sidi Bel Abbes (UDL). His Research interests Signal Processing for Telecommunications, Wireless Networks, High-Speed Communications and Optical OFDM Communication Networks.

 <https://orcid.org/0000-0002-6992-3239>

E-mail: alidjebbari@yahoo.com  
Department of Telecommunications  
University of Sidi Bel Abbes  
Sidi Bel Abbès 22000, Algeria



**Sid Ahmed Elahmar** received his B.Sc. degree in Electronics from the University of Djillali Liabes, Sidi Bel Abbes (UDL), Algeria in 1994, the M.Sc. degree from the University of Sciences and Technology of Oran (USTO), Algeria in 1996 and the Ph.D. degree in Signal Processing from UDL in 2007. He is Professor of Communications

Engineering and president of the scientific committee with the Telecommunications Department Djillali Liabes University. His research interests include UWB Wireless Communications, Cognitive Cooperative Communications, Long-Reach Radio-over-Fiber Communications, and 5G Communication Networks.

 <https://orcid.org/0000-0002-1357-2169>

E-mail: silahmar@yahoo.fr  
Department of Telecommunications  
University of Sidi Bel Abbes  
Sidi Bel Abbès 22000, Algeria

# Unequally Spaced Antenna Array Synthesis Using Accelerating Gaussian Mutated Cat Swarm Optimization

Prasanna K. Kumar, Lakshman Pappula, B. T. P. Madhav, and V. S. V. Prabhakar

Department of ECE, Koneru Lakshmaiah Education Foundation, Guntur, India

<https://doi.org/10.26636/jtit.2022.154821>

**Abstract**—Low peak sidelobe level (PSLL) and antenna arrays with high directivity are needed nowadays for reliable wireless communication systems. Controlling the PSLL is a major issue in designing effective antenna array systems. In this paper, a nature inspired technique, namely accelerating Gaussian mutated cat swarm optimization (AGMCSO) that attributes global search abilities, is proposed to control PSLL in the radiation pattern. In AGM-SCO, Gaussian mutation with an acceleration parameter is used in the position-updated equation, which allows the algorithm to search in a systematic way to prevent premature convergence and to enhance the speed of convergence. Experiments concerning several benchmark multimodal problems have been conducted and the obtained results illustrate that AGMCSO shows excellent performance concerning evolutionary speed and accuracy. To validate the overall efficacy of the algorithm, a sensitivity analysis was performed for different AGMCSO parameters. AGMCSO was researched on numerous linear, unequally spaced antenna arrays and the results show that in terms of generating low PSLL with a narrow first null beamwidth (FNBW), AGMCSO outperforms conventional algorithms.

**Keywords**—Gaussian mutation, cat swarm optimization, linear antenna array, PSLL.

## 1. Introduction

Numerous antenna arrays are used in mobile, satellite, radar, and other wireless communication systems as they offer good signal quality, enhanced directivity, extended spectrum efficiency and wide coverage. To avoid interference with other communication systems operating nearby, there is a need to maintain a low peak sidelobe level (PSLL). Because of the increasing electromagnetic deterioration, nulls need to be kept at the desired directions with low sidelobes and fixed first null beam width (FNBW).

There are many approaches to shaping side lobe power in the radiation pattern. The designer may either alter the antenna's position or may use complex weights to obtain the desired radiation pattern (low PSLL). The weights apply to amplitude and phase inputs of each radiation element in the antenna array. Implementation of non-uniform amplitude and phase weights in uniformly placed antenna arrays

is a complex problem. Instead, unequally spaced antenna arrays with uniform feeding provide greater flexibility in shaping side lobe power in the radiation pattern [1].

In this paper, we rely on aperiodic antenna array synthesis due to its simple feed network. An illustration of an unequally spaced array is shown in Fig. 1. It may be designed by altering the distance between the antenna's elements. The problem of unequally spaced antenna array synthesis involves non-linear and non-convex optimization using a set of classical gradient-based algorithms deployed in nature-inspired optimization techniques. Several nature-inspired optimization techniques, namely genetic algorithm (GA) [2]–[6], differential evolution (DE) [7]–[12], particle swarm optimization (PSO) [13]–[22], ant colony optimization (ACO) [23]–[25], cat swarm optimization [26]–[32], grey wolf optimization (GWO) [33]–[34], and bee colony optimization (BCO) [35]–[36] have been implemented while synthesizing unequally spaced antenna arrays.

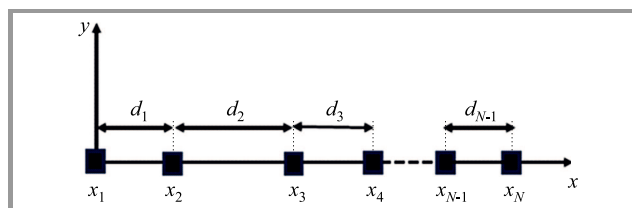


**Fig. 1.** A linear antenna array with non-uniform spacing.

Some of the important algorithms relied upon in antenna array synthesis have been discussed in detail in the literature. Yan *et al.* [2] proposed a simple and versatile GA for antenna array pattern synthesis and the approach involves array excitation weighting vectors used as complex number chromosomes. GA has been applied to synthesize linear and circular arrays to achieve  $-20$  dB PSLL levels. Chen KS *et al.* proposed, in paper [4], a modified real genetic algorithm (MGA) for the synthesis of sparse linear arrays by optimizing the elements' positions to reduce peak sidelobe level. The result of the synthesis showed that MGA achieved a PSLL of  $-20.562$  dB with 37 elements. Numerical simulations demonstrated superb efficiency and robustness of this algorithm. The improved genetic algo-

rithm (IGA) was proposed by Cen *et al.* [5]. It simultaneously changes the weight coefficients and inter-sensor spacings of a linear aperiodic array. The authors extended the research to include the impact of steering angles on the sidelobe level with fixed main beamwidth. The results have shown superiority of PSLL compared to other GA variants. A computationally efficient global optimization method of differential evolution (DE) was proposed for the synthesis of uniform amplitude arrays by Kurup *et al.* [7]. Phase-only synthesis and position-only syntheses were discussed to achieve low sidelobe levels by Lin *et al.* [9].

Goudos *et al.* [11] proposed a design technique based on a self-adaptive DE (SADE) algorithm which has been applied to real-valued microwave design problems including linear-array synthesis, patch-antenna design, and microstrip filter design. The authors compared the SADE strategy with popular PSO and DE variants and proved its effectiveness. Zhang *et al.* [17] enhanced search diversity by integrating a parameter selection strategy into classical differential evolution. In this research, a modified DE based on a harmony search algorithm known as HSDEA was developed to optimize linear aperiodic arrays by ensuring a minimum peak sidelobe level. Simulations showed that a PSLL of  $-22.631$  dB had been achieved for a 32-elements array. HSDEA converges faster and requires fewer calculations for synthesizing a linear aperiodic array, compared with other methods. PSO [13] is a recently developed high-performance optimizer. It is similar to GA or evolutionary algorithms, but requires fewer computational resources. Boeringer *et al.* [13] proposed PSO to synthesize antenna arrays using amplitude-only, phase-only, and complex tapering. Several comparative studies were conducted by comparing PSO with GA and ACO. Khodier *et al.* [14] proposed PSO for a synthesis of linear antenna arrays and formulated the objective function for PSLL and null placement. Rajo-Iglesias *et al.* [23] proposed ACO using real numbers for synthesizing linear antenna arrays. They synthesized 10- and 32-element array systems. For a 32-element linear array, ACO gives a PSLL of  $-17.5$  dB and a  $7.7^\circ$  beamwidth.

To increase the efficiency of antenna arrays by ensuring high directivity and low sidelobe levels, CSO was proposed for synthesizing linear antenna arrays by Pappula *et al.* [31]. CSO is used to optimize the distance between the antenna's parts in order to generate a radiation pattern with low PSLL and deep nulls in the desired directions. CSO has shown superiority over GA and PSO. Li *et al.* [34] proposed the GWO algorithm, which mimics the social behavior of grey wolves, to synthesize linear arrays. The objective is to suppress peak sidelobe level under various constraints. Performance is further verified while optimizing the design of a dual-band E-shaped patch antenna and a wideband magnetoelectric dipole antenna.

All these techniques have demonstrated alternatives to traditional gradient-based algorithms exist and may be relied upon while searching for the global solution. But in

the synthesis of antenna arrays, the feasible range of solutions is extremely wide and the search for an optimal solution with a fast convergence rate poses a major challenge. Algorithms that incorporate an exhaustive search function are needed to seek the optimal solution with a fast convergence rate.

Cat swarm optimization (CSO) [26] is a newly developed technique that mimics the original behavior of cats. Chu and Tsai introduced this technique in [37]. It has been implemented while dealing with numerous engineering problems in the real world [37] and has shown improved performance over GA and PSO.

However, while solving complex non-linear problems, conventional CSO suffers from premature convergence and locks in local minima. In a position-updated equation of CSO, due to the random mutation process, this leads to the aforementioned problems. This issue is restricted to a wide range of applications of the traditional CSO.

In this paper, we have introduced Gaussian mutation with an accelerating parameter in the position-updated equation – a solution offering fast convergence that may be accurately compared with CSO. The proposed AGMCSO is applied while synthesizing unequally spaced antenna arrays to suppress PSLL, while simultaneously maintaining narrow FNBW. Then, a detailed comparison of AGMCSO with state-of-the-art algorithms is presented.

This article is organized as follows: details of the traditional CSO approach are discussed in Section 2 and are followed by the introduction of AGMCSO in Section 3. Section 4 presents the test functions on which AGMCSO is being implemented and a comparison of numerical outcomes for 30-dimensional problems between AGMCSO, CSO, PSO is obtained. Section 5 addresses the application of AGMCSO in complex EM design problems.

## 2. Modified Cat Swarm Optimization

CSO is modeled by observing the hunting skills of a cat. The algorithm is classified into two modes of operation: seeking mode and tracing mode. Cats are assigned to the mode depending on the mixture ratio (MR).

In the seeking mode (SM), by observing the surroundings, a cat being in its rest position will always be on alert. The cat's movements are very slow. The relevant model uses the following [32]:

- seeking range of the selected dimension (SRD), which determines the amount of available range,
- counts of dimensions to change (CDC) – this parameter determines the number of dimensions to be mutated.,
- seeking memory pool (SMP) – determining the number of copies of cats to be created for mutation.

The following are the phases observed in the SM:

- build  $K$  copies of  $i$ -th cat based on SMP;
- $(K - 1)$  copies are subject to the mutation mechanism. All dimensions are randomly mutated according to CDC and SRD, either by adding SRD to or subtracting it from the parent location;
- the fitness values of newly updated copies are analyzed;
- choose the best value from the  $K$  copies is chosen and replaced with the cat's position.

In the tracing mode (TM), cats attempt to change their locations rapidly by tracking the targets. The shift in the location is statistically inferred by following the cat's tracing actions. In this mode, the algorithm's steps are:

- in the  $D$ -dimensional solution space the position and velocity of the  $m$ -th cat is:

$$P_m^g = [P_{mn}] \quad \text{where } n = 1, \dots, D, \quad (1)$$

$$Vel_m^g = [Vel_{mn}] \quad \text{where } n = 1, \dots, D, \quad (2)$$

- for each dimension the position and velocity of  $m$ -th cat is updated as:

$$Vel_m^{g+1} = [Vel_{m,n}] = \omega \cdot Vel_{m,n}^g + C \cdot r \cdot (P_{gbest} - P_{m,n}^g), \quad (3)$$

$$P_{m,n}^{g+1} = P_{m,n}^g + Vel_{m,n}^{g+1}, \quad (4)$$

where  $g$  represents the generation number,  $m$  is the cat's index in a swarm,  $n$  represents the cat's position index,  $Vel_{m,n}^g$  is the velocity of the  $m$ -th particle,  $C$  represents the acceleration coefficient,  $r$  is the arbitrary number between 0 and 1,  $P$  is the weight of the inertia, and  $P_{gbest}$  is the best cat's position.

The fitness values are assessed after the tracing mode. If the required solution is not attained based on the mixture ratio, the adjusted cats are dispersed to SM and TM. This is repeated until the desired solution is acquired. However, it has been observed that in SM mode, the random mutation process leads to a poor and premature convergence rate.

### 3. Accelerating Gaussian Mutation Based CSO

The probability of sensing range is steadily decreased as the cat is in a resting position. It resembles a Gaussian distribution curve with a zero mean. The sensing range is focused around the cat's rest position and gradually becomes low as it moves far from the cat's position, i.e. compared to large mutations, the probability of developing lower mutations is higher. The Gaussian distribution curve resembles the cat's behavior in the seeking mode, as illustrated in Fig. 2.

It may be observed that there is a higher likelihood of minor mutations which lead to a more rigorous local search

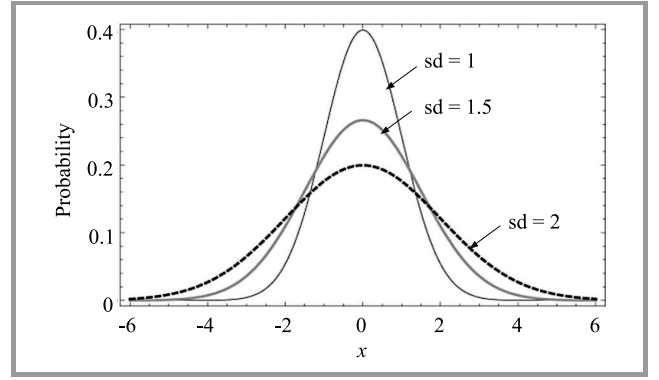


Fig. 2. Gaussian density function with three standard deviations.

along with a global search. The standard deviation  $\sigma$  and the mean  $\mu$  of Gaussian distribution density function is:

$$f_{normal}(p; \mu, \sigma) = \frac{1}{\sqrt{2\pi\sigma^2}} e^{-\frac{(p-\mu)^2}{2\sigma^2}}. \quad (5)$$

According Eq. (5), the Gaussian random number  $G$  is:

$$G(\mu, \sigma^2) = \mu + \sigma G(0, 1). \quad (6)$$

Here  $G(0, 1)$  is the Gaussian random number normally distributed with a standard deviation of 1 and a zero mean. From Fig. 2 it is evident that both large and small mutation values can be produced from the standard deviation value of 1. The method is modified with the help of Gaussian mutation to improve solution accuracy and convergence.

A mutant individual  $x_i^m$  is generated by Gaussian mutation which is:

$$x_i^m = x_i + G(0, \sigma^2) = x_i + \sigma \cdot G(0, 1), \quad (7)$$

where  $x_i$  is the unmutated individual, and  $\sigma$  is conveyed as the selected dimension's mutated value. Therefore, the position of each dimension of  $i$ -th cat is:

$$x_i^m = x_i + \left[ SRD \cdot \left( 1 - \frac{g}{gen} \right) \cdot x_i \cdot G(0, 1) \right]. \quad (8)$$

To enhance the local convergence properties, we have adopted an accelerating component in the  $x_i^m$ .

#### 3.1. Time Complexity of AGMCSO

The SM time complexity is considered as  $O[N_n \cdot \log(N_n)]$ , where  $N_n$  is  $S_n \cdot \text{Dim} \cdot (\text{SMP} - 1)$  [32], and  $S_n$  is the number of cats in SM, Dim is the number of dimensions, the SMP pool searching for a memory. The process time complexity of TM may be mentioned as  $O(N_n)$ , where  $N_n$  is  $T_n \cdot \text{Dim}$ , and  $T_n$  is tracing the number of cats. The number of cats in TM is to be smaller than the number of cats in SM. The worst-case time complexity of the tracing mode process is dominated by SM worst-case time complexity. The suggested method's total worst-case time complexity is considered as  $O[N_n \cdot \log(N_n)]$ . Time complexity of the proposed AGMCSO approach and of the conventional CSO algorithm is the same, as we did not introduce any complicated variants in the proposed AGMCSO.

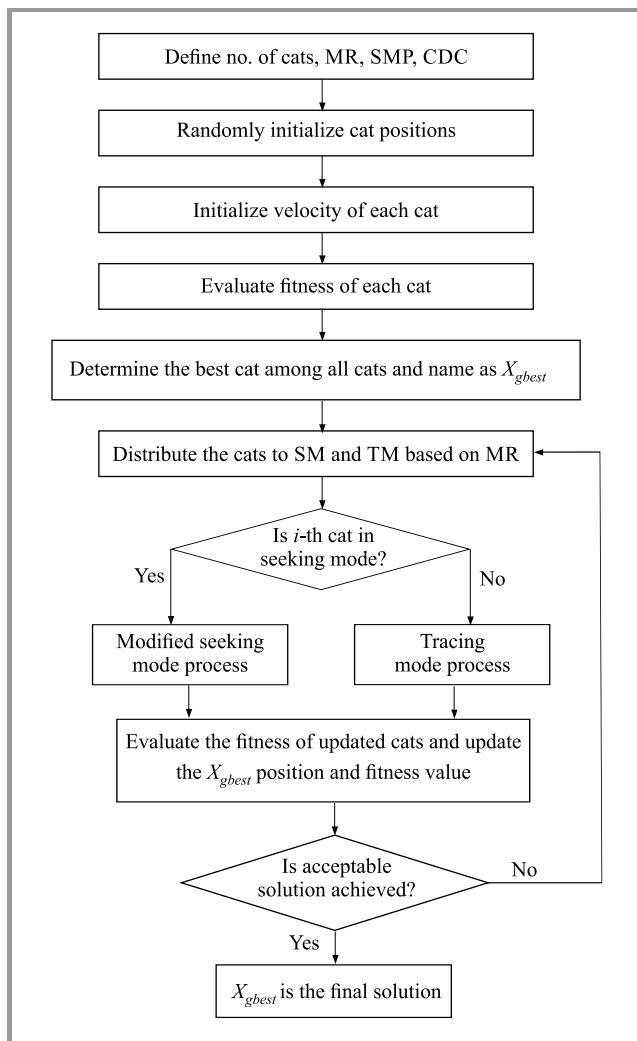


Fig. 3. Steps of the modified CSO algorithm.

### 3.2. Description of AGMCSO Algorithm

Figure 3 demonstrates the 7 phases of the modified CSO algorithm, which are:

1. in the D-dimensional solution space, a finite amount of cats is initialized randomly;
2. the velocity of the cats is initialized;
3. the fitness value of each cat is calculated, the cat with the highest fitness value is picked and the appropriate position of the cat is stored in the memory as  $X_{gbest}$ ;
4. the cats are shifted to the SM and TM depending on their flags, according to MR. In turn, if the cat's flag is set to SM, the cat will be directed to SM. Otherwise, the cat will move to the TM process;
5. the fitness of each altered cat is calculated after two modes have been completed and the cat's best position is stored as  $X_{i,j}$ ;
6.  $X_{gbest}$  and  $X_{i,j}$  fitness values are compared and the best position is updated as  $X_{gbest}$ ;
7. the program ends, if the required solution is obtained or else steps from 4–7 are repeated.

## 4. Benchmark Functions

In order to estimate the efficiency of techniques influenced by nature, common benchmark issues are used. They are classified into a few different categories and are considered to be multimodal or unimodal. Table 1 presents the characteristics of such benchmark problems. The global optimum  $x^*$ , global solution  $f(x^*)$ , acceptable solution and

Table 1  
Benchmark test functions

Name	Symbol	Description	$x^*$	$f(x^*)$	Search range
Sphere	$f_1(x)$	$\sum_{i=1}^D x_i^2$	$0, \dots, 0$	0	$[-5.12, 5.12]^D$
Zakharov	$f_2(x)$	$\sum_{i=1}^E x_i^2 + \left[ \sum_{i=1}^D 0.5ix_i \right]^2 + \left[ \sum_{i=1}^D 0.5ix_i \right]^4$	$0, \dots, 0$	0	$[-5, 10]^D$
Rosenbrock	$f_3(x)$	$\sum_{i=1}^{D-1} [100(x_{i+1} - x_i^2)^2 + (x_i - 1)^2]$	$1, \dots, 1$	0	$[-5, 10]^D$
Levy	$f_e(x)$	$\sin^2(\pi\omega_1) + \sum_{i=1}^{D-1} (\omega_i - 1)[1 + 10\sin^2(\pi\omega_i + 1)] + (\omega_d - 1)^2[1 + \sin^2(2\pi\omega_d)]$	$1, \dots, 1$	0	$[-10, 10]^D$
Ackley	$f_5(x)$	$-20e^{-b\sqrt{\frac{1}{D}\sum_{i=1}^D x_i^2}} - e^{\frac{1}{D}\sum_{i=1}^D \sqrt{\cos(cx_i)}} + a + e^1$	$0, \dots, 0$	0	$[-32, 32]^D$
Rastrigin	$f_6(x)$	$10d + \sum_{i=1}^D [x_i^2 - 10\cos(2\pi x_i)]$	$0, \dots, 0$	0	$[-5, 10]^D$
Griewank	$f_7(x)$	$\sum_{i=1}^D \frac{x_i^2}{4000} - \prod_{i=1}^D \cos\left(\frac{x_i}{\sqrt{i}}\right) + 1$	$0, \dots, 0$	0	$[-600, 600]^D$

search range of the benchmark problems have been listed. Problems  $f_1 - f_4$  are unimodal and  $f_5 - f_7$  are multimodal. For all cases the acceptable solution is set at  $10^{-6}$ . Numerous trials have been performed using seven benchmark functions to compare the proposed AGMCSO using

Table 2  
AGMCSO, CSO and PSO parameters

AGMCSO		CSO		PSO	
Factor	Amount	Factor	Amount	Factor	Amount
Primary cats	50	Primary cats	50	Swarm size	135
SRD	0.8 (80%)	SRD	0.3 (30%)	$r_1, r_2$	[0, 1]
CDC	80%	CDC	80%	$c_1$	2
SMP	5	SMP	5	$\omega$	0.2-0.9
MR	0.8	MR	0.8	-	-
$r$	[0, 1]	$r$	[0, 1]	-	-
$\omega$	0.2-0.9	$\omega$	0.2-0.9	-	-
$c_1$	2	$c_1$	2	-	-

Table 3  
Comparison of average CPU time, convergence speed and SR

Function		AGMCSO	PSO	CSO
$f_1$	FEA	<b>1360</b>	-	47450
	Time	<b>0.0877 s</b>	-	3.45 s
	SR	<b>100%</b>	0	100%
$f_2$	FEA	<b>2108</b>	-	-
	Time	<b>0.104 s</b>	-	-
	SR	<b>100%</b>	0	0
$f_3$	FEA	<b>340</b>	-	38090
	Time	<b>0.058 s</b>	-	7.24 s
	SR	<b>100%</b>	0	100%
$f_4$	FEA	<b>2006</b>	-	-
	Time	<b>0.0757 s</b>	-	-
	SR	<b>100%</b>	0	0
$f_5$	FEA	<b>2380</b>	145800	38480
	Time	<b>0.1254 s</b>	10.12	4.53 s
	SR	<b>100%</b>	34	100%
$f_6$	FEA	<b>2312</b>	-	69550
	Time	<b>0.0726 s</b>	-	4.64 s
	SR	<b>100%</b>	9	199%
$f_7$	FEA	<b>1394</b>	-	194740
	Time	<b>0.1143 s</b>	-	82.42 s
	SR	<b>100%</b>	0	100%

Notes:  
 Bold figures indicate the best results obtained (with all algorithms taken into consideration).  
 “-” means no runs performed by the algorithm have achieved the acceptable solution.  
 FEA is calculated to achieve the adequate solution over the number of successful runs.  
 SR shows the percentage of independent runs that have efficiently found the adequate solution.

a 30-dimensional problem with the classic PSO and CSO approaches. The simulation parameters are listed in Table 2. For all the experiments the average value, the average standard deviation and the number of function evaluations needed to achieve the acceptable solution (FEA) are listed in Table 3. The accuracy of solutions obtained using the proposed AGMCSO, CSO and PSO approaches for a 30-dimensional problem is presented in Table 4.

Table 4  
Comparison of solution accuracy for 30-D problems between AGMCSO, CSO, PSO (bold figures mean the best result)

	AGMCSO	CSO	PSO
$f_1$	<b><math>7.77 \cdot 10^{-291} \pm 0</math></b>	$3.41 \cdot 10^{-40} \pm 1.99 \cdot 10^{-41}$	$30.6 \pm 19$
$f_2$	<b><math>7.8 \cdot 10^{-268} \pm 0</math></b>	$2.72 \cdot 10^{-52} \pm 0.24 \cdot 10^{-23}$	$5 \cdot 10^{20} \pm 15$
$f_3$	<b><math>50 \pm 0</math></b>	$29.6 \pm 2.1$	$168 \pm 6.7$
$f_4$	<b><math>0 \pm 0</math></b>	$3.1 \cdot 10^{-24} \pm 0.15 \cdot 10^{-40}$	$18.1 \pm 23$
$f_5$	<b><math>8.88 \cdot 10^{-16} \pm 0</math></b>	$4.68 \cdot 10^{-5} \pm 3.05 \cdot 10^{-5}$	$1 \pm 0.6$
$f_6$	<b><math>0 \pm 0</math></b>	$3.18 \cdot 10^{-14} \pm 0.169$	$3.5 \pm 8.9$
$f_7$	<b><math>0 \pm 0</math></b>	$1.23 \cdot 10^{-4} \pm 2.5 \cdot 10^{-4}$	$5.1 \pm 1.8$

Computational complexity is the main performance metric for evaluating performance of an algorithm. It may be measured by the average CPU time or by the average FEA required to reach an acceptable solution. The success rate (SR) indicator is specified as the percentage of independent runs that have effectively achieved the desired solution. The results obtained illustrate that AGMCSO outperforms CSO and PSO in terms of convergence rate and solution

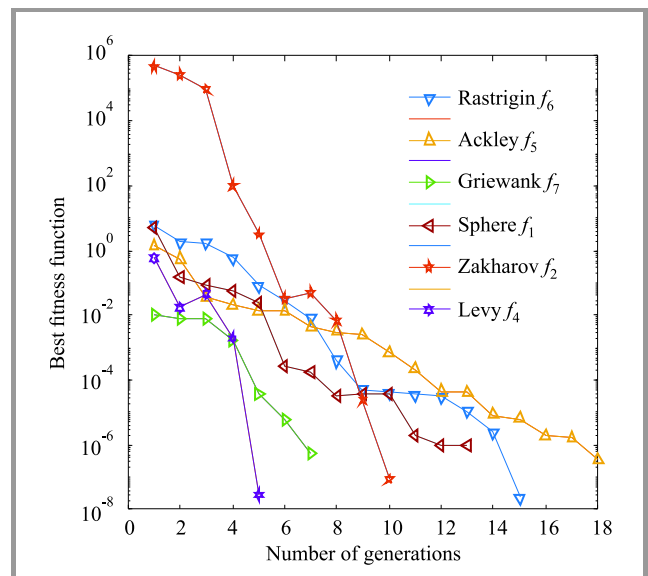


Fig. 4. Evolutionary process of fitness functions  $f_1, f_2,$  and  $f_4-f_6$  for 30 dimensions.

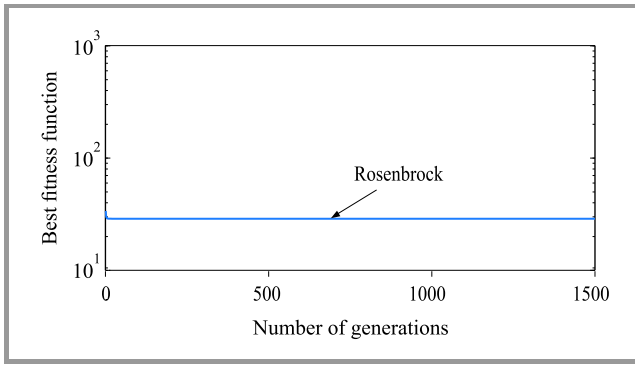


Fig. 5. Evolutionary process of fitness function  $f_3$ .

accuracy. AGMCSO achieved global solutions for all 30-dimensional multi-modal problems with minimum function evaluations. AGMCSO achieves acceptable solutions faster than CSO and PSO. For example, if we consider the 30-D multimodal Griewank function  $f_7$  AGMCSO requires, on average, 1394 function evaluations vs. a 194740 needed by CSI in order to reach adequate solution accuracy of  $10^{-6}$ . Table 3 shows that for all the benchmark functions, the SR for AGMCSO is 100% for all the dimensions whereas the PSO and CSO fails to reach 100% of SR.

Figure 4 shows the convergence plots between the number of generations and the fitness function for  $f_1, f_2, f_4-f_6$ . A similar convergence plot for  $f_3$  is shown in Fig. 5.

4.1. Comparisons with Other Evolutionary Algorithms

Table 5 presents a comparison of the proposed AGMCSO solution with a few existing 30-D algorithms. The algorithms include fast evolutionary algorithm (FEP), adaptive differential evaluation with optional archive (JADE), comprehensive learning PSO (CLPSO), orthogonal learning particle swarm optimization (OLPSO-L), detecting, shrink-

ing and local learning strategy PSO (DSLPSO), enhanced parallel cat swarm optimization (EPCSO), and cat swarm optimization with adaptive parameter control (NCSO). Except for the Rosenbrock function  $f_3$ , AGMCSO offers the best accuracy and also outperforms the current updated CSO algorithms. The average number of FEAs needed to achieve the suitable solution is also smaller.

5. AGMCSO Applications

Here, two examples of the AGMCSO algorithm are presented based on linear array designs selected from the literature.

5.1. Linear Antenna Array

Consider an  $M$ -element, uniformly illuminated linear antenna array positioned on the  $x$  axis (Fig. 6). The antenna array factor in the azimuth plane of  $M = 2N$  is:

$$AF(X, \theta) = 2 \sum_{n=1}^N \cos[kX_n \cos(\theta)] \quad M = 2N, \quad (9)$$

where the azimuthal angle is given as  $\theta$ , the  $n$ -th element position is given as  $X_n$ , the wavenumber is given by  $k = \frac{2\pi}{\lambda}$  and the wavelength by  $\lambda$ .

Selection of the distance between the antenna’s elements is crucial. The positioning of adjacent elements too far apart leads to grating lobes, and positioning the too close to each other leads to mutual coupling. Thus, the constraint of adjacent element spacing has to be considered during the optimization process. The distance between antenna elements within the array is constrained as  $|x_i - x_j| \geq 0.25\lambda$ . With the parameter configuration for AGMCSO, CSO and PSO algorithms retrieved from Table 2, the algorithm is executed 10 times to show the efficacy of the suggested method.

Table 5  
Comparison of AGMCSO with evolutionary algorithms (bold print = best result)

Function	FEP [38]	JADE [8]	CLPSO [15]	OLPSO-L [18]	DSL-PSO [20]	EPCSO [27]	NCSO [29]	AGMCSO
$f_1$	$5.7 \cdot 10^{-4} \pm 1.3 \cdot 10^{-4}$	$1.3 \cdot 10^{-54} \pm 9.2 \cdot 10^{-54}$	$4.4 \cdot 10^{-14} \pm 1.71 \cdot 10^{-14}$	$1.1 \cdot 10^{-38} \pm 1.21 \cdot 10^{-38}$	$1.3 \cdot 10^{-49} \pm 7.31 \cdot 10^{-49}$	$0 \pm 0$	$1.68 \cdot 10^{-21}$	<b><math>7.77 \cdot 10^{-291} \pm 0</math></b>
$f_2$	–	–	–	–	–	–	–	<b><math>7.8 \cdot 10^{-291} \pm 0</math></b>
$f_3$	$5.0 \pm 5.8$	$0.3 \pm 1.1$	$21 \pm 2.9$	$1.2 \pm 1.4$	$51 \pm 42$	N/A	23.5	<b><math>-1.019</math></b>
$f_4$	–	–	–	–	–	–	–	<b><math>0 \pm 0</math></b>
$f_5$	$180 \pm 2100$	$4.4 \cdot 10^{-15} \pm 0$	$0 \pm 0$	$4.14 \cdot 10^{-14} \pm 0$	$1.2 \cdot 10^{-14} \pm 4.6 \cdot 10^{-15}$	$6.40 \cdot 10^{-15} \pm 3.7 \cdot 10^{-15}$	$6.54 \cdot 10^{-12}$	<b><math>8.88 \cdot 10^{-16} \pm 0</math></b>
$f_6$	$460 \pm 1200$	$0 \pm 0$	$4.85 \cdot 10^{-10} \pm 0.361$	$0 \pm 0$	$4.7 \cdot 10^{-16} \pm 9.71 \cdot 10^{-17}$	$86 \pm 10$	76.6	<b><math>0 \pm 0</math></b>
$f_7$	$1600 \pm 2200$	$2.0 \cdot 10^{-4} \pm 1.4 \cdot 10^{-3}$	$31 \pm 0.46$	$0 \pm 0$	$170 \pm 2.21 \cdot 10^{-3}$	$3.50 \cdot 10^{-3} \pm 7.10 \cdot 10^{-3}$	0	<b><math>0 \pm 0</math></b>

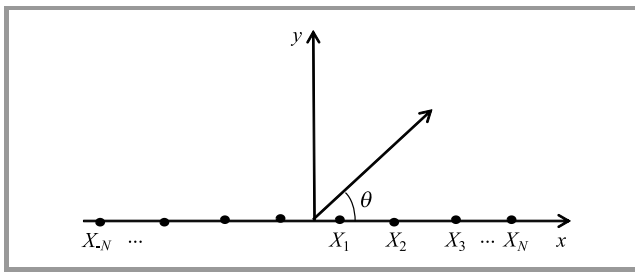


Fig. 6. Illustration of linear antenna array with non-uniform spacing.

In the design process, the aim is to minimize the peak side-lobe level in the sidelobe region by optimizing the spacings between the antenna’s elements using the proposed AGMCSO method. The objective function can be modeled as:

$$Obj(X) = \max \left( \frac{|AF(X, \theta_0)|}{|AF_{max}|} \right), \quad (10)$$

where  $X = (X_1, X_2, \dots, X_N)$  is the element position vector,  $\theta_0$  is defined as the angular region excluding the main lobe, the main peak of the pattern is  $AF_{max}$ .

Table 6  
Positions of a 20-element array optimized using AGMCSO and CSO

Element ( $n$ )	Position $\frac{x_n}{\lambda}$	
	AGMCSO	CSO
1	0.2642	0.2504
2	0.5288	0.7625
3	0.7920	1.2441
4	1.0920	1.7153
5	1.3470	2.3773
6	1.7122	2.8824
7	2.0428	3.5296
8	2.4654	4.3169
9	2.9505	5.2229
10	3.5994	6.0549

In the first example, a 20-element array is synthesized using the proposed AGMCSO and CSO approaches to minimize PSLL in the sidelobe region. Table 6 shows AGMCSO- and CSO-optimized element positions relative to Z. The array patterns obtained using the AGMCSO algorithm along with the CSO-optimized array and uniformly illuminated periodic array (UIPA) are shown in Fig. 7. Convergence characteristics for 10 independent runs are shown in Fig. 8. The comparison of convergence characteristics of AGMCSO and CSO is shown in Fig. 9. The comparison of PSLL obtained using CSO, fully informed particle swarm optimization (FIPSO) [17], perturbation particle swarm optimization (PPSO) [17] and AGMCSO is presented in Table 7.

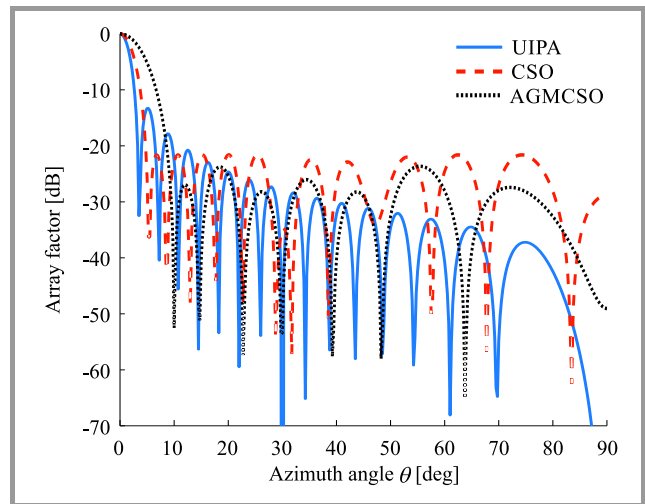


Fig. 7. Radiation pattern of the 20-element array using AGMCSO, CSO and UIPA.

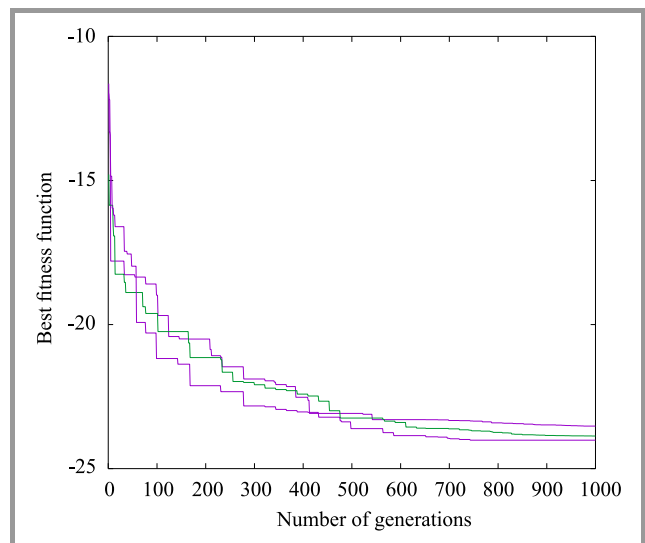


Fig. 8. Evolutionary process of the fitness value of a 20-element array using AGMCSO.

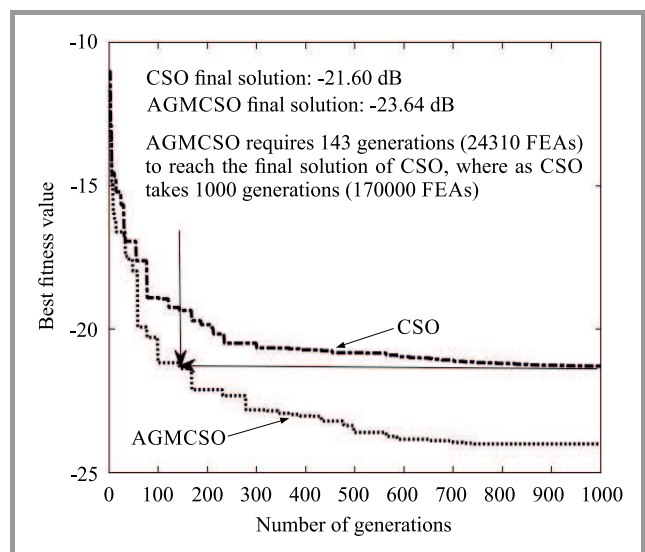


Fig. 9. Evolutionary process of the fitness value of a 20-element linear array using CSO and AGMCSO.

Table 7  
Comparative results for the synthesis of a 20-element linear unequally spaced array

Number of elements	Algorithm	PSLL [dB]	Aperiodic FNBW	UIPA FNBW
20	CSO	-21.60	10	3.5
	FIPSO	-20.58		
	PPSO	-16.85		
	AGMCSO	-23.64		

AGMCSO generate the value of -23.64 dB, whereas CSO, DE, FIPSO and PPSO -21.29 dB, -18.42 dB, -20.58 dB, and -16.84 dB, respectively. AGMCSO shows a low PSLL level that is by -2 dB lower compared with CSO. It can be seen from Fig. 9 that AGMCSO outperforms CSO in terms of the convergence rate. AGMCSO takes 24310 FEAs to reach the final solution with CSO of -21.29 dB. The success rate of achieving a similar final value of AGMCSO is evident from Fig. 8.

5.2. 32-element Linear Array

In the second example, a 32-element array is synthesized to achieve the minimum PSLL. Table 8 shows the positions of elements optimized by using AGMCSO and CSO. A comparison of the PSLL obtained using CSO, DE, CLPSO and AGMCSO is shown in Table 9. The best PSLL for a 32-element linear array in 10 runs was found to be -20.69 dB for CSO, -22.65 dB for DE [7], -22.75 dB

Table 8  
Positions of a 32-element array optimized using AGMCSO and CSO

Element (n)	Position $\frac{x_n}{\lambda}$	
	AGMCSO	CSO
1	0.3934	0.2952
2	0.6988	0.9181
3	1.0263	1.5182
4	1.3399	2.1504
5	1.7294	2.8029
6	2.1038	3.4503
7	2.3565	4.1665
8	2.8756	4.8664
9	3.2624	5.5887
10	3.7256	6.3456
11	4.1031	7.0395
12	4.7333	7.8415
13	5.2702	8.6343
14	5.8879	9.7310
15	6.7224	11.4967
16	7.4994	12.2483

Table 9  
Comparative results for the synthesis of a 32-element linear unequally spaced array

Number of elements	Algorithm	PSLL [dB]	Aperiodic FNBW	UIPA FNBW
32	CSO	-20.69	5	3.5
	DE	-22.65		
	CLPSO	-22.75		
	AGMCSO	-23.40		

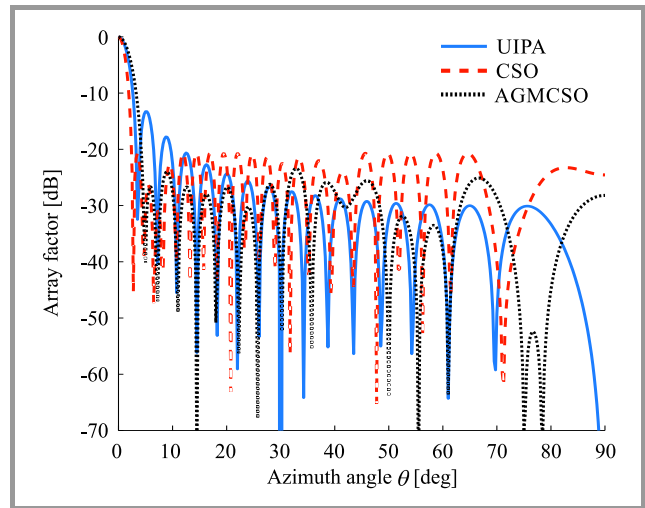


Fig. 10. Radiation pattern of the 32 elements array using AGMCSO, CSO, and UIPA.

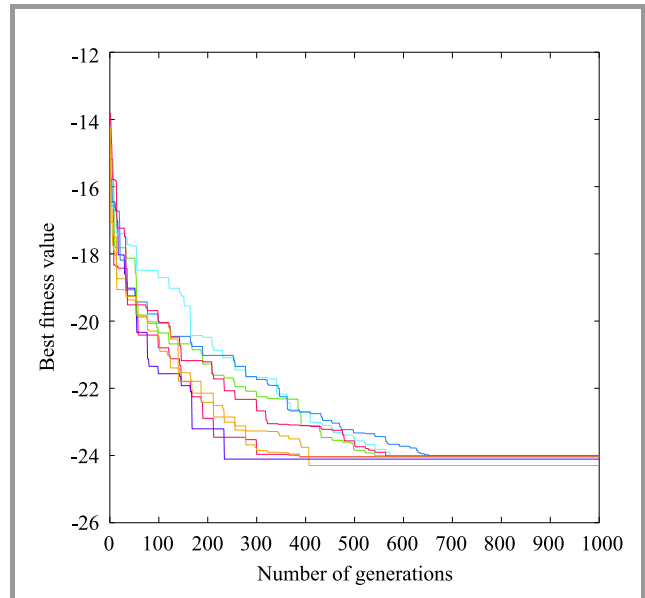
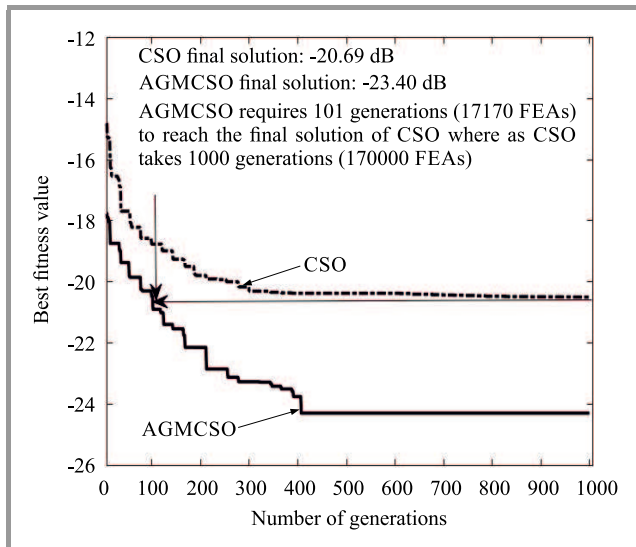


Fig. 11. Evolutionary process of the fitness value of the 32 elements array using AGMCSO.

for CLPSO [15] and -23.4076 dB for AGMCSO. The radiation pattern achieved using AGMCSO, along with UIPA and CSO, is shown in Fig. 10. The convergence character-

istics for a 32-element linear array using AGMCSO for 10 independent runs are shown in Fig. 11. The convergence plots of AGMCSO and CSO are shown in Fig. 12.



**Fig. 12.** Evolutionary process of the fitness value of a 32-element linear array using CSO and AGMCSO.

AGMCSO produces a PSLL that is by  $-2.71$  dB lower compared with CSO (Table 9). CSO takes 170000 FEAs to reach its final solution. AGMCSO requires 24310 FEAs to reach the final solution of CSO (Fig. 12) and the deviation in achieving the final solution is low for several independent runs and shows the reliability of the proposed AGMCSO method (Fig. 11).

Overall, AGMCSO outperforms the traditional CSO approach in terms of low PSLL and convergence speed. Accelerated Gaussian mutation leads to defining positions located at better locations, by preventing premature convergence. AGMCSO had shown superior results compared to the classic CSO approach, in terms of solution accuracy and offers a PSLL value that is by  $-2$  dB lower compared to CSO. Computational speed is greatly enhanced by the proposed AGMCSO methods. AGMCSO outperforms CSO in terms of convergence speed and requires 15% of the CSO's FEAs to reach the final solution of CSO.

## 6. Conclusion

In this paper, unequally spaced arrays with low PSLL have been designed using a modified AGMCSO optimization algorithm. The Gaussian mutation with an acceleration parameter has been introduced in the position-updated equation of the traditional CSO approach to enhance solution accuracy and convergence rate. The effectiveness of AGMCSO has been benchmarked using multimodal, 30-, 100- and 1000-dimensional problems. The simulations show that the proposed AGMCSO algorithm outperforms popular optimization techniques in terms of solution accuracy and convergence rate. A detailed analysis of the impact of all AGMCSO parameters on its overall performance has

been carried out. We have applied AGMCSO in the synthesis of unequally spaced antenna arrays to suppress PSLL. 20- and 32-element linear arrays have been synthesized and the numerical results illustrate that AGMCSO outperforms the conventional and modified algorithm in terms of low PSLL with narrow FNBW.

## References

- [1] D. Khzmalyan and A. S. Kondrat'yev, "Phase-only synthesis of antenna array amplitude pattern", *Int. J. Electron.*, vol. 81, no. 5, pp. 585–589, 1996 (DOI: 10.1080/002072196136490).
- [2] K. K. Yan and Y. Lu, "Sidelobe reduction in array pattern synthesis using genetic algorithm", *IEEE Trans. Anten. Propag.*, vol. 45, no. 7, pp. 1117–1122, 1997 (DOI: 10.1109/8.596902).
- [3] F. J. Ares-Pena, J. A. Gonzalez, E. Lopez, and S. R. Rengarajan, "Genetic algorithms in the design and optimization of antenna array patterns", *IEEE Trans. Anten. Propag.*, vol. 47, no. 3, pp. 506–510, 1999 (DOI: 10.1109/8.768786).
- [4] K. Chen, Z. He, and C. Han, "A modified real GA for the sparse linear array synthesis with multiple constraints", *IEEE Trans. Anten. Propag.*, vol. 54, no. 7, pp. 2169–2173, 2006 (DOI: 10.1109/TAP.2006.877211).
- [5] L. Cen, Z. L. Yu, and W. Ser, "Linear aperiodic array synthesis using an improved genetic algorithm", *IEEE Trans. Anten. Propag.*, vol. 60, no. 2, pp. 895–902, 2012 (DOI: 10.1109/TAP.2011.2173111).
- [6] T. Reshma, K. V. Reddy, D. Pratap, and V. Agilan, "Parameters optimization using fuzzy rule-based multi-objective genetic algorithm for an event-based Rainfall-Runoff model", *Water Resour. Manag.*, vol. 32, no. 3, pp. 1501–1516, 2018 (DOI: 10.1007/s11269-017-1884-2).
- [7] D. G. Kurup, M. Himidi, and A. Rydberg, "Synthesis of uniform amplitude unequally spaced antenna arrays using the differential evolution algorithm", *IEEE Trans. Anten. Propag.*, vol. 51, no. 9, pp. 2210–2217, 2003 (DOI: 10.1109/TAP.2003.816361).
- [8] J. Q. Zhang and A. C. Sanderson, "JADE: Adaptive differential evolution with optional external archive", *IEEE Trans. Evol. Comput.*, vol. 13, no. 5, pp. 945–958, 2009 (DOI: 10.1109/TEVC.2009.2014613).
- [9] C. Lin, A.-Y. Qing, and Q.-Y. Feng, "Synthesis of unequally spaced antenna arrays by using differential evolution", *IEEE Trans. Anten. Propag.*, vol. 58, no. 8, pp. 2553–2561, 2010 (DOI: 10.1109/TAP.2010.2048864).
- [10] S. K. Goudos, K. Siakavara, and T. Samaras, "Sparse linear array synthesis with multiple constraints using differential evolution with strategy adaptation", *IEEE Anten. Wirel. Propag. Lett.*, vol. 10, pp. 670–673, 2011 (DOI: 10.1109/LAWP.2011.2161256).
- [11] S. K. Goudos *et al.*, "Self-adaptive differential evolution applied to real-valued antenna and microwave design problems", *IEEE Trans. Anten. Propag.*, vol. 59, no. 4, pp. 1286–98, 2011 (DOI: 10.1109/TAP.2011.2109678).
- [12] F. Zhang, W. Jia, and M. Yao, "Linear aperiodic array synthesis using differential evolution algorithm", *IEEE Anten. Wirel. Propag. Lett.*, vol. 12, pp. 797–800, 2013 (DOI: 10.1109/LAWP.2013.2270930).
- [13] D. W. Boeringer and D. H. Werner, "Particle swarm optimization versus genetic algorithms for phased array synthesis", *IEEE Trans. Anten. Propag.*, vol. 52, no. 3, pp. 771–779, 2004 (DOI: 10.1109/TAP.2004.825102).
- [14] M. M. Khodier and C. G. Christodoulou, "Linear array geometry synthesis with minimum sidelobe level and null controlling using particle swarm optimization", *IEEE Trans. Anten. Propag.*, vol. 53, no. 8, pp. 2674–2679, 2005 (DOI: 10.1109/TAP.2005.851762).
- [15] J. J. Liang, A. K. Qin, P. N. Suganthan, and S. Baskar, "Comprehensive learning particle swarm optimizer for global optimization of multimodal functions", *IEEE Trans. Evol. Comput.*, vol. 10, no. 3, pp. 281–295, 2006 (DOI: 10.1109/TEVC.2005.857610).

[16] S. K. Goudos *et al.*, "Application of comprehensive learning particle swarm optimizer to unequally spaced linear array synthesis with side lobe level suppression and null control", *IEEE Anten. Wirel. Propag. Lett.*, vol. 9, pp. 125–129, 2010 (DOI: 10.1109/LAWP.2010.2044552).

[17] W.-B. Wang, Q.-Y. Feng, and D. Liu, "Application of chaotic particle swarm optimization algorithm to pattern synthesis of antenna arrays", *Progr. in Electromag. Res.*, vol. 115, pp. 173–189, 2011 (DOI:10.2528/PIER11012305).

[18] Z. H. Zhan, J. Zhang, and Y. Li, "Orthogonal learning particle swarm optimization", *IEEE Trans. Evol. Comput.*, vol. 15, no. 6, pp. 281–295, 2011 (DOI: 10.1109/TEVC.2010.2052054).

[19] R. Bhattacharya, T. K. Bhattacharyya, and R. Garg, "Position mutated hierarchical particle swarm optimization and its application in synthesis of unequally spaced antenna arrays", *IEEE Trans. Anten. Propag.*, vol. 60, no. 7, pp. 3174–2181, 2012 (DOI: 10.1109/TAP.2012.2196917).

[20] X. Xia, J. Liu, and Z. Hu, "An improved particle swarm optimizer based on tabu detecting and local learning strategy in a shrunk search space", *Appl. Soft Comput.*, vol. 23, pp. 76–90, 2014 (DOI:10.1016/j.asoc.2014.06.012).

[21] L. A. Bewoor, V. C. Prakash, and S. U. Sapkal, "Evolutionary hybrid particle swarm optimization algorithm for solving np-hard no-wait flow shop scheduling problems", *Algorithms*, vol. 10, no. 4, pp. 1–17, 2017 (DOI: 10.3390/a10040121).

[22] A. Ahilan *et al.*, "Segmentation by fractional order Darwinian particle swarm optimization based multilevel thresholding and improved lossless prediction based compression algorithm for medical images", *IEEE Access*, vol. 7, pp. 89570–89580, 2019 (DOI: 10.1109/ACCESS.2019.2891632).

[23] R. R. Eva and Q. T. Oscar, "Linear array synthesis using an ant colony optimization based algorithm", *IEEE Trans. Anten. Propag.*, vol. 49, no. 2, pp. 70–79, 2007 (DOI: 10.1109/MAP.2007.376644).

[24] M. S. Kumar and M. Venkatesan, "Multi-objective task scheduling using hybrid genetic ant colony optimization algorithm in cloud environment", *Wirel. Pers. Commun.*, vol. 107, pp. 1835–1848, 2019 (DOI: 10.1007/s11277-019-06360-8).

[25] C. J. Malar *et al.*, "Multi constraints applied energy efficient routing technique based on ant colony optimization used for disaster resilient location detection in mobile ad-hoc network", *J. of Ambient Intell. and Human. Comput.*, vol. 12, pp. 4007–4017, 2021 (DOI: 10.1007/s12652-020-01767-9).

[26] G. Panda, P. M. Pradhan, and B. Majhi, "IIR system identification using cat swarm optimization", *Expert Syst. Appl.: an Int. J.*, vol. 38, no. 10, pp. 12671–12683, 2011 (DOI: 10.1016/j.eswa.2011.04.054).

[27] P.-W. Tsai, J.-S. Pan, S. M. Chen, and B. Y. Liao, "Enhanced parallel cat swarm optimization based on the Taguchi method", *Expert Syst. with Appl.*, vol. 39, no. 7, pp. 6309–6319, 2012 (DOI:10.1016/j.eswa.2011.11.117).

[28] L. Pappula and D. Ghosh, "Linear antenna array synthesis using cat swarm optimization", *AEU – Int. J. Electron. Commun.*, vol. 68, no. 6, pp. 540–549, 2014 (DOI: 10.1016/j.aeue.2013.12.012).

[29] J. Wang, "A new cat swarm optimization with adaptive parameter control", in *Genetic and Evolutionary Computing: Proceeding of the Eighth International Conference on Genetic and Evolutionary Computing, October 18-20, 2014, Nanchang, China*, H. Sun *et al.*, Eds. *AISC*, vol. 329, pp. 69–78. Springer, 2015 (DOI: 10.1007/978-3-319-12286-1\_8).

[30] T. Nireekshana, G. Kesava Rao, and S. Sivanaga Raju, "Available transfer capability enhancement with FACTS using cat swarm optimization", *Ain Shams Engin. J.*, vol. 7, no. 1, pp. 159–167, 2016 (DOI: 10.1016/j.asej.2015.11.011).

[31] L. Pappula and D. Ghosh, "Synthesis of linear aperiodic array using Cauchy mutated cat swarm optimization", *AEU – Int. J. of Electron. and Commun.*, vol. 72, pp. 52–64, 2017 (DOI: 10.1016/j.aeue.2016.11.016).

[32] L. Pappula and D. Ghosh, "Cat swarm optimization with normal mutation for fast convergence of multimodal functions", *Appl. Soft Comput.*, vol. 66, pp. 473–491, 2018 (DOI: 10.1016/j.asoc.2018.02.012).

[33] R. Rajakumar, J. Amudhavel, P. Dhavachelvan, and T. Vengattaraman, "GWO-LPWSN: Grey Wolf optimization algorithm for node localization problem in wireless sensor networks", *J. of Comp. Netw. and Commun.*, vol. 2, pp. 1–10, 2017 (DOI:10.1155/2017/7348141).

[34] X. Li and K. M. Luk, "The grey wolf optimizer and its applications in electromagnetics", *IEEE Trans. on Antenn. and Propag.*, vol. 68, no. 3, 2020 (DOI: 10.1109/TAP.2019.2938703).

[35] M. Rajeswari, J. Amudhavel, S. Pothula, and P. Dhavachelvan, "Directed bee colony optimization algorithm to solve the nurse rostering problem", *Computat. Intell. and Neurosci.*, vol. 2017, Article ID 6563498, 2017 [Online]. Available: <https://downloads.hindawi.com/journals/cin/2017/6563498.pdf>

[36] R. S. Raghav, J. Amudhavel, and P. Dhavachelvan, "Enhanced artificial bee colony optimization for solving economic load dispatch", *IIOAB J.*, vol. 8, no. 2, pp. 208–216, 2017 [Online]. Available: [https://www.iioab.org/IIOABJ\\_8.2\\_208-216.pdf](https://www.iioab.org/IIOABJ_8.2_208-216.pdf)

[37] S.-C. Chu and P.-W. Tsai, "Computational intelligence based on the behavior of cats", *Int. J. Innov. Comput., Inform. and Contr. (IJICIC)*, vol. 3, no. 1, pp. 163–173, 2007 [Online]. Available: <https://citeseerx.ist.psu.edu/viewdoc/download?doi=10.1.1.103.3698&rep=rep1&type=pdf>

[38] X. Yao, Y. Liu, and G. M. Lin, "Evolutionary programming made faster", *IEEE Trans. Evol. Comput.*, vol. 3, no. 2, pp. 82–102, 1999 (DOI: 10.1109/4235.771163).



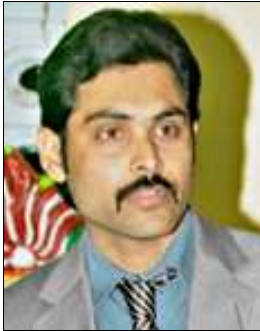
**K. Prasanna Kumar** completed his Ph.D. from Koneru Lakshmaiah Education Foundation in 2021, focusing on antenna arrays and optimization techniques. He is currently working as the Head of R&D at St. Peter's Engineering College, Hyderabad. He had obtained his M.Tech. from Pydah College of Engineering and Technology and B.Tech. in ECE from MVGR College of Engineering. He has 13 years of teaching experience and handled various academic and administrative roles.

E-mail: [prasannakorada@gmail.com](mailto:prasannakorada@gmail.com)  
 Department of ECE  
 St. Peter's Engineering College  
 Hyderabad, India



**Lakshman Pappula** completed his Ph.D. from Indian Institute of Technology Bhubaneswar in 2017, specializing in antenna arrays and optimization techniques. He also completed his M.Sc. in RF and Microwave Engineering. Currently, he is working as the Deputy HOD and an Associate Professor at the Department of Electronics and Communications Engineering, KLEF, Guntur, Andhra Pradesh, India. His interests include antenna theory, electromagnetic fields and propagation, communication theory, soft computing, artificial neural network, radar and navigational aids, wireless and communication theory.

E-mail: lakshman.pappula@kluniversity.in  
Department of ECE  
Koneru Lakshmaiah Education Foundation  
Guntur, India



**B. T. P. Madhav** works as Professor and Associate Dean at KLEF. His research interests include antennas, liquid crystals applications and wireless communications.

E-mail: btpmadhav@kluniversity.in  
Department of ECE  
Koneru Lakshmaiah Education Foundation  
Guntur, India



**V. S. V. Prabhakar** completed his Ph.D. from JNTU, Kakinada in the field of VLSI design. He completed his M.Sc. in chip systems in Sweden, and B.Tech. from Osmania University. Currently, he is working as Professor and Director, Industry Connect, at the Koneru Lakshmaiah Education Foundation. He also worked as Cisco Chair in

IIDT, Tirupathi, as Head of Department, ECE in KLEF, and as Principal at the Avanthi Institute of Engineering and Technology.

E-mail: prabhakarvsv@kluniversity.in  
Department of ECE  
Koneru Lakshmaiah Education Foundation  
Guntur, India



# Information for Authors

*Journal of Telecommunications and Information Technology (JTIT)* is published quarterly. It comprises original contributions, dealing with a wide range of topics related to telecommunications and information technology. **All papers are subject to peer review.** Topics presented in the JTIT report primary and/or experimental research results, which advance the base of scientific and technological knowledge about telecommunications and information technology.

JTIT is dedicated to publishing research results which advance the level of current research or add to the understanding of problems related to modulation and signal design, wireless communications, optical communications and photonic systems, voice communications devices, image and signal processing, transmission systems, network architecture, coding and communication theory, as well as information technology.

Suitable research-related papers should hold the potential to advance the technological base of telecommunications and information technology. Tutorial and review papers are published only by invitation.

**Manuscript.** TEX and LATEX are preferable, standard Microsoft Word format (.doc) is acceptable. The authors JTIT LATEX style file is available:

<https://www.itl.waw.pl/en/jtit-for-authors>

Papers published should contain up to 10 printed pages in LATEX authors style (Word processor one printed page corresponds approximately to 6000 characters).

The manuscript should include an abstract about 150–200 words long and the relevant keywords. The abstract should contain statement of the problem, assumptions and methodology, results and conclusion or discussion on the importance of the results. Abstracts must not include mathematical expressions or bibliographic references.

Keywords should not repeat the title of the manuscript. About four keywords or phrases in alphabetical order should be used, separated by commas.

The original files accompanied with pdf file should be submitted by e-mail: [redakcja@itl.waw.pl](mailto:redakcja@itl.waw.pl)

**Figures, tables and photographs.** Original figures should be submitted. Drawings in Corel Draw and PostScript formats are preferred. Figure captions should be placed below the figures and can not be included as a part of the figure. Each figure should be submitted as a separated graphic file, in .cdr, .eps, .ps, .png or .tif format. Tables and figures should be numbered consecutively with Arabic numerals.

Each photograph with minimum 300 dpi resolution should be delivered in electronic formats (TIFF, JPG or PNG) as a separated file.

**References.** All references should be marked in the text by Arabic numerals in square brackets and listed at the end of the paper in order of their appearance in the text, including exclusively publications cited inside. Samples of correct formats for various types of references are presented below:

- [1] Y. Namiyama, Relationship between nonlinear effective area and mode field diameter for dispersion shifted fibres, *Electron. Lett.*, vol. 30, no. 3, pp. 262–264, 1994.
- [2] C. Kittel, *Introduction to Solid State Physics*. New York: Wiley, 1986.
- [3] S. Demri and E. Orłowska, Informational representability: Abstract models versus concrete models, in *Fuzzy Sets, Logics and Knowledge-Based Reasoning*, D. Dubois and H. Prade, Eds. Dordrecht: Kluwer, 1999, pp. 301–314

**Biographies and photographs of authors.** A brief professional authors biography of up to 200 words and a photo of each author should be included with the manuscript.

**Galley proofs.** Authors should return proofs as a list of corrections as soon as possible. In other cases, the article will be proof-read against manuscript by the editor and printed without the author's corrections. Remarks to the errata should be provided within one week after receiving the offprint.

**Copyright.** Manuscript submitted to JTIT should not be published or simultaneously submitted for publication elsewhere. By submitting a manuscript, the author(s) agree to automatically transfer the copyright for their article to the publisher, if and when the article is accepted for publication. The copyright comprises the exclusive rights to reproduce and distribute the article, including reprints and all translation rights. No part of the present JTIT should not be reproduced in any form nor transmitted or translated into a machine language without prior written consent of the publisher.

For copyright form see:

<https://www.itl.waw.pl/en/jtit-for-authors>

---

*Journal of Telecommunications and Information Technology* has entered into an electronic licencing relationship with EBSCO Publishing, the worlds most prolific aggregator of full text journals, magazines and other sources. The text of *Journal of Telecommunications and Information Technology* can be found on EBSCO Publishings databases. For more information on EBSCO Publishing, please visit [www.epnet.com](http://www.epnet.com).

*(Contents Continued from Front Cover)*

**An Investigation of the MIMO Space Time Block Code Based Selective Decode and Forward Relaying Network over  $\eta$ - $\mu$  Fading Channel Conditions**

*R. Shankar et al.*

*Paper*

79

**Improved CSE with DLS-MMSE Criteria in TH-UWB System**

*A. Djebbari and S. A. Elahmar*

*Paper*

93

**Unequally Spaced Antenna Array Synthesis Using Accelerating Gaussian Mutated Cat Swarm Optimization**

*P. K. Kumar, L. Pappula, B. T. P. Madhav, and V. S. V. Prabhakar*

*Paper*

99



National Institute  
of Telecommunications

**Editorial Office**

National Institute  
of Telecommunications  
Szachowa st 1  
04-894 Warsaw, Poland

tel. +48 22 512 81 83  
fax: +48 22 512 84 00  
e-mail: [redakcja@il-pib.pl](mailto:redakcja@il-pib.pl)  
[editorial.office@il-pib.pl](mailto:editorial.office@il-pib.pl)  
<http://www.nit.eu>